Robust design and optimization of forming processes

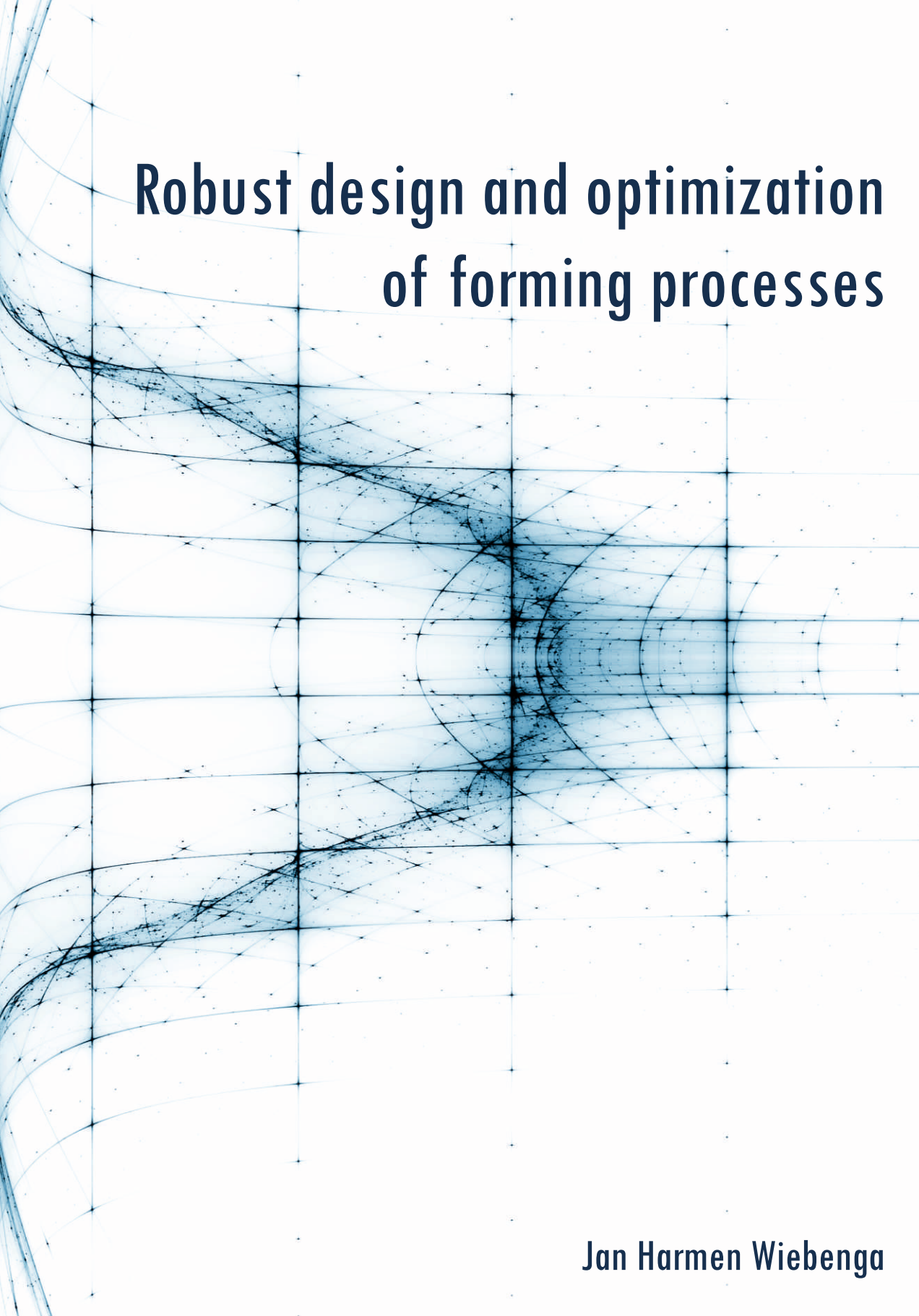

Jan Harmen Wiebenga

ROBUST DESIGN AND OPTIMIZATION OF FORMING PROCESSES

Jan Harmen Wiebenga

De promotiecommissie is als volgt samengesteld:

Voorzitter en secretaris:	
Prof. dr. G.P.M.R. Dewulf	Universiteit Twente
Promotor:	
Prof. dr. ir. A.H. van den Boogaard	Universiteit Twente
Leden:	
Dr. ir. E.H. Atzema	Tata Steel
Prof. D. Banabic	Technical University of Cluj-Napoca
Prof. dr. ir. F.J.A.M. van Houten	Universiteit Twente
Prof. dr. ir. J. Huétink	Universiteit Twente
Prof. dr. ir. A. van Keulen	Technische Universiteit Delft

This research was carried out under project number M22.1.08.303 in the framework of the Research Program of the Materials innovation institute (M2i) in the Netherlands (www.m2i.nl).

Robust design and optimization of forming processes
Wiebenga, Jan Harmen
PhD thesis, University of Twente, Enschede, The Netherlands
February 2014

ISBN 978-90-77172-96-4
Keywords: Forming processes, finite element simulations, robust optimization, uncertainty, material scatter.

Printed by Ipskamp Drukkers B.V., Enschede, The Netherlands

Cover: Abstract representation of a Gaussian distribution in space; an artist impression.

ROBUST DESIGN AND OPTIMIZATION OF FORMING PROCESSES

PROEFSCHRIFT

ter verkrijging van
de graad van doctor aan de Universiteit Twente,
op gezag van de rector magnificus,
prof.dr. H. Brinksma,
volgens besluit van het College voor Promoties
in het openbaar te verdedigen
op vrijdag 21 februari 2014 om 14.45 uur

door

Jan Harmen Wiebenga

geboren op 22 mei 1985

te Groningen

Dit proefschrift is goedgekeurd door de promotor

Prof. dr. ir. A.H. van den Boogaard

Summary

The simulation of forming processes has become a standard procedure in the development of metal products. A current trend in the metal forming industry is the coupling of Finite Element (FE) simulations with an optimization procedure. Using a so-called simulation-based optimization approach, forming processes can be designed for which optimal use is made of the material and process capabilities. The next step is to transfer the numerically designed process to the factory and initiate production, whereby the controllable process settings are set to their optimal deterministic values. However, in practice metal forming processes are subject to input uncertainty or variation. One can think of the variation of material properties, fluctuating process settings or changing environmental conditions. In cases where these uncertainties are neglected in simulation-based optimization, very often an optimal deterministic process design is found which is at the limits of the material and process capabilities. The presence of input variation might lead to violation of the limits in practice, resulting in product rejects. To avoid this undesirable situation, uncertainty has to be taken into account explicitly in the optimization of forming processes.

An optimization strategy has been developed for modeling and efficiently solving simulation-based robust optimization problems of forming processes. The strategy consists of the following main stages: modeling, variable screening, robust optimization, validation and sequential improvement. In the modeling step, input variation is quantified and accounted for explicitly in the optimization strategy. For solving, use is made of a metamodel-based approach combined with Monte Carlo analyses to obtain the statistical measures of the objective function and constraints. The metamodel-based approach is utilized to efficiently couple the computationally expensive FE simulations with an optimization algorithm. The strategy enables finding the optimal process design which meets the constraints, even in the presence of uncertainty. This type of optimal design is referred to as a *robust design* in this thesis.

The strategy has been applied to robust optimization problems of various

industrial metal forming processes, i.e. a roll forming process, a V-bending process, a stretching process and a stretch-drawing process. Several research topics have been treated in more detail and evaluated by application to the industrial forming processes. One of the main challenges in robust optimization of forming processes is to balance the number of time-consuming FE simulations spent on the creation of metamodels with the resulting prediction accuracy of the robust optimum. A sequential robust optimization step has been added to the optimization strategy, based on an expected improvement measure. This step allowed for an increase in the accuracy of the metamodel prediction at regions of interest, as well as an increase in the overall efficiency of the strategy. Next, the topic of numerical noise was evaluated in more detail. Non-linear FE simulations are known to introduce numerical noise, which appears as response scatter around an expected smooth response and has a numerical cause. The noisy response data can result in erroneous metamodels and an inaccurate prediction of the robust optimum. Therefore, the robust optimization strategy has been extended to handle and minimize the deteriorating effect of numerical noise in metamodel-based optimization. Finally, a coupling with the sequential optimization step was made, which enables termination of the sequential optimization algorithm based on the magnitude of numerical noise present in the response data.

One of the most dominant sources of input uncertainty in forming processes is the variation of material properties. An accurate and efficient approach for quantifying and modeling material scatter was proposed. By combining mechanical testing and texture analysis, a stochastic set of material data was efficiently determined based on 41 coils of a forming steel. The modeling approach has been validated by the forming of 41 hemispherical cups using a stretching process. The observed experimental scatter could be reproduced accurately and efficiently using numerical simulations. The collective of material has also been used in a final robust optimization study considering a stretch-drawing process. A deterministic and robust optimization study was performed, excluding and including the effect of material and process scatter respectively. In the resulting optima, a series of stretch-drawing experiments were performed to validate the numerically predicted process robustness. The robust optimum was, indeed, more robust in practice compared to the deterministic optimum and a good agreement with numerical results was obtained, showing a reduction in the number of product rejects. This final optimization study demonstrated the following: that it is necessary to include uncertainty in the optimization strategy, that it can be done efficiently, and that it leads to a considerably improved robustness of the resulting forming process.

Samenvatting

Het simuleren van omvormprocessen is een standaardprocedure geworden in de ontwikkeling van metalen producten. Een huidige trend in deze industrie is het koppelen van Eindige Elementen (EE) simulaties aan een optimalisatieprocedure. Met behulp van een zogenaamde 'simulation-based optimization approach' kunnen omvormprocessen worden ontworpen waarbij optimaal gebruik wordt gemaakt van de mogelijkheden van het materiaal en het proces. De volgende stap in de productontwikkeling is om het numeriek ontworpen proces over te zetten naar de fabriek en productie te initiëren. Hierbij worden voor de regelbare procesinstellingen de optimale deterministische instellingen gebruikt. In de praktijk worden metaalomvormprocessen echter beïnvloed door onzekerheid of invoervariatie, bijvoorbeeld variërende materiaaleigenschappen, fluctuerende procesinstellingen of veranderende omgevingscondities. Wanneer deze onzekerheden genegeerd worden in een op simulaties gebaseerde optimalisatie, dan komt daar vaak een optimaal deterministisch procesontwerp uit dat op de grenzen ligt van de mogelijkheden van het materiaal en het proces. Invoervariatie kan dan in de praktijk leiden tot overschrijding van deze grenzen, met afgekeurde producten tot gevolg. Om deze ongewenste situatie te voorkomen moet onzekerheid expliciet meegenomen worden in de numerieke optimalisatie van omvormprocessen.

In dit onderzoek is een strategie ontwikkeld voor het modelleren en 'robuust' optimaliseren van metaalomvormprocessen met behulp van simulaties. In de strategie onderscheiden we de volgende fases: modelleren, screening van variabelen, robuuste optimalisatie, validatie en sequentiële verbetering. In de modelleringsfase wordt invoervariatie gekwantificeerd en expliciet meegenomen in de optimalisatiestrategie. Hierbij worden, door het toepassen van metamodellen gecombineerd met Monte Carlo analyses, de vereiste statistische gegevens verkregen van de doelfunctie en de nevenvoorwaarden. Met behulp van metamodellen worden de EE-simulaties, die veel rekentijd vergen, efficiënt gekoppeld aan een optimalisatie-algoritme. Zo kan een optimaal

procesontwerp verkregen worden dat ook bij onzekerheden voldoet aan de gestelde nevenvoorwaarden. Een dergelijk optimaal procesontwerp wordt in dit werk een *robuust ontwerp* genoemd.

De strategie is toegepast op verschillende industriële metaalomvormprocessen: een rolvormproces, een V-buigproces, een strekproces en een dieptrekproces. Hierbij zijn meerdere onderzoekspunten uitgebreid aan de orde geweest. Een van de grootste uitdagingen bij het robuust optimaliseren van omvormprocessen is het vinden van een balans tussen enerzijds het aantal kostbare EE-simulaties dat wordt gedaan om metamodellen te creëren en anderzijds de voorspellende waarde van het robuuste optimum. Er werd aan de optimalisatiestrategie daarom een sequentiële optimalisatiestap toegevoegd die de verwachte verbetering van het metamodel meeneemt. Door deze stap wordt de voorspelling van het metamodel op relevante locaties nauwkeuriger, waardoor tevens de efficiëntie van de strategie als geheel verbetert. Vervolgens is uitgebreid gekeken naar numerieke ruis. Niet-lineaire EE-simulaties staan erom bekend dat zij numerieke ruis kunnen introduceren. Numerieke ruis heeft een numerieke oorzaak en is te herkennen aan variatie van responswaardes rondom een verwachte gelijkmatige responsfunctie. De aanwezigheid van numerieke ruis in de responsgegevens kan foutieve metamodellen en een onnauwkeurige voorspelling van het robuuste optimum tot gevolg hebben. De robuuste optimalisatiestrategie is uitgebreid om hier rekening mee te houden en het nadelige effect ervan te minimaliseren. Tenslotte is er een koppeling gemaakt met de sequentiële optimalisatiestap, waardoor het mogelijk wordt om het sequentiële verbeteringsalgoritme te stoppen afhankelijk van de hoeveelheid numerieke ruis in de responsgegevens.

Een van de belangrijkste bronnen van onzekerheid bij omvormprocessen zijn de wisselende eigenschappen van het gebruikte materiaal. Er werd daarom een nauwkeurige en efficiënte werkwijze ontwikkeld voor het kwantificeren en modelleren van materiaalvariaties. Door 41 rollen staal van dieptrekkwaliteit te onderwerpen aan een combinatie van mechanische testen en textuuranalyse is een stochastische verzameling materiaalgegevens verkregen. De modelleringswerkwijze is gevalideerd door met behulp van een strekproces 41 producten te vormen. De hierdoor verkregen experimentele responsspreiding kon nauwkeurig en efficiënt gereproduceerd worden middels EE-simulaties. Het materiaalcollectief is tevens gebruikt in een laatste onderzoek naar robuuste optimalisatie van een dieptrekproces. Hierbij is een deterministische en een robuuste optimalisatie uitgevoerd, exclusief en inclusief het effect van materiaal- respectievelijk procesvariatie. De resulterende optima zijn vervolgens onderworpen aan een serie dieptrekexperimenten om de numerieke voorspelling van de robuustheid te valideren. Het robuuste optimum bleek in de praktijk

inderdaad robuuster dan het deterministische optimum. Bovendien bleek er een goede overeenkomst te zijn tussen de experimentele en numerieke resultaten, die beide een afname van het aantal afgekeurde producten laten zien. Uit deze optimalisatiestudie blijkt dat het noodzakelijk is om invoervariatie expliciet mee te nemen in de optimalisatiestrategie, dat dit efficiënt gedaan kan worden, en dat dit kan leiden tot een significante verbetering van de robuustheid van omvormprocessen.

Contents

Chapter 1

Introduction

1.1 Background

Many products around us contain metal parts, produced by forming processes. In the course of time, metal forming has transformed from a handcraft in ancient times to a highly automated mass production process nowadays. Ultimate goals in the metal forming industry are zero failure production, reducing the costs of new products and decreasing the time-to-market. To achieve these goals, companies exploiting metal forming processes continuously strive for, among other things, product quality improvements by process optimization.

An introduction on metal forming processes is provided in this chapter. Special emphasis is given to the important aspect of quality improvement within the metal forming industry. Tools utilized for this purpose are finite element simulations and optimization techniques which will be introduced next. The main research topic of this thesis is subsequently introduced: designing robust forming processes using computer simulations. The related difficulties and current shortcomings will be discussed, building up towards the formulation of the research objective. The research objective is presented in Section 1.2 and the outline of the research is provided in Section 1.3, describing the relation between the chapters presented throughout this thesis.

1.1.1 Metal forming processes

Different classes of metal forming processes can be distinguished. A commonly used classification is based on the stress state that occurs during forming, although highly simplified, since local stress states can be far more complex.

Figure 1.1 *Car body structure of a Volkswagen Polo [149]*

[74]. The following classes of forming processes can be distinguished, including example processes per group:

- Compressive forming: extrusion or rolling
- Tensile forming: stretching or expanding
- Tensile and compressive forming: deep drawing or hydroforming
- Forming under bending: folding or bending
- Forming under shear: shear spinning

Applications of these processes are widely found in many industries, for example the aerospace, packaging, household appliances and automotive industry. Regarding the latter, Figure 1.1 shows a car body structure of a Volkswagen Polo [149]. Many of the car body parts are produced by different types of forming processes, e.g. deep drawing of the body panels, rolling of the support members and drawing of the wiring.

Product quality is an important aspect in the production of metal parts. Any quality issue in a mass production process can cause delay in production, lead to amplified problems in a subsequent assembly step or can cause problems during usage of the product. Avoiding these issues is therefore crucial to prevent resulting additional costs and customer dissatisfaction. What is more, due to the continuously increasing competition in industry, process improvements and cost reductions are vital. Controlling product quality is therefore very important in the metal forming industry.

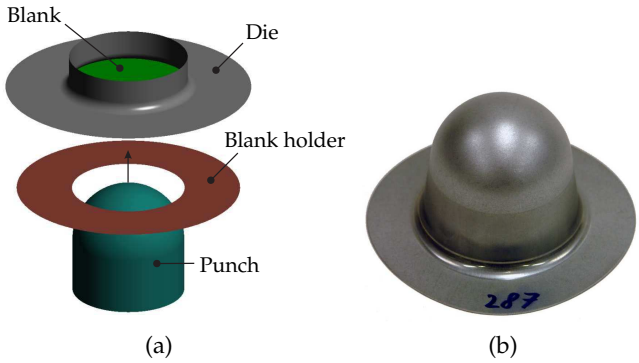

Figure 1.2 *(a) Example deep drawing process and (b) resulting cup product*

This thesis will focus on forming processes including sheet metal forming applications by rolling, bending, stretching and deep drawing. An example of a deep drawing process and the resulting cup product is given in Figure 1.2. The tooling is specially designed to deform a blank using a press. The blank or sheet is hereby drawn into the die opening by the punch, while restraining forces act on the blank enforced by the blank holder and the die. The final product quality primarily depends on the used sheet material, sheet dimensions, process design and process settings.

Traditionally, experimental trial-and-error approaches were followed to find a process design that resulted in defect-free products. When considering the deep drawing process of Figure 1.2, a process setting that can be changed is the Blank Holder Force (BHF) which controls the material flow into the die opening. In the trial-and-error approach, the BHF is changed based upon experience until the required quality demands are achieved. Setting it too high will result in a limited material flow and severe stretching of the material. As a result, the product can show early failure in production due to fracture. Setting it too low will result in wrinkles in the flange of the product. Such products are of low quality and unsuitable for further use in e.g. a subassembly. Clearly, both situations lead to product rejects.

The trial-and-error approach can result in a product quality which is acceptable but often far from optimal. To explain this in more detail, a process window of a deep drawing process is given in Figure 1.3. The BHF is plotted on the vertical axis and the Drawing Ratio (DR) is plotted on the horizontal axis. The DR stands for the ratio between the initial sheet diameter and punch diameter. Fracture or wrinkling of the product will occur in the shaded areas. The intersection point of the wrinkling limit and fracture limit corresponds to the Limiting Drawing

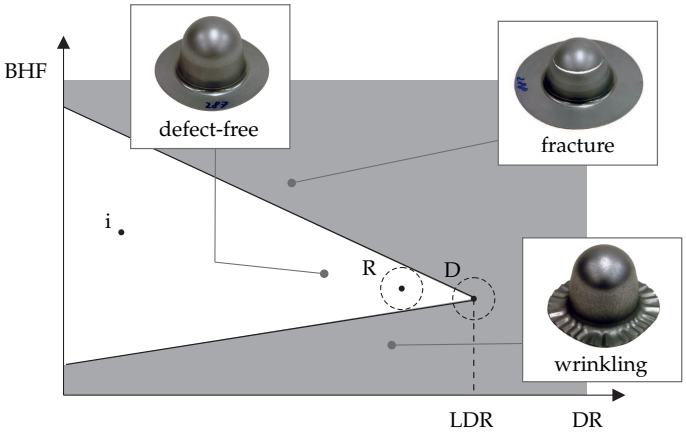

Figure 1.3 *Process window of a deep drawing process*

Ratio (LDR). The further it is situated to the right, the more severe the permissible material deformation can be and hence the better the formability of the product. In this point, products can be produced for which optimal use is made of the material. Until the 1980s, a point was sought in the defect-free area based on experience and trial-and-error approaches in the factory. A resulting initial defect-free process design is indicated by 'i' in Figure 1.3, leaving space for improvement of the process.

1.1.2 Finite element method

In the late 1980s, the trial-and-error approach was moved from the factory to the computer by the introduction of computer simulations. Numerical simulations tools, such as the Finite Element Method (FEM), are commonly used for solving a wide variety of engineering problems. In the context of metal forming processes, usage of Finite Element (FE) simulations allows for an accurate prediction of the behavior of metal forming processes and resulting products. Through numerous successful applications in industry, it is demonstrated that usage of FE simulations in the design of forming processes can significantly decrease the required development time and costs.

FE simulations are widely used for finding a numerical solution to complex field problems. It is applicable to any type of field problem, e.g. heat transfer, magnetic fields or stress analysis. The fully continuous field is hereby represented by a piecewise continuous field defined by a finite number of elements and nodes. Figure 1.4 presents an FE model of the cup product, clearly demonstrating the

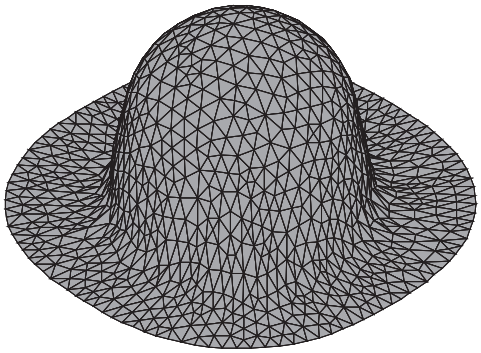

Figure 1.4 *Discretized FE model of a cup product*

applied discretization. Using this model, the product shape, residual stresses and strains can be predicted. Moreover, the occurrence of fracture and wrinkling can be predicted.

Discretization introduces an approximation, so the results from FE computations are rarely exact. However, the discretization error can be reduced by using e.g. more elements. Increasing the number of elements will increase the computation time. Clearly, there is a trade-off between prediction accuracy and calculation time. To obtain results with satisfying accuracy for an industrial product, generally many elements and time steps are required. As a result, non-linear FE simulations of metal forming processes are often very time-consuming. Depending on the problem and FE code under consideration, a simulation can easily take hours or days to run.

1.1.3 Optimization

A current trend in the metal forming industry is the coupling of FE simulations with optimization techniques. This has been possible in great part thanks to the development of faster computers and more sophisticated computing techniques. The coupling of FE simulations with a suitable optimization algorithm attracted academic interest in the previous decade and is currently finding many applications in industry, especially in the automotive industry. This trend is driven by the increasing demands placed upon car manufacturers to reduce vehicle weights, especially for the car body. A possibility to achieve weight reduction for a car body part is to make better use of the material by optimizing the process, see Figure 1.3. By coupling FE simulations with optimization techniques, companies are trying to seek the limits of what

is possible using forming processes. This approach extends the use of FE simulations in the process design; it has proven to be much more efficient than the conventional trial-and-error approach, and assists in fulfilling higher technical and economical requirements.

First, optimization in general will be discussed in more detail before introducing the objective of this thesis. The basic idea of optimization is to minimize an *objective function* f by finding the optimal value of *design variables* $\mathbf{x}$. Several types of restrictions or constraints can be present like *equality constraints* $\mathbf{h}$, *inequality constraints* $\mathbf{g}$ or *box constraints*. The latter type of constraint is sometimes denoted as *bounds*, defining the domain in which the design variables are allowed to vary by an upper and a lower bound. These bounds are denoted by $\mathbf{ub}$ and $\mathbf{lb}$ respectively. In general, an optimization problem can be described by the following formulation:

$$\begin{aligned} &\min_{\mathbf{x}} \ f(\mathbf{x}) \\ &\text{s.t.} \ \ \mathbf{h}(\mathbf{x}) = \mathbf{0} \\ &\qquad \mathbf{g}(\mathbf{x}) \leq \mathbf{0} \\ &\qquad \mathbf{lb} \leq \mathbf{x} \leq \mathbf{ub} \end{aligned} \tag{1.1}$$

Solving an optimization problem can be defined as finding the values of the design variables which minimize (min) the objective function subject to (s.t.) constraints. Note that equality constraints are usually eliminated before the optimization process. In the context of the considered deep drawing process, a possible objective is to maximize the product height by finding the optimal values for the BHF, sheet diameter and punch diameter. Finding the optimal values for these design variables requires an optimization algorithm suitable for the specific problem. The constraints can be divided further into linear or non-linear constraints and explicit or implicit constraints. Implicit constraints require running FE simulations to evaluate whether the constraints are satisfied or not, whereas explicit constraints do not since they depend directly on the design variables. The discussed wrinkling and fracture limits are examples of implicit constraints.

The *deterministic optimum* resulting from the optimization of the deep drawing process is given in Figure 1.3 and denoted by 'D'. The optimum is constrained by both the fracture and wrinkling limit and equals the LDR. Compared to the initial optimum 'i' resulting from the trial-and-error approach, again a defect-free product is obtained but with an increased height. Evidently, the coupling of FE

simulations with optimization techniques contributes to a further improvement of the considered process by making better use of the material and process capabilities.

1.1.4 From numerical design to robust production

The next step is to transfer the numerically designed process to the factory and initiate production. The controllable process variables are hereby set to their optimal deterministic values. However, in a real manufacturing environment, the process is influenced by *uncertainty* or *noise variables* showing randomness and variability. That is, many settings of the process will show variation and cannot be exactly controlled. One can think of changing environmental or process conditions. These sources of variation influence the product quality, which will also show variation.

Uncertainties during production are inevitable. Quality control is therefore introduced to take care of the process variation. A commonly applied method is Statistical Process Control (SPC) which uses statistical techniques to monitor and control product quality [94]. However, quality control cannot compensate for a poor initial process design with respect to process variation. Until now these variations are seldom accounted for in the numerical design process, often resulting in a design for which product quality is highly sensitive to process variation. Neglecting the presence of uncertain variables in optimization will often lead to a deterministic optimum that lies at the boundary of one or more constraints, as is the case for the deterministic optimum in Figure 1.3. The process variation is translated to the product response, which will now also display variation. The response variation is schematically represented in Figure 1.3 by the dashed circle around the deterministic optimum. Note that this is a schematic representation since formally response scatter cannot be displayed in the BHF-DR domain. A great part of the response variation violates the fracture and wrinkling constraint. Since the constraints represent a sharp border between acceptable products and rejects, variation will now lead to wrinkling or fracture of the product and thus a significant scrap rate.

In the case of deterministic optimization, it is assumed that the considered variables can be exactly controlled and set to certain values in practice. Running the FE simulation for selected values of the design variables yields one value for the output. The input and the output of a numerical optimization procedure will be deterministic as well. As discussed above, this assumption does not hold. To avoid this undesirable situation, uncertainties have to be taken into account explicitly in the numerical optimization strategy. The goal is to find a *robust*

optimum, indicated by 'R' in Figure 1.3, for which the process design is optimal while accounting for the presence of uncertainty. Note that the dashed circle line around the robust optimum, representing a schematic depiction of the response variation, does not violate the constraints, thus not resulting in product rejects. When transferring such a robustly designed process to the factory, the number of product rejects is expected to decrease compared to the deterministic optimal process design. Moreover, the need for quality control is minimized.

1.1.5 Robust by design

Robust optimization of metal forming processes requires the explicit quantification and integration of uncertainty in the numerical optimization strategy. The main reasons for many engineers to hold on to deterministic optimization rather than including uncertainties are: lack of knowledge, the increase in computational costs and the resulting lack of resources. It has been emphasized earlier that for deterministic optimization, each response evaluation is performed by running a computationally expensive non-linear FE calculation. Since an optimization algorithm requires many response evaluations, a series of simulations must be performed. Clearly, even if uncertainties are not accounted for, an efficient optimization strategy is required to minimize the number of simulations.

When including uncertainties in an optimization strategy, the number of required simulations increases further. This is because evaluation of both the objective function and constraints is more costly under uncertain conditions. Moreover, the number of variables included in the optimization problem generally increases. This makes the efficiency of an optimization strategy including uncertainties crucial.

1.2 Objective of this thesis

The objective of this thesis is to develop an optimization strategy applicable to forming processes liable to uncertainty. In this work, examples are considered of sheet metal forming processes which are representative for forming processes. The goal of the optimization strategy is to determine the optimal process design which meets the constraints even under the presence of uncertainty. Such an optimal design is referred to as a *robust design* in this thesis.

In order to find the optimal robust design, uncertainty must be quantified and included in the optimization strategy. It should enable quantification of the

response variation and, ideally, the prediction of the scrap rate of a process. The robust optimization strategy should be efficient and suitable for use with computationally expensive FE simulations, i.e. it should require a minimum number of simulations to find the global robust optimum.

Current research on robust design and optimization of forming processes follows a qualitative approach. That is, these approaches only allow for trend prediction of response variation rather than quantification of response variation. Moreover, these approaches are seldom applied in an industrial environment. This thesis presents an industrially applicable and experimentally validated optimization strategy that enables robust design and optimization of forming processes.

1.3 Outline

This thesis is divided into 9 chapters. The current chapter, **Chapter 1**, describes the background and objective of this research.

Chapter 2 provides a review on optimization under uncertainty. Different sources of uncertainties that can be encountered in the optimization process are identified. Different methods and numerical techniques for solving optimization problems including uncertainty are reviewed and the advantages and shortcomings are discussed. Finally, an optimization method and numerical technique is chosen for further use in this work.

Chapter 3 is the heart of this work and will present the robust optimization strategy. It builds on the review of Chapter 2 and will be introduced by going through the ten steps included in the strategy. Some steps are introduced globally and discussed in more detail in the subsequent chapters. The strategy will be demonstrated in Chapter 4 to Chapter 8 by application to robust optimization problems of multiple industrial metal forming processes.

Chapter 4 will first demonstrate the working principle of the robust optimization strategy by application to a roll forming process. It is applied to compensate for product defects occurring in roll forming production, among other things caused by variation of material properties. The optimal robust process settings of the roll former are determined to prevent defects in production. Finally, the numerical results are validated by roll forming experiments.

Chapter 5 extends the robust optimization strategy by adding the ability of sequential optimization. In case the numerically predicted optimum does not match with the FE simulation prediction at this location, a sequential optimization step can applied. This step is included to efficiently increase the

accuracy of the robust optimization strategy at regions of interest containing the optimal robust design. The sequential optimization algorithm is evaluated by application to an industrial V-bending process, including a comparison to experimental results obtained by performing a series of production trial runs.

Chapter 6 treats the topic of numerical noise. Non-linear FE simulations are known to introduce numerical noise, meaning that a small change in the input variable settings may give a relatively large difference in response due to e.g. automatic step size adaptation or adaptive remeshing. The response difference is for the greater part a numerical artifact rather than a physical response change. In severe cases, the optimization algorithm does not converge to its global optimum because of the resulting noisy response data. An extension of the robust optimization strategy is presented for dealing with numerical noise in the optimization of forming processes.

Chapter 7 treats one of the major sources of variation in metal forming processes, i.e. material scatter. To analyze the effect of material scatter on a sheet metal forming process using FE simulations, an accurate input in terms of material property scatter is required. This chapter presents an accurate and economic approach for measuring and modeling material properties and its associated scattering. The numerical results are validated by the forming of a series of cup products using a collective of materials. The goal is to reproduce the experimental scatter efficiently using FE simulations.

Chapter 8 describes a final optimization study considering the deep drawing process as discussed in Section 1.1.1. A deterministic and robust optimization study is described, excluding and including the effect of process variation and material scatter respectively. The numerically predicted optima are experimentally validated to determine the difference in the number of product rejects between both optima. The results demonstrate how this work assists in further increasing product quality and stretching the limits of forming processes.

Chapter 9 concludes this thesis with a summary of the key conclusions and recommendations for future research.

Chapter 2

A review on optimization under uncertainty

2.1 Introduction

Many processes and engineering problems around us are affected by uncertainty. As outlined in Chapter 1, optimization of such processes requires the explicit integration of uncertainty in the optimization strategy. The combination of optimization techniques, numerical simulations and uncertainty is often referred to as *Optimization Under Uncertainty* (OUU) [125].

Optimization strategies have been developed that account for uncertainty in a pragmatic way. A first approach was made by implementing safety factors. The factor should compensate for performance variability caused by input variation. Larger safety factors are correlated with higher levels of uncertainty. In most cases these factors are derived based on past experience but do not absolutely guarantee safety or satisfactory performance [15]. In recent years, an increasing number of optimization approaches have been developed that explicitly account for uncertainty. An overview is provided by Beyer and Sendhoff [17] and Park et al. [109]. Moreover, this trend is reflected by several recent PhD research projects on the topic of OUU [3, 57, 67, 69, 105, 134, 153] where metal forming processes are considered by Bonte [19] and de Souza [134].

This chapter provides a review on OUU with a special emphasis on applications in metal forming. First, different sources of uncertainty are identified and a classification scheme is proposed in Section 2.2. Next, approaches to mathematically quantify and account for uncertainty in optimization are reviewed in Section 2.3. Mathematical techniques available for solving OUU problems are reviewed in Section 2.4, accompanied by applications encountered in the literature in Section 2.5. Since OUU is a very broad research topic, it is not

intended to present a detailed overview of all developed methods and techniques with their applications encountered in the literature. Instead, a global overview is presented to give the reader an idea of the approaches available for coping with uncertainty. Fundamental differences between modeling methodologies will be pointed out so they can be used as a guideline for developing a suitable approach to OUU in metal forming processes.

2.2 Sources of uncertainty

OUU requires information about the uncertainties influencing the process under consideration. As a first step, different sources of variation are identified since each type of uncertainty requires a different approach for use in an optimization procedure. There are different possibilities to classify uncertainties, as reported by Beyer and Sendhoff [17]. Figure 2.1 depicts a process diagram of a model used to describe the physical process. It represents the schematic relationship between the input of the model and the process response [151]. A metal forming process has an output or response f and $\mathbf{g}$ which depend on the input. Focusing on the response f, this can be described by:

$$f = f(\mathbf{x}, \mathbf{p}) \tag{2.1}$$

The input can be divided into design variables $\mathbf{x}$ and parameters $\mathbf{p}$. Parameters are set constant for the process or optimization problem under consideration, whereas the variables can be varied. The parameters are provided by the environment in which the process is embedded, e.g. temperature or humidity. It can also represent a constant process setting or a fixed tooling radius. The response of the system can be controlled by the design variables $\mathbf{x}$. One can think of variable process settings like the BHF or the drawing velocity. Note that parameters and design variables can be interchanged. For example, the BHF is a design variable if it is used as a variable to influence the response for optimization. It is a parameter if the BHF is set constant in the process.

The uncertainty is the input that cannot be controlled by the designer in an industrial setting. Different types of uncertainty can be present:

A *Parameter uncertainty*. This type of uncertainty, denoted by $\mathbf{z}_\mathrm{p}$, is caused by changing environmental or operating conditions. Parameter uncertainty

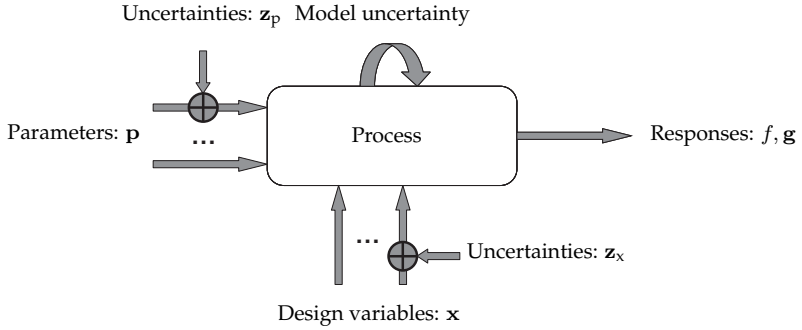

Figure 2.1 *Process diagram*

will often enter the process in terms of a perturbation $\mathbf{z}_p$ of the parameter $\mathbf{p}$:

$$f = f(\mathbf{x}, \mathbf{p} + \mathbf{z}_p) \tag{2.2}$$

Examples of parameter variations are temperature variation, material thickness scatter and variation of material properties. Once a material has been selected, the material properties cannot be controlled anymore and the variation must now be taken into account as noise variables. Chapter 7 is devoted to dealing with material scatter in OUU in metal forming processes.

B *Design variable uncertainty*. This type of uncertainty is caused by the limited degree of accuracy with which a design variable can be controlled. One can think of actuator inaccuracy, variation of drawing velocity or BHF variation. Design variable uncertainty will often enter the process in terms of a perturbation $\mathbf{z}_x$ of the design variables $\mathbf{x}$:

$$f = f(\mathbf{x} + \mathbf{z}_x, \mathbf{p}) \tag{2.3}$$

C *Model uncertainty*. Several types of model uncertainty can be distinguished. Firstly, when using numerical techniques to describe the physical process, the designer has to deal with model uncertainties like numerical noise [26, 141]. The response can be affected by, for example, automatic step size adaptation or adaptive remeshing. The resulting model uncertainty depends on the input of the system. Chapter 6 is devoted to dealing with

numerical noise in OUU in metal forming processes. Moreover, generally simplifying model assumptions have to be made when using numerical techniques to describe the physical process. These assumptions introduce model uncertainty. Also, measurement errors and discretization errors can be counted as model uncertainty. The last type considers the uncertainty of e.g. a constraint definition. As an example, a Forming Limit Curve (FLC) is often used as a fracture constraint in the optimization of sheet metal forming processes. Uncertainty is present in the definition of an FLC. Moreover, the shape and position of the curve is uncertain since it is based on experimental data [68]. The presence of model uncertainty in the process diagram is represented in Figure 2.1 by an arrow coming out of the system and entering the system again, since it can be seen as an internal error of the model.

In summary, the first step in solving OUU problems is the identification and classification of the different types of uncertainty. The types as defined in A–C cause response variation of f and $\mathbf{g}$. Other classifications of uncertainty can be found in [50, 67, 93].

2.3 Accounting for uncertainty

In this section, optimization methods reported in the literature to mathematically quantify and account for uncertainty will be discussed. Methods will be reviewed that are suitable for use in the context of this work. OUU methodologies can be classified based on the manner of handling uncertainty. The prevailing methods in structural engineering handle uncertainty in a *probabilistic* way. That is, these models explicitly include probabilistic or stochastic distributions of input uncertainty to account for and quantify response uncertainty. An introduction on describing input uncertainty or randomness in a probabilistic way is given in Appendix A. In case probabilistic distributions of the uncertain variables are unknown, for example by lack of experimental data, one can resort to *possibilistic* approaches [17, 98]. These approaches do not require detailed probabilistic input information of the uncertain variables [67]. As a consequence, quantitatively nothing is known about the response variation. Common possibilistic approaches to OUU are *worst-case scenario*, *interval modeling* and *fuzzy sets*. Applications of these approaches to metal forming processes can be found in [31, 33, 40, 71, 87, 98].

One of the objectives of this work is to model and include input uncertainty or input variation in an optimization strategy to enable quantification of the

response uncertainty. This favors the use of probabilistic approaches to account for uncertainty in OUU in metal forming processes. Moreover, it is mentioned in Section 1.1.4 that statistical techniques such as SPC are used in the metal forming industry to monitor and control product quality. For this purpose, product and process measurements are performed to collect stochastic input and response data. The availability of probabilistic input data can be optimally exploited in the probabilistic approaches for quantification of response variation. The remainder of this chapter will focus on probabilistic approaches to account for uncertainty.

Next, two probabilistic approaches are introduced, i.e. the reliability-based optimization approach in Section 2.3.1 and robust optimization approach in Section 2.3.2. Section 2.3.3 will discuss the aspects of reliability and robustness in the context of OUU in metal forming processes. Finally, the optimization formulation to be solved in this work is presented in Section 2.3.4.

2.3.1 Reliability-Based Design Optimization (RBDO)

The *Reliability-Based Design Optimization* (RBDO) approach handles noise variables in a probabilistic way. It provides the means for determining the optimal solution of a certain objective function, while ensuring a predefined small probability that a product or process fails [50].

The probability of violating some predefined constraint or *limit state* is calculated given complete or partial information on the probability density functions of uncertain variables. Figure 2.2 shows a normally distributed probability density function for a reference situation. Also indicated are a Lower and Upper Specification Limit, denoted by LSL and USL respectively. The challenge is to design a process for which the response distribution lies between the LSL and USL. Any violation of these limits will lead to product rejects. To demonstrate the working principle of RBDO, a reference situation is given which violates the USL. To achieve a certain reliability level in RBDO, the whole of the probability density function of the response is shifted, see Figure 2.2. This is done by explicitly and accurately determining the area in the tail of the distribution that is outside the specification limit. Typically, reliability-based design optimization is formulated as:

$$\begin{aligned} &\min_{\mathbf{x}} \; f(\mathbf{x}) \\ &\text{s.t.} \;\; \Pr[\mathbf{g}(\mathbf{x}, \mathbf{z}_{\mathrm{x}}, \mathbf{z}_{\mathrm{p}}) \leq \mathbf{0}] \geq P_0 \\ &\qquad \mathbf{lb} \leq \mathbf{x} \leq \mathbf{ub} \end{aligned} \tag{2.4}$$

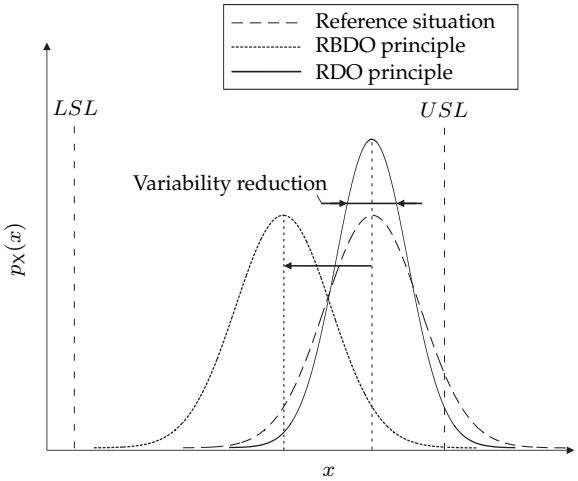

Figure 2.2 *Principle of Reliability-Based Design Optimization (RBDO) and Robust Design Optimization (RDO) [19]*

with $\Pr[\,]$ the probability of constraint satisfaction and $\mathbf{lb}$ and $\mathbf{ub}$ the lower and upper bounds of the design variables respectively. The limit state $\mathbf{g} = \mathbf{0}$ separates the region of failure ($\mathbf{g} > \mathbf{0}$) and success ($\mathbf{g} < \mathbf{0}$) and is a function of the design variables $\mathbf{x}$ and the uncertain variables $\mathbf{z}_\mathrm{x}$ and $\mathbf{z}_\mathrm{p}$. P_0 is referred to as the reliability level [17, 19, 128] or performance requirement [125]. The reliability level is generally close to 1 which means that failure can only occur in extreme events. The above inequality can be expressed by a multi-dimensional integral which leads to:

$$\Pr[\mathbf{g}(\mathbf{x}, \mathbf{z}_\mathrm{x}, \mathbf{z}_\mathrm{p}) \leq \mathbf{0}] = \int_{\mathbf{g}(\mathbf{x}, \mathbf{z}_\mathrm{x}, \mathbf{z}_\mathrm{p}) \leq \mathbf{0}} p(\mathbf{z}_\mathrm{x}, \mathbf{z}_\mathrm{p}) \, \mathrm{d}\mathbf{z}_\mathrm{x} \, \mathrm{d}\mathbf{z}_\mathrm{p} \geq P_0 \tag{2.5}$$

in which $p(\mathbf{z}_\mathrm{x}, \mathbf{z}_\mathrm{p})$ is the joint probability density function of uncertain variables $\mathbf{z}_\mathrm{x}$ and $\mathbf{z}_\mathrm{p}$. If the variables are statistically independent, the joint probability density function may be replaced by the product of the individual probability density functions in the integral as shown in Equation (A.9).

From a theoretical point of view, RBDO is a well-established concept. However, computing the integral in Equation (2.5) appears as a technically involved problem. This is because it is often a multi-dimensional integral equation for which the joint probability density function and/or limit state function $\mathbf{g}$ is unknown in explicit form. In the case of metal forming processes, FE

simulations are required to evaluate $\mathbf{g}$. For solving Equation (2.5), one can resort to approximate reliability techniques such as a Monte Carlo analysis, which will be discussed in Section 2.4.2. Other well-known techniques are the First- and Second-Order Reliability Method, FORM and SORM respectively [42, 49]. A disadvantage of the RBDO approach is the focus on high accuracy in the tail of the response, which requires detailed statistical input data and many FE simulations to be determined accurately. The latter aspect makes RBDO time-consuming for application to metal forming processes.

2.3.2 Robust Design Optimization (RDO)

The concept of robust optimization is closely connected with the name of Taguchi who introduced this influential design philosophy. Taguchi, who is the pioneer of robust design, said: *"Robustness is the state where the technology, product, or process performance is minimally sensitive to factors causing variability (either in the manufacturing or users environment) and aging at the lowest unit manufacturing cost"* [137].

In this section, the *Robust Design Optimization* (RDO) approach is addressed. Similar to the RBDO approach, uncertainties are handled in a probabilistic way. The principle of robust optimization is depicted in Figure 2.3. Robust optimization focuses on optimizing towards a design that is relatively insensitive with respect to uncertainties. This means that the variability of the response f is quantified and minimized. Selecting variable setting x_2+z_2 instead of x_1+z_1 will yield a narrower response distribution and thus a more robust design. Note that this approach is different from the RBDO approach, which focuses on the area in the tail of the distribution that is outside the specification limit, see Figure 2.2.

The probabilistic measure of robustness is generally expressed by the variance of the objective function, given by Equation (A.4) [17, 125]. Fundamentally, the robust optimization formulation is given by:

$$\begin{aligned} &\min_{\mathbf{x}} \ \sigma_{\mathrm{f}}(\mathbf{x}) \\ &\text{s.t.} \ \ \mathbf{g}(\mathbf{x}) \leq \mathbf{0} \\ &\qquad \mathbf{lb} \leq \mathbf{x} \leq \mathbf{ub} \end{aligned} \tag{2.6}$$

In this case, the width of the response distribution is minimized and the constraints are handled deterministically.

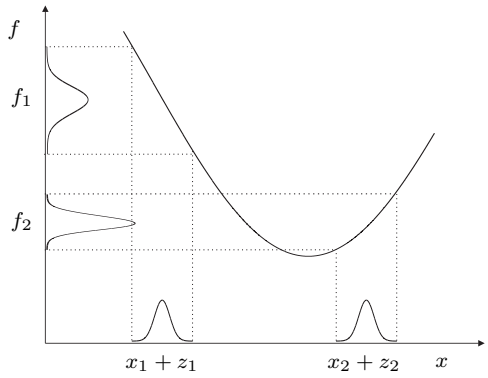

Figure 2.3 *Principle of Robust Design Optimization (RDO) [19]*

2.3.3 A comparison between RBDO and RDO

The choice for using the RBDO approach or the RDO approach depends on the objective of the optimization study. Fundamentally, the RBDO approach focuses on the probability of constraint violation where compensation is achieved by shifting the response distribution. RDO emphasizes insensitiveness of the objective function. In other words, the robustness is increased by reducing the variability of the response distribution.

Looking at the application of these approaches to forming processes, both can be criticized. If one purely focuses on constraint violation in the case of RBDO, any error in the mean response prediction will have a significant effect on the prediction of the probability of failure. Since these errors will be present when using FE simulations to describe the real forming process, focusing on this aspect only can, in this case, lead to erroneous results. Looking at solving the multi-dimensional integral in Equation (2.5), special focus is placed on the tail of the response distribution to calculate the probability of failure or reliability. Accuracy at low probabilities requires detailed statistical input data, making it inaccurate if this data is not sufficient to permit a reliability analysis. Moreover, an increasing number of objective function evaluations is required to evaluate Equation (2.5) compared to Equation (2.6) [125, 135]. If only a limited number of FE simulations can be performed, care must be taken in interpreting the predicted reliability in the RBDO approach.

In the case of the RDO approach, process robustness does formally not include the position of the response distribution with respect to the uncertain constraints. In other words, purely minimizing the variability of the response can lead to a very robust process, but with a high number of product rejects if the response

distribution is located at or near the specification limits. Therefore, reliability with respect to the specification limits has to be included in the optimization procedure. But even if reliability is taken into account, purely minimizing the variability of the response can lead to an optimum at a 'plateau-like' region of the feasible design space. It can be questioned whether the mean performance at this location of the design space is also satisfactory for the optimization problem under consideration.

2.3.4 Variance-based robust optimization

Ultimately, the goal in OUU in metal forming processes is to optimize the process by limiting the deteriorating effects of uncertainty to an acceptable level. For this purpose, both process robustness and process reliability have to be taken into account to end up with a conceivable optimization formulation for use in an industrial setting.

To obtain a reliable process, the probability of failure of a design has to be assessed with respect to the constraints. Reliability is included in the optimization formulation used in this work by replacing the integral formulation of Equation (2.5) by a so-called *moment matching constraint formulation*. The constraints are written as:

$$\boldsymbol{\mu}_{\mathrm{g}}(\mathbf{x}) + \mathbf{k}_{\mathrm{g}}\boldsymbol{\sigma}_{\mathrm{g}}(\mathbf{x}) \leq \mathbf{0} \tag{2.7}$$

where $\boldsymbol{\mu}_{\mathrm{g}}$ and $\boldsymbol{\sigma}_{\mathrm{g}}$ are vectors containing the mean and standard deviation of the uncertain constraints. These are less costly to compute compared to the evaluation of probabilistic feasibility through Equation (2.5) and are more reliable for small sample sizes and limited stochastic input data [56, 67, 69, 76]. This formulation can be applied both in the RBDO and RDO approach and is widely used in the literature [19, 31, 32, 64]. The vector $\mathbf{k}_{\mathrm{g}}$ contains the constants that stand for the probability of constraint satisfaction assuming a normal distribution. For example, $k_{\mathrm{g}} = 3$ stands for a 3σ probability which represents a chance of 99.73% that $g(x) \leq 0$ if the constraint is indeed normally distributed.

In the case of OUU in metal forming processes, the robustness is judged important for implementation in the optimization formulation since, in general, a more robust process has a higher potential to result in a reliable process. In other words, it is easier to satisfy all uncertain constraints with a process having limited response variation compared to a process having significant response

variation. Different types of optimization formulations can be found in the literature to include robustness. One possibility is to apply a *multi-objective* type of optimization formulation, also known as the *weighted sum formulation*. This formulation is introduced to consider the minimization of the mean performance and the response variance simultaneously. It is composed of the mean and the standard deviation of the objective function:

$$\alpha \frac{\mu_{\mathrm{f}}(\mathbf{x})}{\mu'_{\mathrm{f}}} + (1-\alpha)\frac{\sigma_{\mathrm{f}}(\mathbf{x})}{\sigma'_{\mathrm{f}}} \tag{2.8}$$

where μ'_{f} and σ'_{f} are the function values at the individual optima in terms of mean performance and variance respectively. The value of the weighing factor α is determined depending on the importance of minimization of the mean performance or variance. When using this robustness measure, the search for an optimal design is a multiple criteria decision [30, 75, 129]. Finding a compromise solution is known as *robust multi-objective optimization* in which a set of *Pareto-optimal solutions* can be considered as possible compromise solutions.

Equation (2.8) can also be written in a form comparable to Equation (2.7) and only considering the mean μ_{f} and standard deviation σ_{f} of the response distribution. The set of optimal solutions is reduced to a single optimum by setting α constant before optimization. In this case, both the location and the width of the response distribution are adapted simultaneously. As a result, the robust optimization formulation to be solved in this work is given by:

$$\begin{aligned} &\min_{\mathbf{x}} \ \mu_{\mathrm{f}}(\mathbf{x}) + \alpha\sigma_{\mathrm{f}}(\mathbf{x}) \\ &\text{s.t.} \ \ \boldsymbol{\mu}_{\mathrm{g}}(\mathbf{x}) + \mathbf{k}_{\mathrm{g}}\boldsymbol{\sigma}_{\mathrm{g}}(\mathbf{x}) \leq \mathbf{0} \\ &\qquad \mathbf{lb} \leq \mathbf{x} \leq \mathbf{ub} \end{aligned} \tag{2.9}$$

2.4 Numerical approaches to robust optimization

The next step is to solve the probabilistically described robust optimization problem, i.e. solve Equation (2.9). Recall from Section 1.2 that the focus of this work is on optimization techniques suitable for use in simulation-based optimization, or *simulation optimization* [17]. In this *black-box scenario*, the objective function is not available as an explicit, closed form of the input variables. Also, the derivatives or gradients with respect to input variables are

not readily available and each evaluation of the responses is time-consuming. The optimization algorithm should be efficient and generally applicable. This means that the algorithm must be suitable for different metal forming processes and must be suitable for coupling with numerical simulations.

Different numerical techniques can be used for solving Equation (2.9). First, the Taguchi method is introduced in Section 2.4.1. Next, the Monte Carlo Analysis and metamodel approach are introduced in Section 2.4.2 and Section 2.4.3 respectively. These techniques are combined in this work to solve Equation (2.9) as further outlined in Section 2.4.4. Numerical techniques that directly use the response values of FE simulations as an input for optimization, instead of first introducing a metamodel, are not reviewed in this chapter. The large number of response evaluations generally required for optimization makes these direct search methods unsuitable for use in OUU in metal forming processes.

2.4.1 Taguchi method

The principle of the Taguchi method is depicted in Figure 2.3. The approach aims at reducing the variability in the response by identifying proper settings of design variables [110, 137].

The mean and variance of the response are evaluated by using a Design Of Experiments (DOE) based on an inner and outer crossed array design, see Figure 2.4a. The inner array consists of the design variables whose settings can be specified during the design process. The outer array consists of the noise variables. After performing experiments based on this type of DOE, the results are analyzed by calculating a *Signal-to-Noise Ratio* (SNR). This represents a performance criterion that takes the process mean and variance into account. The optimal design variable settings are identified by maximizing the SNR following a 'pick-the-winner' approach. Applications in the field of metal forming processes are presented in [12, 69, 80, 86, 99, 106, 127].

The principle of the Taguchi method is easy to understand and does not require a strong background in statistics [109]. However, the Taguchi method has several drawbacks. First of all, the SNR is criticized since it combines the mean and variance of the response and hence, mean and variance are confounded. This means that one cannot distinguish which variables affect the mean and which variables affect the variance. Other drawbacks of the Taguchi method are the many function evaluations required for the crossed array design and the impossibility of taking into account interaction effects between design variables [60, 67, 144].

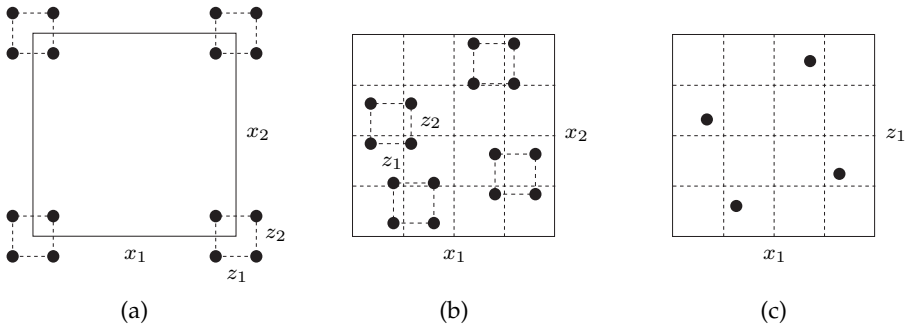

Figure 2.4 *Different DOE types: (a) Taguchi's crossed array design, (b) direct variance modeling in dual response surface modeling and (c) combined design for single response surface modeling*

2.4.2 Monte Carlo Analysis

The Monte Carlo Analysis (MCA) is widely used for stochastic analysis and can be regarded as the most general simulation technique for this purpose [4, 102]. An example of an MCA sampling of 2000 points for a set of normally distributed variables z_1 and z_2 is given in Figure 2.5. Based on this sampling, the mean and variance of the response distribution can be calculated, see Equations A.3 and A.4 respectively. The prediction accuracy for the stochastic measures depends on the number of samples, therefore a large number of response evaluations is generally required. The mean and variance of the response distribution can be calculated in space by repeating the MCA a number of times at different design variable settings. Next, the optimal robust design can be determined by providing these approximations to an optimization algorithm.

Similar to the advantages of the Taguchi method, the MCA is a general simulation technique, it is easy to understand and does not require a strong background in statistics. However, the naive MCA approach is computationally expensive, especially when combined directly with simulations. Therefore, only a limited number of MCA samples will generally be evaluated using advanced simulation techniques like adaptive Monte Carlo simulation [71], subset simulation [11, 63], importance sampling [117, 138] or descriptive sampling [72]. These methods improve the efficiency of the analysis when compared with direct Monte Carlo analyses, but still lead to a large number of function evaluations. An alternative is to combine the MCA with a metamodel approach as outlined next.

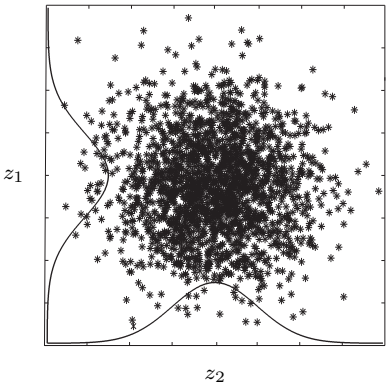

Figure 2.5 *Monte Carlo Analysis (MCA) input generation*

2.4.3 Metamodel approach

The metamodel approach is an often used and well-known approach to couple FE simulations with an optimization procedure. An overview of metamodeling applications in structural optimization is provided by Barthelemy and Haftka [13]. The application of metamodeling techniques in optimization has been encouraged by the high computational costs of simulations and the large number of analyses required for an increasing number of variables as indicated by Roux et al. [116]. The basic idea of the metamodel approach is to construct an approximate model or surrogate model by sampling in the design space using a DOE. The goal of a DOE in the context of this work is to minimize the number of time-consuming FE simulations while ensuring a proper initial basis for fitting the metamodels. It must be noted here that metamodeling techniques do not solve a problem by themselves, they are combined with an optimization algorithm that uses the metamodel for obtaining the required response information. Two main metamodel approaches can be distinguished when considering robust optimization, i.e. the dual and single response surface method.

Dual response surface method

The response information required for creating a dual response surface method model is obtained by the DOE as given in Figure 2.4b. Repeated simulations are performed for the noise variables at a certain design variable setting. This results in two responses, i.e. one for the mean and one for the variance of each response. This procedure is repeated at multiple design variable settings from which two

metamodels can be constructed. The DOE allows for direct variance modeling as outlined by Myers and Montgomery in [100]. Next, robust optimization can be performed by combining both metamodels with an optimization algorithm, solving Equation (2.9).

The resulting metamodels provide a direct understanding of the change in mean and variance as a function of the design variables. Moreover, this approach allows for metamodel improvement by sequentially adding DOE points, it includes interaction effects, and the mean and variance are not confounded anymore as was the case in the Taguchi approach. The main disadvantage of this approach is the fact that many response evaluations are required for noise assessment at each design variable setting.

Single response surface method

In the case of the single response surface method, a DOE is created in the combined design-noise variable space for determining the relationship between the variables and the process response [100]. See the DOE in Figure 2.4c. Note that this design is plotted for a single noise and design variable in contrast to the designs in Figures 2.4a and 2.4b. Next, a single metamodel is fitted in the combined space, which explains the name single response surface method. To obtain an estimate of the mean and variance of the response, an MCA can be run on the metamodel. Since the MCA is performed on the metamodel, it is very efficient. Next, robust optimization can be performed by combining both estimates with an optimization algorithm to solve Equation (2.9).

Note that many different DOE and metamodel types can be selected for use in the single response surface method. Metamodel techniques commonly encountered in the literature for the single response surface method are Response Surface Methodology (RSM), Kriging and neural networks. An impression of a quadratic RSM metamodel for two variables is given in Figure 2.6. The metamodel types will be evaluated in more detail in Chapter 3.

Similar advantages as given for the dual response surface method also hold for the single response surface method. Compared to direct variance modeling, the sampling in the combined design space for the single response surface method results in a more efficient approach for evaluating the effect of design and noise variables on the considered responses. However, the metamodel approach becomes exponentially more time-consuming with an increasing number of design and noise variables. This is the main weakness of the metamodel approach and is referred to as the *curse of dimensionality* in Beyer and Sendhoff [17].

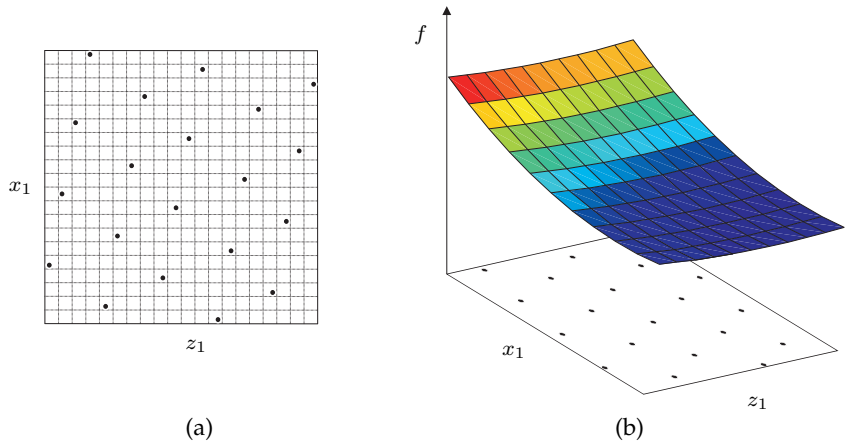

Figure 2.6 *Impression of (a) a combined DOE in design-noise variable space and (b) resulting metamodel*

2.4.4 Combining numerical techniques

The single response surface method in combination with the MCA is used in this work for solving Equation (2.9). The use of the single response surface method has several advantages in the context of OUU in forming processes. Firstly, the main goal of introducing metamodels of the considered response functions is to limit the computational burden by reducing the number of required FE simulations compared to a direct coupling of simulations with an optimization algorithm. Secondly, it enables the black-box scenario, meaning that no preliminary restrictions have to be made regarding the FE code. Thirdly, since both the response function as well as the gradients of the response function to be optimized are now available explicitly, one can combine the metamodel with different types of optimization algorithms to find the solution of Equation (2.9). A more detailed discussion on the combination of the metamodel approach with the MCA and an optimization algorithm is provided in Chapter 3. Other advantages of the use of metamodels are the possibility for sequential improvement and parallel computing. Sequential improvement is treated in Chapter 5. Parallel computing is possible since the required sample points needed for constructing a metamodel are independent points and are defined prior to execution by a DOE [37, 100]. Finally, the metamodels allow for visualization of the main and interaction effects between variables and the responses. This can provide valuable insight into the problem under consideration, even without solving the actual robust optimization problem.

2.5 Literature review on robust optimization of forming processes

In this section, a literature overview is presented focusing on applications of the metamodel approach in robust optimization of metal forming processes. Many applications of the metamodel approach in deterministic optimization of metal forming processes can be found, see e.g. [19, 20, 61, 101, 111]. When considering uncertainty, also RBDO problems in metal forming are commonly solved using the metamodel approach, see e.g. [62, 70, 115, 120, 135, 154]. Various applications of the metamodel approach in robust optimization (not considering metal forming processes) can be found in [64, 69, 76].

Publications on robust optimization of metal forming processes combined with metamodels are presented in Table 2.1. Note that different types of robust optimization formulations are applied in the literature. In many cases, the weighted sum formulation given by Equation (2.8) is used, after which a discussion follows on the trade-off between minimization of the mean performance and the variance of the final optimum.

Gantar et al. [39] focused on the evaluation of the effect of seven noise variables on the stability of a deep drawing process of a rectangular product. An RSM metamodel was created by evaluating the objective function several times using FE simulations based on a Box-Behnken (BB) DOE. The process was critical with respect to wrinkling and fracture of the product. Secondly, an MCA has been applied onto the response surface. The robust optimum was determined by minimizing the variance of the response following Equation (2.6) with respect to different settings of the BHF.

Table 2.1 *Literature overview on robust optimization of metal forming processes using the metamodel approach*

Ref.	Process	DOE	Metamodel	Algorithm	Formulation
[39]	Deep drawing	BB	RSM	MCA	(2.6)
[82]	Deep drawing	CA, CCD	DRSM	SSRD	(2.7), (2.8)
[19]	Deep drawing	LHD	RSM, Kriging	SAO	(2.6), (2.7)
[138]	Deep drawing	LHD	SVR	IS	(2.7),(2.8)
[56]	Deep drawing	UD	RSM	1stOpt	(2.7), (2.8)
[136]	Deep drawing	OLHS	DRSM	PSO	(2.7), (2.8)

In Li et al. [82] a robust optimization procedure for a deep drawing process has been proposed. The objective was to minimize the thickness variation subject to the condition of no wrinkling or fracture. The design variables were chosen to be the BHF, friction coefficient between the die and blank, and the punch radius. Three noise variables were included in the study, i.e. the initial thickness of the blank, the friction coefficient and a variable reflecting the scatter in material properties. Use was made of the Dual Response Surface Method (DRSM). The DOE was based on a combination of a Crossed Array (CA) design and a Central Composite Design (CCD). The weighted sum formulation of Equation (2.8) has been applied and constraints were handled using the moment matching formulation of Equation (2.7). The optimization procedure was referred to as *Six Sigma Robust Design* (SSRD).

Bonte [19] proposed a robust optimization procedure and applied it to a deep drawing process of a small cylindrical cup product. Three noise variables were incorporated, i.e. the material thickness, the flow-stress and a material property factor that influences the strain-induced transformation rate. The objective was to improve the shape accuracy of the cup, which has been achieved by combining FE simulations, a DOE based on a Latin Hypercube Design (LHD), RSM and Kriging metamodels, and a Sequential Approximate Optimization (SAO) algorithm which includes an MCA. The process robustness was optimized solving Equation (2.6) where constraints were evaluated using Equation (2.7). As a result, an improved shape accuracy and process robustness was obtained. The final optimum that was found using the metamodel has been checked by performing a (small) MCA using FE simulations.

Tang and Chen [138] proposed a robust optimization procedure for which the feasibility was verified by a deep drawing process of a square cup. A Support Vector Regression (SVR) metamodel has been created using a DOE based on an LHD. The weighted sum formulation of Equation (2.8) and the Importance Sampling (IS) technique was used to determine the robust optimum. The objective of the optimization problem was to obtain a uniform thickness distribution subject to constraints considering defects such as fracture, wrinkling, and insufficient stretching. The constraints were formulated using Equation (2.7). The material properties were considered uncertain following from a range of material experiments. Finally, the deterministic optimum and robust optimum were numerically compared, showing an increased reliability and decreased response variation for the robust optimum.

In Hou et al. [56], a metamodel-based robust optimization procedure was proposed and demonstrated considering a deep drawing process of an automotive part. A Uniform Design (UD) has been applied to generate a DOE.

After running the FE simulations, a metamodel based on RSM was constructed. Onto this metamodel, an MCA was performed to determine how the input variable variation affects the final product quality. A data processing software (1stOpt) was used for the optimization procedure. The objective was to prevent wrinkling and fracture of the product. This has been achieved by applying the weighted sum formulation of Equation (2.8). The constraints were formulated according to Equation (2.7). As a result, both the probability of fracture and wrinkling for the automotive part was reduced significantly compared to a deterministic optimal design.

A final application of robust optimization in sheet metal forming processes using the metamodel approach can be found in Sun et al. [136]. In this paper, a draw bead design was optimized to prevent wrinkling and fracture of a deep drawing process of an automotive part. The Optimal Latin Hypercube Sampling (OLHS) technique has been used in combination with the DRSM and Particle Swarm Optimization (PSO) method to optimize the geometric variables of the draw bead design. The weighted sum formulation of Equation (2.8) was applied in combination with Equation (2.7). The resulting optimum was validated using an experiment, resulting in a satisfactory product which showed no wrinkling or fracture.

2.6 Closure

In this chapter, a review on optimization under uncertainty in forming processes is described. Both probabilistic and possibilistic methods are introduced to account for uncertainty in optimization. The ability to explicitly include stochastic input scatter and quantify response variation favors the use of a probabilistic approach to OUU in forming processes. The division of the probabilistic evaluation into RBDO and RDO is discussed after which an optimization formulation is proposed including both process robustness and process reliability. The variance-based robust optimization problem to be solved in this work is given in Equation (2.9). This robust optimization formulation will be solved using the single response surface approach combined with an MCA. This metamodel-based approach will be used to couple the time-consuming FE simulations with an optimization algorithm as presented next in Chapter 3.

Chapter 3

Robust optimization strategy

3.1 Introduction

In this chapter, a robust optimization strategy is proposed for modeling and solving simulation-based robust optimization problems. It builds on the literature review of Chapter 2, where it is reasoned that a metamodel-based optimization approach is most suitable for coupling the time-consuming FE simulations with an optimization algorithm. The strategy consists of the following main stages: modeling, variable screening, robust optimization, validation and sequential improvement. These stages can be further subdivided into ten steps as shown in Figure 3.1. This flowchart serves as a guide through the process of mathematically modeling and solving robust optimization problems.

The robust optimization strategy will be explained by going through the ten steps mentioned in Figure 3.1. The proposed strategy is a collection of existing and newly developed mathematical tools which are combined to enable the efficient solving of robust optimization problems. The strategy and incorporated tools will be demonstrated in more detail by application to industrial forming processes in the subsequent chapters. The strategy is implemented and solved by the MATLAB-based optimization software OPTFORM developed at the University of Twente.

3.2 Modeling

Step 1 in the robust optimization strategy is to model the optimization problem under consideration. Both design and noise variables have to be selected

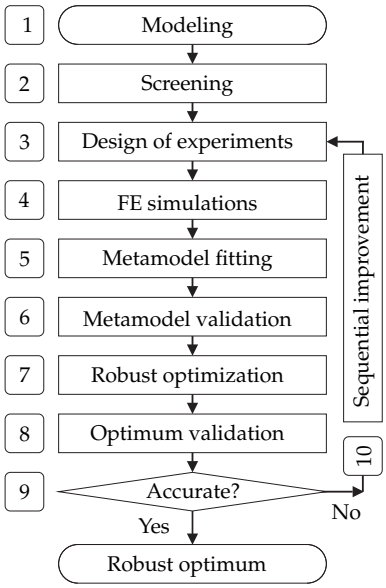

Figure 3.1 *Flowchart of the robust optimization strategy*

and ranges have to be quantified. The ranges of the design variables $\mathbf{x}$ are bounded by lower bounds ($\mathbf{lb}$) and upper bounds ($\mathbf{ub}$). For the noise variables $\mathbf{z}$ (either design variable uncertainty $\mathbf{z}_\mathrm{x}$ or parameter uncertainty $\mathbf{z}_\mathrm{p}$) a normal distribution is assumed, described per noise variable by a mean value μ_z and a corresponding variance σ_z^2, i.e. $\mathbf{z} \sim \mathcal{N}(\boldsymbol{\mu}_\mathrm{z}, \boldsymbol{\sigma}_\mathrm{z}^2)$. The parameters $\mathbf{p}$ are not explicitly mentioned since these are set to a certain fixed value before optimization. If the parameters can only be controlled to a limited degree in practice, a known or estimated variation can be added to account for this uncertainty $\mathbf{z}_\mathrm{p}$. The robust optimization formulation used in this work is given in Equation (2.9) and repeated in Equation (3.1) for convenience, completed with the noise variables.

$$
\begin{aligned}
&\min_{\mathbf{x}} \ \mu_\mathrm{f}(\mathbf{x}) + \alpha\sigma_\mathrm{f}(\mathbf{x}) \\
&\text{s.t.} \ \ \boldsymbol{\mu}_\mathrm{g}(\mathbf{x}) + \mathbf{k}_\mathrm{g}\boldsymbol{\sigma}_\mathrm{g}(\mathbf{x}) \leq \mathbf{0} \\
&\qquad \mathbf{lb} \leq \mathbf{x} \leq \mathbf{ub} \\
&\text{where } \mathbf{z} \sim \mathcal{N}(\boldsymbol{\mu}_\mathrm{z}, \boldsymbol{\sigma}_\mathrm{z}^2)
\end{aligned}
\tag{3.1}
$$

3.3 Variable screening

Before proceeding with the actual robust optimization step, variable screening is performed in **step 2** of the strategy. For industrial metal forming processes, the optimization problem defined in the first step may contain many design and noise variables. As mentioned in Section 2.4.3, metamodels suffer from the so-called *curse of dimensionality*, i.e. the algorithm becomes exponentially more time-consuming with an increasing dimension of the optimization problem. Variable screening is therefore performed to reduce the number of variables.

Generally, the majority of response variation in an optimization problem is caused by a limited number of design and noise variables. It is therefore likely that many of the variables initially included have little or no effect on the objective function and constraints under consideration. Using screening techniques, one can determine the variables that have the greatest effect on the responses and eliminate the unimportant ones. This results in a reduced size of the optimization problem, which increases the efficiency of the robust optimization procedure.

Screening techniques

The screening techniques used in this work are classical screening techniques as described by Montgomery [94, 95] and Yang and El-Haik [151]. The number of design and noise variables can be reduced based on a factorial DOE [100]. Factorial designs are considered that assign two levels to each of the k design and noise variables. An impression of a full factorial design with $k = 3$ is provided in Figure 3.2a. Note that for robust optimization, the DOE is applied into a single k-dimensional space where k is the sum of the number of design and noise variables. For the upper and lower bound of a noise variable, one can set these at e.g. $\mu_z \pm 3\sigma_z$ depending on the problem under consideration.

After running the FE simulations at the variable settings provided by the DOE, an RSM model is fitted, see Appendix C.1. A two-level full factorial design allows for estimating the main and interaction effects of the variables on the response. A three-level full factorial design allows for additionally estimating the quadratic effects. For a two-level full factorial design, the number of simulations equals 2^k, increasing exponentially with k. For $k = 3$ variables, the required number of FE simulations n equals 8 as depicted in Figure 3.2a. Estimating main and interaction effects comes at a significant cost for an increasing number of variables. Estimating quadratic effects comes at even higher costs.

For variable reduction, enough 'understanding' of the problem under consideration is obtained by evaluating the main effects only as reasoned in Appendix B.

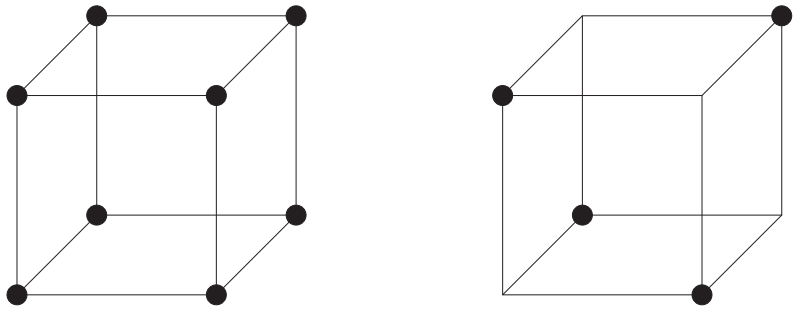

Figure 3.2 *(a)* 2^3 *full factorial design and (b)* 2^{3-1}_{III} *fractional factorial design*

The main effects provide the magnitude and direction of the influence of different variables on the response. This information can be obtained by running a fraction of the full factorial design, saving on the required number of FE simulations. As an example, a $(1/2)^q$ fraction of a 2^k full factorial design is taken, resulting in a 2^{k-q} fractional factorial design. A commonly used DOE for variable screening is a resolution III fractional factorial design, see Figure 3.2b. This design allows for independently estimating the main effects using $2^{k-q}_{\text{III}} = 2^{3-1}_{\text{III}} = 4$ FE simulations. Details on choosing an appropriate fraction q of a full factorial design are provided in Appendix B.

The resolution of the fractional factorial design describes the ability to separate main effects and interactions from one another. A resolution III design allows for independently estimating the main effects. Interaction effects cannot be estimated accurately since these are aliased or confounded with the main effects. That is, the reduction of the total number of simulations using a resolution III fractional factorial design comes at a cost of being able to determine only $(1/2)^q$ part of the total number of regression coefficients of the RSM model, see Appendix B. However, keeping in mind that the strategy should be efficient for use in conjunction with time-consuming FE simulations, the gain in efficiency by only considering main effects for variable reduction is at this point more important than the accuracy.

After running the FE simulations at the variable settings provided by the resolution III fractional factorial design, an RSM model is fitted. From the RSM model, so-called *Pareto plots* and *Main Effect plots* can be obtained. Based on these plots, one can determine the most important design and noise variables, i.e. those variables that have the greatest effect on the responses.

Pareto plots

An example Pareto plot for 4 variables is provided in Figure 3.3a. It visualizes the main effect of different variables on the response. The main effect per variable for a two-level fractional factorial design is defined as [100]:

$$\text{main effect}(x_1) = \frac{\sum y(x_1^+) - \sum y(x_1^-)}{n/2} \tag{3.2}$$

where n is the number of simulations and $y(x_1^+)$ and $y(x_1^-)$ are the response measurements at the high and low levels of a variable respectively. The main effects for all variables are displayed in the Pareto plot in descending order. Additionally, the percentual cumulative effect is plotted, which can assist in determining how many variables should be included in an optimization problem to ensure a certain percentage of control over the response variation.

The dashed line in Figure 3.3a represents the error effect which can be calculated by [100]:

$$\text{error effect} = \frac{\sqrt{n\ \text{SSE}}}{n/2} \tag{3.3}$$

where the error sum of squares (SSE) is given by Equation (D.1). Only the design variables having a larger effect than the error effect are assessed as significant. In the case of the example Pareto plot in Figure 3.3a, variables x_1, x_2 and x_3 are assessed as significant. Variable x_4 is assessed as not significant and can be removed from the robust optimization problem.

Main effect plots

The direction of the effect can be visualized using main effect plots. Figure 3.3b shows the direction of main effect for variable x_3, which is assessed as most significant in the Pareto plot. Note that the total effect coincides with the height of the bar in the Pareto plot. Variables that are assessed as not significant based on the Pareto plot can be removed from the optimization problem by setting it to the level that minimizes the objective function under consideration.

Note that this screening procedure explicitly considers continuous variables. In the case where discrete variables are considered, other screening techniques can

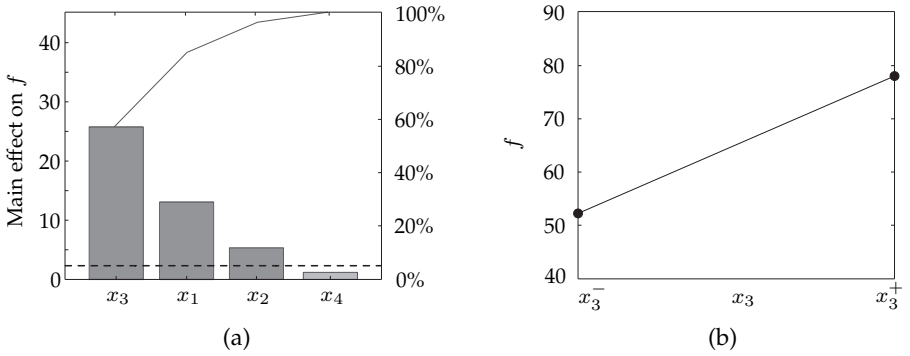

Figure 3.3 *(a) Pareto plot of main effects and (b) main effect plot*

be followed for variable reduction. These techniques are not explicitly mentioned here since these type of variables are not considered in the subsequent chapters. The interested reader is referred to [19] for a screening procedure including discrete variables.

Finally, the combination of Pareto plots and main effect plots enables the selection of design and noise variables that significantly influence the response variation. Different approaches can be followed for the selection of variables. Variables can be selected based on their significance with respect to the error effect. One can also select variables to ensure a certain percentage, e.g. 80%, of control over the response variation. Both approaches are applied in this work. The latter approach is more commonly applied in the literature since it generally results in a greater variable reduction compared to the former.

3.4 Robust optimization

The next step is to solve the reduced robust optimization problem defined in Equation (3.1) by the creation of metamodels for each response function. In the case of robust optimization, metamodels are generated for obtaining the statistical measures of the objective function and constraints in the design space. As outlined in Section 2.4.3, different metamodel-based robust optimization methods can be distinguished. In this work, the single response surface method is applied.

3.4.1 Design of experiments

At the basis of a metamodel is a DOE plan in the combined design–noise variable space. When dealing with deterministic computer experiments, space-filling designs are preferred over other DOE types to minimize the model prediction error as reported by Santner et al. [122]. Therefore, a space-filling LHD is used. Figure 2.6a presents an LHD of 20 DOE points in the combined design–noise variable space. Optima are commonly encountered on the boundary of the design space. The LHD is therefore combined with a Full Factorial Design (FFD) which places DOE points at all corners of the design domain, see Figure 3.2a. As mentioned in Section 3.3, the number of FE simulations for an FFD increases exponentially with the number of variables. This problem is partially alleviated by first reducing the number of variables in a screening step. The combined usage of an LHD + FFD DOE ensures that both the interior and the boundaries of the design space are well sampled.

In **step 3** of the robust optimization strategy, a combined LHD + FFD sampling is created. The size of an initial DOE for computer experiments is recommended to be chosen equal to 10 times the number of variables by Schonlau [124] which will be used in this work as well. However, this must be seen as a guideline for the engineer since the general goal is to perform a minimum number of initial simulations while ensuring a proper initial basis for fitting the metamodels. As an example in Figure 2.6a, 4 FFD points can be added to the 20 LHD points. The final required number of DOE points for accurately modeling the responses is unknown beforehand and depends on the problem under consideration (response complexity, metamodel type, etc.). In case an initial metamodel approximation does not result in an accurate fit of the response data, the DOE scheme can be improved in a later stage of the robust optimization strategy (step 10) by applying a sequential improvement step.

3.4.2 Run FE simulations and fit metamodels

After running the FE simulations (**step 4**) corresponding to the settings specified by the DOE, a single metamodel is fitted in the combined design space as shown in Figure 2.6b. Different metamodel types can be used for this purpose. The question is which type of metamodel to use without having *a priori* knowledge of the underlying true response function. Some authors [5, 64, 76, 128] state that Kriging or neural networks as metamodeling techniques are considered to be more suitable approximation methods than RSM, since the former methods can provide a more accurate prediction of non-linear response functions. Others

[62, 116] argue that the use of RSM models is more suitable, especially in combination with response values contaminated with numerical noise.

Since the shape and complexity of the response behavior in the design space is unknown beforehand and different metamodel types can be accurate for different types of responses, a family of metamodels is fitted (**step 5**) using:

- Response Surface Methodology (RSM)
- Kriging
- Neural Networks (NN)

The theoretical background for these models is provided in Appendix C. For RSM, polynomial models with an increasing complexity are fitted, i.e. linear models, linear + interaction models, pure quadratic or elliptic models and full quadratic models. For Kriging, models are fitted using a constant, linear and quadratic polynomial trend function combined with a Gaussian exponential function. In NN, tangent sigmoid and linear functions are selected as the basis functions. As a result, a family of metamodels is obtained with varying abilities to accurately describe the response behavior.

3.4.3 Metamodel validation

The performance of each metamodel is subsequently validated (**step 6**) using ANalysis Of VAriance (ANOVA) techniques as reported by Myers and Montgomery [100] and described in more detail in Appendix D. The statistical techniques incorporated in ANOVA allow for estimating how well a metamodel reflects the response behavior. A commonly used measure to evaluate the significance of a metamodel with respect to the response measurements is the coefficient of determination R^2. The R^2-value ranges between 0 and 1. In general, a larger R^2-value indicates a better approximation of the response measurements by the metamodel. An R^2-value of 1 indicates that the metamodel perfectly fits the response measurements.

The ANOVA techniques presented in Appendix D are based on a random error term ε present after fitting the regressing metamodels to the response measurements, see Equation (C.1) and Appendix D. In case a metamodel interpolates through the response measurements, these statistics cannot be used since the remaining fitting error is zero in the DOE points. Instead, validation of the metamodels is performed based on Leave One Out Cross Validation (LOOCV) where the ability of a metamodel to predict untried measurements is tested [100].

Using LOOCV, one leaves out a measurement point x_{-i} and fits the metamodel through the remaining response measurements. The difference between the real value $y(x_i)$ and the predicted value $\hat{y}_{-i}(x_i)$ is the prediction error e_{-i}:

$$e_{-i} = y(x_i) - \hat{y}_{-i}(x_i) \tag{3.4}$$

The selected data point is referred to as the validation data, and the remaining DOE points as the training data. By replacing ε with the prediction error e_{-i}, one can again calculate the coefficient of determination. This coefficient is now referred to as the prediction R^2-value, i.e. R^2_{pred}. Using LOOCV, the level of fit of each metamodel is calculated. For each response, the metamodel is selected with the best performance, i.e having the highest R^2_{pred}-value.

3.4.4 Metamodel-based robust optimization

For the objective function and each constraint, a metamodel is selected for use in robust optimization. For solving Equation (3.1), a prediction of the response mean and standard deviation as a function of the design variables is required. This prediction can be obtained analytically in the case of RSM as reported by Montgomery [94]. When Kriging or NN techniques are employed instead of RSM, an analytical derivation of the statistical measures is not possible. Instead, an MCA of 10,000 function evaluations is run on the metamodels at each evaluation of the optimization algorithm. Since the MCA is performed on the metamodels, it is very efficient. The resulting predictions of the mean and standard deviation are used by a gradient-based optimization algorithm for solving Equation (3.1). The algorithm is started at all DOE points to minimize the risk of the overall optimization procedure from getting trapped in a local optimum. Similar multi-start strategies are reported in [19, 124]. For optimization, use is made of the MATLAB algorithm `fmincon` whereas for the MCA use is made of the `mca` function [92].

3.5 Validation of the robust optimum

Initially, a minimum number of DOE points is chosen in the third step of the strategy to limit the required number of expensive function evaluations. As a result, the initial solution of the approximated problem is only an estimation of the true optimum of the underlying response function. To obtain an accurate and

reliable solution, the metamodel prediction accuracy in the optimum has to be validated (**step 8**). For a deterministic optimum, this can be done by performing a single FE simulation. The metamodel is assessed as accurate if the prediction in the deterministic optimum agrees with the FE simulation result. If this is the case, it is expected that also the optimum of the underlying response function is approximated with sufficient accuracy. If this is not the case, a sequential improvement step can be applied which will be discussed in Chapter 5.

For validation of the metamodel accuracy after robust optimization, multiple FE simulations are performed around the robust optimum. In case an accurate local metamodel prediction is obtained with respect to the FE simulation results, it is expected that also the robust optimum of the underlying response function is approximated with sufficient accuracy. Obviously, only a limited number of FE simulations can be performed resulting in a coarse estimation of the metamodel prediction accuracy and robust optimum (**step 9**).

Note that up to now, only numerical validation is discussed. The error of the FE simulations and metamodel approximation with respect to the physical process is still unknown. Validation of the numerically predicted responses with the physical process is therefore recommended and also applied in this thesis for the considered forming processes, as described in the following chapters.

3.6 Sequential improvement

If the accuracy of an initial metamodel is not sufficient, a sequential improvement step can be applied to update the metamodel successively (**step 10**). A sequential optimization algorithm is proposed and discussed in detail in Chapter 5.

In the subsequent chapters, the proposed robust optimization strategy is applied to a number of industrial metal forming processes. First, the working principle of the strategy will be demonstrated by application to a roll forming process in Chapter 4. This chapter will mainly focus on steps 1–7 of the strategy. In Chapter 5, special attention is given to steps 8–10, validation and sequential improvement by application to a V-bending process. An extension of the strategy is described in Chapter 6 and Chapter 7 by adding mathematical tools for dealing with numerical noise and for modeling material scatter respectively. Finally, the strategy is applied in a demonstrator study considering the robust optimization of a deep drawing process including experimental validation of the numerical results as described in Chapter 8.

Chapter 4

Application to a roll forming process*

4.1 Introduction

Application of the robust optimization strategy to a roll forming process is described in this chapter. A schematic impression of the process is given in Figure 4.1, demonstrating how a strip of sheet metal is progressively bent to a V-shaped product. The bending is achieved through sets of rolls mounted on consecutive stands having a predefined inter-distance. Roll forming is, compared to rival metal forming processes, an efficient and low-cost method for the production of constant-profile parts with high lengths and in large quantities.

During the roll forming process, each set of rolls performs an incremental part of the bend to finally obtain a desired cross-section profile. Despite its visual simplicity, the deformation during the bending process is complex. As the strip of sheet metal moves through the rolls, the material may experience longitudinal elongation and bending, transverse bending and shear. In addition, undesirable strains are generated in the sheet, also referred to as redundant deformations. These strains are known to cause product defects like longitudinal bow, twist, edge wave and springback. This chapter focuses on reduction of the product defects longitudinal bow and springback. Longitudinal bow is defined as the maximum height deviation from a straight product as a function of the strip length. Springback is caused by the elastic recovery of the material after rolling and is defined as the angle difference between the final bending angle of the product and the tooling angle.

*This chapter is based on: J.H. Wiebenga, M. Weiss, B. Rolfe and A.H. van den Boogaard. Product defect compensation by robust optimization of a cold roll forming process. *Journal of Materials Processing Technology*, 213(6), 978-986, **2013**.

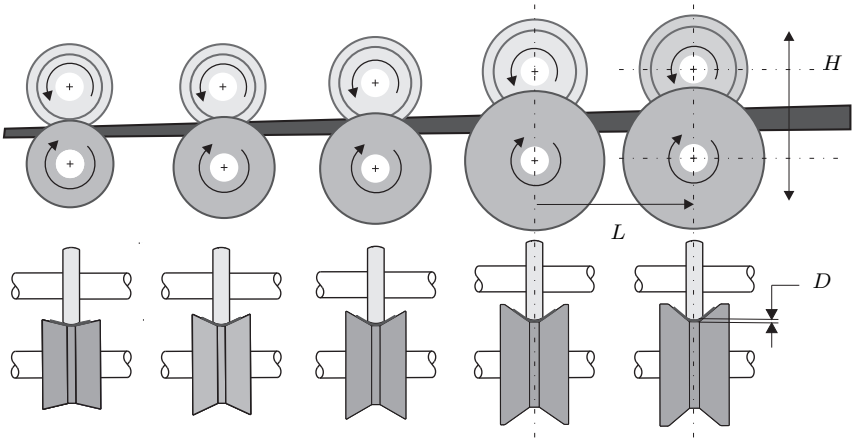

Figure 4.1 *Schematic impression of the roll forming process*

The relation between the occurrence of product defects and the roll forming process design is demonstrated both experimentally and numerically in several studies, see e.g. [53, 81, 85, 121]. Numerical deterministic optimization of the process design to minimize the occurrence of product defects is reported in [108, 152]. Additional to the process design, the quality of the final product is known to be highly sensitive to the material properties and the unavoidable variations of these properties during mass production. The effect of the yield stress on the longitudinal bow and peak strain is demonstrated in sensitivity studies by Lindgren [84] and Han et al. [52]. The sensitivity of the springback behavior with respect to the yield stress and the strain hardening exponent has been investigated by Bui and Ponthot [21]. It is shown that the dimensional quality of roll formed products will decrease when using a high-strength material instead of a low-strength material. With an increasing usage of Advanced High Strength Steels (AHSS) in recent years, avoiding product defects in roll forming will become even more difficult due to the combination of reduced formability and larger variation of material properties generally observed in the forming of AHSS.

Prevention of product defects while simultaneously minimizing the sensitivity to unavoidable sources of variation can be achieved by optimizing the roll forming process in a robust way. By combining FE simulations with robust optimization techniques, a robust roll forming process can be designed, producing the desired results under varying process conditions. Another approach to eliminate product defects during roll forming, extensively described by Halmos [51], is the usage of a straightener unit, twist forming unit or over-bend rolls. This additional

tooling is placed after the last forming stand to compensate for product defects. In this work, compensation of product defects is achieved using an adjustable roll former. This roll former allows for the adjustment of the bottom and the top roll of the final stand to simultaneously compensate for longitudinal bow and springback.

This literature review shows that the research topics of optimal deterministic process design, the influence of scattering material properties and the usage of adjustable tools have been treated separately in the field of roll forming. In this chapter, these three approaches are combined. That is, the robust optimization strategy is combined with the usage of an adjustable roll former. Using the family of metamodels to replace the computationally expensive roll forming FE simulations, the optimal robust process settings for the adjustable tools are determined while accounting for the influence of material scatter. Using the robust optimization strategy, it is ensured that both the magnitude of the defect and the effect of material scatter on the product quality are minimized. A combined numerical and experimental approach is followed for the validation of the numerical model and the numerical trends found in the robust optimization study.

For the purpose of this research, the roll forming process of an AHSS V-section profile is considered. Initial roll forming trials at the Deakin University (a partner in this research) showed that a significant amount of longitudinal bow and springback occurs in the product. To enable compensation of product defects throughout the production process, an adjustable roll former is used. The roll forming process and corresponding FE model are introduced in Section 4.2. Section 4.3 describes the validation of the nominal FE model using initial roll forming trials. The subsequent application of the proposed robust optimization strategy is described in Section 4.4. Finally, the trends found in the numerical study are verified by a series of roll forming experiments. A discussion is provided in Section 4.5. Finally, Section 4.6 will present the conclusions of this chapter.

4.2 Roll forming process of a V-section profile

The geometry of the V-section profile used in this study, the accompanying so-called *flower pattern* design and the dimensions of the pre-cut strip are presented in Figure 4.2. The material is an AHSS Dual Phase (DP) 780 with a nominal thickness (t) of 2 mm. The product is formed by 5 stands (see Figure 4.1) with an inter-distance of 305 mm and a bending radius of 15 mm. Each stand applies a

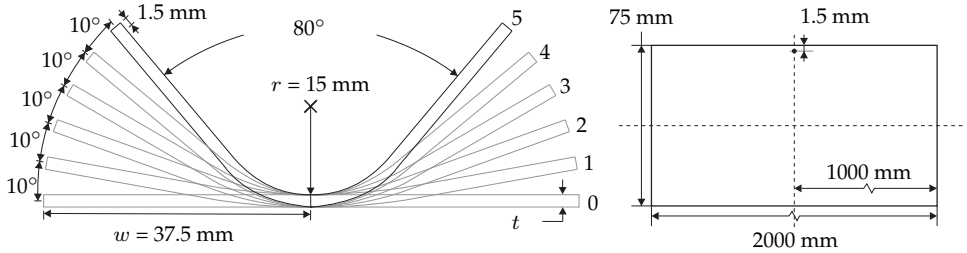

Figure 4.2 *Flower pattern of the V-section profile and dimensions of the pre-cut strip*

bending angle of 10° resulting in a final product angle of 80°. A 2000 mm pre-cut strip of 75 mm width is fed into the rolls at a speed of 22.5 mm/s whereby both the top and bottom rolls are driven.

4.2.1 Numerical model

Roll forming FE simulations are used to determine main and interaction effects between controllable process settings and uncontrollable variation of incoming material properties with respect to the product defects. MSC.Marc has been used as FE code and due to symmetry, only half of the sheet is modeled and subsequently discretized using 9450 solid elements. An 8-node enhanced assumed strain element (type 7) is utilized which allows the ability to capture pure bending using a single element through the thickness [97]. The rolls are modeled using an analytical rigid surface description. The total displacement of the rolls is 4100 mm using 3500 increments. One simulation of the frictionless roll forming of a pre-cut strip takes about 9 hours on a 3.5 GHz Intel Xeon processor with 16 GB RAM memory.

4.2.2 Variation modeling

For describing the material behavior of DP780, Hooke's law and Swift's isotropic strain hardening law are adopted as material models, see Equation (4.1) and Equation (4.2) respectively. The nominal material properties are obtained from uniaxial tensile tests. The resulting coefficients for the Swift hardening law are listed in the second column of Table 4.1. The scatter of the material properties around their mean value (μ_z) is based on the experimental work presented by Abspoel et al. [2] and de Souza and Rolfe [27] and given in the remainder of Table 4.1. The material properties are assumed to vary according to a normal distribution where the scatter is defined in terms of the standard deviation (σ_z). In

Table 4.1 *Material properties of Dual Phase (DP) 780 where the variation is based on [2, 27]*

Variable	Mean (μ_z)	Std. dev. (σ_z)	Min. ($\mu_z - 3\sigma_z$)	Max. ($\mu_z + 3\sigma_z$)
t	2 mm	0.01 mm	1.97 mm	2.03 mm
σ_y	586 MPa	13 MPa	547 MPa	625 MPa
R_m	894 MPa	20 MPa	834 MPa	953 MPa
ε_0	0.0024			
n	0.138			
E	210 GPa			

order to accurately represent the true scatter of the DP780 material and to prevent overestimation of the response variation, a full correlation between the yield stress (σ_y) and the ultimate tensile stress (R_m) is used as reported in [2, 27]. The strain hardening exponent (n) remains constant at 0.138 from which the strength coefficient (K) can be calculated using Equation (4.3) [2].

$$\sigma = E\varepsilon_e \tag{4.1}$$

$$\sigma_y = K(\varepsilon_0 + \varepsilon_p)^n \tag{4.2}$$

$$K = R_m \frac{e^n}{n^n} \tag{4.3}$$

4.2.3 Process adjustment

To enable continuous product defect compensation during production, a roll former with an adjustable final roll stand is utilized. This stand facilitates the re-adjustment of the roll gap (D), the vertical alignment (H) and the inter-distance (L) between the final roll stands, see Figure 4.1. The nominal settings and bounds of the design variables are given in Table 4.2.

Table 4.2 *Nominal settings and bounds of the design variables*

Variable	Nominal setting	Lower bound	Upper bound
H	0 mm	-5 mm	10 mm
L	305 mm	205 mm	405 mm
D	2 mm	1.9 mm	2.5 mm

4.3 Experimental validation of the nominal FE model results

Before proceeding with the numerical robustness analysis, the outcomes of the nominal FE model with respect to the product's main defects are experimentally validated. In addition to longitudinal bow and springback, also the longitudinal strain in the edge of the V-section profile is validated since Paralikas et al. [108] show that the reduction of longitudinal edge strains can result in a reduction of bow. Other typical roll forming defects, like edge wave or twist, have not been observed in the experimental studies and are therefore not considered in this study.

Longitudinal bow is defined as the maximum height deviation from a straight product as a function of the strip length, see Figure 4.3. A three-dimensional image of the rolled product is generated by scanning the formed product using an EXAscan high resolution scanner from which the bow is determined [35]. The springback is defined as the angle difference between the final bending angle of the product θ and the tooling angle of 80°, see Figure 4.3. The final bending angle is measured at the front, center and end of the product to enable studying flanging. Flanging is defined as the difference in front and center bending angle, and center and end bending angle. The numerical and experimental strain measurements are taken halfway along the length of the strip at 1.5 mm away from the outer edge as indicated in Figure 4.2. The experimental strain as a function of the strip displacement through the roll former is recorded using

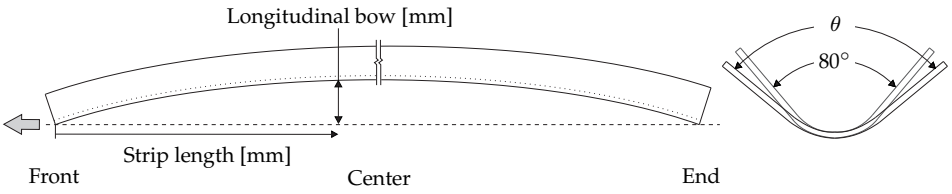

Figure 4.3 *Definition of longitudinal bow and springback*

strain gauges. The following experimental results are obtained by performing 3 experimental repetitions at the nominal roll forming settings (see Table 4.2) where the nominal material thickness is selected to be 2 mm. Preliminary roll forming trials are performed to determine the exact amount of shaft deflection during forming. This is followed by a re-adjustment of the roll gap to account for tool deflection. The experimental results are compared with the simulation results obtained from the numerical model introduced in Section 4.2.1.

4.3.1 Longitudinal bow

The experimental and numerical results for longitudinal bow are presented in Figure 4.4. The 3 experimental longitudinal bow profiles show a slight non-symmetric behavior over the length of the strip, which is not the case in the numerical result. The magnitude of the numerical longitudinal bow prediction is in good agreement with the experiment.

4.3.2 Longitudinal edge strain

Figure 4.5 shows the experimental and numerical results for longitudinal edge strain development as a function of the strip displacement through the roll former. A single rolled product was equipped with a strain gauge resulting in 1 experimental strain measurement. The numerical results are in good agreement with the experimental edge strain measurement, especially for the prediction of the peak longitudinal edge strain. However, looking in detail at the residual longitudinal edge strain after passing each station, an increasing error can be observed. The residual plastic longitudinal edge strain after passing the 5^{th} roll stand causes a permanent elongation of the edge. This is detected both experimentally as well as numerically, although the magnitude is overestimated numerically.

4.3.3 Final bending angle

The experimental and numerical results for the springback angle measured at the front, center and end of the strip are presented in Figure 4.6. The vertical bars in the experimental results show the average variation in springback angle for the 3 experimental repetitions, demonstrating a good repeatability. A difference in front and center bending angle, and center and end bending angle is observed experimentally and also predicted numerically. The experimentally determined

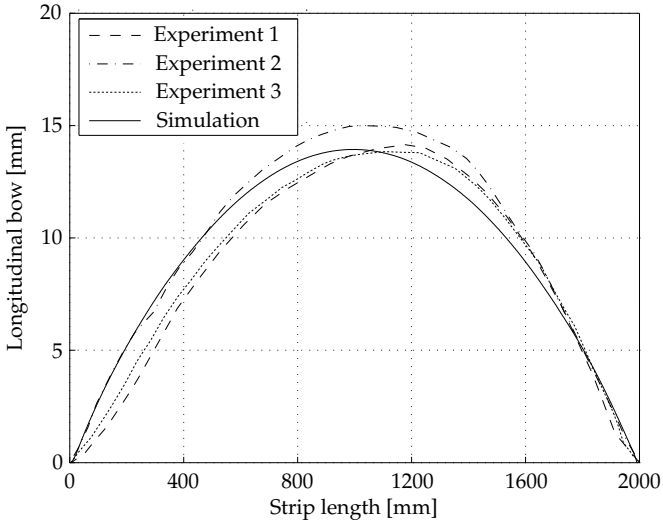

Figure 4.4 *Experimental and numerical results for longitudinal bow as a function of the strip length*

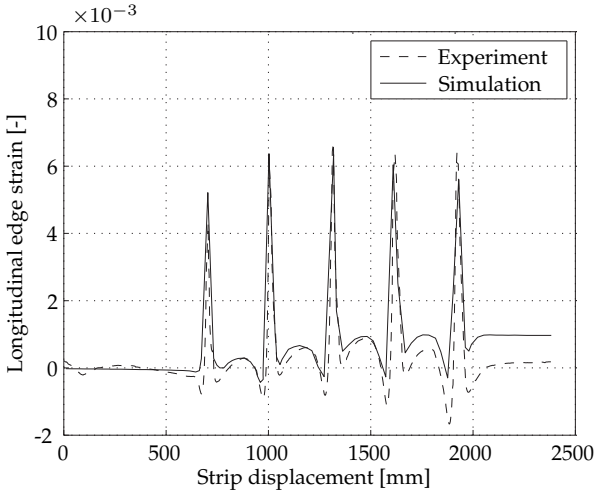

Figure 4.5 *Experimental and numerical results for longitudinal edge strain development as a function of the strip displacement through the roll former*

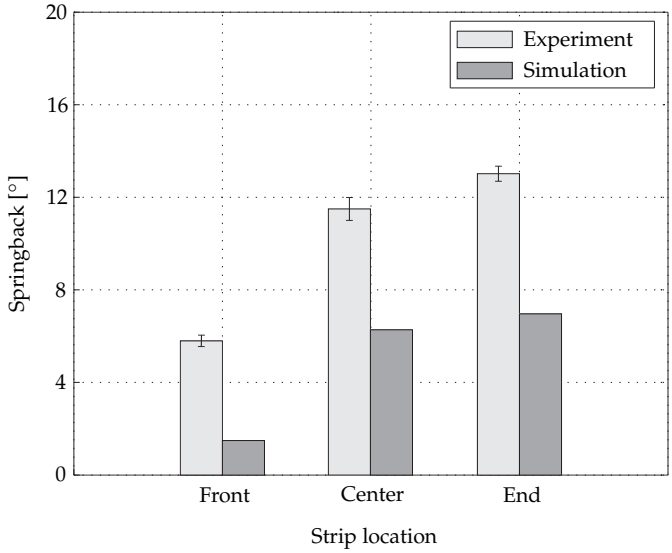

Figure 4.6 *Experimental and numerical results for the springback angle measured at the front, center and end of the strip*

springback angle at the center of the section is $11.5° \pm 0.5°$ and at the front and back end $5.8° \pm 0.3°$ and $13.2° \pm 0.4°$ respectively.

Looking at the numerical prediction, the springback angle is underestimated. Similar magnitudes of deviation between experimental and numerical springback results have also been observed in the literature for which several causes are discussed. Groche et al. [48] described a springback validation study where experimental springback angles are compared with 7 analytical approaches. The difference in springback angle is related to changing material properties such as a changing Young's modulus during bending. In another study by Beiter and Groche [14], it is suggested that some simplifying assumptions made in the numerical analysis of the roll forming process may cause discrepancies between experimental and numerical springback results. As mentioned in Section 4.2.1, the rolls are modeled using an analytical rigid surface description and this neglects the effect of tool deformation during rolling. The initial roll gap of each stand in the experiment is adjusted to compensate for possible initial spacing on the tools, shafts and bearings as mentioned in Section 4.3. However, the limited stiffness of the roll former remains an issue to be considered in the comparison of experimental and numerical results. This aspect is also addressed by Saenz de Argandon et al. [119] showing that, especially in the roll forming of AHSS, tool deflection can be significant and does affect the forming radius

and therefore also springback. This suggests that the numerical underestimation of springback observed in this study may be due to an overly stiff behavior of the forming rolls in the numerical model. A final possible cause discussed here is the limited number of elements through the material thickness of the strip, which limits the accuracy with which the stress state can be described. A single nominal simulation with a total of 7 elements through the material thickness shows that the center springback prediction improved to 7.2°. This suggests that a better correlation with the experimental springback results may be achievable by using more elements through the material thickness, although the angle difference remains significant. The resulting numerical model led to an increased calculation time of 130 hours, which is unacceptable for use in the robust optimization study. Given that the numerical model captures the trends for flanging correctly and gives an accurate representation of longitudinal bow, the FE model is assessed as acceptable for further use in the optimization study. A continuation of this discussion is provided in Section 4.5.

4.4 Robust optimization

Both the experimental and numerical results show a significant amount of longitudinal bow and springback in the V-section profile. The next step is to determine the causes of the product defects and determine how these defects can be compensated for by optimizing the process set-up. This requires determining main and interaction effects between the defects and the controllable process settings and uncontrollable variation of material properties. Determining these relations experimentally would require a significant amount of material, time and manpower. Instead, FE simulations are used to create metamodels of the product defect responses in the design space.

4.4.1 Modeling

Following Figure 3.1, the first step in the robust optimization strategy is to define the objective, constraints, design variables and noise variables of the optimization problem. The design variables and noise variables have been discussed and quantified in Section 4.2.2 and Section 4.2.3 respectively. The main product defects for the V-section profile are longitudinal bow and center springback. An initial study showed that flanging could not be affected by the design variables included in the optimization study. In other words, the difference in front and center bending angle, and center and end bending angle could not be significantly

reduced but also did not worsen. Therefore, these responses are not included in the objective or constraints of the optimization study. They are, however, visualized in the remainder of this chapter to demonstrate the insensitivity of these responses to the design variables. The objective of this study is to optimize the product dimensional quality by minimizing longitudinal bow and center springback. Bow is taken into account as the objective function f_{b} by taking the absolute value of the mean μ_{b} combined with the variation of bow σ_{b}. The robust optimum should also satisfy $\pm 3\sigma_{\mathrm{cs}}$-constraints on the Center Springback (CS) angle where the USL and LSL is chosen to be 2° and -2° respectively. The quantified robust optimization formulation is now given by:

$$
\begin{aligned}
&\min_{\mathbf{x}} \ |\mu_{\mathrm{b}}| \pm 3\sigma_{\mathrm{b}} \\
&\text{s.t.} \ -2 \leq \mu_{\mathrm{cs}} - 3\sigma_{\mathrm{cs}} \\
&\qquad \mu_{\mathrm{cs}} + 3\sigma_{\mathrm{cs}} \leq 2 \\
&\qquad -5 \leq H \leq 10 \\
&\qquad 205 \leq L \leq 405 \\
&\qquad 1.9 \leq D \leq 2.5 \\
&\text{where } t \sim \mathcal{N}(2, 0.01^2) \\
&\qquad \sigma_{\mathrm{y}} \sim \mathcal{N}(586, 13^2)
\end{aligned}
\tag{4.4}
$$

4.4.2 Main effects on product defects

The main effects of the design and noise variables are calculated using the screening techniques as indicated in step 2 of Figure 3.1. The upper and lower bound of the noise variables are hereby set at $\mu_{\mathrm{z}} \pm 3\sigma_{\mathrm{z}}$. The resulting main effects are visualized in Pareto plots for longitudinal bow and center springback in Figure 4.7a and Figure 4.7b respectively. Clearly, all variables significantly affect at least one of the responses. It is reasoned that no further variable reduction is required here since only 5 variables are included in the robust optimization problem.

The Pareto plots show that the roll gap D has the largest effect on both the longitudinal bow and center springback. This is similar to what is experienced in the production process. The longitudinal bow and springback are sensitive to the vertical alignment H and inter-distance L. The effect of yield stress variation σ_{y} on bow is minimal, whereas it is significant for springback. The effect of material thickness variation t is significant for both responses, especially for longitudinal bow.

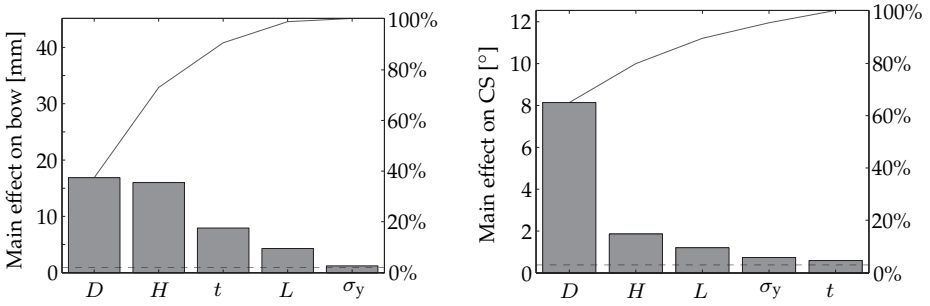

Figure 4.7 *Main effects of the design and noise variables on (a) longitudinal bow and (b) Center Springback (CS)*

Table 4.3 *ANalysis Of VAriance (ANOVA) results for the best metamodel fit of each response*

Response		Metamodel	R^2_{pred}
Longitudinal bow	f_{b}	NN	0.99
Front springback	g_{fs}	RSM	0.99
Center springback	g_{cs}	RSM	0.98
End springback	g_{es}	RSM	0.98

4.4.3 Metamodel results

The next step is the creation and validation of metamodels for longitudinal bow and springback (step 3-6 in Figure 3.1). A combined LHD+FFD sampling is created of 50 DOE points. After running the FE simulations corresponding to the settings specified by the DOE, the longitudinal bow and springback values of the product are extracted from the FE results. The family of metamodels as described in Section 3.4 is fitted and the metamodel quality is assessed by ANOVA and cross validation. The ANOVA results for the different responses are presented in Table 4.3. For the longitudinal bow, an NN model resulted in the most accurate fit, whereas for the springback responses full quadratic RSM response surfaces are selected. The resulting R^2_{pred}-values indicate that both the objective function and the constraint can be described accurately by the response surfaces.

From the single metamodel of each response, the response mean and standard deviation are determined as a function of the design variables. Impressions of the longitudinal bow and springback metamodels as a function of the design

variables are shown in Figure 4.8a and Figure 4.8b respectively. For visualization purposes, the remaining variables are set to their nominal settings as reported in the second column of Table 4.2. The vertical bars represent the $\pm 3\sigma$ bounds of bow and springback variation around the mean value caused by the influence of noise variables.

Evaluating the shape of the models in Figure 4.8a, a decrease of the longitudinal bow is observed for increasing H and L. Also, the springback angle decreases for a positive vertical alignment H (see Figure 4.8b) but it is less affected by the inter-station distance. Also note that flanging is not significantly affected by any of the design variables, while both the longitudinal bow and springback are strongly influenced by the roll gap D. As long as the roll gap D is larger than the nominal material thickness t, the material is only bent between the rolls. For $D<t$, the material is coined between the rolls. Due to coining and the resulting elongation of the product's bottom part, both springback and bow are reduced.

Looking at the robustness of the process, a significant variation of longitudinal bow is observed caused by the scatter of the material thickness and yield stress. This is mainly caused by the material thickness variation, see Figure 4.7a. At the nominal process settings, a $\pm 3\sigma_{\mathrm{b}}$ bow variation of 6.9 mm around the mean value of 11.6 mm can be observed (See Table 4.4). At this setting, the springback angle at the center of the product shows a $\pm 3\sigma_{\mathrm{cs}}$ variation of 0.57° around the mean value of 4.69°. For varying design variable settings, a change in the robustness is observed, although minor.

4.4.4 Optimal robust process settings

The set of metamodels is used for solving Equation (4.4), see step 7 in Figure 3.1. The optimal robust process settings and accompanying responses are presented in Table 4.4.

The mean response of longitudinal bow can be reduced to approximately zero by simultaneously decreasing the depth setting and increasing the inter-distance and vertical alignment. In other words, longitudinal bow can be fully compensated by adjusting the process settings of the final roll forming stand. Moreover, a 2.1 mm decrease of bow variation is achieved. However, the scatter of bow around the mean value remains significant. Both the variation of yield stress and material thickness still causes a bow variation of $\pm$ 4.8 mm. For the center springback, a reduction of 3.32° is achieved at the expense of a slight variation increase of 0.05°. Similar trends can also be observed for the front and end springback angle. Note that the upper constraint on center springback is exactly satisfied in the robust optimum.

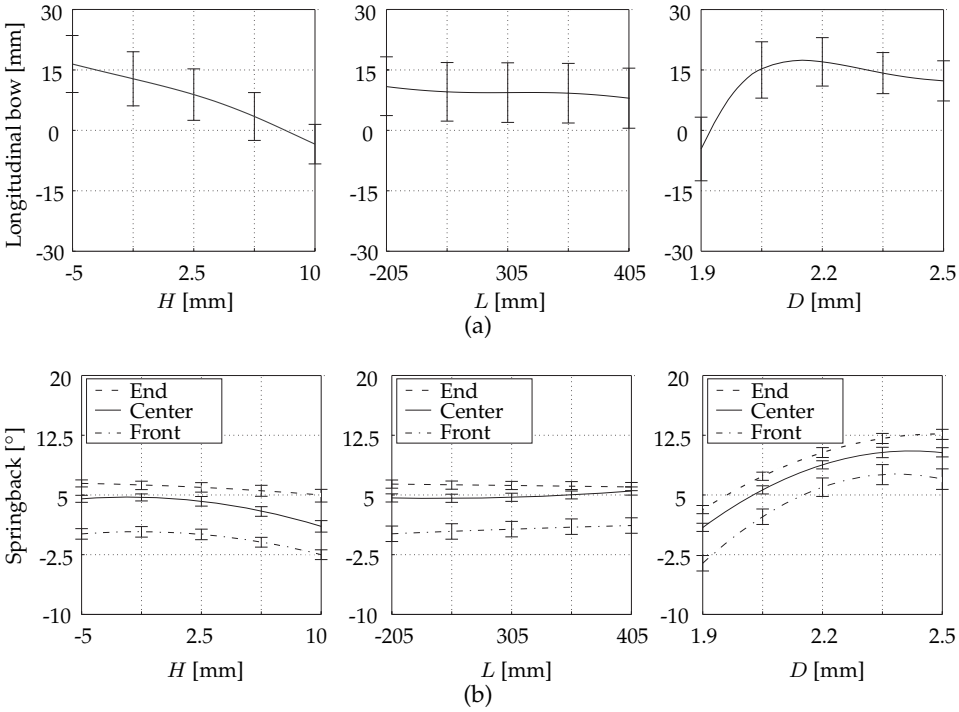

Figure 4.8 *Effect of design and noise variables on (a) longitudinal bow and (b) on front, center and end springback*

Table 4.4 *Nominal settings, optimized robust process settings, optimized deterministic process settings and corresponding responses*

Variable	Nominal	Robust	Deterministic
H	0 mm	10 mm	-1.2 mm
L	305 mm	371 mm	279 mm
D	2 mm	1.97 mm	1.90 mm
Response	$\mu \pm 3\sigma$	$\mu \pm 3\sigma$	$\mu \pm 3\sigma$
f_{b}	11.6 mm $\pm$ 6.9 mm	-0.1 mm $\pm$ 4.8 mm	0.0 mm $\pm$ 7.7 mm
g_{fs}	0.64° $\pm$ 1.06°	-2.27° $\pm$ 1.11°	-3.34° $\pm$ 1.03°
g_{cs}	4.69° $\pm$ 0.57°	1.37° $\pm$ 0.62°	1.63° $\pm$ 0.59°
g_{es}	6.65° $\pm$ 0.53°	5.39° $\pm$ 0.54°	3.75° $\pm$ 0.47°

4.4.5 Optimal deterministic process settings

As a comparison, also a deterministic optimization study is performed. The noise variables in Equation (4.4) are hereby set constant at their mean value. As a result, 2 deterministic optima are identified. The optimal design variable settings of the first deterministic optimum is very near to the optimal robust settings, see Table 4.4. At these settings, the mean value of the objective function is close to zero and the mean value of 1.37° for center springback satisfies the deterministic constraint $-2^\circ \leq g_{\text{cs}} \leq 2^\circ$.

The optimal deterministic process settings and accompanying responses of the second deterministic optimum are presented in the last column of Table 4.4. Compared to the optimal robust settings, the material is coined more severely. Decreasing the roll gap to D = 1.90 mm results in a negative bow, which is compensated for by a negative vertical alignment and a reduction of the inter-distance. An MCA onto the metamodels is performed at the optimal deterministic design variable settings to determine the stochastic measures of the responses. The mean value of the objective function is zero, meaning that longitudinal bow is fully compensated. The mean value of 1.63° for center springback has increased compared to the robust optimum, but still satisfies the deterministic constraint $-2^\circ \leq g_{\text{cs}} \leq 2^\circ$. However, looking at the variation around the mean values caused by the influence of the noise variables t and σ_{y}, an increasing amount of bow variation is observed. Moreover, adding the center springback variation to its mean value results in violation of the robust optimization constraint $\mu_{\text{cs}} + 3\sigma_{\text{cs}} \leq 2^\circ$ given in Equation (4.4). To summarize, whereas the deterministic optimization study results in 2 deterministic optima, the robust optimization formulation excludes the second deterministic optimum based on an improved robustness with respect to longitudinal bow and more desirable values for the center springback response. Also note that the robust optimum is favorable from a practical point of view since more coining results in higher tool wear.

4.4.6 Experimental validation

Based on the numerical robust optimization study, a significant improvement of the product quality can be achieved by changing the process settings of the adjustable tooling in the final roll stand. Moreover, the metamodels provide the engineer with clear trends on how to compensate for multiple defects simultaneously. Based on variable screening described in Section 4.4.2, both longitudinal bow and springback are most significantly affected by the roll gap.

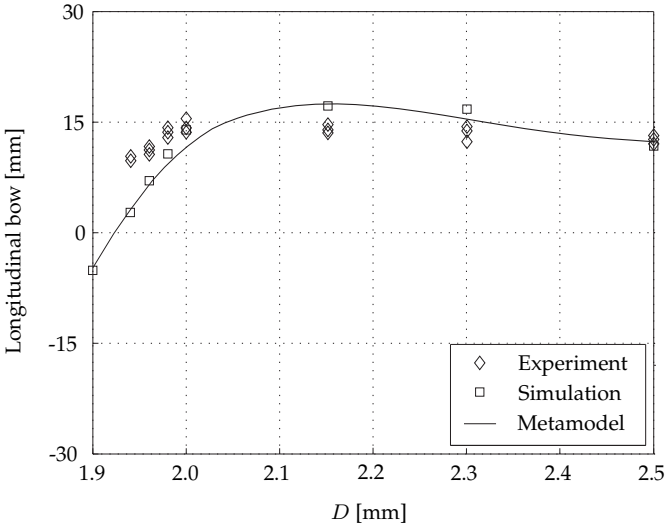

Figure 4.9 *Experimental and numerical results for longitudinal bow as a function of the roll gap D*

Next, experimental validation of the numerical trends is described whereby the roll gap in the final stand is adjusted. As discussed in Section 4.3.3, a reduction of the roll gap in the experiment will cause deformation of the roll stand. To compensate for the lack of tooling deformation in the numerical model, a comparison between the FE model results and experimental results is made by looking at the resulting thickness reduction for $D<t$ instead of the actual roll gap. It is assumed here that comparable process forces act on the product in the experimental and numerical situation. For the process setting D = 1.98 mm, a material thickness reduction (coining) of 0.01 mm is numerically predicted in the bottom of the part. To achieve a comparable thickness reduction in the experiment, the roll gap was adjusted to 1.5 mm prior to rolling. In addition, a thickness reduction of 0.02 mm was achieved with a roll gap of 1.3 mm in the experiment and 1.96 mm in the numerical model. Finally, a thickness reduction of 0.04 mm was achieved with a roll gap of 1.0 mm in the experiment and 1.94 mm in the numerical model. A further thickness reduction was not possible, since this would have led to permanent bending of the roll shafts or damaging of the bearings. For $D \geq t$, the effect of the numerical overestimation of the stiffness of the roll former on the responses is negligible. For this situation, the actual roll gap as set prior to the experiment is therefore used to compare the numerical and experimental results.

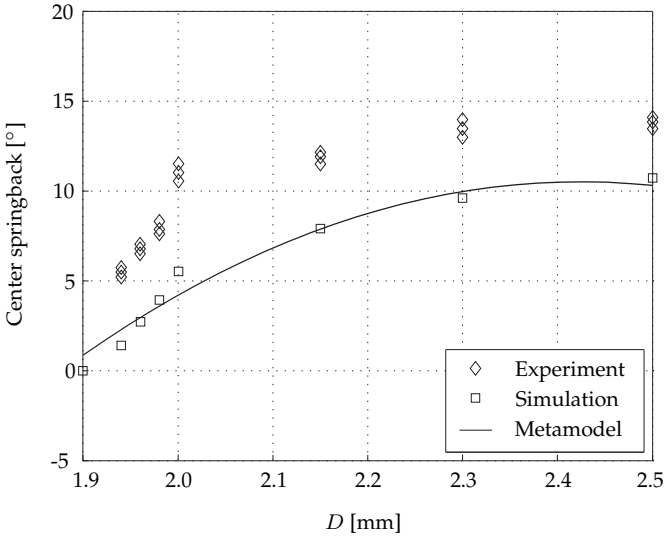

Figure 4.10 *Experimental and numerical results for center springback as a function of the roll gap D*

Figure 4.9 and Figure 4.10 show the experimental longitudinal bow and center springback values respectively as a function of the roll gap. Per roll gap setting, 3 experimental repetitions have been performed. The resulting bow and springback values are visualized by the diamond markers. The solid line shows the metamodel prediction at the nominal process settings for L and H (see Table 4.2) with t = 2 mm and σ_y = 586 MPa. Additional FE simulations have been performed at these specific settings. The resulting response values are visualized by the square markers.

The longitudinal bow values obtained by the experiments and simulations are in good agreement on the whole, see Figure 4.9. The NN model can represent the non-linear behavior of the numerical response accurately over the whole range of D. As predicted numerically, bow reduction is achieved in the experiment by decreasing the roll gap. However, the degree of bow reduction seems to be slightly less in the experiment compared to the metamodel predictions and the simulation results.

The change in roll gap has a significant effect on springback as shown in Figure 4.10. The discrepancy in experimental and numerical springback results (as discussed in Section 4.3.3) can again be recognized for D = 2 mm, decreasing for $D<t$ and $D>t$. Overall, the experimental trend of the springback change is in good agreement with the metamodel prediction and the simulation results.

4.5 Discussion

It was already discussed in Section 4.3.3 that a discrepancy in experimental and numerical springback results is present. Several causes for this discrepancy were outlined, supported by the literature. Despite this difference, robust optimization was performed using the nominal FE model of the roll forming process. The results in Figure 4.10 show that the final experimental trend of the springback change is in good agreement with the metamodel prediction and the simulation results.

Using the robust optimization strategy, valuable insights on the relations between design variables and noise variables, and common roll forming defects, are obtained. This supports the usage of the nominal FE model, despite its initial offset in results. Moreover, the metamodel results from the robust optimization study provide the process engineer with an intuitive understanding of how to adjust process settings to both compensate for product defects and simultaneously control the sensitivity to unavoidable scatter of material properties. Note, however, that for the prediction of reliability or scrap rate of this roll forming process, also the mean prediction of the numerical model must agree with the experimentally measured springback angle. For the case as discussed above, the scrap rate would be underestimated since the numerical model underestimates the springback angle. In practice, the roll forming process is more critical with respect to springback than predicted numerically.

4.6 Conclusions

The numerical and experimental study demonstrates the working principle of the robust optimization strategy for product defect compensation in a roll forming process. The dimensional quality of the considered AHSS V-section profile is improved by changing the process settings of the adjustable rolls in the final forming stand. The roll forming defects longitudinal bow and springback are compensated for without the need of additional tooling such as an end-straightener. More specifically, the numerical results for longitudinal bow show both a reduction of the magnitude and the sensitivity with respect to scatter of material properties. However, the variation of bow around the mean value remains high. Looking at the average center springback angle, a significant reduction of 70% is achieved with the robust optimization strategy.

Chapter 5

Sequential robust optimization*

5.1 Introduction

When using a metamodel approach to couple FE simulations with a robust optimization procedure, an initial metamodel generally only serves to find a first estimate of the optimum. Especially if the true objective function is highly non-linear or the metamodel is based on a limited number of response evaluations only, the initial metamodel approximation may be inaccurate. As a result, a difference between the prediction of the metamodel-based optimum and the FE simulation can be present. To obtain a more reliable and accurate solution, the metamodels have to be validated and if required improved successively. A sequential improvement step can be performed which adds new DOE points to the original DOE in a smart way to efficiently increase the accuracy of the metamodel prediction at regions of interest.

To enable sequential optimization, a sequential improvement step is added to the robust optimization strategy. See Figure 3.1. For the sequential improvement of metamodels, an algorithm is required to select the location of the next infill point. After evaluating the response at the new infill point by an FE simulation, the metamodels are updated by taking into account the additional response and subsequently validated (step 8 and 9 in Figure 3.1). An optimization procedure is started and the new prediction of the robust optimum is determined. The sequential improvement strategy continues to add DOE points (step 10 in Figure 3.1) until the metamodel prediction accuracy near the optimum is acceptable.

*This chapter is based on: J.H. Wiebenga, A.H. van den Boogaard, and G. Klaseboer. Sequential robust optimization of a V-bending process using numerical simulations. *Structural and Multidisciplinary Optimization*, 46(1), 137-153, **2012**.

Several sequential deterministic improvement algorithms have been proposed in the literature, of which a selection will be introduced in Section 5.2. An extension of a deterministic algorithm to account for the influence of noise variables is presented in Section 5.3. By means of two studies, the applicability and efficiency of the sequential robust improvement algorithm is demonstrated. The first study (Section 5.4) concerns an analytical test function. It is demonstrated that adding a sequential optimization step to the robust optimization strategy can further increase the efficiency and accuracy of the strategy to determine the robust optimum. In the second study (Section 5.5) these findings are replicated by application to an industrial V-bending process including experimental validation of the robustness results. Finally, Section 5.6 will present the conclusions of this chapter.

5.2 Sequential deterministic improvement

The following sequential deterministic optimization strategies are based on the *Improvement* which is defined by Schonlau [124] as:

$$\mathrm{I}(\mathbf{x}) = \begin{cases} 0 & \text{if } y(\mathbf{x}) > f_{\min} \\ f_{\min} - y(\mathbf{x}) & \text{otherwise} \end{cases} \tag{5.1}$$

The improvement is calculated by taking the difference between a function value $y(\mathbf{x})$ with respect to the minimum feasible tested (or calculated) response of the true objective function value $f_{\min}$ if $y(\mathbf{x}) < f_{\min}$. In case a metamodel is used, the function value $y(\mathbf{x})$ can be replaced by the metamodel prediction $\hat{y}(x_0)$ at an untried setting x_0.

A straightforward sequential optimization criterion, referred to as the *Most likely Improvement*, is given by $\mathrm{MI} = \max_{\mathbf{x}} \mathrm{I}(\mathbf{x})$ [34]. For this criterion, the location of the infill point is determined by maximizing the improvement. The FE model is subsequently re-evaluated at the predicted metamodel optimum. The additional FE model evaluation is used to update the metamodel. Practical applications can be found in e.g. [5, 114]. However, this approach may stall early due to, for instance, the presence of local minima in the underlying (multimodal) model, depending on the global accuracy of the initial metamodel.

Next to a mean value prediction $\hat{y}(x_0)$, a metamodel can provide additional uncertainty information. Figure 5.1a shows a 0^{th} order Kriging model fit of a function using 4 initial sampling points. The resulting metamodel provides

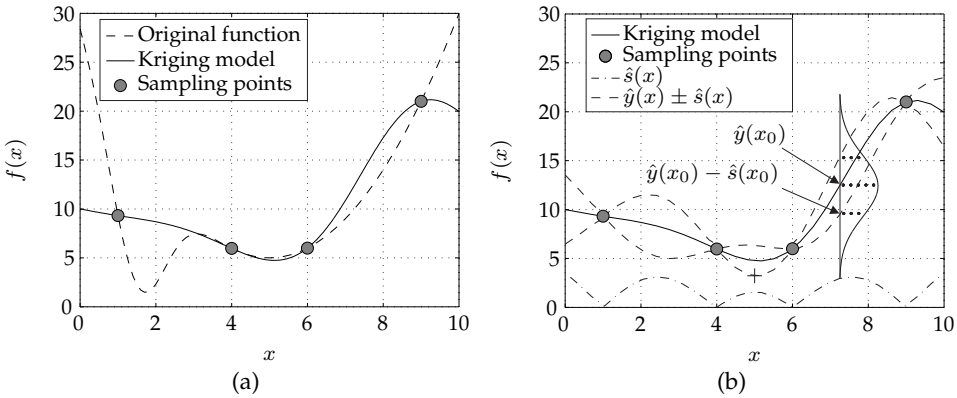

Figure 5.1 *(a) Original function and Kriging metamodel fit using 4 initial DOE points and (b) sequential improvement employing uncertainty information of the metamodel*

a poor fit of the original function. Also note that the global minimum of the original function is not predicted correctly. At each untried variable setting x_0, the mean value of the objective function $\hat{y}(x_0)$ and a standard deviation $\hat{s}(x_0)$ can be calculated. The latter variable is a measure for the *prediction error* or *prediction uncertainty* at point x_0. In other words, the predictor $\hat{y}(x_0)$ represents a realization of a stochastic process Y in which the randomness is governed by the uncertainty $\hat{s}(x_0)$ about the true objective function at an untried setting x_0 [118, 122].

Note that $\hat{s}(x_0)$ represents a type of uncertainty that is related to the metamodel uncertainty, which is different from the sources of uncertainty discussed in Section 2.2. The so-called *posterior distribution* at x_0 can be modeled as a normal distribution with $Y \sim \mathcal{N}(\hat{y}(x_0), \hat{s}^2(x_0))$, see the distribution in Figure 5.1b. For RSM, Kriging and NN, the estimate of the prediction error $\hat{s}$ equals the square root of Equations (C.6), (C.16) and (C.22) respectively. The additional uncertainty information can be used in a sequential improvement algorithm to select the location of an infill point. Note that at each update of the metamodel, also the posterior distribution is revised [82].

A sequential deterministic improvement algorithm that directly makes use of prediction uncertainty information is based on a *Lower Confidence Bound* (LCB) or *Merit Function* (MF):

$$f_{\text{merit}}(\mathbf{x}) = \hat{y}(\mathbf{x}) - w\hat{s}(\mathbf{x}) \tag{5.2}$$

The idea of this approach is to perform new evaluations in promising but less explored regions of the search space. The parameter w can be used to tune the algorithm to search more locally ($w \to 0$) or globally ($w \to \infty$). In Bonte [19] it has been shown that choosing w = 1 provides a good compromise between both extreme cases. For w = 1 the merit function equals the lower dashed line in Figure 5.1b, i.e. $\hat{y}(x) - \hat{s}(x)$. The location of the infill point can be found by *Minimizing the Merit Function* (MMF). The minimum of the merit function is indicated by the cross mark in Figure 5.1b. Note that for $w = 0$, the algorithm reduces to the MI-algorithm.

A parameter-free sequential deterministic improvement algorithm that also makes use of prediction uncertainty information is presented by Jones et al. [65] and Schonlau [124]. The proposed *Efficient Global Optimization* (EGO) strategy adds additional sample points at locations where the *Expected Improvement is Maximum* (MEI). The expected value of a stochastic process, in this case Y, is given by Equation (A.3) and the probability density function of the stochastic process Y is denoted here by $p_Y(y)$. By evaluating the improvement with respect to a random variable Y, consequently the improvement also becomes a random variable. Replacing $y(\mathbf{x})$ in Equation (5.1) with the stochastic process Y and combining it with Equation (A.3) results in the Expected Improvement (EI) given by:

$$\mathrm{E}(I) = \int_{-\infty}^{f_{\min}} (f_{\min} - y) p_Y(y)\, \mathrm{d}y \tag{5.3}$$

As shown by Jones et al. [65], Equation (5.3) can be expressed in closed form given by Equation (5.4). In the case of a metamodel approximation, the stochastic process Y is described by a mean value $\hat{y}(\mathbf{x})$ and standard deviation $\hat{s}(\mathbf{x})$. Since both $\hat{y}$ and $\hat{s}$ depend on the design variables $\mathbf{x}$, the EI is also a function of $\mathbf{x}$ although for notational simplicity the dependence on $\mathbf{x}$ is omitted here:

$$\mathrm{E}(I) = \begin{cases} (f_{\min} - \hat{y})\Phi\left(\frac{f_{\min} - \hat{y}}{\hat{s}}\right) + \hat{s}\phi\left(\frac{f_{\min} - \hat{y}}{\hat{s}}\right) & \text{if } \hat{s} > 0 \\ 0 & \text{if } \hat{s} = 0 \end{cases} \tag{5.4}$$

In this equation, ϕ and Φ are the probability density and cumulative distribution function of the standard normal distribution respectively. The first term in Equation (5.4) is the difference between the current minimum and the prediction $\hat{y}(\mathbf{x})$, penalized by the probability of improvement. Hence, it contributes to the EI

if $\hat{y}(\mathbf{x})$ is smaller than $f_{\min}$. The second term is large where the error $\hat{s}(\mathbf{x})$ is large, i.e. when there is much uncertainty about whether $\hat{y}(\mathbf{x})$ will be better than $f_{\min}$. The criterion is thus capable of searching both locally (first term) and globally (second term). Note that the $\mathrm{E}(I) = 0$ if $\hat{s} = 0$ which is the case in the DOE points for interpolating metamodels. Maximizing the EI finally provides the coordinates of the infill point $\mathbf{x}'$.

The functioning of the MEI algorithm is demonstrated in Figure 5.2. The EI is computed as a function of x as depicted in Figure 5.2a. The cross mark indicates the location at which the EI is maximum, providing the coordinates of the first infill point. After evaluating the objective function at this location, the metamodel is fit to the set of 5 DOE points and the EI is updated based on the newly calculated MSE through Equation (C.16). Figure 5.2b and Figure 5.2c depicts the state after 2 and 3 updates respectively. Note how the algorithm search area shifts from a local search to a more global search. After the addition of seven infill points, the maximum EI is around 0.02 as can be seen in Figure 5.2d. The 0^{th} order Kriging model fit reproduces the original function fairly well, especially in the relevant area of the two minima.

As a *stopping criterion* or *termination criterion*, a threshold for the EI can be set:

$$\max \mathrm{E}(I) < \Delta_{\mathrm{s}} \tag{5.5}$$

in which Δ_{s} is an arbitrarily chosen threshold value. From Figure 5.2 several typical aspects of the EI become clear. Firstly, the EI can behave extremely multimodally which supports the algorithm in searching both locally and globally. Secondly, by comparing the magnitude of the EI in Figure 5.2a and Figure 5.2b, it can be seen that the EI does not necessarily have to decrease monotonically for an increasing number of infill points. Finally, the EI equals zero in already evaluated points, i.e. $\mathrm{E}(I) = 0$ where $\hat{s} = 0$, which prevents the algorithm from placing infill points at identical locations.

5.3 Sequential robust improvement

In this section, special attention is given to sequential improvement algorithms that accommodate for the peculiarities of robust optimization problems. The presence of noise variables requires a different approach for choosing the optimal settings of a new infill point in comparison to the deterministic case. In the evaluation of the robust objective function, it is typically irrelevant to determine

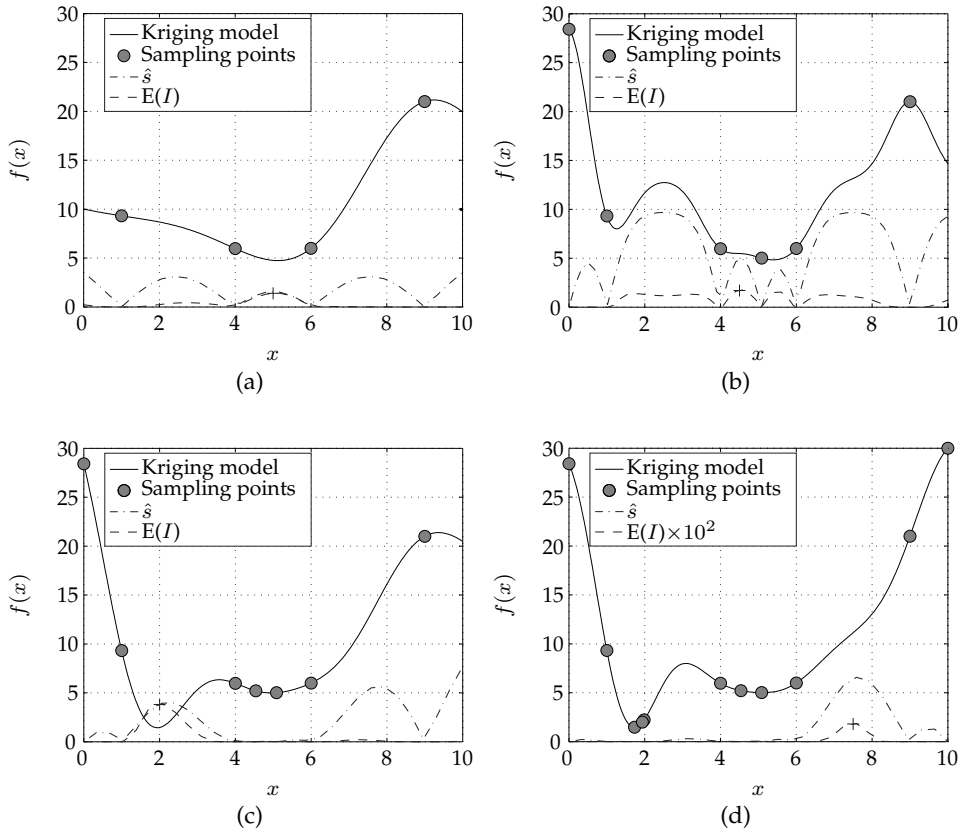

Figure 5.2 *(a) Expected Improvement (EI) criterion and resulting location for the first infill point (cross mark), updated metamodel after addition of (b) 2 and (c) 3 infill points, (d) final metamodel after 7 updates*

optimal settings for $\mathbf{z}$ that result in a better objective function value. This is because these variables are uncontrollable in practice. On the other hand, for an accurate assessment of the robust objective function, the deteriorating effects of the noise variables are of interest. The ultimate goal is to find a suitable location of the infill point. At this setting, denoted by $\mathbf{x}'$ and $\mathbf{z}'$, a new FE simulation is performed to increase the fidelity of the metamodel.

Focusing on the sequential deterministic optimization algorithm given in Equation (5.4), several difficulties arise if noise variables are taken into account. In the case of deterministic optimization, the function value $\hat{y}(x_0)$ is a direct prediction of the objective function value $\hat{f}(x_0)$. The infill point $\mathbf{x}'$ that is most promising with respect to the objective function can now be determined using Equation (5.4). In case noise variables are present, a prediction of the objective function is obtained by applying an MCA onto the metamodel. The most promising location of the infill point ($\mathbf{x}'$, $\mathbf{z}'$) with respect to the robustness criterion, instead of the metamodel itself, cannot be directly predicted. Moreover, the current best solution of the objective function $f_{\min}$ in the deterministic case is a single FE simulation response. In case noise variables are present, the current best solution is not well-defined. Finally, the prediction uncertainty $\hat{s}$ associated with respect to the objective function f is not accounted for. This is because the MSE only quantifies the estimated prediction error between global approximation $\hat{y}$ and the original function y.

Only a limited amount of literature is available that considers sequential improvement algorithms in which noise variables are taken into account. Williams et al. [150] proposed an extension of the EI-algorithm in which the objective function is minimized in a sense that it averages the influence of the noise variables. That is, the objective function at a fixed setting of the design variables is the mean of the deterministic response over the distribution of the noise variables. This approach is thus limited to objective functions that only consider the mean value. Moreover, the noise considered in this work is a result of measurement errors. Consequently, it is assumed that the magnitude of the error is small with respect to the magnitude of the real objective function (up to 5%). Clearly, this is a different type of noise than considered in the robust optimization of metal forming processes. An extension and application of this method can be found in [57, 58]. Similar to the algorithm discussed in [150], an improvement-based sequential optimization algorithm is proposed in [77, 78]. This algorithm searches for an optimal setting for both the design variables and the noise variables in contrast to the algorithm proposed in [150]. However, the objective function can only comprise the mean value or the variance of the response, a combination of both is not considered.

The sequential robust optimization algorithm that is applied in this work has been proposed by Jurecka et al. [66]. The search for an infill point in the design–noise variable space is divided into two steps. First, $\mathbf{x}'$ is determined in the design variable space after which $\mathbf{z}'$ is identified in the noise space. Determining $\mathbf{x}'$ requires the evaluation of the robust objective function f. This is done by applying an MCA onto the metamodel. As a result, the majority of the MCA sampling points that are incorporated in the prediction of the robustness criterion are untested, i.e. not evaluated using FE simulations. An uncertainty $\hat{s}$ about the predictor $\hat{y}$ at each untested point $(\mathbf{x}, \mathbf{z})$ remains present. As a result, two stochastic variables are obtained in the same probability space. Each point $(\mathbf{x}, \mathbf{z})$ is now a realization of the stochastic noise variable Z and the posterior error distribution in this point. The stochastic process Y can now be written as:

$$(Y|Z) \sim \mathcal{N}(\hat{y}(Z), \hat{s}^2(Z)) \tag{5.6}$$

To evaluate the prediction uncertainty with respect to the robustness criterion, the conditional variance formula is used:

$$\begin{aligned}
\operatorname{var}(Y) &= \mathrm{E}\big(\operatorname{var}(Y|Z)\big) + \operatorname{var}\big(\mathrm{E}(Y|Z)\big) && (5.7)\\
&= \mathrm{E}\big(\hat{s}^2(Z)\big) + \operatorname{var}\big(\hat{y}(Z)\big) && (5.8)\\
&= \mathrm{E}\big(\mathrm{MSE}(Z)\big) + \sigma_{\mathrm{Y}}^2 && (5.9)\\
&= \int_{-\infty}^{\infty} \mathrm{MSE}(z) p_{\mathrm{Z}}(z)\,\mathrm{d}z + \sigma_{\mathrm{Y}}^2 && (5.10)\\
&\approx \frac{1}{n}\sum_{i=1}^{n} \mathrm{MSE}(z_i) + \sigma_{\mathrm{Y}}^2 && (5.11)
\end{aligned}$$

The presence of the prediction uncertainty adds an additional term to the prediction variance of the stochastic process Y. This term equals the mean of the MSE over the noise space, see Equation (5.9) and Equation (5.10). Going from Equation (5.9) to Equation (5.10), the integral expression of Equation (A.3) is used where $p_{\mathrm{Z}}(z)$ is the probability density function of the stochastic process Z. The mean value of the MSE can subsequently be approximated by an MCA as given in Equation (5.11) using n observations. The expected value of the stochastic

process Y is not influenced by the presence of prediction uncertainty since:

$$\mathrm{E}(Y) = \mathrm{E}\big(\mathrm{E}(Y|Z)\big) = \mathrm{E}\big(\hat{y}(Z)\big) = \mu_{\mathrm{Y}} \tag{5.12}$$

Returning back to the definition of the EI in Equation (5.3), a revision has to be done. This is because the definition of the current best solution of the robustness criterion can now also be seen as a stochastic process with $(Y^*|Z) \sim \mathcal{N}(\hat{y}^*(Z), \hat{s}^{*2}(Z))$. The EI can now be written as:

$$\mathrm{E}(I) = \int_a^b (\hat{y}^* - y)(p_{\mathrm{Y}}(y) - p_{\mathrm{Y}^*}(y))\,\mathrm{d}y \tag{5.13}$$

with $p_{\mathrm{Y}}(y)$ and $p_{\mathrm{Y}^*}(y)$ the probability density function of the stochastic process Y and current best solution Y^* respectively. The integration bounds a and b depend on the intersection points of $p_{\mathrm{Y}}(y)$ and $p_{\mathrm{Y}^*}(y)$ which can be calculated analytically [66].

As a first step, the current best solution is calculated by evaluating the robustness criterion for all settings of the design variable $\mathbf{x} = \mathbf{x}_l$ that are part of the set of DOE points. The robustness criterion can now be calculated according to its definition, e.g. $f = \mu_{\mathrm{Y}} + 3\sigma_{\mathrm{Y}}$, and its optimal 'tested' value can be determined. Subsequently, the EI can be maximized by evaluating Equation (5.13) for a grid of points $\mathbf{x}$ representing the candidate infill points in the design variable space. Evaluating and maximizing Equation (5.13) for each candidate infill point $\mathbf{x}$ finally results in the location of the infill point $\mathbf{x}'$.

The next step is to explore the noise space to find settings of the noise variables $\mathbf{z}'$ with respect to the robustness criterion. It has been mentioned before that it is typically irrelevant to determine settings for $\mathbf{z}$ that result in a better objective function value since the noise variables are uncontrollable in practice. On the other hand, for a reliable assessment of the robust objective function, the deteriorating effects of the noise variables are of interest. The infill point is therefore placed at the location where the prediction quality is low and where, in addition, the individual prediction considerably influences the robustness criterion. Maximizing the product of the error prediction and the probability of occurrence results in the optimal noise variable settings:

$$\mathbf{z}' = \arg\max(\hat{s}^2(\mathbf{x}', \mathbf{z}) p_{\mathrm{Z}}(\mathbf{z})) \tag{5.14}$$

Together, these settings $(\mathbf{x}', \mathbf{z}')$ define the infill point at which a new FE simulation is performed. The corresponding FE response is added to the set of responses and the metamodel is updated. The update sequence continues until a threshold value for the EI is reached, see Equation (5.5).

To summarize the sequential improvement strategy for robust optimization:

- Perform steps 1-7 of the robust optimization strategy as indicated in Figure 3.1.
- Validate the metamodel accuracy (steps 8 and 9 in Figure 3.1) by evaluating the stopping criterion of Equation (5.5) or using FE simulations as indicated in Section 3.4.3.
- If the stopping criterion is fulfilled, the sequential optimization procedure is terminated or else, sequentially improve the metamodel (step 10 in Figure 3.1) by adding infill points until Equation (5.5) is fulfilled.
- Determine the location of the infill point $(\mathbf{x}', \mathbf{z}')$ by first exploring the design variable space to find $\mathbf{x}'$:
  - Perform an MCA onto the metamodel at all settings of the design variable $\mathbf{x} = \mathbf{x}_l$ that are part of the set of DOE points.
  - Determine the current best solution Y^* by evaluating the robust objective function according to its definition, e.g. $f = \mu_Y + 3\sigma_Y$.
  - Evaluate the EI using Equation (5.13) for a grid of points $\mathbf{x}$ representing the candidate infill points in the design variable space. Maximizing the EI results in $\mathbf{x}'$.
- Next, explore the noise variable space at $\mathbf{x}'$ to find $\mathbf{z}'$:
  - Solve Equation (5.14).
- Add the infill point to the original set of DOE points.
- Run an FE simulation at $(\mathbf{x}', \mathbf{z}')$.
- Add the corresponding FE simulation response to the set of responses.
- Return to step 5 of the robust optimization strategy as indicated in Figure 3.1.

5.4 Application to an analytical test function

The performance of the sequential improvement algorithm is demonstrated next using an analytical test function. The Branin function is a classical deterministic optimization test function with 3 local optima. To use the Branin function for robust optimization purposes, one of the two variables is considered to be a noise variable:

$$y(x,z) = (z - \frac{5x^2}{4\pi^2} + \frac{5x}{\pi} - 6)^2 + 10(1 - \frac{1}{8\pi})\cos(x) + 10 \tag{5.15}$$

where $-5 \leq x \leq 10$ and z is assumed to follow a normal distribution according to $z \sim \mathcal{N}(\mu_z, \sigma_z^2)$ with mean $\mu_z = 7.5$ and standard deviation $\sigma_z = 2.5$. For the noise variable, a total range of $\mu_z \pm 3\sigma_z$ is used. A graphical representation of the Branin function is given in Figure 5.3.

As an objective of the optimization study, it is chosen to minimize $f = \mu_y + 3\sigma_y$. The reference solution is obtained beforehand by performing MCAs of 10,000 samples at an equidistant grid of 100 design variable settings using the analytical function. An impression of the reference solution is represented by the solid line in Figure 5.4a. Note that the 3 local optima of the deterministic Branin function

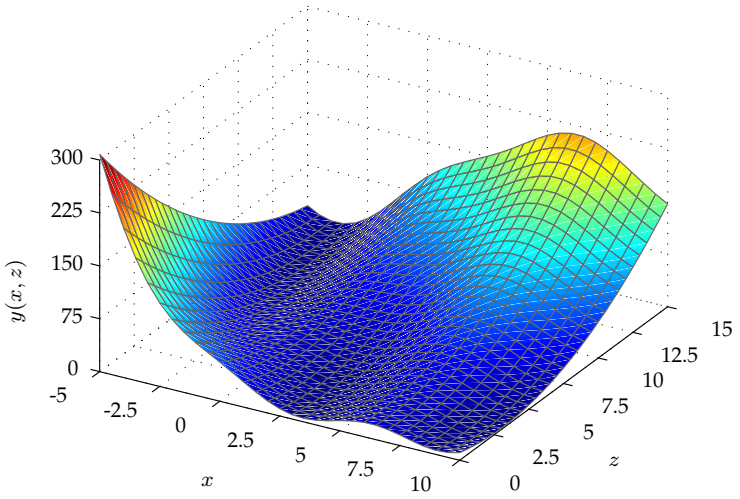

Figure 5.3 *Graphical representation of the Branin function*

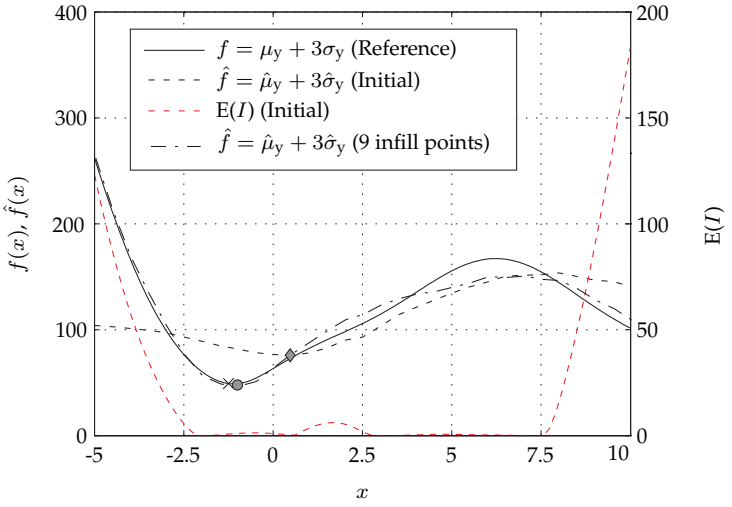

(a)

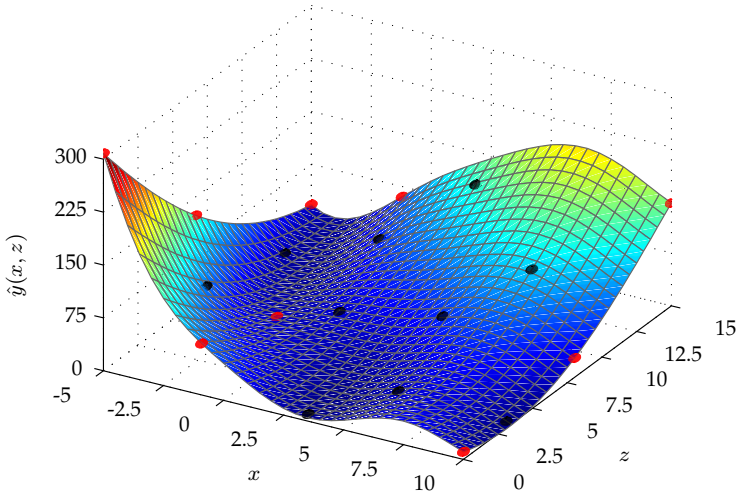

(b)

Figure 5.4 *(a) Reference objective function, Expected Improvement (EI) and approximated objective function after 0 (initial) and 9 infill points and (b) Kriging model approximation based on 10 original DOE points (black markers) and 9 additional infill points (red markers)*

reduce to a single robust optimum if one of the two variables is considered to be a noise variable. The robust optimum is visualized by the cross mark in Figure 5.4a at $x_{\text{ref}} = -1.4$ with an optimal objective function value of $f_{\text{ref}} = 48.6$, see Table 5.1.

The Branin function is first evaluated based on an initial LHD of 10 DOE points. A 0^{th} order Kriging model is used for evaluation of the Branin function. An initial objective function prediction with the Kriging model is obtained in a similar manner as the reference model, see the dashed line in Figure 5.4a. The Kriging model is subsequently used for robust optimization. The initial approximation of the optimal objective function value is found to be $\hat{f}_{\text{opt}} = \hat{\mu}_{\text{y}} + 3\hat{\sigma}_{\text{y}} = 74.5$ at the design variable setting $x_{\text{opt}} = 0.4$. See the diamond marker in Figure 5.4a and Table 5.1.

A significant deviation of both the optimal objective function value and the optimal design variable setting is observed by comparing the reference values f_{ref} and x_{ref} with the initially obtained values of $\hat{f}_{\text{opt}}$ and x_{opt}. The sequential robust optimization procedure is therefore applied to increase the accuracy of the objective function prediction. The EI, calculated using Equation (5.13) based on the initial Kriging model, is given in Figure 5.4a. Maximizing the EI results in the design variable coordinate $x' = 10$ of the first infill point. Evaluation of Equation (5.14) results in the noise variable setting $z' = 15$. After determining the response at the location $(x', z') = (10, 15)$, the metamodel is updated. As a result, also the prediction error and the EI are revised. This procedure is repeated until the stopping criterion is met, in this case set to $\Delta_{\text{s}} = 0.1$. In total 9 infill points are added, after which the EI drops below the threshold.

The final result after 9 infill points is depicted in Figure 5.4a and Figure 5.4b. The focus of the sequential improvement algorithm varies between a global search, resulting in infill points at the boundaries of the design variable domain, and a local search in x. The local search converges to the robust optimum, resulting in 3 infill points in the vicinity of $x_{\text{ref}} = -1.4$. Evaluating the robust optimum using the final metamodel (based on 10 original DOE points and 9 additional infill points), an optimal value of the robustness criterion of $\hat{f}_{\text{opt}} = 46.9$ is found for $x_{\text{opt}} = -1.3$. See the circular marker in Figure 5.4a and Table 5.1. From this, it can be concluded that the accuracy of the robustness criterion prediction in the vicinity of the robust optimum has been improved significantly by sequentially adding 9 infill points.

As a comparison, the robust optimization procedure is repeated with an initial space-filling LHD of 19 points. The optimal objective function prediction, based on the resulting Kriging model, is determined at $\hat{f}_{\text{opt}} = 56.6$ for $x_{\text{opt}} = -1.0$. This prediction is less accurate compared to the prediction based on 10 initial DOE points and 9 additional infill points added by the EI algorithm. Based

Table 5.1 *Optimal objective function values and design variable settings for the Branin test function*

	f_{ref}	x_{ref}
Reference solution	48.6	-1.4

DOE size	$\hat{f}_{\text{opt}}$	x_{opt}
10 initial LHD points	74.5	0.4
10 initial LHD points + 9 seq. added points	46.9	-1.3
19 initial LHD points	56.6	-1.0

on the results summarized in Table 5.1, it is shown that the prediction accuracy increases more rapidly by placing the infill points at qualified locations compared to increasing the initial size of the LHD for the Branin test function. The next step is to verify this finding by application of the sequential robust optimization strategy to an industrial V-bending process.

5.5 Application to a V-bending process

The sequential robust optimization strategy will now be applied to optimize a V-bending process. The industrial application is performed in cooperation with Philips Consumer Lifestyle. An impression of the production process and final product is shown in Figure 5.5. A piece of sheet metal is placed in between a punch (upper tool) and a die (lower tool), after which the punch is lowered by a prescribed displacement. During the bending process, the material experiences local elastic and plastic deformation. After withdrawal of the punch, the product shows elastic springback. The challenge of this study is to optimize the process such that products are produced within specifications in a robust way subject to

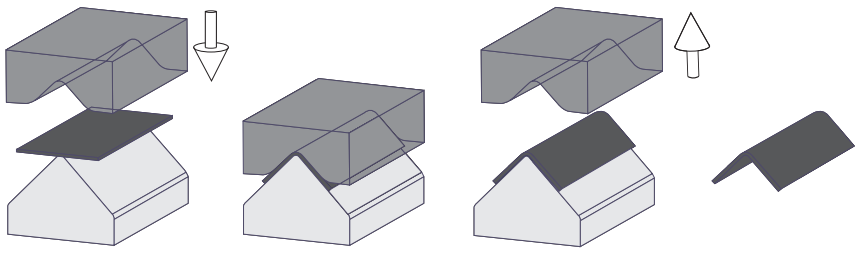

Figure 5.5 *Impression of the V-bending process and final product*

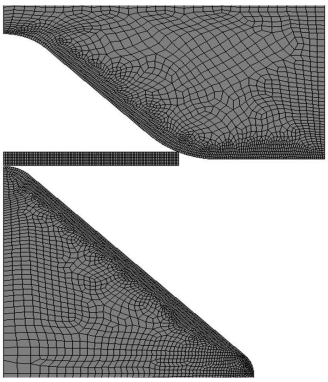

Figure 5.6 *Two-dimensional FE model of the V-bending process*

variation in material behavior. Moreover, the goal is to demonstrate the efficiency and applicability of the sequential robust optimization strategy and to gain more insight into the effect of noise variables on the production process.

Figure 5.6 shows the FE model of the part and tools. A two-dimensional model is created assuming a plane strain condition. The implicit code MSC. Marc has been used as FE code. Due to symmetry of the product, only one half of the geometry has been modeled. The sheet metal is discretized using 500 quadrilateral elements with 5 elements through thickness. Both the die and punch are modeled to be deformable using quadrilateral elements. It has been determined in a validation step preceding the optimization study that the usage of deformable tools is essential for an accurate simulation result. One simulation takes about 7 minutes where the complexity of the FE model, and with that the calculation time, is intentionally limited for the purpose of this research.

The sheet material is a stainless steel for which the nominal material properties are obtained by uniaxial tensile tests. The material is modeled as an elastic-plastic material. For the elastic material behavior, a Young's modulus (E) of 210 GPa is used. The material hardening is isotropic and the Von Mises yield criterion is applied. The experimentally obtained true stress-strain curve is implemented in the FE model as a table to describe the plastic material behavior. The yield stress (σ_{y}) is determined to be 350 MPa. Variation in σ_{y} is modeled by vertically shifting the true stress-strain curve. The tooling material is a tool steel for which only the elastic material behavior is modeled using a Poisson's ratio of 0.3 and a Young's modulus of 210 GPa.

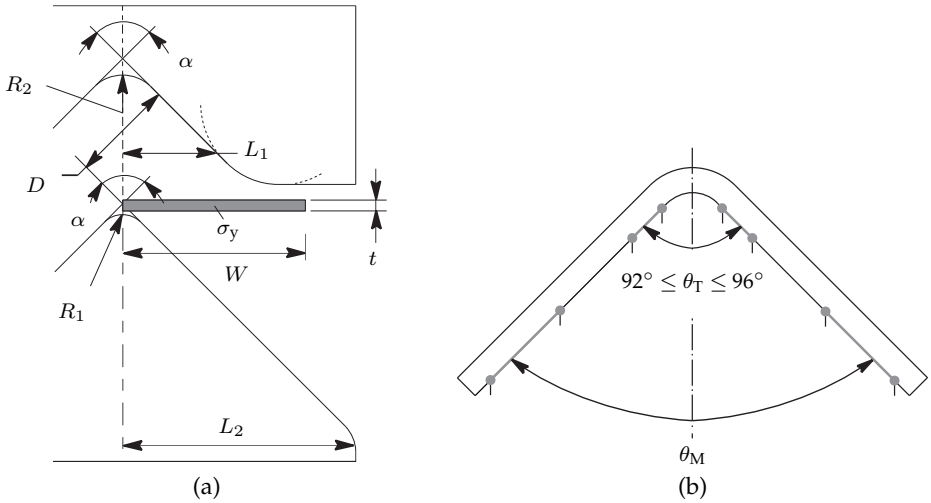

Figure 5.7 *(a) Definition of design and noise variables and (b) angles defining the flange shape of the final product*

5.5.1 Modeling and variable screening

The initial set of design and noise variables is shown in Figure 5.7a. The design variables are the angle of the die and the punch (α), the width of the sheet (W), the final distance (D) between the flange of the die and punch (if no deformation of the tooling would occur), the dimensions of the punch (L_1) and the die (L_2), the radius of the die (R_1) and punch (R_2). As with the process in practice, the material thickness (t) and yield stress (σ_y) are considered uncertain. The bounds of the design variables are given in Table 5.2, quantification of the noise variables is given in Table 5.3.

Table 5.2 *Bounds of the design variables*

Variable	Lower bound	Upper bound
α	92°	93°
W	6.0 mm	7.5 mm
D	0.4 mm	0.65 mm
L_1	4.0 mm	5.0 mm
L_2	8.5 mm	11 mm
R_1	1.0 mm	1.3 mm
R_2	1.8 mm	2.1 mm

Table 5.3 *Quantification of the noise variables*

Variable	Mean (μ_z)	Std. dev. (σ_z)	Min. ($\mu_z - 3\sigma_z$)	Max. ($\mu_z + 3\sigma_z$)
t	0.51 mm	0.01 mm	0.48 mm	0.54 mm
σ_y	350 MPa	6.66 MPa	330 MPa	370 MPa

To ensure a correct performance of the final product, requirements on the flange shape are prescribed. The flange shape is defined by a transition angle (θ_T) and a main angle (θ_M) spanned up by the marked line segments, see Figure 5.7b. The transition angle should satisfy the constraint as given in Figure 5.7b whereas the target angle for the main angle is 90°. In the current V-bending process, active steering of D is required to obtain products that satisfy the requirements. The goal of the optimization study is to obtain a robust and reliable process without the need to adjust D. The main angle is taken into account as the objective function f while satisfying $\pm 3\sigma$-constraints on the transition angle. The quantified robust optimization formulation is given by:

$$
\begin{aligned}
\min_{\mathbf{x}} \; & |\mu_{\theta_M} - 90| + 3\sigma_{\theta_M} \\
\text{s.t. } & 92 \leq \mu_{\theta_T} - 3\sigma_{\theta_T} \\
& \mu_{\theta_T} + 3\sigma_{\theta_T} \leq 96 \\
& 92 \leq \alpha \leq 93 \\
& 6.0 \leq W \leq 7.5 \\
& 0.4 \leq D \leq 0.65 \\
& 4.0 \leq L_1 \leq 5.0 \\
& 8.5 \leq L_2 \leq 11 \\
& 1.0 \leq R_1 \leq 1.3 \\
& 1.8 \leq R_2 \leq 2.1 \\
\text{where } & t \sim \mathcal{N}(0.51, 0.01^2) \\
& \sigma_y \sim \mathcal{N}(350, 6.66^2)
\end{aligned}
\tag{5.16}
$$

Variable screening is first performed to reduce the size and complexity of the optimization problem using the screening techniques as discussed in Section 3.3. A resolution III fractional factorial design of 16 simulations is used for independently estimating the main effects of the 9 design and noise variables. The upper and lower bound of the noise variables are hereby set at $\mu_z + 3\sigma_z$

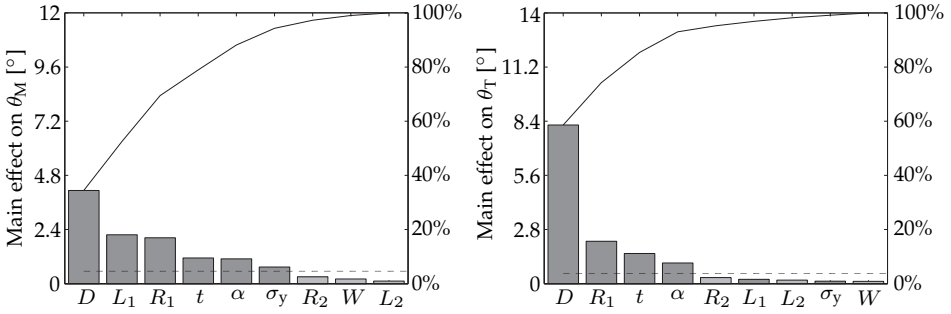

Figure 5.8 *Pareto plots of the (a) main angle θ_M and (b) transition angle θ_T*

and $\mu_z - 3\sigma_z$ respectively. The resulting Pareto plots for the main and transition angle are presented in Figure 5.8a and Figure 5.8b respectively. Similar to what is experienced in the production process, variable screening shows that the depth setting D has the largest effect on both angles. The main and transition angle are highly sensitive to the bending radius R_1, bending angle α and the variation in material thickness t. The change in the dimension of the punch L_1 and variation of the yield stress σ_y only affect θ_M and hardly affect θ_T. Design and noise variables having a higher effect on the angle response than the error effect (dashed line in the Pareto plots) are considered significant and are included in the optimization problem. As a result, the number of variables is reduced to 4 design variables (D, L_1, R_1, α) and 2 noise variables (t, σ_y). The omitted variables (R_2, L_2 and W) are set to their nominal process settings to minimize the required changes in the current production process.

The significance of these variables is verified using experimental data for the V-die bending process available in the literature. Leu and Hsieh [79] recognize the strong influence of increasing the coining force to reduce springback after unloading. This corresponds to decreasing the depth setting in the current work to a value for D which is smaller than the nominal material thickness. The significant effect of D is also experimentally verified in [104] and [140]. Moreover, experimental results reported by Huang and Leu [59] and Tekaslan et al. [139, 140] for the main angle confirm the importance of the bending radius R_1, material thickness t, and bending angle α. Lastly, the importance of material properties σ_y is experimentally verified in [104]. Varying the dimension of the punch L_1 is not considered in these experimental works, although Figure 5.8a shows that the effect on the main angle is significant.

5.5.2 Metamodel fitting

The next step is the creation of metamodels. Following the rule of thumb mentioned in Section 3.4, an LHD of 10 times the number of variables is generated, where the reduced number of variables equals 6 in this case. The resulting 60 DOE points are distributed in the combined six-dimensional design–noise variable space and serve as a basis for the initial metamodel. Using ANOVA, a 2^{nd} order Kriging model is identified as the most accurate fit for both f and g. In addition to this metamodel, four 2^{nd} order Kriging models are constructed based on an initial LHD of 30, 100, 200 and 300 points to investigate the influence of the initial DOE size. Moreover, a large reference data set is constructed by performing 6000 FE simulations in the combined six-dimensional design space. These simulations are performed according to a predefined grid. The points per dimension of the grid are distributed in an equidistant manner. The number of points per dimension are presented in Table 5.4. A reference model is subsequently obtained by spline interpolation of the resulting response set. In the remainder of this chapter, these models are referred to as 30LHD, 60LHD, 100LHD, 200LHD, 300LHD and reference model.

Note that for this simple case a reference model is created for validation purposes with a lot of computational effort. However, a reference model will not be available in realistic problems. The goal of the sequential robust optimization is to calculate the robust optimum with a minimum number of FE simulations. With the reference model available, the performance of the algorithm can be checked.

Impressions of the reference models are given in Figure 5.9. Figures 5.9a and 5.9b show the reference model of the main angle as a function of the distance D, and the material thickness t and yield stress σ_{y} respectively. Figures 5.9c and 5.9d show the reference model of the transition angle as a function of the distance D, and the material thickness t and yield stress σ_{y} respectively. The constraints on the transition angle are visualized by the two horizontal planes. For visualization purposes, the remaining variables are set to their nominal process settings as shown in the second column of Table 5.5.

Evaluating the shape of the models in Figure 5.9, an increase of the main angle

Table 5.4 *Number of points per dimension used to create a grid of 6000 points in the design space*

Dimension	α	R_1	L_1	D	t	σ_{y}
Number of points per dimension	4	5	4	5	5	3

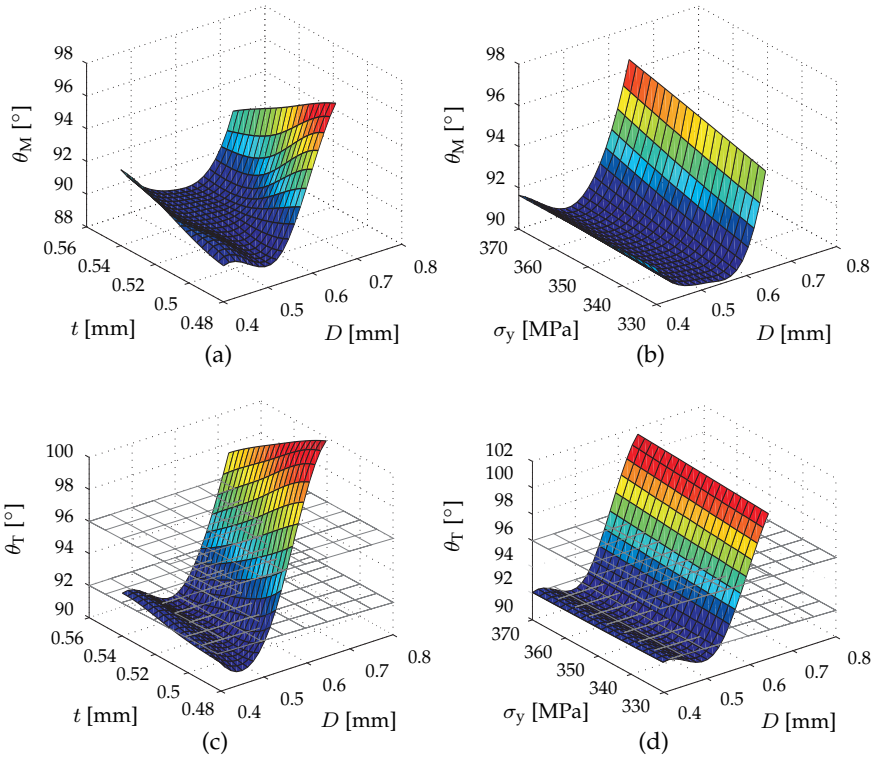

Figure 5.9 *Reference model impressions of the (a,b) main and (c,d) transition angle*

is observed for large D. As long as the distance D is larger than the material thickness t, the material is only bent and not yet flattened. For increasing D, the material is less bent which results in an increase of the main angle. Once the distance D is smaller than the material thickness, the material is flattened subsequent to bending. Due to flattening of the material, the main angle will approach the nominal tooling angle of 92°. Also note the interaction effect between D and t in Figures 5.9a and 5.9c. The slope in the noise variable direction changes as a function of D. In between the extreme settings of D, an area can be observed for which the slope in the noise variable direction is small. For this specific setting, this could potentially yield a process which is robust with respect to the noise variable t. Looking at Figures 5.9b and 5.9d, again an area can be observed for which the noise variable σ_y has minimal influence on the main and transition angle respectively. Looking at the main effects of the plotted variables, it can be observed that the depth setting has the highest effect on both

angles followed by the material thickness and yield stress. This corresponds to the results of the study described in Section 5.5.1. Comparing the shape of the reference model with respect to the main angle (Figures 5.9a and 5.9b) and the transition angle (Figures 5.9c and 5.9d), a very similar behavior of the angle change can be observed. Note that the lower constraint on the transition angle, represented by the lower plane, significantly decreases the feasible area also excluding the robust area.

5.5.3 Robust optimization

The set of 2nd order Kriging models resulting from the different initial DOE sizes are used for sequential robust optimization. An initial optimization study did not result in a $\pm 3\sigma$ process. This was caused by a non-robust behavior of the transition angle in the feasible design space. Therefore, the robustness requirements on the constraints and objective function are slightly relaxed. The revised and reduced robust optimization formulation now reads:

$$
\begin{aligned}
\min_{\mathbf{x}} \; & |\mu_{\theta_M} - 90| + 2\sigma_{\theta_M} \\
\text{s.t. } & 92 \leq \mu_{\theta_T} - 2\sigma_{\theta_T} \\
& \mu_{\theta_T} + 2\sigma_{\theta_T} \leq 96 \\
& 92 \leq \alpha \leq 93 \\
& 0.4 \leq D \leq 0.65 \\
& 4 \leq L_1 \leq 5 \\
& 1 \leq R_1 \leq 1.3 \\
\text{where } & t \sim \mathcal{N}(0.51, 0.01^2) \\
& \sigma_y \sim \mathcal{N}(350, 6.66^2)
\end{aligned}
\tag{5.17}
$$

The optimal value of the objective function obtained from each metamodel is represented by the first marker of each line in Figure 5.10. For the 60LHD model, the optimal response values are given in the third column of Table 5.5. The corresponding optimal process settings are included where f is the objective and g_1 and g_2 are the lower and upper constraint on the transition angle respectively. The reference model is subsequently utilized for robust optimization using similar techniques as applied onto the metamodels. The resulting optimal reference process settings and response values are presented in Figure 5.10 and in the last column of Table 5.5. Evaluation of the nominal process settings (with D =

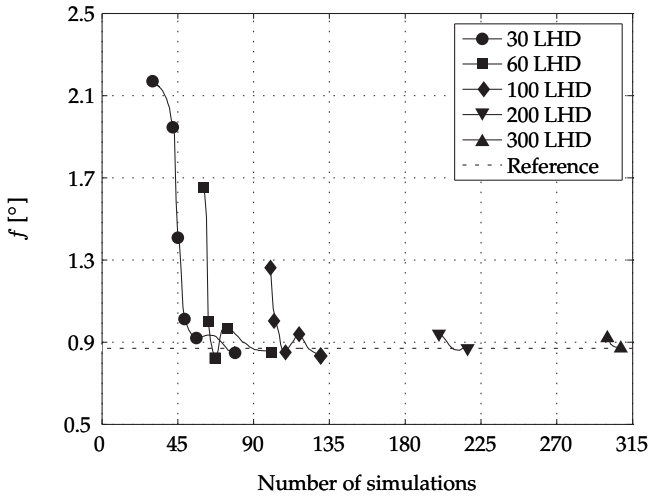

Figure 5.10 *Sequential robust optimization results for varying initial DOE sizes*

0.51 mm) using the reference model shows a very robust but unreliable process, see the second column of Table 5.5. A small standard deviation for the transition angle response is observed but the lower constraint is violated by far.

Figures 5.11 and 5.12 present the optimal process results for the main and transition angle as a function of D. The vertical bars represent the $\pm 2\sigma$ bounds of angle variation around the mean value caused by the influence of the noise variables. Based on the initial 60LHD model of the main angle presented in Figure 5.11, the optimal distance D is found to be 0.54 mm corresponding to a mean value of the main angle of 90.9° and a standard deviation of 0.35°. The resulting objective function value deviates 0.73° from the optimal reference value of 0.87°. This discrepancy is relatively large compared to the accuracy which is required for the V-bending process. Looking at the initial optimal values of the objective function values for the 30LHD and 100LHD metamodels as presented in Figure 5.10, a deviation of 1.31° and 0.39° from the reference solution is observed respectively. The discrepancies decrease with an increasing number of initial DOE points. Evaluation of the 200LHD and 300LHD model shows an accurate initial prediction of the optimal objective function value.

Once an optimum is obtained by the robust optimization strategy, the 2σ-requirements for the constraints on the transition angle are satisfied per definition. However, the constraint predictions are based on a metamodel approximation. The reference model can be used to validate the prediction of the optimal constraint values based on the 60LHD model. Figure 5.12 depicts

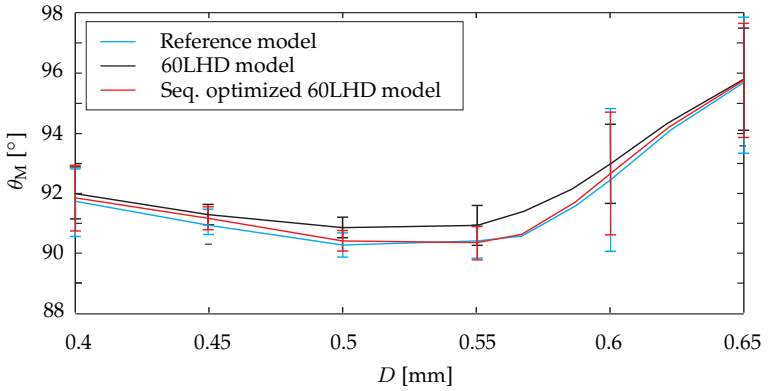

Figure 5.11 *Optimal process results for the main angle as a function of the distance D*

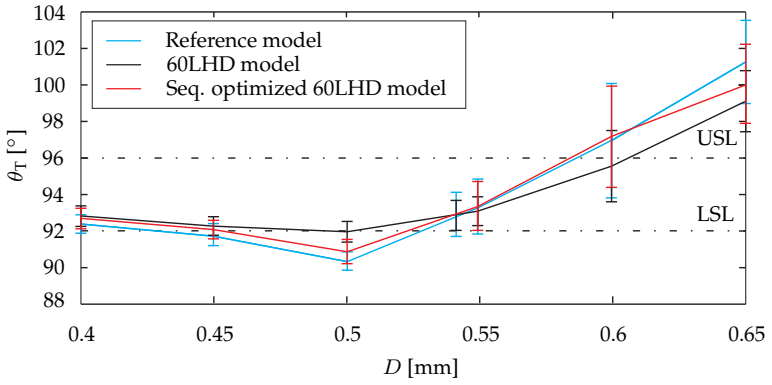

Figure 5.12 *Optimal process results for the transition angle as a function of the distance D*

an additional set of $\pm 2\sigma$ bars at $D = 0.54$ representing the 60LHD and reference model prediction. A comparison shows that the 60LHD model underestimates the standard deviation. For the 60LHD model, an initial robust optimum is found that satisfies the constraints, whereas the reference model shows slight violation of the lower constraint. In the case of deterministic optimization, neglecting the influence of the noise variables will result in an optimum that lies at the boundary of the lower constraint on θ_T for D = 0.53 mm for the reference model. The variation in t and σ_y will in this case lead to a high number of violations of the constraint in the real V-bending process. From this, it can be concluded that the effect of adding noise is significant if one compares the deterministic to the robust optimal reference settings for D.

The above analysis shows that the optimal distance D, which is actively adapted in the current process, is critical with respect to the lower constraint. A

Table 5.5 *Current, optimized and reference process settings and response values of the V-bending process where the Robust Optimization (RO) results and Sequential Robust Optimization (SRO) results are obtained using the metamodel initially built up out of 60 DOE points*

Variables and responses	Nominal process settings	RO results	SRO results	Reference process settings
α	92 °	92.4°	92.7°	92.8°
R_1	1.15 mm	1.16 mm	1.14 mm	1.12 mm
L_1	5 mm	4.8 mm	4.9 mm	4.9 mm
D	0.51 mm	0.54 mm	0.55 mm	0.56 mm
f	0.63°	1.60°	0.85°	0.87°
g_1	90.2°	92.0°	92.0°	92.0°
g_2	91.1°	93.6°	94.9°	95.6°

comparison of the optimal setting based on the 60LHD model shows a shift from the nominal process setting towards the more robust reference setting (see Table 5.5). However, a small discrepancy remains present mainly caused by an inaccurate prediction of the stochastic constraint measures. Overall, it can be stated that the prediction of the optimal process behavior based on the 60LHD model deviates from the reference model for both the main and transition angle. This leaves room for the sequential robust optimization step to increase the accuracy of the standard deviation and mean value prediction in the robust optimum for both the objective function and constraints. Before applying the sequential robust optimization algorithm in Section 5.5.5, experimental validation of the numerical results is performed.

5.5.4 Experimental validation

To investigate the robustness of the nominal production process and to validate the numerical results, three production trial runs are performed with the nominal process settings as specified in Table 5.5 with D = 0.53 mm. To reflect the whole

range of material thickness variation that can occur in practice, 3 material coils are selected with a minimum (Run 1), nominal (Run 2) and maximum (Run 3) material thickness within the $\mu \pm 3\sigma$ range as specified for the noise variable t in Equation (5.17). For each trial run, 30 products are retrieved from the production process and the main and transition angles are measured. This enables studying the effect on the main and transition angle of both coil-to-coil thickness variation (comparing results between runs) and in-coil thickness variation (results per run).

The experimental results for the main and transition angle per trial run (Run 1-3) are visualized using box plots in Figure 5.13a. The median of each set of 30 measurements is shown as the center line in the box. The boxes to the left and right of the median represent two quartiles containing 25% of the data points each. The horizontal line, or whisker, extends up to the lowest and highest measured value and covers the remaining 50% of the angle measurements. Possible outliers are measurements that fall outside the limits of the whiskers and are depicted as asterisks. In addition to the experimental results, a comparison is made with the numerical robustness prediction obtained by performing an MCA onto the reference model (Ref.) at the nominal process settings with D = 0.53 mm. See the lower box in Figure 5.13a.

Evaluating the box plots in Figure 5.13a, a larger effect of coil-to-coil variation is observed for the main angle in comparison to the transition angle. Looking at the main angle, springback increases for decreasing material thickness. Note that the springback angle is the difference between the measured angle and the nominal tooling angle of 92°. This effect corresponds to experimental V-die bending results reported in [104]. Both the mean value and the range of main angle variation is predicted accurately by the reference model. Also for the transition angle, the prediction of the mean value is in good agreement with the experimental results. However, the reference model shows a slight overestimation of the scatter around the mean value. As already predicted numerically and discussed in Section 5.5.3, also the experimental results show that the process performance is critical with respect to the lower specification limit of the transition angle.

Both the screening step and the robust optimization procedure show that the main and transition angle are most significantly influenced by the depth setting D. To validate the numerical trends, a final trial run (Run 4) is performed whereby D is increased to 0.55 mm and the coil with a nominal material thickness is used. The experimental and numerical (Ref.) results are presented in Figure 5.13b. For both angles, the numerical prediction of the mean value is in good agreement with the experimental results, whereas the scatter around

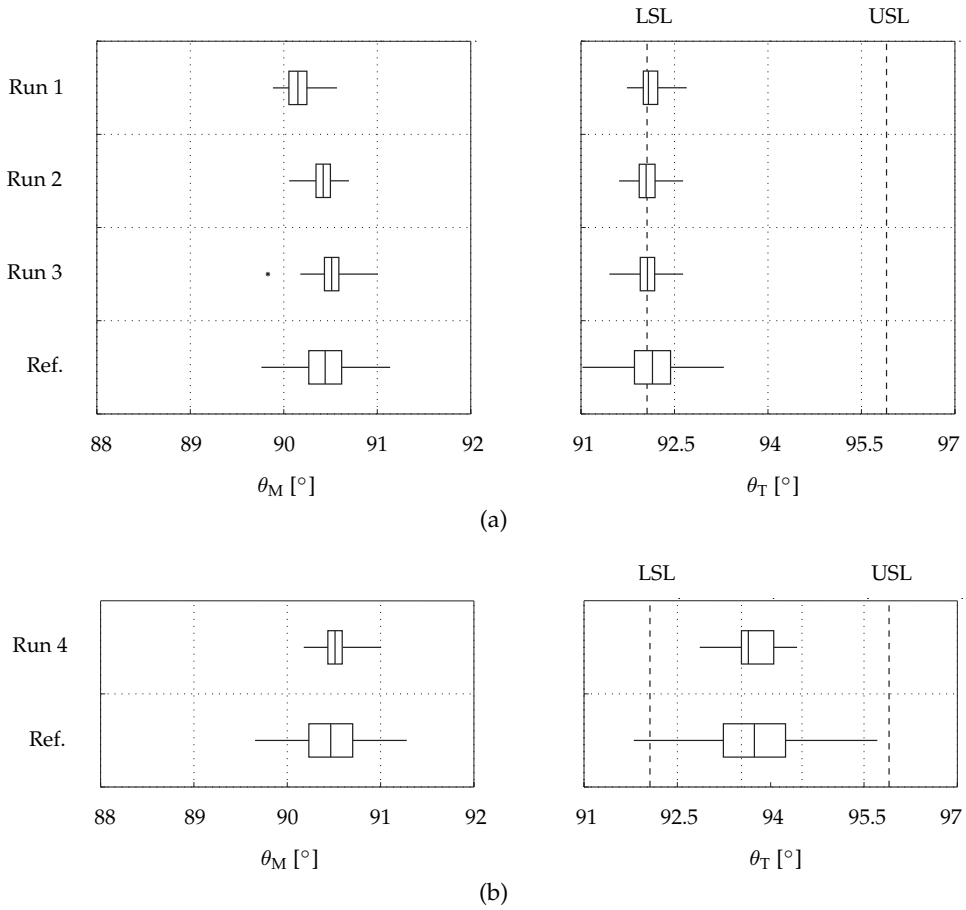

Figure 5.13 *Experimental results (Run 1-4, 30 measured products per run) and numerical results obtained from the reference model (Ref.) for the nominal process settings with (a) D = 0.53 mm and (b) D = 0.55 mm*

the mean value is overestimated. This discrepancy is expected to decrease if the number of measured products is increased and/or different coils are used in the production process. Note that the numerically observed trend of an increasing mean value of the transition angle for an increasing depth setting is confirmed by the experiments. This makes the process less critical with respect to the lower specification limit of the transition angle.

In summary, the numerical trends obtained from the reference model are in good agreement with the experimental results, especially for the mean value prediction. Returning back to the initially created metamodel set, the numerical prediction of the optimal process behavior based on the 60LHD model deviates from the reference model and thus from the experimental results. The next step is to decrease this discrepancy by application of the sequential robust optimization algorithm.

5.5.5 Sequential robust optimization

The results of applying the sequential robust optimization procedure to the set of metamodels are presented in Figure 5.10. A clear difference in behavior of the algorithm can be observed for different initial DOE sizes. For the 30LHD metamodel, a slower initial convergence is obtained in comparison to the 60LHD and 100LHD model. Evaluation of the infill point locations for the 30LHD model shows that the first 12 points are added globally. The limited initial DOE size forces the algorithm to first decrease the metamodels prediction error globally before searching locally. Decreasing the initial DOE size below 30 results in a low quality metamodel, unsuitable for evaluation of the EI criterion. In total 49 points are added to the initial 30 DOE points after which the EI drops below the threshold value, arbitrarily set to $\Delta_s = 0.5$. However, Figure 5.10 shows that an accurate prediction of the objective function value is already obtained after adding 20 DOE points.

For the 60LHD metamodel, the EI algorithm mainly adds infill points clustering around the robust optimum. A fast convergence of the objective function value prediction is observed towards the reference solution. Note, however, that the 30LHD model outperforms the 60LHD model after having added 30 infill points. The same can be observed for the 60LHD model and the 100LHD model after adding 40 infill points to the 60 initial DOE points. In total, an additional 42, 30, 17 and 8 infill points are added to the 60LHD, 100LHD, 200LHD and 300LHD model respectively. The latter two models show a minor improvement of the prediction accuracy.

The process settings of the robust optimum based on the 60LHD model after sequential robust optimization, are given in the fourth column of Table 5.5. The optimal settings of α, R_1, D and L_1 have converged further towards the reference solution. The optimal process results obtained after sequential optimization of the 60LHD model are presented in Figure 5.11 and Figure 5.12. The discrepancy between the sequentially updated metamodel prediction and the reference model is decreased significantly. Especially, the optimal values of the objective function and constraint based on the sequentially updated 60LHD model show good resemblance with the optimal reference values.

Overall, it can be stated that application of the sequential robust optimization strategy to the V-bending process resulted in a significant improvement of the process robustness and reliability. The deteriorating effects of noise variables are minimized by changing the tooling angle and increasing the process depth setting. This will minimize the need for active control of the depth setting in the current process.

5.6 Conclusions

In this chapter, steps 8–10 of the robust optimization strategy are discussed in detail, i.e. the validation and sequential improvement step. A sequential improvement algorithm is presented based on an expected improvement measure. The robust optimization strategy is successfully applied to an analytical test function and industrial V-bending process.

For the V-bending application, a significant improvement of the robustness and reliability is obtained by optimizing the process design while accounting for the deteriorating effects of noise variables. Experimental validation of the numerical robustness results shows a good agreement with the experimental results. Moreover, it is demonstrated that the sequential optimization step improves the accuracy of the objective function and constraint prediction at regions of interest in an efficient way. Especially the accurate prediction of the constraint formulation (both mean value and variance) has proven to be critical in this region for determining the correct location of the robust optimum. Finally, it is concluded that the prediction accuracy of the metamodels increases more rapidly by placing the infill points at qualified locations compared to increasing the initial size of the DOE. Adding a sequential improvement step to the robust optimization strategy enables a further increase of the overall efficiency of the strategy.

Chapter 6

On the effect of numerical noise*

6.1 Introduction

The use of metamodels in an optimization procedure hinges on the assumption that the metamodel is a correct representation of the FE simulation responses and that the FE simulation correctly predicts the physical process. However, it is well known that this is often not the case and that different sources of errors are present. Oden et al. [103] state that quantification of these errors is required to increase the reliability and utilization of simulation methods in the future. Simpson et al. [133] recognize such errors as a major issue to be solved in future research on metamodel-based optimization, especially with the continuous increase of the computational complexity of FE simulations.

Computer simulations are deterministic by nature, meaning that repeated runs for the same input variables will yield exactly the same result [65, 118, 122]. However, a small change of the input variable settings can cause the FE code to have a different mesh or different number of increments. Consequently, this may give a relatively large difference in response which is for the greater part a numerical artifact rather than a physical response change. This artifact is referred to as numerical noise in this work and is the main focus of this chapter.

Sources of numerical noise are discretization errors, adaptive mesh refinement, automatic (adaptive) step-size selection, round-off errors or changing contact conditions as discussed by Tekkaya and Martins [141]. These errors often appear as fluctuations around an expected smooth response and have a numerical cause.

*This chapter is based on: J.H. Wiebenga, and A.H. van den Boogaard. On the effect of numerical noise in approximate optimization of forming processes using numerical simulations. *International Journal of Material Forming*, DOI 10.1007/s12289-013-1130-2, **2013**.

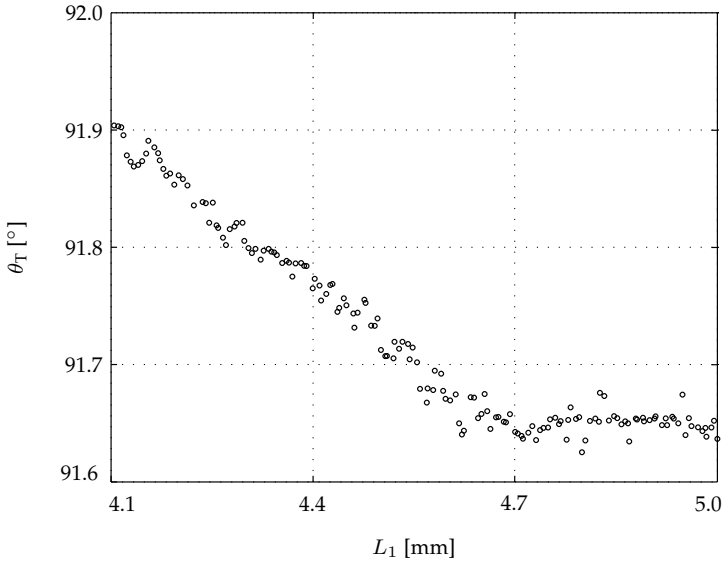

Figure 6.1 *FE simulation response of the V-bending application demonstrating the presence of numerical noise*

Other sources of noisy or perturbed response behavior in optimization problems are demonstrated in [43, 143]. Achieving a good compromise between accurate simulation results (by reducing these errors) and optimization results on the one hand and computational efficiency on the other hand is an on-going challenge. An increasing number of commercial FE codes offer numerical tools such as automatic procedures for re-meshing or mesh refinement to answer to this need. Although these techniques have proven their value for a single deterministic simulation, it is known that they may cause convergence problems when used in optimization [145].

To demonstrate numerical noise, consider Figure 6.1 showing results for 200 FE simulations of the V-bending application discussed in Section 5.5. The transition angle θ_T is plotted as a function of L_1 as defined in Figure 5.7. This V-bending application will be further evaluated in Section 6.5. The FE simulation response clearly shows deviations from the expected smooth numerical response, demonstrating the presence of numerical noise.

Several metamodel-based approaches have been proposed in the literature which account for the presence of numerical noise [43, 46, 107]. These approaches make use of RSM approximations to filter out numerical noise. Although very suitable for this purpose, these models also show low flexibility with respect

to a possible strong non-linear response behavior in the design space. As an example, note the bend in the response at $L_1 = 4.7$ mm in Figure 6.1 which cannot be accurately described by a linear or quadratic RSM model. Moreover, Oden et al. [103] already mentioned that many naturally arising research questions regarding numerical noise remain open, i.e. how to minimize its deteriorating effect on prediction quality and how to quantify numerical noise.

A general approach is presented in this chapter to handle and minimize the deteriorating effect of noisy response data in metamodel-based optimization. Both deterministic and robust optimization problems are considered. For the latter, the effect of numerical noise on the prediction accuracy of the statistical measures is considered and the above-mentioned research questions will be answered. It is demonstrated in Chapter 5 that the metamodel quality can be improved by sequentially adding infill points, but the quality improvement is limited if numerical noise is present. Therefore, a coupling is made with the sequential improvement algorithm to eliminate this effect. Moreover, a termination algorithm is presented based on the magnitude of noise present in the response. This can be used in addition to Equation (5.5) and avoids relying solely on an arbitrarily chosen threshold value to terminate the EI algorithm in case numerical noise is present.

This chapter is organized as follows, the deteriorating effect of numerical noise on the metamodel prediction accuracy is demonstrated using an analytical test function in Section 6.2. Numerical noise is subsequently quantified and its effect is minimized by the application of local approximation and regularization techniques respectively in Section 6.3. These techniques are subsequently incorporated in the robust optimization strategy of Chapter 3 and a coupling is made with the sequential improvement algorithm in Section 6.4. This combined approach is applied to the sequential optimization of two industrial metal forming processes in Section 6.5 and Section 6.6, i.e. a V-bending application and a cup-stretching application respectively. The V-bending application is considered in this chapter as a deterministic optimization problem, whereas the cup-stretching application is considered as a robust optimization problem. A discussion is provided in Section 6.7. Finally, Section 6.8 will present the conclusions of this chapter.

6.2 Effect of numerical noise

Due to the presence of numerical noise, response data may be perturbed or noisy. The usage of metamodels to approximate the noisy response can result in a low

quality response approximation and may even magnify the prediction error [131]. Combining the resulting metamodels with an optimization algorithm is likely to result in an inaccurate prediction of the optimum.

6.2.1 Bias-variance trade-off

Following the metamodel-based optimization strategy, the metamodel prediction $\hat{y}(x)$ of the simulation-based response $y(x)$ can be formulated as (see Appendix C):

$$y(x) = \hat{y}(x) + \varepsilon \tag{6.1}$$

When considering deterministic computer experiments, the remaining fitting error ε should ideally be zero in the DOE points. This corresponds to a zero *bias error* which means that the metamodel should interpolate through the response values at the DOE points. The bias error can be decreased by increasing the flexibility of the metamodel (e.g. increasing the order of polynomial) or by using interpolating metamodels. However, the prediction accuracy of such models deteriorates when dealing with noisy data since decreasing the bias error will tend to provide a larger *variance error* as a result of over-fitting. The variance error is the variation of the metamodel prediction for different subsets of DOE points extracted from the complete set. The variance error can again be decreased by smoothing the metamodel, but if this idea is taken too far then the bias error will increase again as a result of under-fitting. This natural trade-off is referred to as the *bias-variance trade-off* [18].

Both the bias and variance error can be decreased by increasing the number of DOE points. However, when using computationally expensive FE simulations, the number of points is severely limited. As long as data is sparse, i.e. the number of DOE points is small, interpolating models are still able to generate a smooth approximation of the noisy data. However, as discussed in Chapter 5, metamodels based on sparse data will generally only serve as a first estimate of the true response function. By combining these models with a sequential improvement step, data becomes more dense in a local region of the design space, which may again result in erroneous metamodel predictions if the calculated response data is contaminated with noise.

6.2.2 Application to an analytical test function

To demonstrate these phenomena and the effect of noise, consider the following analytical test function with $0 \leq x \leq 1$:

$$y(x) = (6x-2)^2 \sin(12x-4) + \varepsilon \qquad \varepsilon \sim \mathcal{N}(\mu_\varepsilon, \sigma_\varepsilon^2) = \mathcal{N}(0, 1^2) \tag{6.2}$$

Two data sets are considered for training, a smooth and a perturbed data set. For the latter, the analytical test function is perturbed with a normally distributed noise (ε) with mean $\mu_\varepsilon = 0$ and constant standard deviation $\sigma_\varepsilon = 1$ where the magnitude of the perturbation is assumed to be small compared to the overall change in response behavior. Both data sets contain 20 DOE points, 10 globally distributed points augmented with 10 local DOE points added near the global optimum of the test function. This is done to create a more dense sampling such as obtained by sequential optimization. A family of Polynomial Models (PM) or RSM models with an order up to 10 is fitted based on the commonly used quadratic loss function or L_2-norm, see Equation (C.3) in Appendix C.1. Application of this loss function is referred to in this chapter as the *basic* form. The deviation of the metamodel $\hat{y}(x)$ from the test function $y(x)$ is determined using the Root Mean Square Error (RMSE) evaluated at n points x_i:

$$\text{RMSE} = \sqrt{\text{MSE}} = \sqrt{\frac{1}{n}\sum_{i=1}^{n}(\hat{y}(x_i) - y_i)^2} \tag{6.3}$$

The results for the smooth and perturbed data set are presented in Figures 6.2 and 6.3 respectively. The resulting error estimates for the smooth and perturbed data set are given in Table 6.1 and denoted by RMSE_S and RMSE_P respectively. If no noise is present in the data, increasing the order of the polynomial will decrease the RMSE_S. The best fit for the smooth data set is found to be a polynomial fit of order 10. Now for the perturbed data set, the best approximation of the test function is found to be a polynomial fit of order 8, see Table 6.1. Decreasing the order to 6 will result in a poor representation of the test function and a high bias error, especially near the optimum, see Figure 6.3. On the other hand, increasing the order of the polynomial fit to 10 will decrease the bias error, but increase the variance error. This can be recognized in Figure 6.3 by the over-fitting of the polynomial model at the sparsely sampled regions of the design space. The increasing flexibility of the model is becoming more tuned to the noise present

in the data. For the perturbed data set, the polynomial of order 8 has the best *generalization capability* providing an optimal trade-off between closeness to the data and smoothness of the function.

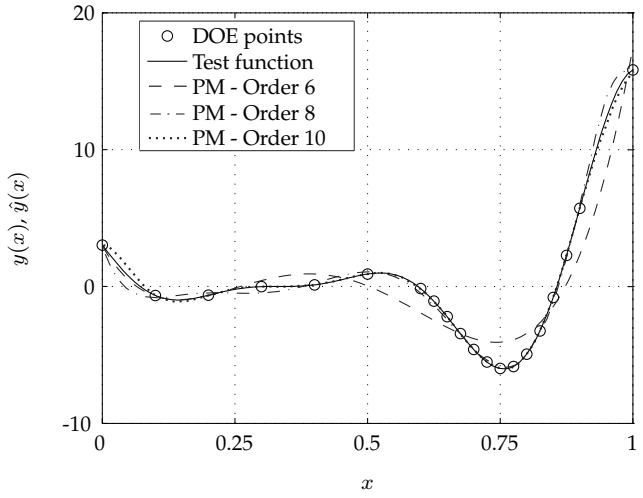

Figure 6.2 *Polynomial Model (PM) approximation of the smooth data set*

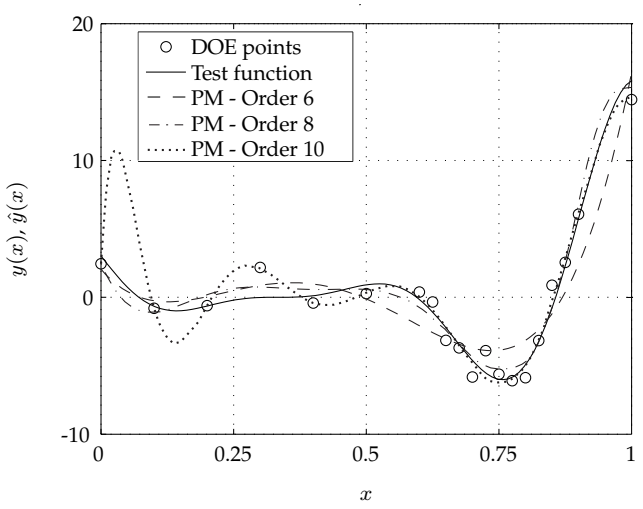

Figure 6.3 *Polynomial Model (PM) approximation of the perturbed data set*

Table 6.1 *Error estimates of the Polynomial Model (PM) approximation in basic and regularized form of the smooth and perturbed data set*

Metamodel form	$RMSE_S$ basic	$RMSE_P$ basic	$RMSE_P$ regularized
PM - Order 6	10.9	11.8	11.2
PM - Order 8	5.0	8.6	7.3
PM - Order 10	1.8	22.1	12.2

6.3 Accounting for numerical noise

Next, two fundamental questions considering numerical noise will be covered: how to minimize its deteriorating effect on prediction quality and how to quantify noise. The former question requires finding the optimal balance between bias and variance errors in the construction of metamodels without *a priori* knowledge of the underlying true response function. This can be achieved by regularization techniques and will be discussed in Section 6.3.1. An approach for estimating the magnitude of noise will be presented in Section 6.3.2.

6.3.1 Regularization

In the case of regularization, the L_2-norm is extended with an additional term [112]. In this work, *ridge regression*, also known as *Tikhonov regularization* [142], is applied where the best model from the family H of metamodels is selected as the solution of:

$$\min_{\hat{y}\in \mathrm{H}} \left(\mathbb{Z}(\hat{y}) = \frac{1}{n} \sum_{i=1}^{n} \left(\hat{y}(x_i) - y_i\right)^2 + \lambda \int \|D^2 \hat{y}(x)\|_{\mathrm{H}} \, \mathrm{d}x \right) \tag{6.4}$$

where λ is the regularization parameter and $D^2\hat{y}(x)$ represents the value of the second derivative of the proposed model. The first term includes the quadratic loss function which enforces closeness to the data or a low bias error. The second term penalizes high local curvature enforcing a smooth metamodel or low variance error. The optimal regularization parameter can be identified by minimizing the Generalized Cross-Validation (GCV) function [47], which is comparable to LOOCV as discussed in Section 3.4.3. This function is based on leaving out an arbitrary element y_i after which the corresponding regularized

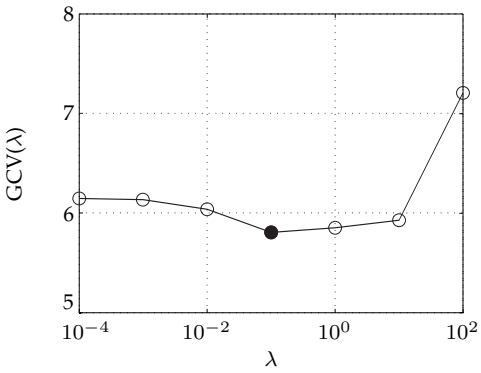

Figure 6.4 *Generalized Cross-Validation (GCV) function for the regularized polynomial model of order 8*

solution $\hat{y}_\lambda$ should predict this observation well. The regularization parameter is chosen that minimizes the GCV function [25]:

$$\text{GCV}(\lambda) = \frac{\frac{1}{n}\sum_{i=1}^{n}(\hat{y}_\lambda(x_i) - y_i)^2}{(1 - tr\ A(\lambda)/n)^2} \tag{6.5}$$

where $A(\lambda)$ is the matrix which produces the regularized solution when multiplied with y, i.e. $\hat{y}_\lambda = A(\lambda)y$.

A description of the regularized fitting procedure for the family of polynomial models is provided in Appendix C.1.1. The RMSE_P results for these models considering the perturbed data set is presented in the fourth column of Table 6.1. For all polynomial models, a closer representation of the test function is obtained by application of regularization, represented by the decreasing RMSE_P values. Also note that for the polynomial model of order 10, the over-fitting is significantly suppressed. Again, the polynomial model of order 8 results in the lowest RMSE_P. The GCV function for this model is plotted in Figure 6.4 from which the optimal regularization parameter $\lambda = 0.1$ can be identified. Application of the remaining metamodel types to the analytical test function will be demonstrated in Section 6.4.

6.3.2 Quantification of noise

Quantification of noise requires determining the deviation between response measurements and the expected smooth, but unknown, underlying true function. For this purpose, a low complexity approximation of the true function is created by smoothing. Each response measurement is replaced by a local average of surrounding measurements such that the level of noise is reduced without (much) biasing the value obtained. In this work, a local smooth approximation is created based on Least-Squares Smoothing (LSS) after the technique used in *Savitzky-Golay* filters [123]. Applying a local smooth approximation benefits from a more densely sampled design space obtained by sequential optimization used to accurately predict a local estimator and thus result in a low bias error. Moreover, the true function is assumed to be low multimodal in a local region of the design space.

In the LSS approach, a polynomial least–squares fit is created inside a moving window [112]. The subsets of DOE points are determined by a nearest neighbors algorithm using an ellipsoid search region for a multi-dimensional moving window. In the case of a one-dimensional moving window, this reduces to finding an equal number of points to the left (n_l) and to the right (n_r) of the DOE point where $n_\mathrm{l} = n_\mathrm{r} = 2$. By utilizing a moving window, it is assumed that relatively distant DOE points have some redundancy which can be used to reduce the level of noise and that the true function can be locally well-fitted by a polynomial function. To account for the irregularly sampled data, an LSS prediction $\hat{y}_\mathrm{lss}$ is made based on a quadratic polynomial approximation (see Appendix C.1):

$$\hat{y}_\mathrm{lss} = \mathbf{X}\boldsymbol{\beta} \tag{6.6}$$

where $\mathbf{X}$ is the design matrix containing the quadratic basis functions and $\boldsymbol{\beta}$ are the regression coefficients. The β's are determined using the least-squares method such that the L_2-norm is minimized considering the points that are within the moving window. For a two-dimensional moving window, an elliptical search region is used to find a minimum of 6 nearest neighbors based on which the regression coefficients of the local quadratic response surface are determined.

For the one-dimensional moving window, this results in:

$$L_2 = \sum_{j=-n_l}^{n_r} \varepsilon_{i+j}^2 = \sum_{j=-n_l}^{n_r} (\hat{y}_{\text{lss}}(x_{i+j}) - y_{i+j})^2 \tag{6.7}$$

This procedure is repeated for each point x_i. The resulting LSS model is expected to be a more accurate description of the true function than the scattered data points. Assuming the error variance (σ_ε^2) to be constant and the errors to be approximately normally distributed, an estimate of the magnitude of noise ($\hat{\sigma}_\varepsilon$) can be obtained using the smooth function by taking the variance of the estimated residuals ($\hat{\varepsilon}_i$) evaluated at all x_i where:

$$\hat{\varepsilon}_i = y_i - \hat{y}_{\text{lss}}(x_i) \tag{6.8}$$

The local LSS model of the perturbed data set is provided in Figure 6.5. The smoothing is applied in a local region around the global optimum with an increased sample density, i.e. $0.6 \leq x \leq 0.9$. Evaluating the magnitude of numerical noise through Equation (6.8) results in $\hat{\sigma}_\varepsilon$ = 0.86. In case $\hat{y}_{\text{lss}}(x_i)$ is replaced by the function $y(x)$ in Equation (6.8), the magnitude of noise is determined at σ_ε = 0.89. Clearly, the local LSS model results in a good estimation of the noise present in the perturbed data set considering the analytical test function. Based on this estimation, one can plot the $\pm 2\hat{\sigma}_\varepsilon$ noise interval around the local LSS model, see Figure 6.5.

6.4 Integration in the robust optimization strategy

If numerical noise is present in the response function, it is shown that application of regularization and local approximation allows the user to minimize the deteriorating effects of numerical noise and quantify its magnitude. Next, these techniques are incorporated in the robust optimization strategy and a coupling is made with the sequential improvement algorithm.

6.4.1 Design of experiments

Regarding the data sampling, the combined usage of an LHD + FFD DOE is proposed in Section 3.4.1 to ensure that both the interior and the outer boundaries

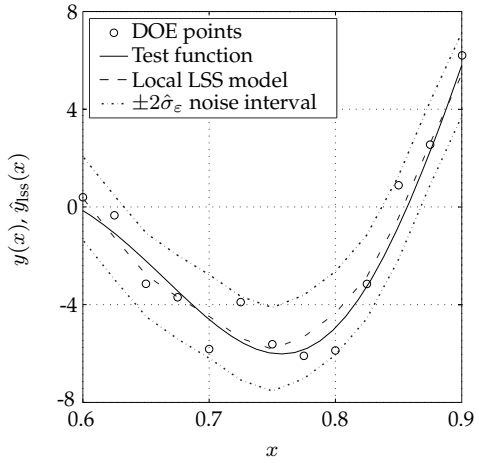

Figure 6.5 *Local Least-Squares Smoothing (LSS) model around the global optimum of the perturbed data set and accompanying $\pm 2\hat{\sigma}_\varepsilon$ noise interval*

of the design space are well sampled. The initial metamodel based on sparse data is subsequently improved at regions of interest by the sequential improvement step. This is simulated for the analytical test function by supplementing the initial DOE of 10 points with an additional 10 DOE points near the global optimum. It is shown that problems can occur if the density of data points varies in the design space. That is, the noise present in the data especially causes over-fitting of the metamodel in the sparsely sampled regions of the design space. This problem is largely resolved by allowing the metamodels to regress the data as demonstrated next.

6.4.2 Fit metamodels

Up to now, only polynomial models have been considered in this chapter. Next, also the remaining metamodel types are evaluated. In the basic form, Kriging and NN models are fitted based on the L_2-norm and show interpolating behavior. Similar to RSM, the loss function can be replaced by a regularized form to account for numerical noise. Descriptions of the Kriging and NN models in regularized form are provided in Appendices C.2.1 and C.3.1 respectively. Application of these metamodels in basic and regularized form to the perturbed data set is presented in Figures 6.6 and 6.7 respectively. Studying Figure 6.6 in more detail, one can recognize the over-fitting behavior of the models caused by forcing the models to interpolate through the perturbed data points. Figure 6.8a shows a detail plot near the global optimum from which the interpolating

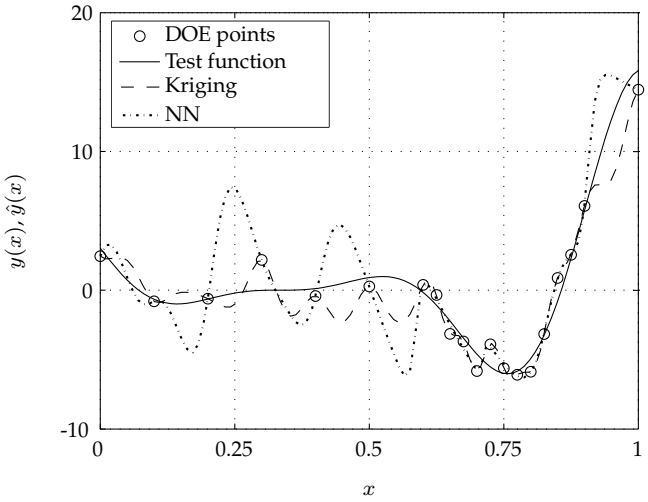

Figure 6.6 *Basic metamodel approximation of the perturbed data set*

behavior becomes even more apparent. Combining these metamodels with an optimization algorithm can result in erroneous results due to e.g. the early stalling of the optimization algorithm in a local optimum. Also note that some additional local optima appear as a result of over-fitting.

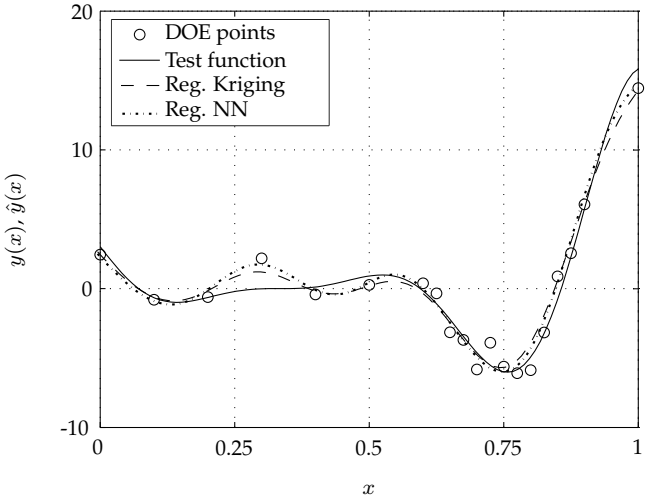

Figure 6.7 *Regularized metamodel approximation of the perturbed data set*

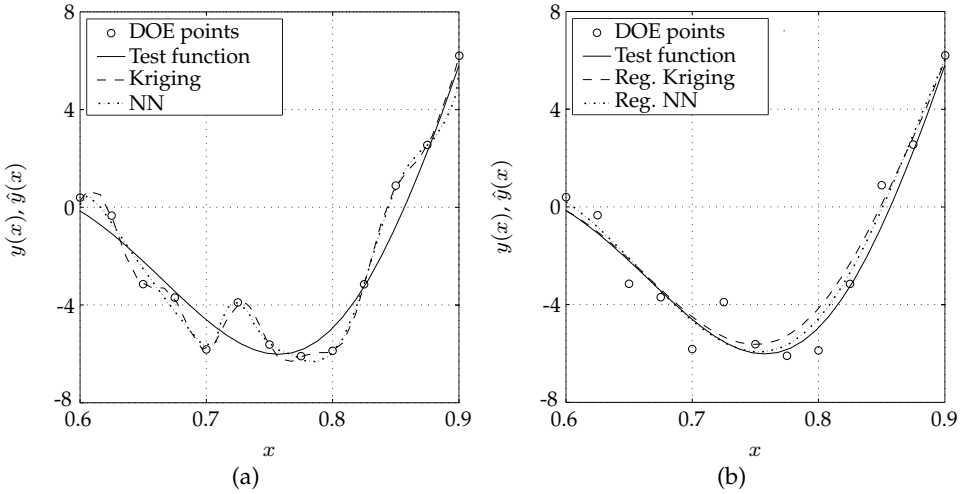

Figure 6.8 *Detail plot of the (a) basic and (b) regularized metamodel approximation of the perturbed data set*

The problem of approximating perturbed response data with a varying sample density in the design space is largely resolved by allowing the models to regress the data, see Figure 6.7 and the detail plot in Figure 6.8b. Note that both the optimal value for the objective function and design variable can be predicted accurately using the regularized metamodels. The significant improvement of approximation accuracy with respect to the test function is also confirmed by the reduction of the RMSE_P for all metamodels, see Table 6.2.

Table 6.2 *Error estimates of the metamodel approximation of the perturbed data set*

Metamodel form	RMSE_P basic	RMSE_P regularized	RMSE_CV basic	RMSE_CV regularized
Polynomial - Order 8	8.6	7.3	3.9	2.5
Kriging	15.2	6.7	4.9	1.4
Neural Network	28.3	6.5	5.8	0.9

6.4.3 Metamodel validation

Until now, the quality of the metamodel approximation is determined in this chapter using the true response function $y(x)$. Equation (6.3) can also be evaluated using LOOCV as outlined in Section 3.4.2. As a result, a Cross-Validation Root Mean Square Error (RMSE_{CV}) is obtained by replacing $\hat{y}(x_i)$ with the metamodel prediction $\hat{y}_{-i}$ at x_{-i}. This is applied for all metamodel types present in the family of metamodels, both in basic form and regularized form. For each response, the metamodel type is chosen here that minimizes the RMSE_{CV}. Alternatively, one could also use the R^2_{pred}-value.

Table 6.2 shows the RMSE_{CV} values for the metamodels in basic and regularized form. Similar to the RMSE_{P} values, the improvement of the approximation accuracy is predicted based on the cross-validation results, although these values are now based on the (perturbed) response measurements instead of the known test function. Model selection is based on the lowest RMSE_{CV} value, i.e. an NN model. This example shows that cross-validation can be used to validate metamodel accuracy even though noise is present in the response measurements.

6.4.4 Optimization and sequential improvement

The regularized metamodels can now be used for optimization and sequential improvement by application of the EI-algorithm. As proposed in Equation (5.5), the termination of the update algorithm is based on an arbitrarily chosen threshold for the EI. If numerical noise is absent in the response data, a fast decline of the EI function is obtained by adding DOE points. However, the quality improvement is limited when numerical noise is present, resulting in an inefficient termination threshold. Therefore, a termination threshold is proposed based on the magnitude of noise present in the data. The approach makes use of the increasing accuracy with which the actual noise is predicted for an increasing number of DOE points.

To explain this in more detail, consider Figure 6.9 in which the local LSS model of the original data set is plotted including the $\pm 2\hat{\sigma}_\varepsilon$ noise interval. In addition, the local LSS model and accompanying $\pm 2\hat{\sigma}_\varepsilon$ noise interval is plotted based on an augmented data set with 4 sequentially added DOE points near the global optimum. Evaluating the magnitude of numerical noise through Equation (6.8) for the initial and augmented local LSS model results in $\hat{\sigma}_\varepsilon$ = 0.86 and $\hat{\sigma}_\varepsilon$ = 0.96 respectively. For a sparse data set, the magnitude of noise is underestimated. Adding DOE points results in a more accurate approximation of the magnitude of noise, converging to σ_ε = 1 for the test function, see Equation (6.2).

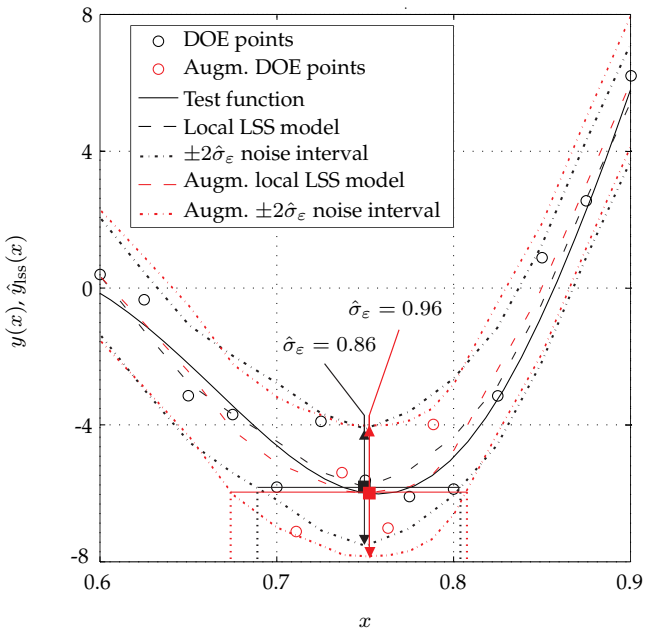

Figure 6.9 *Local LSS model, accompanying $\pm 2\hat{\sigma}_\varepsilon$ noise interval and resulting noise bandwidth of the perturbed data set and augmented data set*

The $\pm 2\hat{\sigma}_\varepsilon$ noise interval for both local LSS models can be translated into noise bandwidths for x. The bandwidths of the original and augmented local LSS model around the global optima (visualized by the solid square markers) are $0.690 \leq x \leq 0.805$ and $0.675 \leq x \leq 0.810$ respectively and are depicted in Figure 6.9. Note how the bandwidth growths for an increasing number of DOE points, converging to a maximum size for $\sigma_\varepsilon = 1$. Now any sequentially added data point will only contribute to an increased metamodel prediction accuracy if it falls outside the noise bandwidth. In other words, the update algorithm is to be terminated if sequentially added points fall within the current noise bandwidth.

The update procedure will automatically terminate based on the noise present in the response data due to the property of an increasing bandwidth for an increasing number of DOE points, and thus increasing accuracy with which σ_ε is calculated. Depending on the calculation time of the FE simulation, the user can choose to terminate the algorithm if multiple subsequent points (e.g. 3 points) fall within the noise bandwidth, also increasing the stability of the update algorithm. The proposed approach will be demonstrated next by the sequential optimization of two metal forming processes.

6.5 Application to a V-bending process

The optimization strategy, including the regularization and local approximation techniques, will now be applied to optimize the V-bending process presented in Chapter 5. The focus in this chapter is on numerical noise, therefore a single design variable and response function is considered in a deterministic optimization study for simplicity. The dimension of the punch L_1 is chosen as the single design variable with values ranging between 4.1 mm and 5 mm, see Figure 5.7. The objective of this study is to determine the setting of L_1 for which the transition angle θ_T equals an arbitrarily chosen target angle of $\theta_\mathrm{t} = 91.75°$.

For the purpose of this research, a reference data set is generated by performing 200 FE simulations. The response values for θ_T and reference model are presented in Figure 6.10. The reference model is obtained by LSS approximation of the response set using $n_\mathrm{l} = n_\mathrm{r} = 10$. The bending angle shows uncorrelated fluctuations around a smooth trend. The smooth response trend line is expected when modeling a physical phenomenon. The fluctuations are particularly caused by changes in the computational mesh and contact conditions. Clearly, numerical noise is present. Evaluating the magnitude of numerical noise through Equation (6.8) for this data set results in $\hat{\sigma}_\varepsilon$ = 0.01. The target objective function value of $\hat{f}_\mathrm{opt} = 91.75°$ is found for the optimal setting $L_{1,\mathrm{opt}} = 4.45$ mm.

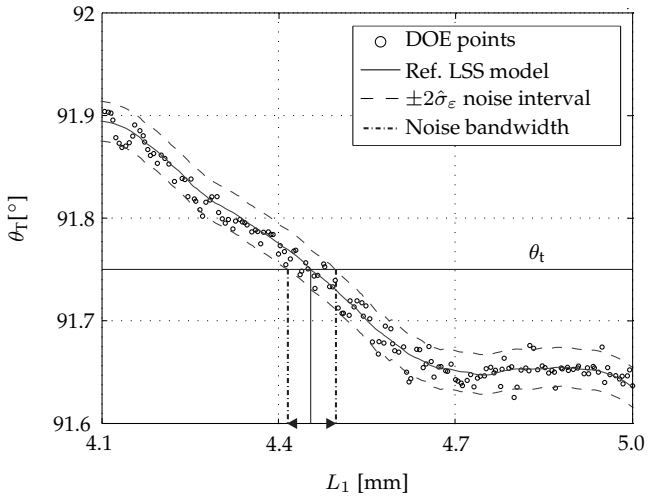

Figure 6.10 *V-bending simulation response and resulting reference LSS model*

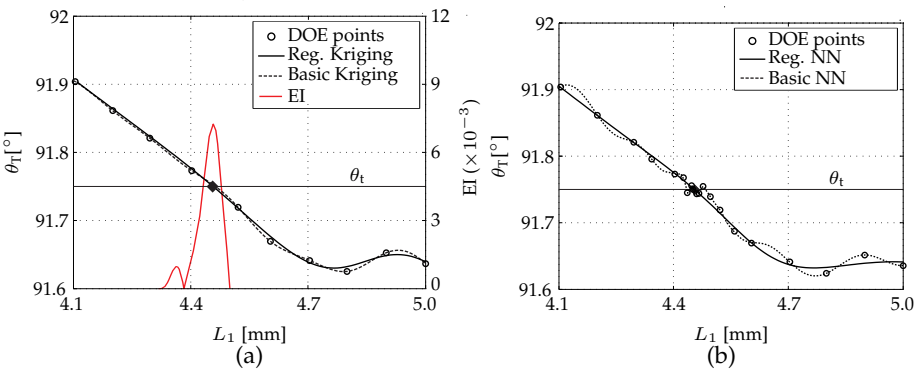

Figure 6.11 *Metamodel approximation of the (a) initial and (b) final updated V-bending data set*

6.5.1 Fit initial metamodels and optimization

An initial LHD + FFD DOE of 10 points is created and the family of regularized metamodels is subsequently fitted and validated using LOOCV. Based on the validation results as presented in Table 6.3, a regularized Kriging model is identified as the most accurate fit for the initial data set. Figure 6.11a presents the initial 10 DOE points and the regularized Kriging approximation. In addition, its basic (interpolating) counterpart is plotted showing a rather smooth behavior. It shows that if perturbed data is very sparse, problems are not likely to occur since perturbations in the data can still be accommodated with a smooth approximate function. This is also reflected in the coefficient of determination of the basic Kriging model, i.e. $R^2_{\text{pred}} = 0.95$. Based on the regularized Kriging model, the optimal objective function value is determined at $L_{1,\text{opt}} = 4.49$ mm, see the diamond marker in Figure 6.11a.

Table 6.3 *Coefficient of determination (R^2_{pred}) of the family of metamodels based on the V-bending data set*

Number of data points	10 (initial)	20 (final)
Reg. Polynomial - Order 2	0.93	0.92
Reg. Kriging	0.98	0.98
Reg. Neural Network	0.97	0.99

6.5.2 Sequential improvement and optimization

The deviation between the optimal design variable setting prediction based on the metamodel and the reference LSS model can be decreased by the sequential improvement step. The EI, given by Equation (5.4) and calculated based on the Kriging model, is given in Figure 6.11a. Maximizing the EI results in the design variable coordinate $L_1^{'} = 4.49$ mm of the first infill point. After determining the response at this location, the family of metamodels is updated. As a result, also the prediction error and the EI are revised.

The intermediate metamodel results and accompanying local LSS models after adding 3, 6 and 9 DOE points are presented in Figures 6.12a, 6.12b and 6.12c respectively. In addition, the $\pm 2\hat{\sigma}_\varepsilon$ noise intervals are plotted where the magnitude of noise is estimated at $\hat{\sigma}_\varepsilon = 0.0069$, $\hat{\sigma}_\varepsilon = 0.0071$ and $\hat{\sigma}_\varepsilon = 0.0078$ respectively. Compared to the reference data set, the magnitude of noise is initially underestimated but converges to the reference solution for an increasing number of locally added DOE points. As a consequence, also the width of the resulting noise bands increase, terminating the update algorithm after adding 10 DOE points. The last 3 subsequent DOE points fall within the noise band.

Figure 6.11b shows the final result of applying the sequential optimization procedure. The validation results of fitting the family of regularized metamodels to the final data set are presented in the last column of Table 6.3. Although very close to the regularized Kriging model, the regularized NN model is identified as the most accurate final fit and plotted in Figure 6.11b with its basic counterpart. Clearly, the basic (interpolating) model shows over-fitting behavior which is also reflected by its low coefficient of determination of $R^2_{\text{pred}} = 0.80$. Also note that this metamodel approximation results in multiple optima that meet the target angle $\theta_{\text{t}} = 91.75°$. All these solutions fall within the bandwidth of noise. The regularized NN model accurately predicts a unique optimal setting of $L_{1,\text{opt}} = 4.45$ mm which meets the reference solution.

This application shows that the presence of numerical noise cannot be neglected in metamodel-based optimization. Especially in the case of dense sampling, for example by sequential optimization, accounting for numerical noise is important to increase the overall accuracy of the optimization results.

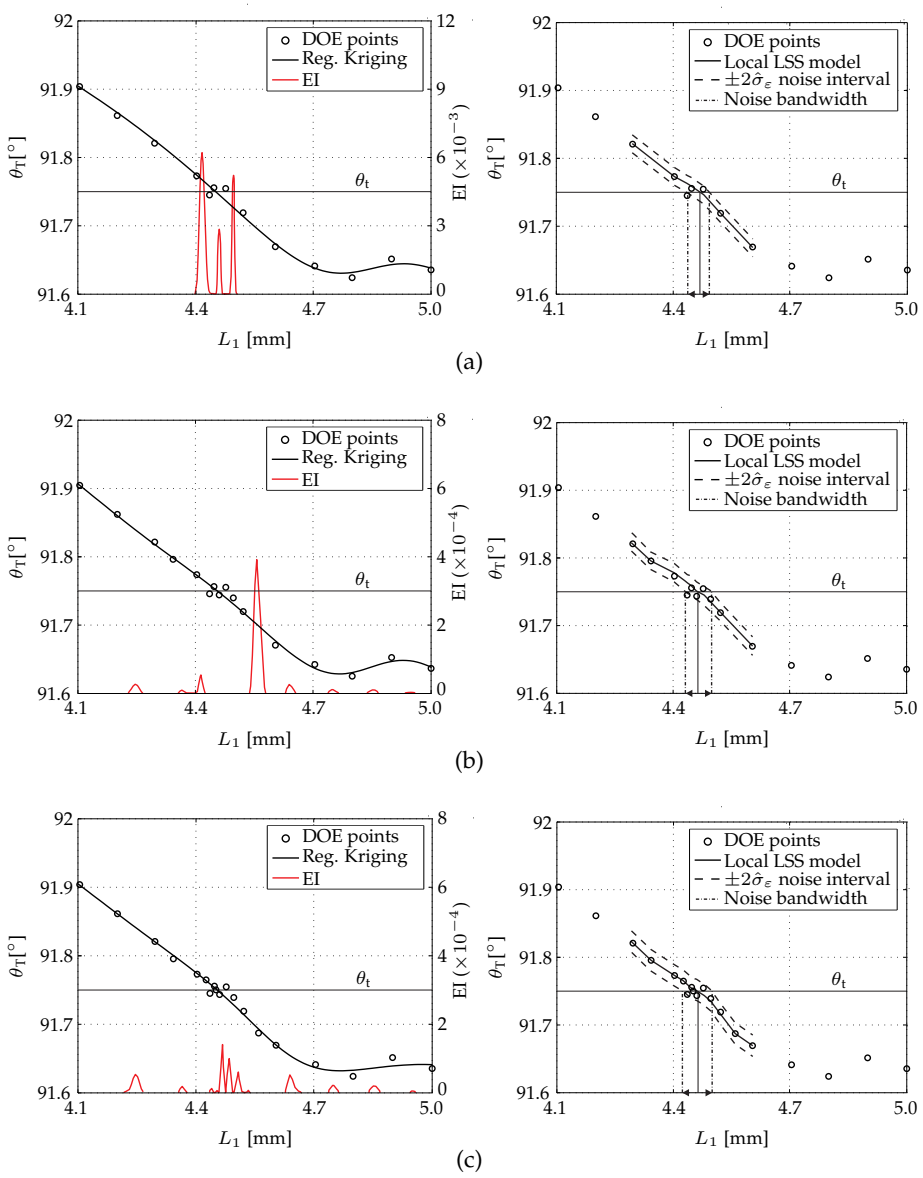

Figure 6.12 *Best metamodel approximation (left) and local LSS approximation (right) of the V-bending data set after (a) 3, (b) 6 and (c) 9 updates*

6.6 Application to a cup-stretching process

The second industrial application considered in this work is a stretching process of a hemispherical cup, performed in cooperation with Tata Steel. See Figure 6.13 for an impression of the process and resulting product. The cup is produced out of a forming steel for which the full anisotropic material behavior is obtained by mechanical testing. The FE code DIEKA [29] is used to set up an FE model of the forming process. The circular blank is discretized using triangular discrete Kirchhoff shell elements with 5 integration points through thickness, see Figure 6.13b. The blank is subsequently stretched by a prescribed punch displacement of 42 mm with the friction coefficient set to 0.14.

During the forming process, the material in the cup wall will be stretched significantly. After 42 mm punch displacement, the material mainly experiences plane strain deformation in a band halfway in the cup wall, see Figure 6.13b. Fracture will occur at this location once the peak strain exceeds the forming limit. To determine the moment of fracture, an accurate prediction of the strain in the cup wall is required.

The maximum major strain (ε_{RD}) is evaluated in the Rolling Direction (RD) of the blank, see Figure 6.13b. The blank radius (R) is chosen as a design variable ranging between 80 mm $\leq R \leq$ 100 mm. Since the target element size of the quarter circle blank is kept constant at 1.4 mm, the number of elements per blank size configuration increases from approximately 6022 to 9424 elements for the smallest and largest blank size respectively. The material thickness (t) shows variation around a mean value. The scatter in material thickness is described by a normal distribution $t \sim \mathcal{N}(\mu_t, \sigma_t^2)$ with $\mu_t = 0.8$ mm and σ_t = 0.02 mm.

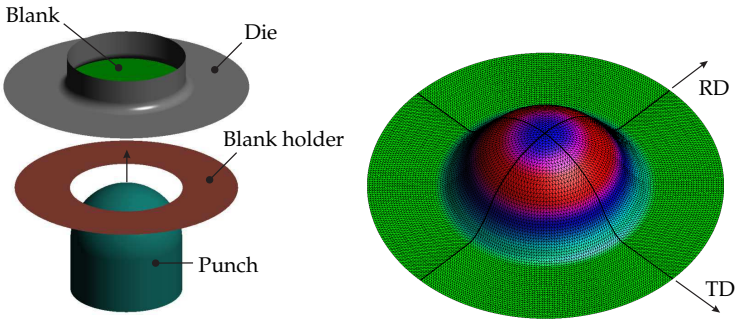

Figure 6.13 *Impression of the (a) stretching process and (b) resulting hemispherical cup product*

As a result, the objective becomes a function of the weighted sum of both the mean μ_f and standard deviation σ_f of the maximum major strain response. Note that σ_f is a measure for the maximum major strain variation caused by scatter of the material thickness t. This measure differs from σ_ε which is the standard deviation of the error caused by numerical noise. The challenge of this robust optimization study is to find the optimal setting R for which ε_{RD} is maximum but does not exceed the forming limit strain for plane strain $\varepsilon_1 = 0.4$. The quantified optimization formulation is given by:

$$\begin{aligned} \min_{R} \; & -\mu_f \\ \text{s.t. } & \mu_f + 3\sigma_f \leq 0.4 \\ & 80 \leq R \leq 100 \\ \text{where } & t \sim \mathcal{N}(0.8, 0.02^2) \end{aligned} \tag{6.9}$$

A reference data set is obtained beforehand by performing 1071 FE simulations at an equidistant grid of 51 $\times$ 21 design and noise variable settings respectively. The upper and lower bound of the noise variable are set at $\mu_t + 3\sigma_t$ and $\mu_t - 3\sigma_t$, respectively. A graphical representation of the maximum major strain in the RD is given in Figure 6.14. The response shows sudden discontinuities in the direction of the blank radius caused by changes in the computational mesh. A more smooth response can be observed in the direction of the blank thickness. Although the characteristics of noise are different compared to the previous application, the sudden discontinuities in the response can be seen as numerical noise since they do not represent the smooth physical performance and thus a similar problem is faced in metamodel-based optimization.

A smooth reference solution is obtained by LSS approximation of the response set using 10 nearest neighbors determined by an elliptical search region. Evaluating the magnitude of numerical noise in the major strain response through Equation (6.8) results in $\hat{\sigma}_\varepsilon$ = 0.003. The LSS model of the reference data set and accompanying $\pm 2\hat{\sigma}_\varepsilon$ noise interval is depicted in Figure 6.15a. Note that for this multi-dimensional optimization problem, the greatest magnitude of numerical noise in the blank radius direction is dominant in determining $\hat{\sigma}_\varepsilon$ for the whole design space. The objective function can now be determined based on the reference data set as well as the LSS model by an MCA. Both results are plotted in Figure 6.15b. Note the significant effect of numerical noise on the robust objective function resulting from the reference data set. In addition, the $\pm 2\hat{\sigma}_\varepsilon$ noise interval of the objective function is plotted, obtained by sampling onto the LSS model. The magnitude of numerical noise for the objective function is

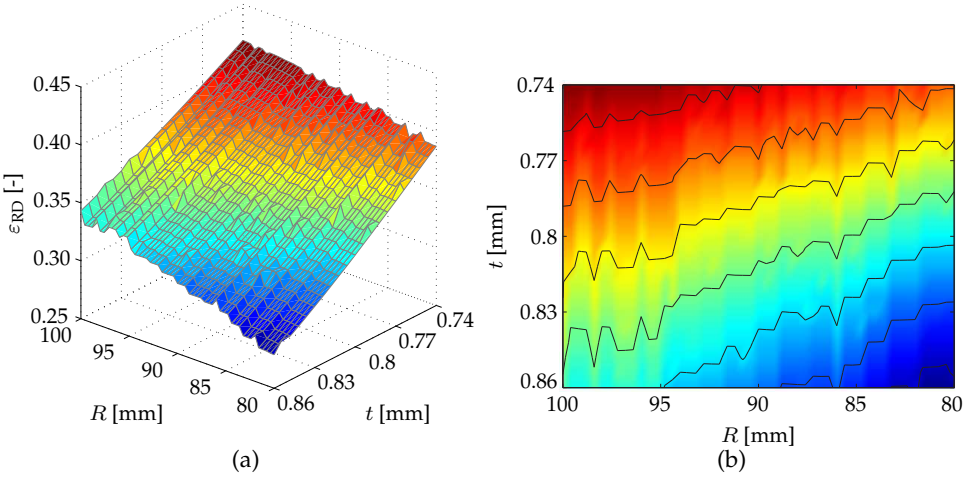

Figure 6.14 *Reference data set of the cup-stretching application represented by a (a) surface plot and (b) contour plot*

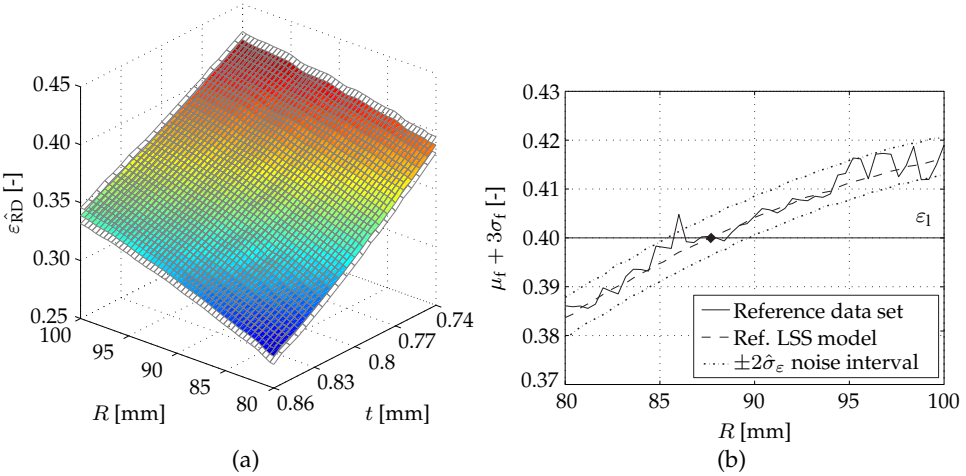

Figure 6.15 *(a) Reference LSS model and accompanying $\pm 2\hat{\sigma}_\varepsilon$ noise interval, and (b) objective function prediction based on the reference data set and reference LSS model*

determined at $\hat{\sigma}_\varepsilon$ = 0.002. Using the reference LSS model of the objective function, the target value of $\hat{f}_{\text{opt}}$ = 0.4 is found for the optimal setting R_{opt} = 87.5 mm, see the diamond marker in Figure 6.15b.

6.6.1 Robust optimization

An initial LHD + FFD DOE of 20 points is created in the two-dimensional combined design–noise variable space. After running the FE simulations, the family of metamodels is fitted. The regularized NN model is identified as the most accurate fit, see Figure 6.16a. The resulting objective function prediction is plotted in Figure 6.16b. Solving Equation (6.9) results in the optimal value R_{opt} = 85.1 mm, see the circle marker in Figure 6.16b. Clearly, sequential robust optimization is required to improve the overall prediction accuracy of the metamodel and to decrease the discrepancy with the optimal value prediction of the reference solution.

6.6.2 Sequential robust improvement

The initial DOE is augmented with additional DOE points by the sequential improvement step. The termination criterion as presented in Section 6.4.4 is reached after adding 19 DOE points. The final regularized Kriging metamodel solution is depicted in Figure 6.17a. The initial and sequentially added DOE points are plotted in Figure 6.17b. Note how the design space has been sampled extensively near the global optimum in the design variable space.

A plot of the final objective function prediction and reference objective function is provided in Figure 6.18a. The final optimum is found close to the reference optimum at R_{opt} = 87.3 mm, see the circle and diamond marker in Figure 6.18a. The local LSS model and accompanying $\pm 2\hat{\sigma}_\varepsilon$ noise interval is provided in Figure 6.18b where the magnitude of noise is estimated at $\hat{\sigma}_\varepsilon = 0.0016$. Although the magnitude of noise is still underestimated compared to the reference data set, the update algorithm is efficiently terminated after adding 3 subsequent DOE points within the noise band. Further improvement of the robust objective function prediction is not expected based on the presence of numerical noise in the FE simulation response.

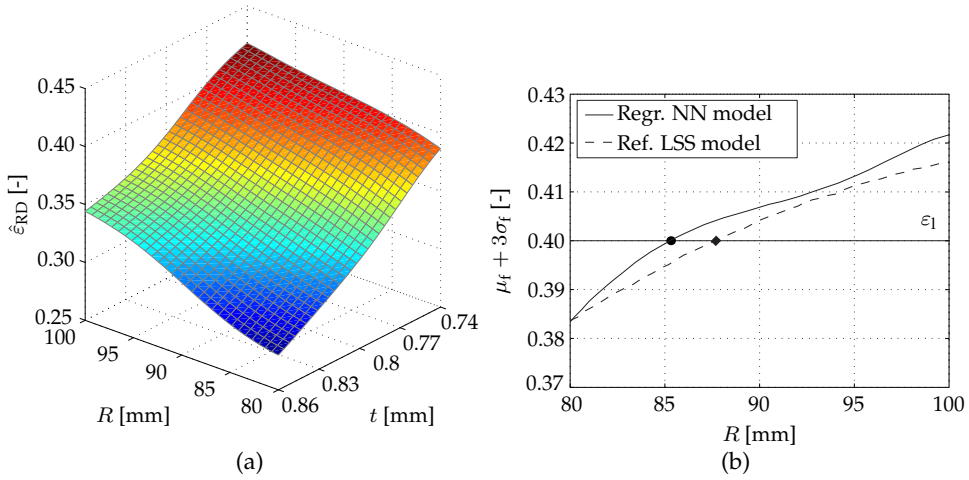

Figure 6.16 *(a) Initial regression NN model and (b) resulting objective function prediction*

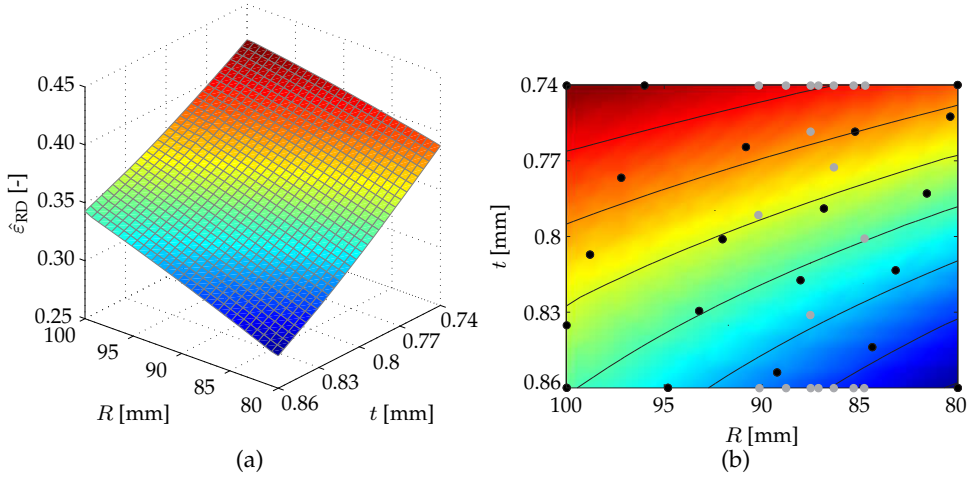

Figure 6.17 *(a) Final regression Kriging model and (b) contour plot showing the initial (black) and added (gray) DOE points*

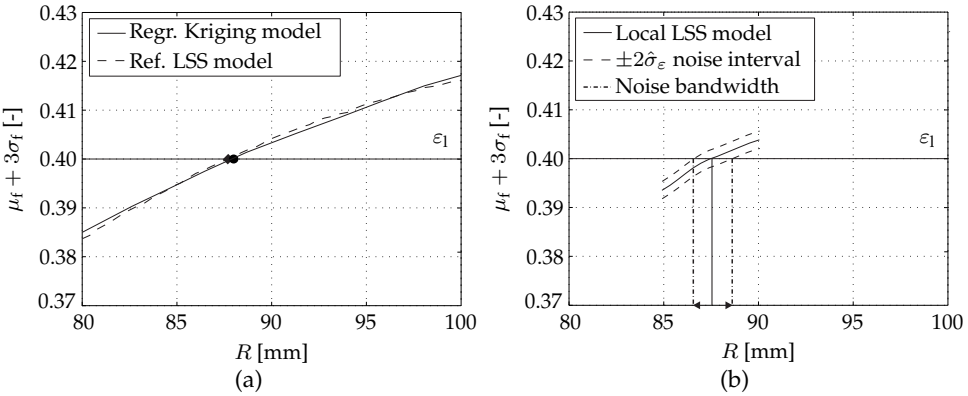

Figure 6.18 *(a) Final objective function prediction and (b) local LSS model*

6.7 Discussion

In case numerical noise is present in the response data, the approach proposed in this chapter becomes applicable.

The robust optimization strategy is extended in this chapter to account for the presence of numerical noise in the response data. One could also argue to set up more detailed FE models (e.g. finer mesh) to reduce the magnitude of numerical noise. However, these models would be more computationally expensive and unsuitable for use in an optimization procedure. Moreover, it is noted here that it is of less interest to accurately determine the exact measure of noise or to provide an accurate estimate of the confidence interval on the objective function value. Again, this would require more detailed FE models or many computationally expensive simulations. If the user is interested in the exact average performance in the optimum, it would be more beneficial to set up a more detailed FE model in the global optimum after termination of the update algorithm.

As a final point of discussion, note that the proposed approach provides a measure for the magnitude of numerical noise present in the data which is subsequently used for determining an efficient termination threshold for the update algorithm. In case no numerical noise is present, the local LSS model will predict a noise bandwidth of approximately zero, preventing the termination algorithm from becoming active. For this reason, it is proposed to use the termination threshold based on numerical noise in combination with Equation (5.5) for the EI-algorithm.

6.8 Conclusions

In this chapter, the presence and deteriorating effect of numerical noise on the approximation quality of metamodels is demonstrated, limiting the accuracy and general usability of metamodel-based optimization techniques. It is shown that the use of regularization in the fitting procedure of metamodels can alleviate the problem when noise is present in the FE simulation response. Quantification of noise is achieved by local smoothing of response data. These techniques are included in the robust optimization strategy and a coupling is made with the sequential improvement algorithm based on expected improvement.

Application of the approach to two industrial optimization cases shows the efficient termination of the update algorithm based on the magnitude of numerical noise present in the response data. The update algorithm stops when no further improvement of the metamodel prediction accuracy is expected with respect to the underlying expected smooth response. Moreover, despite the presence of numerical noise, the approach shows a fast and accurate convergence towards the global optimum while maintaining the benefits of metamodel-based optimization.

Chapter 7

Accounting for material scatter*

7.1 Introduction

In the robust design of sheet metal forming processes, one of the most dominant sources of scatter is the variation of material properties. To account for scatter in the design of forming processes, a common approach is to use safety margins. For example, keeping the strain in a product 10% below the FLC. It will be shown in this chapter that the usage of such safety margins can result in overly conservative designs, not making optimal use of the material and process. The choice for such a margin is arbitrary and application of it to different forming processes implicitly assumes that all processes are equally sensitive to scatter.

Scatter of material properties is already being considered in robustness analyses of forming processes, see e.g. [23, 132]. The approaches used to model material scatter are often simplified in the form of independent scaling of material parameters without accounting for possible parameter correlations [26, 91]. Also, due to the lack of information, engineers are often forced to choose rather simplified material models and work with a limited number of scattering material parameters [2, 41, 55]. Finally, because of limited capacity for material characterization, research on the variation of material properties is often only performed using a small number of samples [45]. All these aspects subsequently limit the accuracy with which the real material behavior and its associated variation can be described for use in robust optimization of forming processes.

The ultimate goal of robust optimization is the accurate prediction and reduction

*This chapter is based on: J.H. Wiebenga, E.H. Atzema, Y.G. An, H. Vegter and A.H. van den Boogaard. Effect of material scatter on the plastic behavior and stretchability in sheet metal forming. *Journal of Materials Processing Technology*, 214(2), 238-252, **2014**.

of the number of product rejects. This requires an accurate numerical prediction of both the mean of the response behavior and the magnitude of response scatter. It has been demonstrated by Atzema et al. [9] and discussed in Chapters 4 and 5 that for quantifying the number of product rejects, it is of no use to quantify the scatter accurately if the mean is off. In order to accurately simulate the effect of material property scatter, the variations and correlations in input variables must be represented with sufficient accuracy [8, 44, 96]. As a consequence, flexible but complex material relations (yield locus model and hardening model) with a large number of variables must be used. Therefore an efficient description of material properties and its associated variation is required.

In this chapter, a study is described demonstrating the effect of material property scatter on the plastic behavior and stretchability in sheet metal forming processes. An approach is presented to efficiently measure and accurately model material property scatter for use in FE simulations. Its effect on a metal forming process is demonstrated numerically and validated experimentally.

This chapter is organized as follows. Section 7.2 describes a hybrid approach for obtaining a stochastic set of material data. To limit the required effort for material characterization, the approach combines mechanical testing and texture analysis. In addition, the applied Vegter yield locus model and Bergström–van Liempt hardening model are briefly introduced. Section 7.3 describes the establishment of the data set, combining a Principal Component Analysis (PCA) with a screening step to manipulate the material data for efficient implementation in FE simulations. The approach and its resulting effect are subsequently demonstrated numerically and validated experimentally in Sections 7.4 and 7.5 on the cup-stretching process, as introduced in Section 6.6. A discussion is provided in Section 7.6. Finally, Section 7.7 will present the conclusions of this chapter.

7.2 Determination of material scatter

The scatter in material behavior is determined with a hybrid approach, combining mechanical testing and texture analysis. Fully determining the stochastic material behavior to the required accuracy by mechanical testing only, requires many expensive tests to obtain the material parameters for both the yield locus description (see Section 7.2.2) and hardening model (see Section 7.2.3). These required tests are discussed in more detail in [147, 148] and will be addressed in Section 7.2.1. Whereas this effort is acceptable in characterizing the (typical) behavior of a steel grade as applied before in Chapters 4 and 5, it

is prohibitively expensive for obtaining a statistical basis for robustness analysis since many coils have to be characterized. The required effort is minimized by replacing part of the mechanical testing by texture analysis as described next.

7.2.1 Material collection

For the purpose of this research, samples from 41 coils of a forming steel DX54D+Z (EN 10327:2004) from multiple casts have been collected to study coil-to-coil variation. The nominal thickness of the studied sheets is 0.79 mm, and measured thicknesses of the individual sheets are in the range of 0.75 mm - 0.83 mm. Moreover, from a single coil, 6 sheets have been collected to study in-coil variation. The DX54D+Z material, a low carbon continuously annealed hot dipped galvanized steel with EDT surface finish, is chosen because of its wide application in cold forming processes in the automotive industry.

Mechanical testing

For the full construction of the yield locus model used in this chapter (see Section 7.2.2), four types of mechanical tests are generally required: a uniaxial, an equi-biaxial, a plane strain tensile test and a shear test. Because of planar anisotropy, the tensile and plane strain tests are performed in three different directions 0°, 45° and 90° with respect to the Rolling Direction (RD). The latter direction is also referred to as Transverse Direction (TD). The shear tests are performed in the 0° and 45° direction only due to symmetry. The equi-biaxial test is direction independent and needs to be performed once.

For the entire material collective, tensile tests in three directions have been performed. This is feasible because the tensile test is highly standardized and efficient. The same holds for thickness measurements for all coils. However, the plane strain, shear and equi-biaxial tests are less common and require much more effort, hence these are not performed for the material collective.

Texture analysis

The stochastic material data for the yield locus construction is obtained by texture measurements onto the full material collective of coils. Using efficient Electron BackScatter Diffraction measurements in combination with polycrystal plasticity, a yield locus is constructed. The model used is proposed by An et al. in [6] and is based on two yield loci derived from the Taylor full constraint model and the

relaxed Pancake model, also referred to as Combined Taylor Full constraint and Pancake model, or CTFP.

7.2.2 Yield locus model

An accurate description of the yield locus and accompanying scatter is required as close to the CTFP derived yield loci as possible. Because of its excellent adaptability, the Vegter yield locus model [147, 148] is used. The parameters of the model are fitted to a few typical data points from the CTFP model. The yield locus in the plane stress and principal stress space (σ_1, σ_2) is explicitly described by a set of quadratic Bezier interpolations between pre-determined stress states, see Figure 7.1. The planar anisotropy is represented by allowing the Bezier interpolations to depend on the angle between the major principal stress and the RD by means of cosine interpolation. Generally, three directions are used to describe orthotropic material behavior resulting in a yield locus description defined by the following 14 parameters:

- Uniaxial stresses: $\sigma_{\text{un},0}$, $\sigma_{\text{un},45}$, $\sigma_{\text{un},90}$
- R-values: r_0, r_{45}, r_{90}
- Plane strain stresses: $\sigma_{\text{ps},0}$, $\sigma_{\text{ps},45}$, $\sigma_{\text{ps},90}$
- Shear stresses: $\sigma_{\text{sh},0}$, $\sigma_{\text{sh},45}$, $\sigma_{\text{sh},90}$
- Biaxial stress: σ_{bi}
- Biaxial R-value: r_{bi}

The results of tensile tests and texture measurements are combined by setting $\sigma_{\text{un},0}$ equal to the stress resulting from the tensile tests in RD. The remaining parameters can be derived from the texture analysis to obtain a full description of the stochastic material behavior. In a pure shear situation, a stress reversal will lead to an equivalent pure shear situation rotated by 90°, i.e. $\sigma_{\text{sh},0}$ equals $\sigma_{\text{sh},90}$. This leads to a total of 13 unique parameters describing the Vegter yield locus model for use in robustness analysis.

The resulting yield loci for the 41 measured coils are plotted in Figure 7.2a. Both the size and shape of the yield loci show variation for different coils. It will be demonstrated in Section 7.6 that a flexible yield locus description is required for an accurate prediction of the mean performance and the response scatter. For the product considered in this chapter, it is determined that especially the accurate

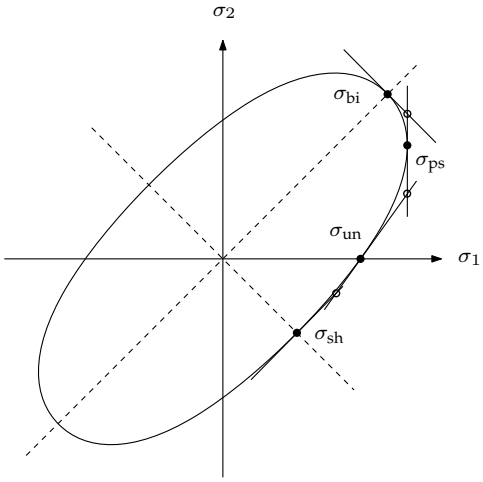

Figure 7.1 *Vegter yield locus points*

description by the Vegter model of the location and scatter of the plane strain point and the biaxial point as measured is important in robustness analysis. This is because the strain distribution in the considered product is very sensitive to these values. Figure 7.3 shows detail plots of yield loci scatter for 2 selected combinations of 2 coils, taken from the collective of 41 materials. It shows both scatter of size and shape of the measured yield loci. Note in Figure 7.3a how two materials can, for example, have identical values for σ_{bi} and have deviating values for $\sigma_{ps,0}$. In Figure 7.3b crossing of yield loci can be observed.

7.2.3 Hardening model

Isotropic hardening is assumed with a Bergström relation (σ_{wh}) [16], extended with the effect of strain rate and temperature (σ_{dyn}) [73, 146]:

$$\sigma_y = \sigma_{wh} + \sigma_{dyn} \tag{7.1}$$

where

$$\sigma_{wh} = \sigma_0 + \Delta\sigma_m \left[\beta \left(\varepsilon + \varepsilon_0 \right) + \left(1 - e^{-\Omega(\varepsilon+\varepsilon_0)} \right)^n \right] \tag{7.2}$$

Term	static	hardening				
Parameter	σ_0	$\Delta\sigma_\mathrm{m}$	β	Ω	ε_0	n
Value	130 MPa	230 MPa	**0.5**	7.2	**0.005**	**0.75**

Term	strain rate				
Parameter	σ_0^*	ΔG_0	m	$\dot{\varepsilon}_0$	T
Value	**600** MPa	**0.8** eV	**2.2**	$\mathbf{10^8}$ s^{-1}	**300** K

Table 7.1 *Nominal Bergström–van Liempt hardening law input parameters for deep drawing steel DX54D+Z*

And

$$\sigma_\mathrm{dyn} = \sigma_0^* \left[1 + \frac{kT}{\Delta G_0} \ln\left(\frac{\dot{\varepsilon}}{\dot{\varepsilon}_0}\right)\right]^m \tag{7.3}$$

The hardening model parameters are determined by fitting the stress–strain curves resulting from the tensile tests in RD. The resulting parameters and their values are summarized in Table 7.1. Although this relation has many parameters, many of these parameters are (near) constant for low carbon steels such as the considered DX54D+Z material. As a result, the flow stress (σ_y) becomes a function of 3 parameters, i.e. the initial static stress (σ_0), stress increment parameter ($\Delta\sigma_\mathrm{m}$) and the remobilization parameter (Ω). The properties that are assumed constant are printed bold in Table 7.1. Note that the dynamic term is set constant, i.e. no variation of the strain rate sensitivity is taken into account. The resulting hardening curves for the 41 measured coils are plotted in Figure 7.2b. Implementation of the yield locus and hardening models in an FE model will allow for prediction of local necking in relation to material property scatter. The onset of local necking will be used in this chapter to numerically predict product failure.

7.3 Data set establishment

The current data set contains 41 parameter sets, a single parameter set for each coil measured. Each parameter set consists of 17 parameters, i.e. 13 parameters describing the yield locus, 3 parameters describing the hardening behavior and a parameter describing the material thickness. Additional parameter sets are determined for the 6 sheets taken from a single coil. The material thickness is

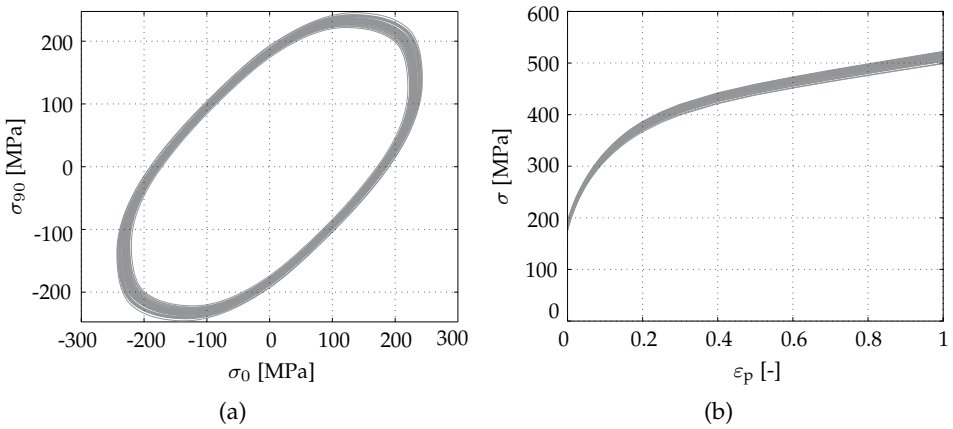

Figure 7.2 *(a) Yield loci and (b) hardening curves for 41 coils of a forming steel DX54D+Z*

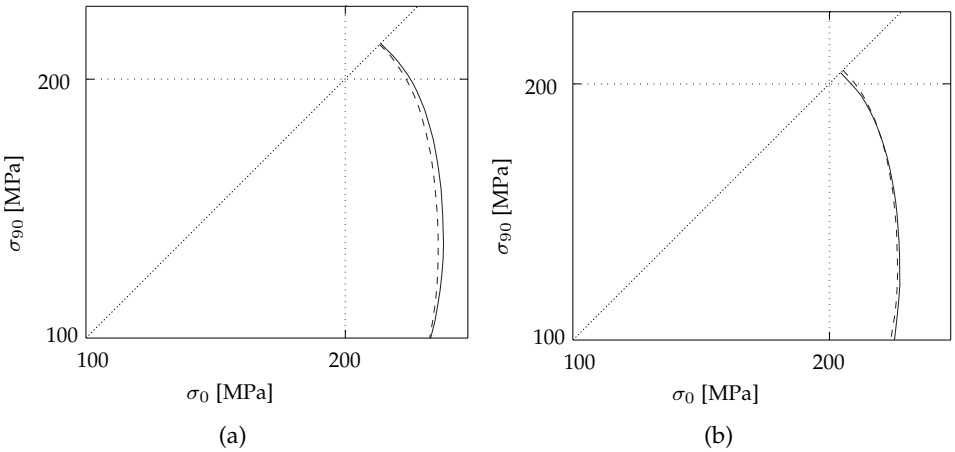

Figure 7.3 *Detail plots of yield loci size and shape scatter for 2 selected combinations of 2 coils of a forming steel DX54D+Z*

included in these data sets to evaluate possible correlations with the remaining mechanical properties which cannot be ruled out from a steel production point of view. All materials originate from a cast slab with a similar thickness, so a thinner material will have a higher rolling reduction. For Interstitial Free (IF) steels, such as the DX54 material employed here, it is known that the development of the favorable texture is sensitive to cold rolling reduction [113]. Before proceeding to define a stochastic description of material property scatter for the whole material collective in Section 7.3.2, the measured material property scatter and correlations are evaluated in more detail in Section 7.3.1.

7.3.1 Measured data scatter and correlations

The measured material property scatter and correlations for the 41 parameter sets are presented in Figure 7.4. The 17 parameters of the yield locus model, hardening model and material thickness (t) are displayed on the horizontal and vertical axis. On the diagonal, a histogram is depicted showing the distribution of the measured data per parameter. For all parameters, the overall distribution can be described accurately by a normal distribution represented by the red line and evaluated by the *Anderson–Darling test* [7]. The scatter plots in the top triangle show the mutual scatter data for 2 different material parameters, where the color of the scatter plots corresponds to the magnitude of correlation coefficients defined by Equation (A.11).

The bottom triangle shows the mutual linear correlation coefficients for different material parameters, calculated according to Equation (A.11). Evaluating Figure 7.4 in detail, strong correlations are observed between the individual stresses and weak correlations are observed between the individual R-values. Weak correlations are found between the R-values and all remaining variables. The same holds for the material thickness (t), i.e. the expected correlation between material thickness and the remaining mechanical properties is not observed in the data set. Medium correlations are observed between the stress increment parameter ($\Delta\sigma_\mathrm{m}$) and the remaining parameters, except for the R-values. The resulting yield loci and hardening curves for the 41 parameter sets are plotted in Figure 7.2.

7.3.2 Principal component analysis

The goal in this chapter is to describe material scatter for the material delivered as DX54D+Z, not just treating the 41 coils individually. The resulting stochastic description of material scatter for the whole material collective must include the

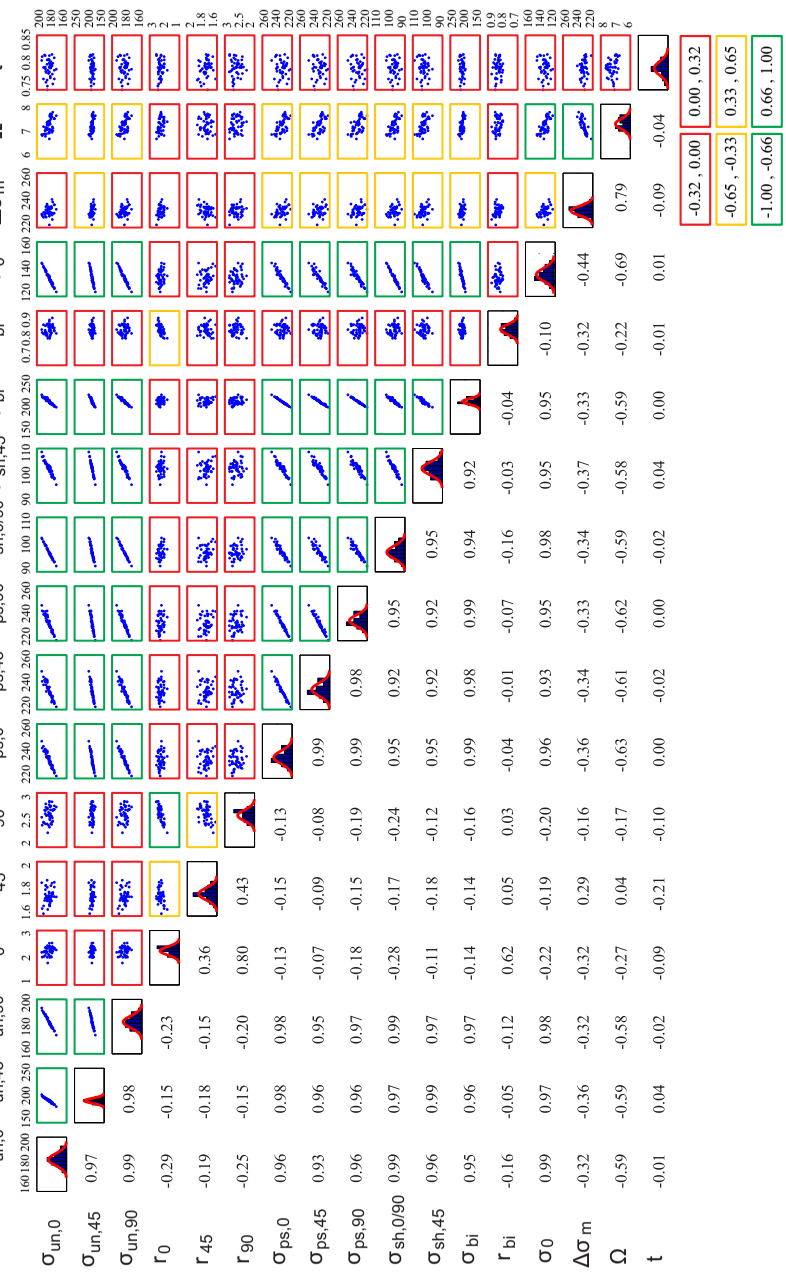

Figure 7.4 *Measured material property scatter and correlations for DX54D+Z*

mean values, the variation and correlations. Additionally, the description should be both accurate and efficient for the subsequent use in FE simulations, enabling determination of a collective effect of material scatter in robustness analysis. To establish a collective data set, a Principal Component Analysis (PCA) is utilized [1, 130]. The goal of a PCA is to identify the most meaningful basis to re-express a data set. Moreover, it will be used in this chapter for reducing the number of parameters to be included in the numerical study by combining it with a screening step.

The PCA procedure uses orthogonal transformation to convert a set of observations of possibly correlated material parameters into a set of linearly uncorrelated parameters called Principal Components (PCs). The PCs are ordered in decreasing variance, i.e. the first PC has the largest variance and the last PC has the smallest variance. The data set to be analyzed by the PCA comprises n measurements of m material parameters and is represented by the $m \times n$ matrix $\mathbf{X}$. In the current example, $m = 17$ and $n = 41$. The data set is first adjusted by subtracting the mean of the material parameters and dividing each element of $\mathbf{X}$ by $\sqrt{n}$. The resulting matrix $\mathbf{X}\mathbf{X}^{\mathrm{T}}$ is the covariance matrix $\mathbf{C}_{\mathrm{X}}$, an $m \times m$ positive semidefinite symmetric matrix of which the diagonal terms represent the variances of the material parameters. The off-diagonal terms are the covariance values representing the degree of linear relationship between parameters, see Equation (A.10). In addition to subtracting the mean of the data set, it is customary to scale the parameters by dividing each parameter by its norm [1].

In the PCA, an eigen-decomposition of the covariance matrix $\mathbf{C}_{\mathrm{X}}$ is performed:

$$\mathbf{C}_{\mathrm{X}}\mathbf{V} = \mathbf{V}\mathbf{\Lambda} \tag{7.4}$$

where $\mathbf{\Lambda}$ is a diagonal matrix with the eigenvalues λ_i on the diagonal. The λ_i's are hereby placed in descending order. $\mathbf{V}$ is a matrix built up out of the eigenvectors of $\mathbf{C}_{\mathrm{X}}$ corresponding to the λ_i's, i.e. $\mathbf{V} = \{\mathbf{v}_1, \mathbf{v}_2, \ldots, \mathbf{v}_m\}$. Next, a transformation matrix $\mathbf{P}$ is defined. $\mathbf{P}$ is an $m \times m$ linear transformation matrix that re-expresses $\mathbf{X}$ into a new data set $\mathbf{Y}$. In the PCA procedure, it is customary to define a transformation matrix $\mathbf{P}$ with eigenvectors in its rows, hence $\mathbf{P} = \mathbf{V}^{\mathrm{T}}$. The resulting ordered set of basis vectors are the PCs of $\mathbf{X}$. Equation (7.4) can now be written as:

$$\mathbf{C}_{\mathrm{X}}\mathbf{P}^{\mathrm{T}} = \mathbf{P}^{\mathrm{T}}\mathbf{\Lambda} \tag{7.5}$$

Premultiplication of Equation (7.5) with $\mathbf{P}$ and using $\mathbf{C}_\mathrm{X} = \mathbf{X}\mathbf{X}^\mathrm{T}$ yields:

$$\mathbf{P}\mathbf{X}\mathbf{X}^\mathrm{T}\mathbf{P}^\mathrm{T} = \mathbf{\Lambda} \tag{7.6}$$

With $\mathbf{Y} = \mathbf{P}\mathbf{X}$, where $\mathbf{Y}$ is the new representation of the data set in terms of PCs, Equation (7.6) can be written as:

$$\mathbf{Y}\mathbf{Y}^\mathrm{T} = \mathbf{\Lambda} \tag{7.7}$$

From Equation (7.7) it becomes clear that the new data set $\mathbf{Y}$ is uncorrelated. The covariance matrix $\mathbf{C}_\mathrm{Y} = \mathbf{Y}\mathbf{Y}^\mathrm{T}$ is a diagonal matrix where the i^th diagonal value is the variance ($\sigma^2_{\mathrm{PC}i}$) along the i^th PC of $\mathbf{X}$.

A schematic overview of the PCA procedure, considering two example material parameters referred to as x_1 and x_2, is presented in Figure 7.5. The orthogonal transformation is represented in Figure 7.5 by steps 1–2. The uncorrelated new representation of the data set is convenient for combined usage of the PCA and a DOE in the PC domain, see steps 2–3 in Figure 7.5. Since the λ_i's are placed in descending order, each successive dimension in $\mathbf{Y}$ is rank-ordered according to variance. That is, the first dimension of the new basis aligns with the axis in the original data set in which the largest amount of scatter is observed. The sampling domain for the DOE is chosen to be limited to $\pm 2\sigma_\mathrm{PC}$, knowing that the data set is jointly normally distributed as evaluated by the *Mardia's test* [90]. The back transformation to the physical parameter domain automatically includes all correlations present in the original data set, see steps 3–4 in Figure 7.5. This combined PCA and DOE approach prevents the sampling of physically unlikely parameter combinations, avoiding possible overestimation of the output scatter in the robustness analysis. The latter statement will be supported with an example in Section 7.6.

7.3.3 Variable screening

Using all 17 PCs in the DOE procedure would result in a significant number of FE simulations to be run in the robustness study. As an example, performing simulations at all corner points of the 17-dimensional design space using an FFD would require 2^{17} = 131072 FE simulations. Dimensionality reduction is therefore required to improve the efficiency of the approach. In some cases, the PCA property of rank-ordering the PCs according to variance is used for

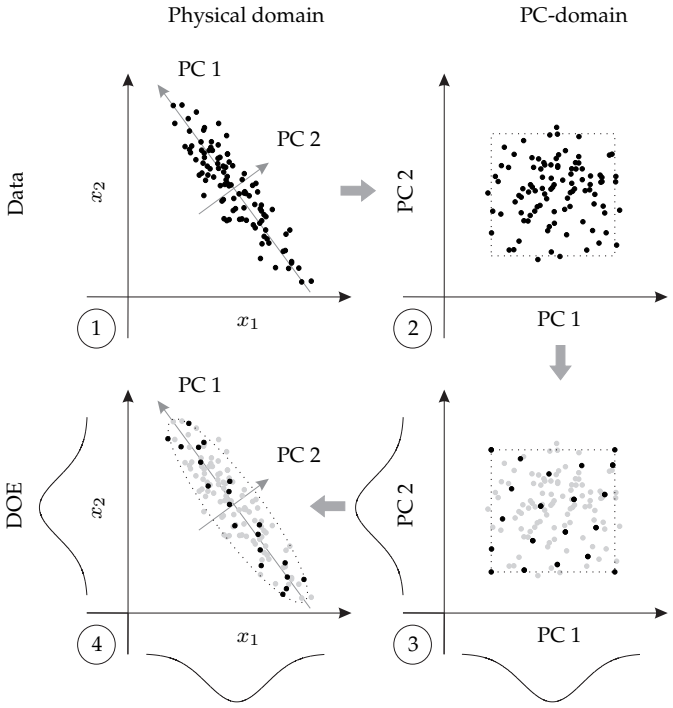

Figure 7.5 *Schematic of the Principal Component Analysis*

dimensionality reduction. Since the majority of variance of the original data set is described by the lower rank PCs, it is reasoned that dropping the higher rank PCs results in a minimal loss of information. This implicitly assumes that the numerical response is equally sensitive to all PCs, so the largest input variance governs the largest output scatter, which as a rule is not the case. This was also concluded by Atzema et al. [10] and will be demonstrated for the cup stretching application in Section 7.4. Instead, the PCA approach is combined with a screening step for dimensionality reduction. In this case, the selection of PCs is based on the sensitivity of the numerical response to each PC. This will be described in more detail and demonstrated in Section 7.4.3.

7.4 Application to a cup-stretching process

The proposed approach is validated by application to the hemispherical cup-stretching process as introduced in Section 6.6. The goal of the numerical study is to reproduce the observed experimental scatter in the forming of 41 cups.

(a) (b)

Figure 7.6 *(a) Considered hemispherical cup (height: 44 mm, blank radius: 100 mm) and (b) detail showing the location of fracture*

7.4.1 Experimental procedure

An impression of the considered hemispherical cup is given in Figure 7.6. The 41 products are formed out of circular 100 mm radius blanks with a nominal thickness of 0.79 mm. The experiments are performed using an Erichsen universal sheet metal testing machine where the blank holder force is set to 350 kN. Tooling with a punch diameter of 100 mm, a die cavity diameter of 105 mm and a die shoulder radius of 8 mm is used. To reduce friction, Teflon foils are used between the blank and punch. No additional lubrication has been used.

The fully clamped blanks are stretched by a prescribed punch displacement at a velocity of 1.5 mm/s. The strains are evaluated on-line using Digital Image Correlation (DIC) measurements. Figure 7.7 shows a typical major strain distribution at the top of the dome just before fracture (44 mm). Initially, equi-biaxial stretching is found on the pole of the dome. At a product height of approximately 38–40 mm, significant plane strain deformation is found near the die shoulder. Further increasing the cup height to approximately 42–44 mm finally results in necking and fracture at this location as shown in Figure 7.6b. The maximum major strain and corresponding minor strain in RD and TD are recorded at product heights of 38 mm, 40 mm, 42 mm and 44 mm. Strain measurements in the diagonal direction (45° with respect to the RD) were not adequate due to the limited evaluation area of the DIC measurements from the top of the dome, as shown in Figure 7.7. Finally, the punch force is recorded as a function of its displacement.

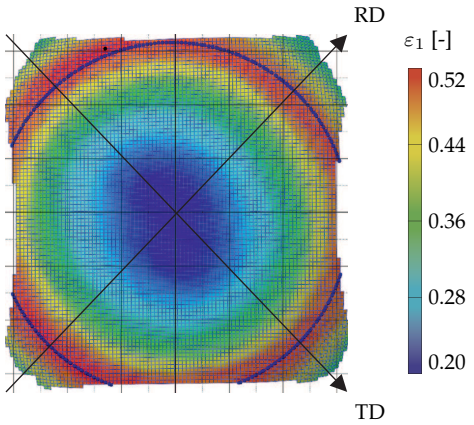

Figure 7.7 *Typical major strain distribution at the top of the dome just before fracture (44 mm), obtained by Digital Image Correlation (DIC) measurements*

7.4.2 Numerical robustness analysis

An impression of the FE model of the stretching process is given in Figure 6.13. As already introduced in Section 6.6, the simulations are performed in the FE code DIEKA [29]. The circular blank is discretized using triangular discrete Kirchhoff shell elements with 5 integration points through thickness. A friction coefficient of 0.14 is utilized to obtain an accurate numerical prediction of the experimentally obtained force–displacement curve, location of fracture and magnitude of the maximum major strain and corresponding minor strain.

7.4.3 Variable screening

Before proceeding to the experimental and numerical results of the robustness study in Section 7.5, a screening step is performed in combination with the PCA approach for dimensionality reduction. A PC is built up out of the individual contributions of all 17 material parameters. The magnitude of the contribution depends on the direction of greatest scatter and the correlation between material parameters. In the PCA, uncorrelated material parameters such as the material thickness will only make a significant contribution to a few PCs. Correlated material parameters, such as stresses, will appear combined in multiple PCs. Using a single PC that includes a major contribution of such a group of correlated parameters allows efficient modeling of the majority of correlated scatter for this group of parameters, enabling the description of e.g. yield locus shape and size scatter using a small number of PCs. If one would resort to physical parameters,

the choice of how to model such a correlated set of material parameters would be left to the user. The next step is to achieve dimensionality reduction based on response sensitivity with respect to the PCs. Each of the 17 PCs will influence each of the following 5 numerical responses to a different extent:

- Major strain (ε_1) in RD and TD
- Minor strain (ε_2) in RD and TD
- Maximum force ($F_{\max}$)

The screening techniques as described below deviate from the analysis as described in Section 3.3 since the PCs are uncorrelated. As a result, the individual effect of each PC on the numerical responses can be determined using a face centered cubic DOE. For this design, the DOE points are located at the center of each face of the design space. In other words, this requires 2 levels of each PC to be evaluated, i.e. $\pm 2\sigma_{\text{PC}}$. This results in a total number of 34 required simulations. The individual effect of each PC on the numerical responses over the full $\pm 2\sigma_{\text{PC}}$ domain is determined and visualized using Pareto plots. In addition, a single FE simulation can be performed at the mean of all noise variables to determine the monotonicity of the responses. Figure 7.8 presents the Pareto plots for the strain responses and the maximum force response as a function of the 17 PCs. The height of the bars in a Pareto plot denotes the magnitude of the effect contributed by each PC. The PCs are sorted based on the magnitude of the effect, from most important to least important. Additionally, the cumulative effect (solid line) is plotted which can be used to determine how many PCs should be taken into account to ensure e.g. 80% control over a response.

Evaluating Figure 7.8 in detail, it is observed that different responses are most significantly influenced by different PCs. Moreover, it is observed that the responses are not per definition most significantly influenced by the PCs having the largest variance. In fact, for controlling the minor strain responses, at least PC numbers 3, 7, 9 and 11 should be included. For controlling the maximum force response, at least PC numbers 5, 6 and 7 should be included. For controlling the major strain response, at least PC numbers 1, 9 and 11 should be included. Finally, following the Pareto principal, combining these 7 PCs (see the dark gray bars in Figure 7.8) ensures 80% of control over all numerical responses .

For the considered responses of the cup stretching application using the forming steel DX54D+Z, it is determined that PC numbers 1, 3, 5, 6, 7, 9 and 11 should be taken into account in the robustness analysis. This results in a significant reduction of dimension from 17 to 7 parameters. Using the remaining 7 PCs,

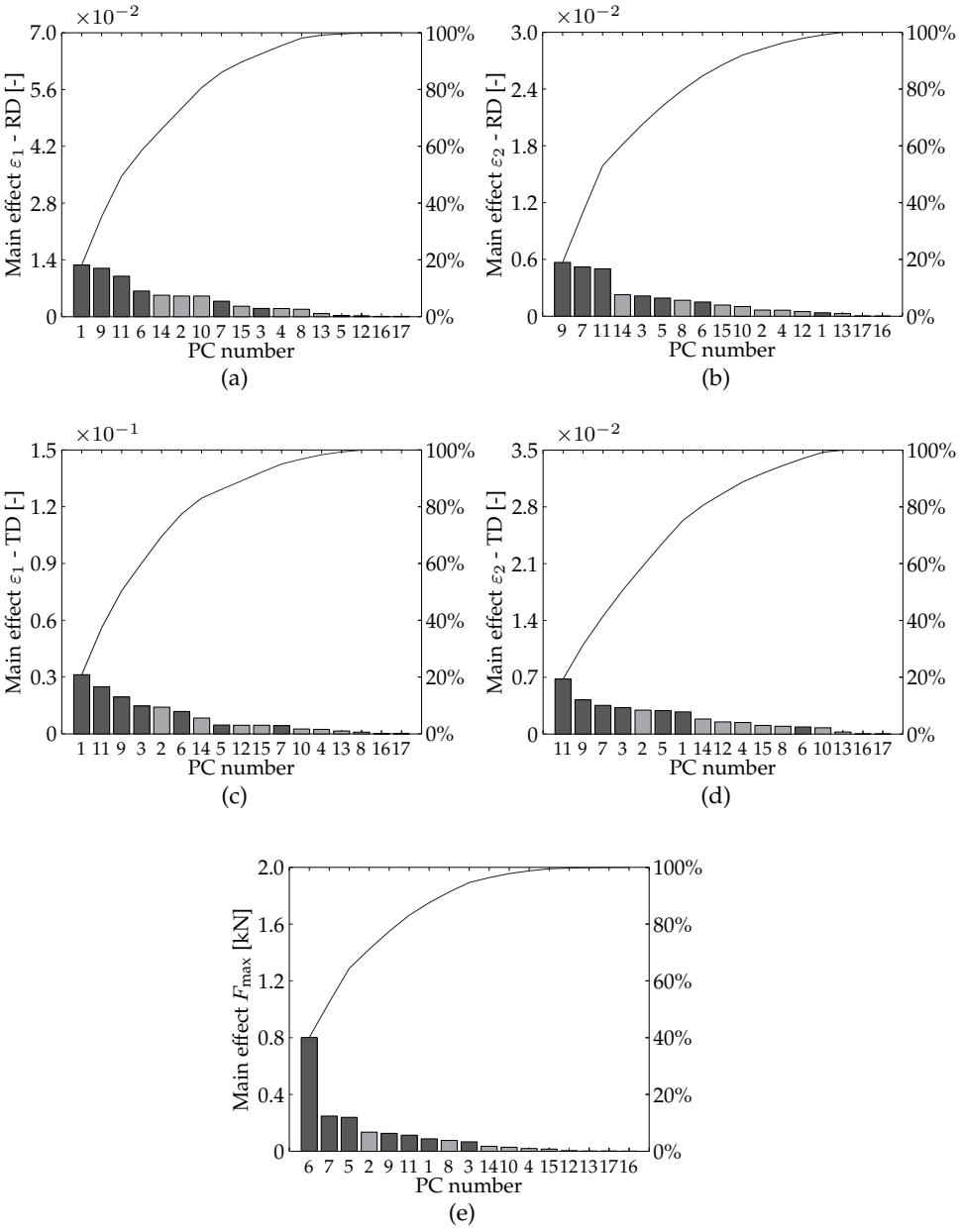

Figure 7.8 *Pareto plots of the (a-d) major and minor strain in RD and TD and (e) maximum force (F_{max})*

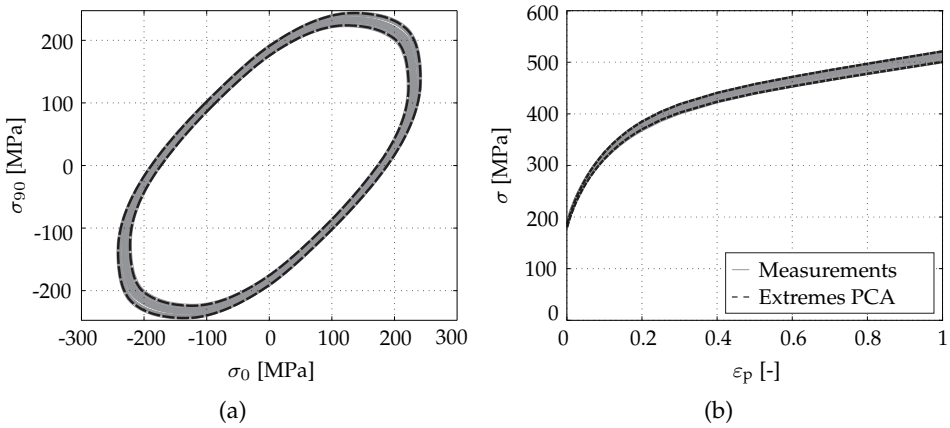

Figure 7.9 *(a) Yield loci and (b) hardening curves as measured for DX54D+Z and modeled (extremes) through the PCA approach*

an LHD of 70 DOE points is generated. Similar to Figure 7.2, the yield loci and hardening curves for the 41 measured coils are plotted in Figure 7.9. The dashed lines in Figure 7.9 show the 2 extreme yield loci and hardening curves out of the 70 LHD generations. The remaining 68 yield loci and hardening curves all fall in between these extremes. From this, it can be concluded that the experimentally measured range of scatter in yield locus and hardening behavior is well represented by the 70 parameter sets. Note that by modeling the correlated scatter in all 13 yield locus parameters, both yield locus size and shape scatter is captured in the 70 parameter sets. As a result of combining the PCA approach with variable screening, an efficient stochastic description of material scatter for the material delivered as DX54D+Z is obtained.

7.5 Results

7.5.1 Experimental results

The experimentally obtained maximum major strain and corresponding minor strain results in RD and TD are presented in Figures 7.10a and 7.10b respectively. The 4 'clouds' of green circle markers represent the 41 strain measurements at different product heights, ranging from 38 mm (bottom cloud) to 44 mm (top cloud). A total of 34 out of the 41 cups show fracture before a product height of 44 mm is reached. At a cup height of 42 mm, almost all the strain points

have exceeded the FLC, although a further height increase before fatal necking (observable as a force drop) is still possible. More importantly, even at a draw depth of 38 mm the typical material shows violation of the 10% strain safety margin below the FLC, whereas even with scatter added all materials achieve a height of 40 mm without onset of necking. As mentioned in the introduction of this chapter, the usage of a safety margin such as 10% strain below the FLC clearly does not make optimal use of the material. Also, the location of the FLC is conservative with respect to the experimental outcomes. Note how the influence of material property scatter increases for increasing product height, resulting in an increased strain scatter. Comparing the results in RD (Figure 7.10a) and TD (Figure 7.10b), products show slightly higher deformation in TD. This brings the material closer to the critical state, which can explain the increased scatter in TD direction. This corresponds to the direction in which the majority of products show fracture initiation in the experiments.

In addition, the gray square markers in Figure 7.10 represent strain measurements for the 6 in-coil sheets. The material properties of these consecutive sheets are approximately similar to each other. Next to strain scatter caused by in-coil variation, one could thus also reason that part of the scatter observed in Figure 7.10 is caused by process scatter and measurement errors, inevitably present in the data. Nonetheless, the amount of strain scatter caused by in-coil variation is less compared to the strain scatter caused by coil-to-coil variation. Also for in-coil variation, products show slightly higher deformation and increased scatter in TD direction. Finally, it is observed that the specific coil, from which the 6 sheets are collected, is a relatively highly formable material compared to the full collective of materials, since 4 out of 6 products can be stretched up to a height of 44 mm without fracture.

A global plot and detailed plot of the experimentally obtained force–displacement curves is given in Figure 7.11a and Figure 7.11b respectively. The experimental procedure is automatically terminated if a force drop is recorded. The maximum force shows a variation of approximately 7 kN at the point of product failure. The black lines show the force–displacement curves for the 6 in-coil sheets. Similar to the strain measurements, less response scatter is observed as a result of in-coil variation.

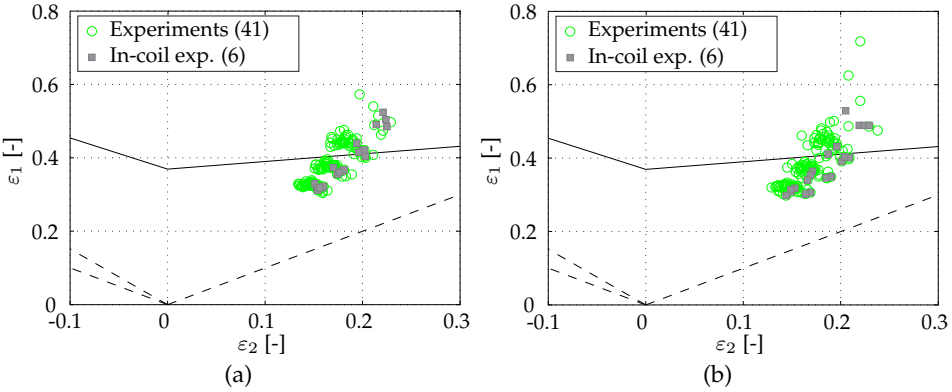

Figure 7.10 *Experimental strain scatter in cup stretching as a function of the product height (38, 40, 42 and 44 mm) in (a) RD and (b) TD*

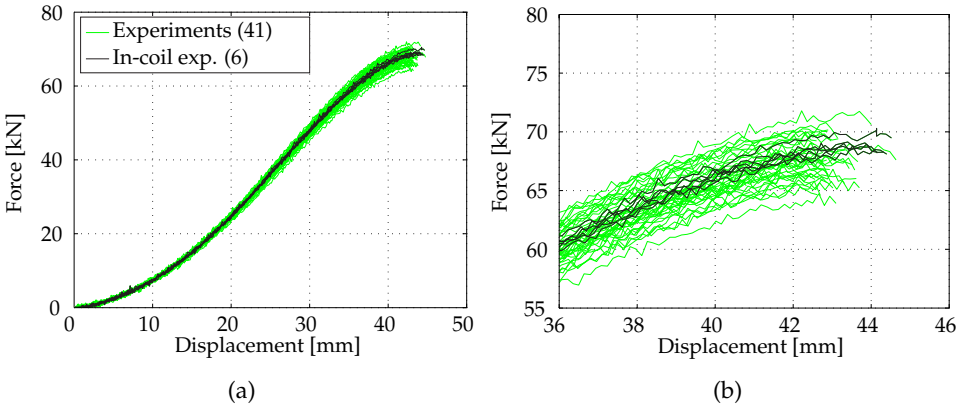

Figure 7.11 *(a) Global plot and (b) detail plot of the experimental force–displacement curves for the cup stretching process*

7.5.2 Numerical results

For the purpose of this research, several parameter sets are evaluated:

- 41 coil-to-coil parameter sets obtained from the hybrid testing procedure
- 6 in-coil parameter sets obtained from the hybrid testing procedure
- 70 parameter sets obtained from the PCA approach

In addition, a metamodel approximation is created based on the PCA parameter sets. To include the effect of material scatter in the robust optimization strategy, a coupling with the PCA approach is presented.

Direct simulations

The numerical prediction of the strain scatter for the set of 41 coil-to-coil and 6 in-coil parameter sets, obtained directly from the hybrid testing procedure, is presented in Figure 7.12. These numerical results are referred to as direct simulations. Starting with a comparison of the 41 parameter sets to the experimental results, a small offset in nominal strain results is present. Nonetheless, the strain scatter is predicted accurately, keeping in mind that a part of the experimental strain scatter can be attributed to process scatter and small errors possibly present in the (DIC) measurements. Also, the increase in strain scatter as a function of the product height is predicted numerically. At a product height of 44 mm, severe local necking is predicted in TD. This is in agreement with the experimental results showing fracture initiation in this direction. Looking at the numerical strain predictions for the 6 in-coil parameter sets, minimal response scatter is predicted in RD, slightly increasing in TD. This corresponds with the experimental observations.

Figure 7.13 shows a comparison of the experimentally measured force–displacement data and the numerical prediction of the direct simulations. The numerical results in Figure 7.13 show a good overall correspondence of the experimentally obtained force levels. The force scatter is dominated by scatter in material thickness. The maximum force scatter is slightly overestimated, mainly by the three highest predicted curves which result from the simulations with the highest material thickness. The detailed plot shows the force–displacement data at maximum product height. The onset of local necking, represented by the force drop, is well predicted numerically. Note that the experimental procedure is terminated if a force drop is recorded whereas the simulations run up to 44 mm. Also, the minimal force scatter for the 6 in-coil parameter sets corresponds with the experimental observations.

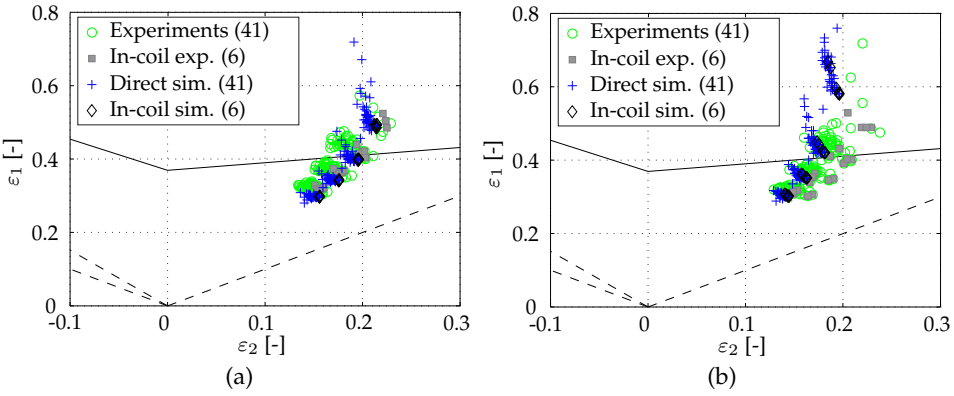

Figure 7.12 *Numerical prediction of strain scatter in cup stretching resulting from the direct simulations as a function of the product height (38, 40, 42 and 44 mm) in (a) RD and (b) TD*

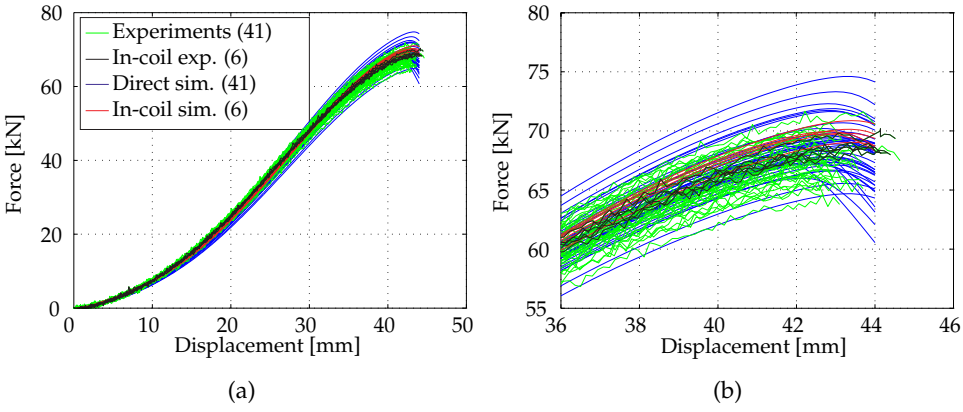

Figure 7.13 *(a) Global plot and (b) detailed plot of the experimental and numerically predicted force–displacement curves resulting from the direct simulations for the cup stretching process*

PCA approach

The numerical prediction of strain scatter for the 41 direct simulations and the set of 70 parameter sets obtained from the PCA approach is presented in Figure 7.14. Comparing both sets, a good correspondence of both the magnitude of major and minor strain and amount of strain scatter is obtained. Figure 7.15 shows a comparison of the experimentally measured force–displacement data and the numerical prediction of the direct simulations and the PCA approach. A good overall correspondence of both the force level, the force scatter and the onset of local necking is observed with the experiments. Following the PCA approach and using only 7 PCs, an accurate and efficient stochastic description of material scatter for the material collective is obtained.

Metamodel approximation

Based on the 70 simulations performed in the PCA approach, a metamodel is built in the design space spanned by the 7 PCs. A quadratic RSM model is used to describe the relation between the 7 PCs and each response function. By subsequently running an MCA of e.g. 500 function evaluations on the metamodel within the PCs ranges, a prediction of the robustness is obtained.

The metamodel prediction of strain scatter is presented in Figure 7.16. Similar to previous numerical results, a small offset in nominal strain results is present compared to the experimental measurements. Nonetheless, the strain scatter is predicted accurately by combining the metamodels with an MCA. Compared to the PCA approach, the strain scatter increases. This can be explained by the MCA sampling since the set of 500 samples contains more extreme material parameter settings compared to the 70 LHD points. Using this robustness prediction, one can include these metamodels in the robust optimization strategy of Chapter 3. Note that this approach also allows for creating metamodels based on both design variables, such as the blank holder force, and scattering variables by using the collective description of material scatter. Treating the 41 coils individually would require evaluation of the 41 parameter sets at each setting of a design variable by FE simulations, resulting in an inefficient procedure for taking into account the influence of material scatter in robust optimization.

7.5.3 Critical area identification

Finally, Figure 7.17 shows the relative influence of material property variation on the product's major strain scatter at 40 mm, 42 mm and 44 mm. The figures

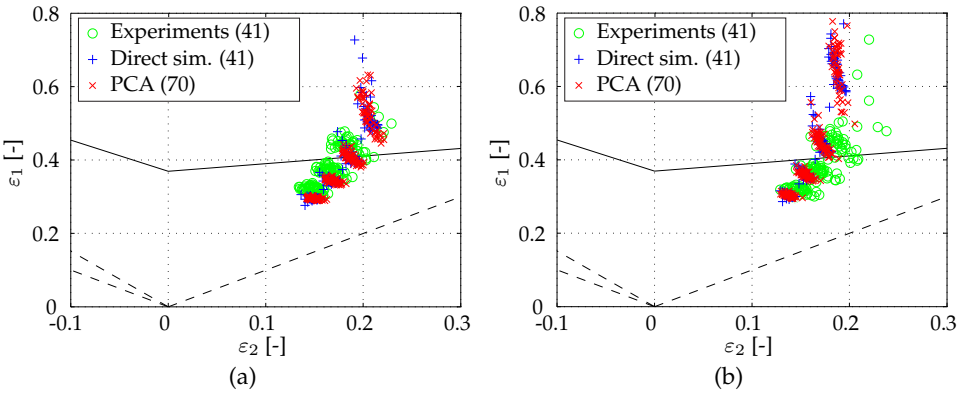

Figure 7.14 *Numerical prediction of strain scatter in cup stretching resulting from the direct simulations and PCA approach as a function of the product height (38, 40, 42 and 44 mm) in (a) RD and (b) TD*

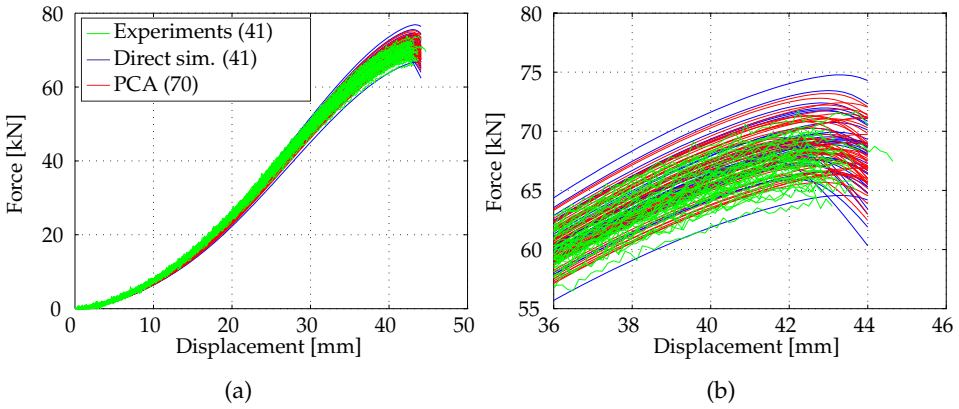

Figure 7.15 *(a) Global plot and (b) detailed plot of the experimental and numerically predicted force–displacement curves resulting from the direct simulations and PCA approach for the cup stretching process*

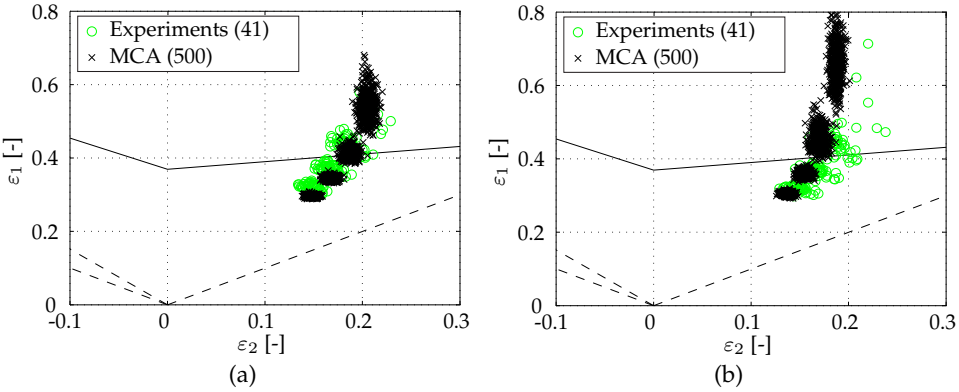

Figure 7.16 *Numerical prediction of strain scatter in cup stretching resulting from the metamodel prediction as a function of the product height (38, 40, 42 and 44 mm) in (a) RD and (b) TD*

are obtained by evaluating the major strain predictions at the nodes for the 70 simulations obtained from the PCA approach. The relative influence of material property variation for the considered material on the major strain can now be visualized by plotting the strain scatter at each node in terms of the standard deviation. Clearly, the sensitivity of the product to the input variation differs locally. The critical region for this product in TD direction can be recognized at 42 mm.

Next to the location of fracture with respect to the materials RD, the radius of fracture can also be evaluated. The radius of fracture is defined as the distance from the center line of the product to the location at which the maximum major

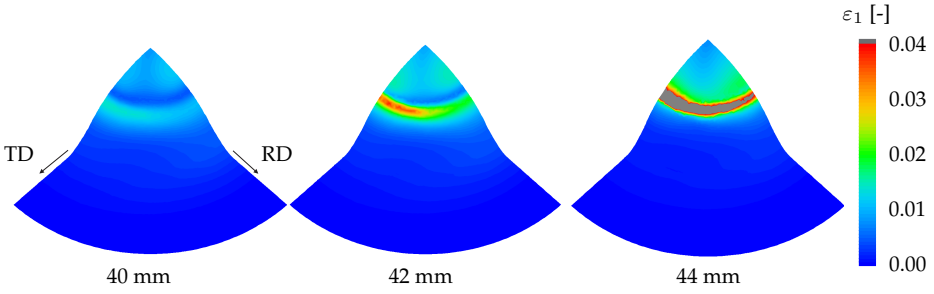

Figure 7.17 *Relative influence of material property variation on the products major strain scatter (in terms of the standard deviation) in cup stretching at 40 mm, 42 mm and 44 mm*

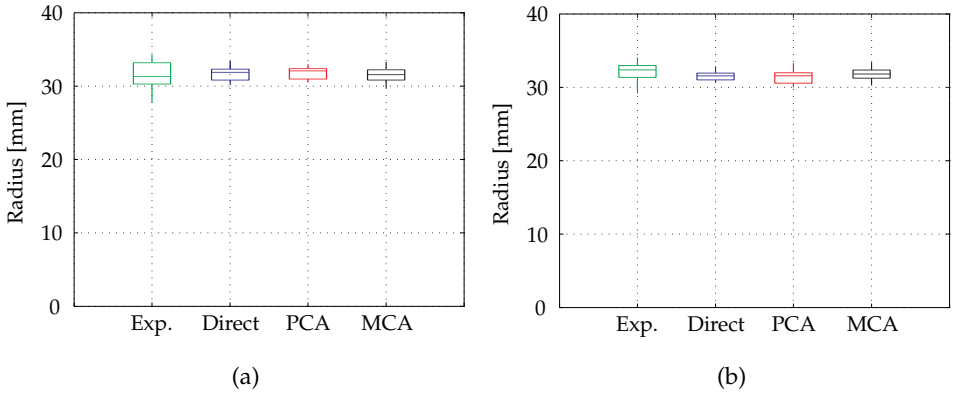

Figure 7.18 *Box plots of experimentally measured and numerically predicted radius of fracture in cup stretching in (a) RD and (b) TD*

strain is recorded. Box plots of the experimentally measured and numerically predicted radius of fracture in RD and TD are provided in Figure 7.18. Overall, the mean radius of fracture is predicted accurately by all numerical approaches compared to the experimentally measured radii. The scatter of the radius of fracture is slightly underestimated numerically. As already mentioned before, part of the experimental strain scatter can be attributed to process scatter and small errors possibly present in the (DIC) measurements. Moreover, it is observed that the numerical prediction of the location of maximum major strain is dependent on the numerical mesh. That is, since strains are evaluated at the nodes, also the scatter in the radius of fracture will be dominated by the distance between nodes. This is another example of numerical noise, as extensively discussed in Chapter 6.

7.6 Discussion

It is mentioned in Section 7.3.2 that the combined PCA and DOE approach prevents the sampling of physically unlikely parameter combinations, preventing possible overestimation of the output scatter in the robustness analysis. To support this statement, an additional robustness analysis is performed in which the correlation between the 17 material parameters is neglected. An uncorrelated LHD of 40 points is constructed in the $\pm 2\sigma$ domain. The results with respect to the strain scatter are presented in Figure 7.19, indeed demonstrating the severe overestimation of output scatter when neglecting the correlations between

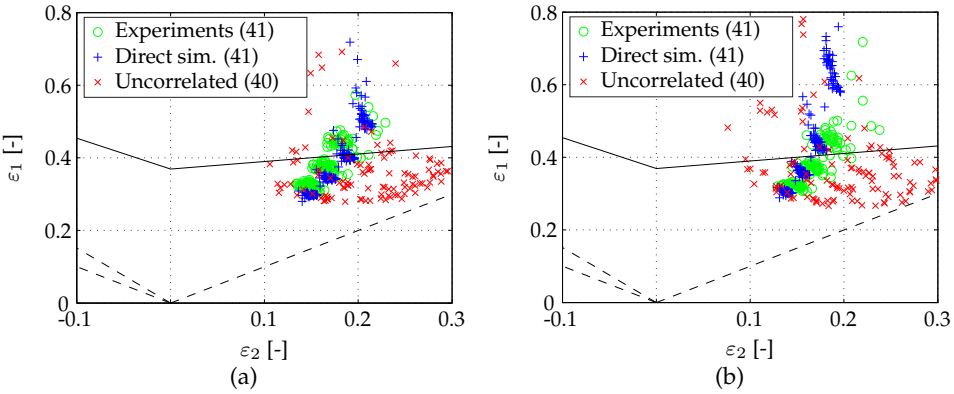

Figure 7.19 *Numerical prediction of strain scatter in cup stretching resulting from the direct simulations and uncorrelated approach as a function of the product height (38, 40, 42 and 44 mm) in (a) RD and (b) TD*

material parameters.

From a steel making point of view, it would be interesting to determine which material parameter is causing the output scatter. However, it is not possible to relate output scatter to a single material parameter if parameters are highly correlated (as for the yielding and hardening behavior). Using the PCA, it is demonstrated that depending on the response of interest in the robustness study, different groups of correlated scattering material parameters are of importance, not the individual magnitude of parameter scatter. Moreover, adaptable material models are required for accurately modeling the measured material behavior. To support this statement, an analysis is performed using the Vegter yield locus model, but only allowing for size scatter and eliminating the effect of shape scatter. This is achieved by assuming a full correlation for all stress components and setting the R-values constant at the average value for each component measured for the full material collective. As a result, material scatter can be described by a single stress component for the yield locus scatter (e.g. $\sigma_{\text{un},0}$), the hardening model parameters ($\Delta\sigma_m$, Ω) and the material thickness (t). For these 4 parameters, a correlated LHD of 40 points is constructed within the $\pm 2\sigma$ domain as applied before. The results for this simplified approach with respect to the strain scatter are presented in Figure 7.20. It shows the significant underestimation of strain scatter in comparison to both the direct simulations and the experimentally obtained results. Clearly, one is unable to accurately describe the experimentally observed strain scatter in both cases,

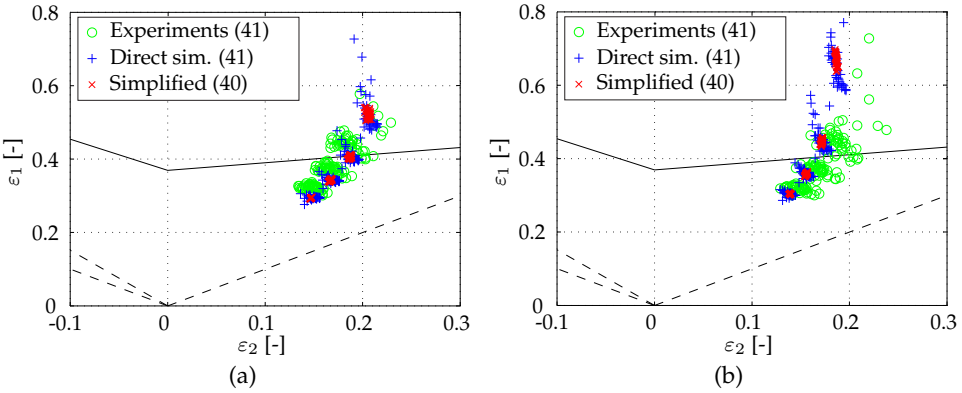

Figure 7.20 *Numerical prediction of strain scatter in cup stretching resulting from the direct simulations and simplified approach as a function of the product height (38, 40, 42 and 44 mm) in (a) RD and (b) TD*

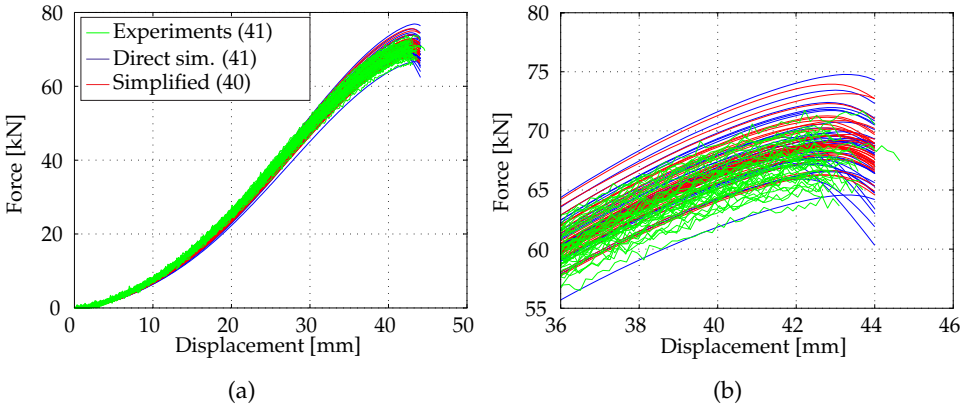

Figure 7.21 *(a) Global plot and (b) detailed plot of the experimental and numerically predicted force–displacement curves resulting from the direct simulations and simplified approach for the cup stretching process*

either if the correlation between material parameters is neglected or by assuming full correlation between yield locus model parameters.

Looking at the numerically predicted force-displacement curves resulting from the simplified approach (see Figure 7.21) and comparing these results with the outcomes from the PCA approach (see Figure 7.15), only a slight decrease of the force scatter is observed. The force–displacement response is dominated

by scatter in material thickness. Since this uncorrelated material parameter is included in the simplified approach, similar results to the PCA approach are obtained. It is mentioned in Section 7.4.3 that uncorrelated material parameters such as the material thickness will only make a significant contribution to a few PCs. By combining the PCA approach with a screening step, these few PCs will be included in the robustness study, resulting in an unambiguous approach for modeling material scatter in sheet metal forming applications.

7.7 Conclusions

The full stochastic material behavior of 41 coils of a forming steel, collected from multiple casts, is determined by an efficient hybrid approach combining tensile tests with texture measurements and modeled for use in robustness analysis. A principal component analysis is utilized to describe material scatter for the material as a collective, not just treating the 41 coils individually. The resulting stochastic description of material scatter includes all mean values, the variation and correlations. For efficient numerical implementation, a significant parameter reduction from 17 to 7 parameters is achieved by combining the principal component analysis with a screening step.

The numerical approach is validated by the forming of 41 hemispherical cups. The observed experimental response scatter can be reproduced accurately using FE simulations and metamodels. The metamodels can subsequently be used in the robust optimization strategy to efficiently and accurately include the effect of material scatter. By ensuring process robustness through this strategy instead of using arbitrary safety margins, forming processes can be designed for which optimal use is made of the material while guaranteeing safety with respect to material scatter.

Chapter 8

Stretching the limits of forming processes*

8.1 Introduction

Published research on robust optimization of forming processes using a metamodel-based strategy is generally confined to numerical studies only. See Chapter 2 for a review of the literature in this field. Experimental validation of the numerically predicted process robustness is seldom performed. This is because validation of process robustness requires performing many experiments to capture even the most pronounced sources of variation. However, only by supporting the numerical results with experimental outcomes is one able to determine whether the numerically predicted robust optimum is, indeed, more robust compared to the deterministic optimum and is as robust as in simulations. For this purpose, the difference in the number of product rejects between both optima needs to be determined experimentally. In this chapter, a metal forming process is optimized in both a deterministic and a robust way. Next, experimental validation of the process robustness in both optima is performed. The results demonstrate how the robust optimization strategy can assist in further stretching the limits of forming processes while remaining robust with respect to sources of variation.

In Chapter 1, the necessity of including uncertainty in optimization was explained using an example forming process. The same stretch-drawing process is considered in this chapter in a final deterministic and robust optimization study. The stretch-drawing process and the optimization problems will be introduced in Section 8.2. Next, the main sources of variation in the forming

*This chapter is based on: J.H. Wiebenga, E.H. Atzema, and A.H. van den Boogaard. Stretching the limits of forming processes by robust optimization: A demonstrator. Submitted. **2014**.

(a) (b)

Figure 8.1 *Hemispherical cup resulting from (a) the stretch-drawing process and (b) FE simulation (quarter part, rendered)*

process are introduced and quantified in Section 8.3. The results of both optimization studies are subsequently presented in Section 8.4. Additionally, the results of numerical robustness analyses in both optima are described. The numerically determined optima are validated by 2 sets of experiments using a collective of materials. The experimental procedure and results are described in Section 8.5 and the difference in robustness between the deterministic and robust optimum is discussed. Moreover, a comparison between the results of the numerical and experimental robustness analyses is made. A discussion is provided in Section 8.6. Finally, Section 8.7 will present the conclusions of this chapter.

8.2 Application to a stretch-drawing process

A deterministic and a robust optimization study are performed, considering the stretch-drawing process of a hemispherical cup. An impression of the process is given in Figure 6.13a. The stretch-drawing process is comparable to the stretching process as introduced in Section 6.6.2, but now also allowing for draw-in of the material.

8.2.1 Experimental procedure

Hemispherical cups are formed from circular blanks with a nominal thickness of 0.79 mm. The same drawing quality forming steel is used as in Chapter 7, i.e. DX54D+Z (EN 10327:2004). An impression of the resulting product is given

in Figure 8.1a. The experiments are performed using an Erichsen universal sheet metal testing machine. To control the process, both the blank size and the BHF are defined as design variables in this study. The blank radius (r) can vary between 80 mm and 90 mm whereas the BHF (F) can vary between 1 kN and 30 kN. Tooling with a punch diameter of 67 mm, a die opening diameter of 77.4 mm and a die shoulder radius of 8.5 mm is used. The blanks are lubricated using Zeller & Gmelin PL61 Multidraw oil. The amount of lubricant applied is 1.5 g/m^2. The blanks are formed by combined stretching and drawing using a prescribed punch displacement at a velocity of 1 mm/s. The optimal combination between stretching and drawing that results in the optimal product quality is unknown *a priori*.

8.2.2 Numerical model

The FE simulations of the stretch-drawing process are performed using the FE code DIEKA [29]. Due to symmetry of the product and material properties, only a quarter of the product is modeled, see Figure 8.1b. The blank is discretized using triangular discrete Kirchhoff shell elements with 5 integration points through thickness. The element size for the blanks with varying blank radii is kept constant at 1.0 mm. An average friction coefficient of 0.18 is utilized.

8.2.3 The optimization problem

The objective of the deterministic optimization study is to maximize the product height (h) while preventing wrinkling and local thinning of the product and requiring a minimal remaining flange width. The product height is used as an optimization objective in this work although generally, the product height is defined by the final required product geometry. However, by doing so, an optimum is obtained which is critical with respect to wrinkling, local thinning and flange width. A difference is now expected between the number of product rejects in the deterministic and robust optimum when performing experimental validation. This makes the product height a suitable optimization objective for the purpose of this demonstrator optimization study.

Several inequality constraints are present in this optimization problem. The constraint on wrinkling is evaluated in the flange of the product using a wrinkling indicator or wrinkling criterion (c). A dimensionless indicator value is obtained from the FE simulations based on the normalized relative curvature change under compressive stresses, see [126]. The wrinkling indicator should not exceed a value of 0.001 at which point wrinkling becomes visible, as will be further

discussed in Section 8.2.4. A minimum material thickness (t) of 70% of the original nominal thickness of 0.79 mm is required. With a fine enough FE mesh, this also precludes severe local thinning or necking. Finally, assuming that the flange is used for a subsequent assembly step, a minimum flange width (w) of 20 mm is required. The formed product should satisfy these three constraints, otherwise it is rejected. The deterministic optimization formulation is now given by:

$$\begin{aligned} \min_{\mathbf{x}} \; & -h \\ \text{s.t.} \; & 0.55 \leq t \\ & c \leq 0.001 \\ & 20 \leq w \\ & 80 \leq r \leq 90 \\ & 1 \leq F \leq 30 \end{aligned} \tag{8.1}$$

The objective of the robust optimization is to maximize the product height subject to the constraints on minimum material thickness, wrinkling and flange width. All constraints should be fulfilled under the presence of material and process scatter and are handled using the moment matching formulation of Equation (2.7) with $k_{\mathrm{g}} = 2$. The robust optimization formulation is now given by:

$$\begin{aligned} \min_{\mathbf{x}} \; & -h \\ \text{s.t.} \; & 0.55 \leq \mu_{\mathrm{t}} - 2\sigma_{\mathrm{t}} \\ & \mu_{\mathrm{c}} + 2\sigma_{\mathrm{c}} \leq 0.001 \\ & 20 \leq \mu_{\mathrm{w}} - 2\sigma_{\mathrm{w}} \\ & 80 \leq r \leq 90 \\ & 1 \leq F \leq 30 \end{aligned} \tag{8.2}$$

Next to the design variables r and F, Equation (8.2) is influenced by material and process scatter. The modeling of these sources of variation will be discussed in Section 8.3.

Table 8.1 *Selected settings for experimental validation of the numerical results*

Setting	r	F	h	observation
1	80 mm	8 kN	60 mm	wrinkling
2	80 mm	21 kN	74 mm	thinning
3	85 mm	8 kN	74 mm	wrinkling, thinning

8.2.4 Experimental validation of the nominal FE model results

Before proceeding with the optimization studies, the results of the FE model are experimentally validated. To allow for a comparison between experimental and numerical results, multiple experiments are performed at selected settings within the design space of the optimization problem, see Table 8.1. Experiments are performed using a blank radius of 80 mm and 85 mm and varying BHFs. For each experiment, the flange width, the minimum material thickness and the amount of wrinkling is determined at a product height (h) as indicated in Table 8.1. For the first and third setting, 3 experimental repetitions are performed. For the second setting, 2 experimental repetitions are performed.

The experimental settings are chosen such that the resulting products are critical with respect to wrinkling and local thinning. For the experiments using a blank radius of 80 mm, initiation of wrinkling in the flange can be seen using a BHF of 8 kN at a product height of 60 mm. Further decreasing or increasing the BHF results in an increasing or decreasing amount of wrinkling respectively. Using a blank radius of 80 mm, local thinning is detected at a product height of 74 mm using a BHF of 21 kN. When increasing the blank radius to 85 mm and using a BHF of 8 kN, initiation of both wrinkling and local thinning is detected at a product height of 74 mm.

The flange widths of the experimentally obtained cups are measured manually in RD and TD. The smallest flange width is obtained in TD when comparing the measurements per cup in both directions. This makes the TD the critical direction for use in optimization. Also, the material thickness is measured manually in RD and TD for the experimentally obtained cups. A point is hereby sought for which the thickness of the product wall is minimum. For the hemispherical cups, this point is located in the top of the product in TD, away from the pole. Similar results were found for the stretching process in Chapter 7.

The experimental and numerical results for flange width are presented in Figure 8.2a. The vertical bars in the experimental results show the variation in flange width for the experimental repetitions, demonstrating a good repeatability. For all experimental settings, the magnitude of the numerical flange width

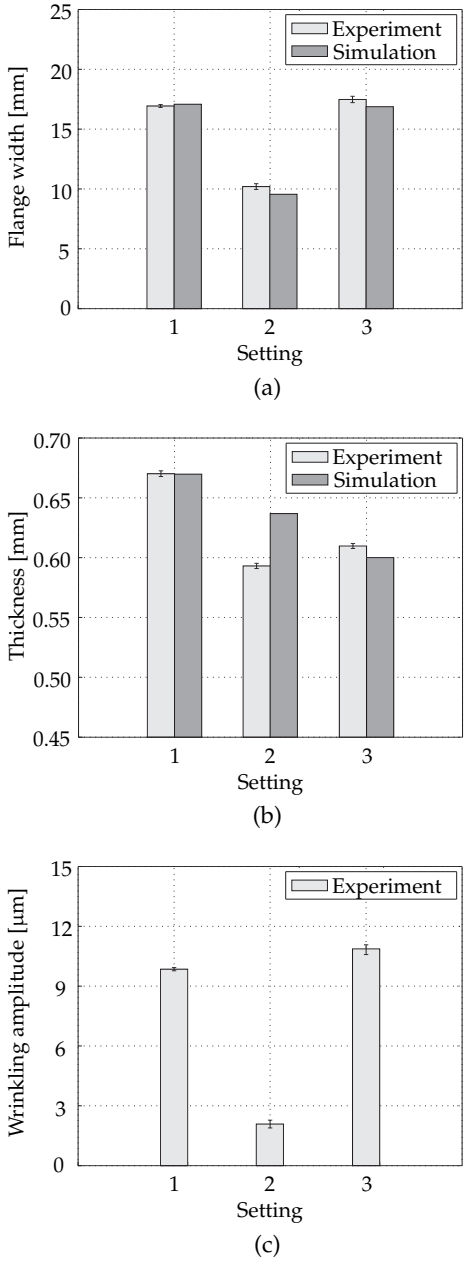

Figure 8.2 *Experimental and numerical results for the (a) flange width and (b) minimum material thickness, and experimental results for the (c) wrinkling amplitude according to the settings provided in Table 8.1*

prediction is in good agreement with the experimental results. Also note that the flange width of all products is smaller than the required 20 mm, meaning that none of these experimental settings are feasible solutions of Equation (8.1).

The experimental and numerical results for minimum material thickness are presented in Figure 8.2b. The experimental results show a good repeatability. For setting 1 and 3, a good agreement between experimental and numerical results is found. However, for setting 2 the material thickness is overestimated numerically. Given that the numerical model accurately predicts the flange width for all settings and material thickness for 2 settings, the FE model is assessed as acceptable for further use in the optimization studies.

For the hemispherical cups, wrinkling in the flange is observed. The wrinkling amplitude is determined by placing the experimentally obtained products in a 360° rotating holder and measuring the vertical deviation of the flange. The measurement is performed by a feeler pin following the flange shape at a predefined radius of 55 mm. The resulting measurement data is corrected for a possible vertical misalignment or overall obliqueness of the product using a Loess curve fit [24]. The wrinkling amplitude is defined as the vertical deviation from the average plane, for which 95% of the measurement data is below this amplitude to account for possible measurement outliers. The wrinkling amplitude for the three experimental settings (see Table 8.1) is given in Figure 8.2c. Light wrinkling for experiment 1 and 3 is detected by visual inspection, corresponding to a wrinkling amplitude of approximately 10 μm. This wrinkling amplitude corresponds to a wrinkling indicator value of 0.001, resulting from the FE simulations at these settings. This value should not be exceeded in the simulations to prevent visible and tangible wrinkling in the products and is therefore chosen as the limit for c as indicated in Section 8.2.3.

8.3 Material and process scatter

Solving Equation (8.2) requires the modeling of material and process scatter that can be encountered in stretch-drawing processes. Modeling and quantification of material scatter is described in Section 8.3.1. Modeling of process scatter is described in Section 8.3.2. For efficient implementation of material and process scatter in FE simulations, variable screening for dimensionality reduction is performed and discussed in Section 8.3.3.

8.3.1 Modeling material scatter

In this chapter, quantification of material scatter is based on a collective of 37 coils of a drawing quality forming steel DX54D+Z collected from multiple casts. Recall from Chapter 7 that a collective of 41 coils was used. However, for 4 coils not enough material was available for experimental validation of the stretch-drawing process. The collective has therefore been reduced to 37 coils.

For modeling material scatter, the same approach is followed as described in Chapter 7. As a result, 37 parameter sets are obtained where each parameter set consists of 17 parameters, i.e. 13 parameters describing the yield locus, 3 parameters describing the hardening behavior and a parameter describing the material thickness. For the robust optimization study, the goal is to describe material scatter for the material delivered as DX54D+Z, not just treating the 37 coils individually. To establish a collective data set, a Principal Component Analysis (PCA) is utilized as described in Section 7.3.2. Using the PCA, an orthogonal transformation is performed after which the material scatter can be described by a new set of basis vectors or Principal Components (PCs). The new representation of the data set becomes fully uncorrelated. Next, a DOE is created in the PC-domain. The subsequent back transformation to the physical parameter domain automatically includes all mean values, variation and correlations present in the original data set.

8.3.2 Modeling process scatter

For modeling process scatter, variation of the the BHF (F) and the friction coefficient (μ) is accounted for in the optimization study. The BHF variation is measured in the Erichsen universal sheet metal testing machine at a nominal BHF of 8 kN. The BHF and friction variation are described using a normal distribution where the scatter is defined in terms of the standard deviation. For the BHF, the standard deviation is determined to be σ_F = 0.25 kN. For friction, the standard deviation is assumed to be σ_μ = 0.01.

Combining material and process scatter, the total number of noise variables adds up to 19 in total. Using all 19 variables in a robust optimization procedure would require running many FE simulations to accurately capture the effect of input scatter. Therefore, variable reduction is required which is achieved by a screening step as described next.

8.3.3 Variable screening

Variable screening is performed to determine the sensitivity of the considered responses to the 19 noise variables. The screening procedure as introduced in Section 7.4.3 is followed. A face centered cubic DOE is created, evaluating 2 levels for each noise variable, i.e. $\pm 2\sigma$. This results in a total number of 38 required FE simulations. The individual effect of each noise variable on the numerical responses is determined and visualized using Pareto plots. In addition, a single FE simulation can be performed at the mean of all noise variables to determine the monotonicity of the responses.

The resulting Pareto plots are shown in Figure 8.3 for the flange width, minimum material thickness and the wrinkling indicator response. The material scatter is described by 17 PCs, denoted by numbers 1–17. The variables are sorted based on the magnitude of the main effect in descending order. Additionally, the cumulative percentual effect (solid line) is plotted. Note that only the first 13 significant variables are plotted, which already account for more than 95% of the total effect.

Each of the noise variables influences the considered numerical responses to a different extent. All responses are strongly dominated by material scatter, especially the minimum material thickness (Figure 8.3b). The flange width is also strongly influenced by the variation of the friction coefficient (Figure 8.3a) whereas the wrinkling response is additionally influenced by the variation of the BHF (Figure 8.3c). For controlling 80% of the response scatter, at least PC numbers 1–7, the BHF and friction variation must be included. This results in a reduction from 19 to 9 noise variables for modeling material and process scatter, and thus a significant efficiency increase for subsequent use in the robust optimization study.

8.4 Deterministic and robust optimization results

The deterministic optimization problem of Equation (8.1) and the robust optimization problem of Equation (8.2) are solved using the optimization strategy as described in Chapter 3. For deterministic optimization, a two-dimensional design space of the design variables is considered, i.e. the blank radius and the BHF. For robust optimization, this expands to a ten-dimensional design space including the additional 9 noise variables resulting from the screening step. Note that the BHF is a combined design and noise variable, spanning up a single dimension.

A DOE based on an LHD is created for both optimization studies using 50 and

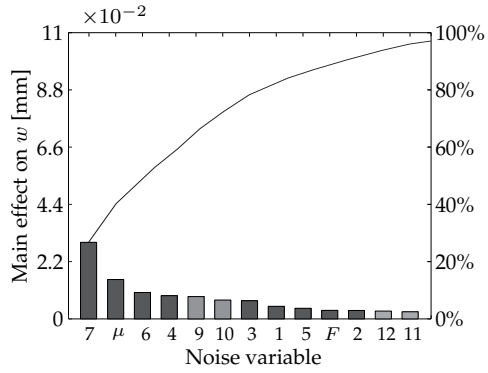

(a)

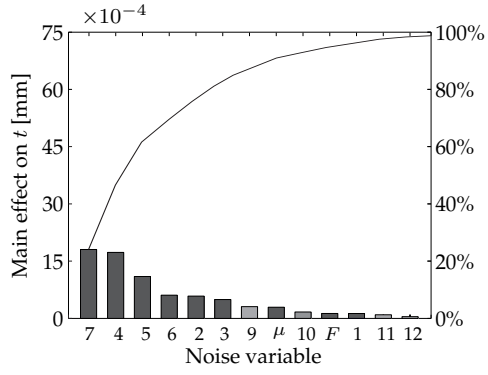

(b)

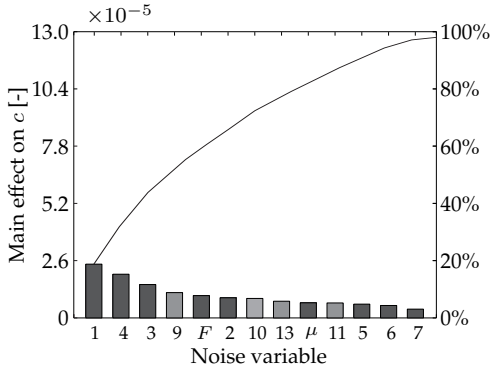

(c)

Figure 8.3 *Pareto plots of the (a) flange width, (b) minimum material thickness and (c) wrinkling indicator response*

Table 8.2 *Numerical optimization results*

	r	F	h
Deterministic optimum	85 mm	8 kN	69 mm
Robust optimum	84 mm	11 kN	65 mm

250 DOE points respectively. Note that an increasing number of DOE points is used than was recommended in the optimization strategy of Section 3.4.1. This choice is made such that the metamodel-based constraint predictions are in good agreement with the experimental results at the settings as indicated in Table 8.1. After running the FE simulations, response values are extracted from the FE results as a function of the product height. For deterministic optimization, the material properties of a single coil out of the collective of 37 coils are used in the FE simulations. This coil is referred to as the *reference material* in the remainder of this chapter and is also used for the experiments described in Section 8.2.4. For robust optimization, the material properties of the collective of material is used, described in terms of the 7 PCs resulting from the screening step. Based on the FE simulation responses, metamodels are fitted. The fitting accuracy is subsequently determined using ANOVA techniques. An NN model is found to be most accurate for the wrinkling and minimum material thickness constraint, whereas for the flange width constraint a full quadratic RSM model is assessed as most accurate for subsequent use in deterministic and robust optimization.

The deterministic optimum and the robust optimum are presented in Table 8.2. The optimal cup height for the deterministic optimum of 69 mm is obtained using a blank radius of 85 mm and a BHF of 8 kN. The robust optimum is found at a more conservative cup height of 65 mm, using a blank radius of 84 mm and a BHF of 11 kN. Impressions of the feasible design space in deterministic and robust optimization at varying product heights are given in Figure 8.4. The constraint predictions in Figure 8.4a are based on FE simulations using the reference material properties. For visualization of the constraints in Figure 8.4b and to enable a comparison between the feasible design space in deterministic and robust optimization, the noise variables are set to the settings of the reference material. The shaded areas indicate the infeasible region of the design space where the constraints are violated. The size of the feasible design space (non-shaded area) decreases for an increasing product height. This is mainly caused by the wrinkling and flange width constraint becoming more critical for an increasing product height. A comparable shape and size of the feasible design space is observed in Figures 8.4a and 8.4b. This indicates that, although going from a two-dimensional design space to a ten-dimensional design space, an

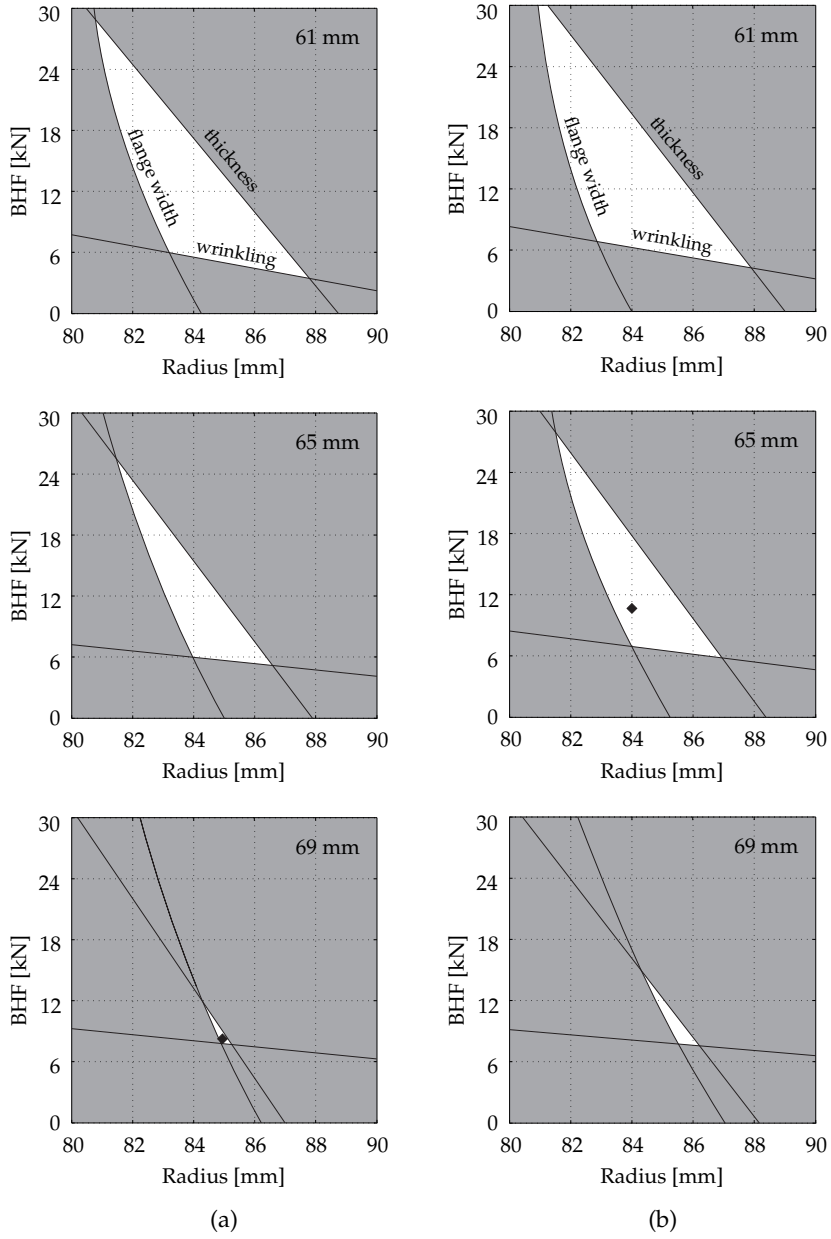

Figure 8.4 *Impressions of the feasible design space (non-shaded area) in (a) deterministic optimization and (b) robust optimization at varying product heights*

accurate constraint prediction is made for robust optimization. In Figure 8.4a, the feasible design space for deterministic optimization reduces to a point at a product height of 69 mm, which is the deterministic optimum. The optimum is indicated with a diamond marker in Figure 8.4a and lies at the boundary of all three constraints. In Figure 8.4b, the robust optimum is found in the feasible design space at a product height of 65 mm, leaving space for response variation.

Referring back to the introduction of this thesis (Chapter 1), neglecting the presence of uncertain variables in optimization will lead to a deterministic optimum that lies at the boundary of one or more constraints, as is the case for the stretch-drawing process. The presence of process variation will now cause violation of the constraints and result in product rejects. To demonstrate this for the stretch-drawing process, the robustness of the deterministic and robust optimum is determined by performing 37 FE simulations in both optima. For this purpose, the 37 material parameter sets obtained from the material collective are used. Process scatter is added to 36 out of 37 simulations by varying the nominal BHF and friction coefficient according to an LHD sampling within the ranges $\pm 2\sigma_F = \pm 0.5$ kN and $\pm 2\sigma_\mu = \pm 0.02$ respectively. For the reference material, no process scatter is added to demonstrate the prediction accuracy of the metamodels as will be discussed below.

Figure 8.5 shows the simulation results in the deterministic and robust optimum for all considered responses, also visualizing the infeasible domain (shaded area) and the reference material. A summary of the number of constraint violations and total number of product rejects in both optima is given in Table 8.3. For the deterministic optimum, 18 out of 37 simulations show violation of the constraints, see Figure 8.5a. Out of these 18 simulations, 15 simulations show violation of the wrinkling constraint, 5 simulations show violation of the flange width constraint and 2 simulations show violation of both the wrinkling and flange width constraint. No violation of the minimum material thickness constraint is predicted numerically. The simulation results using the reference material are obtained at the deterministic optimal process settings (no process scatter is added) and are closely located to all three constraints in Figure 8.5a. The simulation is rejected due to a minor violation of the wrinkling constraint. For a perfect fit of the metamodels in the deterministic optimum, the responses of the reference material should be located at the crossing of the constraints. Keeping in mind that only a part of the total range of response values are plotted in Figure 8.5a, the metamodel prediction is assessed as accurate with respect to the FE model responses.

For the robust optimum, none of the 37 simulations show violation of the constraints, see Figure 8.5b. Also no wrinkling is detected in the simulations.

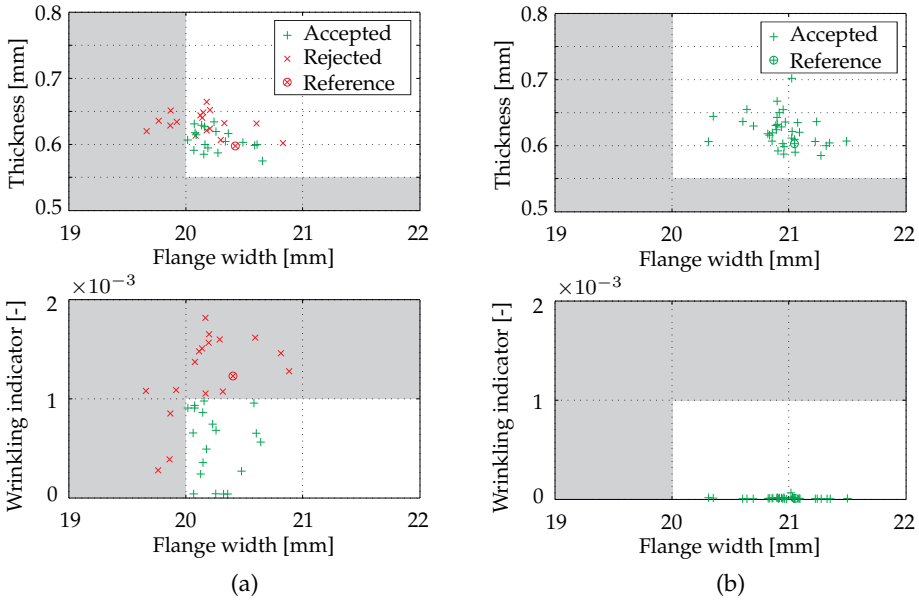

Figure 8.5 *Numerical robustness analysis in (a) deterministic and (b) robust optimum*

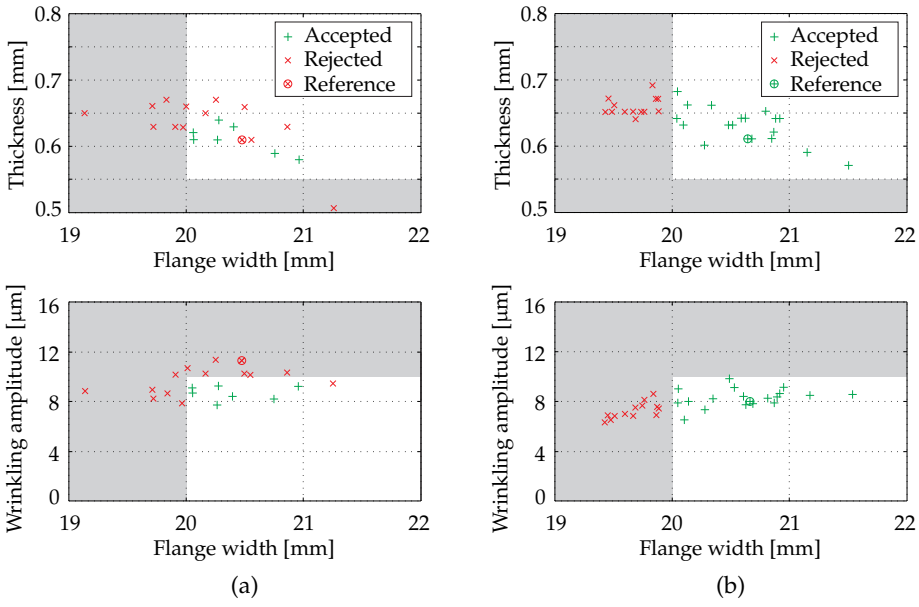

Figure 8.6 *Experimental robustness analysis in (a) deterministic and (b) robust optimum*

Table 8.3 *Numerical and experimental results of constraint violation on minimum material thickness (t), wrinkling (c) and flange width (w), and total number of product rejects in the deterministic and robust optimum*

Numerical results	t	c	w	Rejects
Deterministic optimum	0 / 37	15 / 37	5 / 37	18 / 37
Robust optimum	0 / 37	0 / 37	0 / 37	0 / 37

Experimental results	t	c	w	Rejects
Deterministic optimum	17 / 37	8 / 21	6 / 21	30 / 37
Robust optimum	5 / 37	0 / 32	13 / 32	18 / 37

Values for the flange width and material thickness are found within the feasible area, although close to both constraints. From evaluating the numerically predicted process robustness for both optima in Figure 8.5, it can be concluded that the deterministic optimum is more critical with respect to material and process scatter compared to the robust optimum as expected.

8.5 Experimental validation

The numerical results are experimentally validated to determine whether the numerically predicted robust optimum is, indeed, more robust in practice compared to the deterministic optimum and is as robust as in simulations. Stretch-drawing experiments are performed at the optimal settings as indicated in Table 8.2. At both the deterministic and robust optimal process settings, 37 stretch-drawing experiments are performed using the collective of material. The experiments are terminated at the optimal product height, as given in Table 8.2. If fracture of the product is observed before reaching the optimal product height, the experiment is terminated at the point of fracture. By performing 37 experiments in each optimum, the most pronounced sources of process scatter are expected to be captured in the experimental procedure, allowing for validation of the numerically predicted process robustness.

8.5.1 Evaluation of the experimental results

For the two sets of 37 hemispherical cups, the flange width, the minimum material thickness and the wrinkling amplitude are measured following the procedure as outlined in Section 8.2.4. The experimental results for both optima

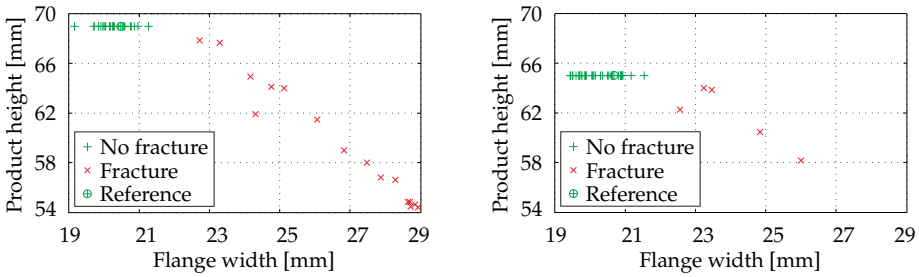

Figure 8.7 *Experimental results for the obtained product heights in the (a) deterministic and (b) robust optimum*

are shown in Figure 8.6 and summarized in terms of constraint violation in Table 8.3. The experimental results for the obtained product heights in both optima are given in Figure 8.7. In the deterministic optimum, 16 products show fracture in the top of the product before reaching the optimal height of 69 mm, see Figure 8.7a. An example of such a product is shown in Figure 8.8a. In the robust optimum, 5 products show fracture before reaching the optimal height of 65 mm, see Figure 8.7b. As a result of early product fracture and subsequent termination of the experiment, the resulting flange width is also larger compared to the products that are formed to the optimal product height. Figure 8.6 presents the experimental results for the non-fractured products, i.e. 21 products in the deterministic optimum and 32 products in the robust optimum. In the deterministic optimum, 1 out of 21 products shows a minimum material thickness smaller than the required 70% of the original thickness, see Figure 8.6a. In the robust optimum, all 32 products show a material thickness exceeding the minimum thickness requirement, see Figure 8.6b. This brings the total number of products violating the minimum material thickness constraint in the deterministic and robust optimum to 17 and 5 respectively, see the second column of experimental results in Table 8.3. Clearly, a significant reduction in the number of constraint violations for minimum material thickness is achieved. Moreover, note that at a product height of 65 mm, 14 products show fracture in the deterministic optimum (Figure 8.7a) whereas only 5 products show fracture in the robust optimum (Figure 8.7b). This demonstrates that the process has become more robust with respect to product fracture using the robust process settings instead of the deterministic process settings.

For the non-fractured products, a reduction in wrinkling is achieved by using the robust optimal process settings compared to the deterministic process settings.

(a) (b) (c)

Figure 8.8 *Cups experimentally obtained in the deterministic optimum rejected based on (a) fracture and (b) wrinkling, and (c) detailed picture of light flange wrinkling*

In the deterministic optimum, 8 out of 21 products show a wrinkling amplitude larger than 10 μm, at which point wrinkling is detected by visual inspection as discussed in Section 8.2.4. An example of such a product is shown in Figure 8.8b. This product is obtained in the deterministic optimum using the reference material. A detailed picture of light flange wrinkling is given in Figure 8.8c. In the robust optimum, none of the 32 products show a wrinkling amplitude exceeding 10 μm.

The flange width of 6 out of 21 products in the deterministic optimum is observed to be smaller than the required 20 mm, see Figure 8.6a. In the robust optimum, the flange width of 13 out of 32 products is observed to be smaller than the required 20 mm, see Figure 8.6b. Although the smallest flange width measured violates the flange width constraint by only 0.54 mm, the process does become more critical with respect to this constraint in the robust optimum.

Finally, looking at the total number of rejects in both optima as indicated in the last column of Table 8.3, 30 out of 37 products in the deterministic optimum show violation of one or more constraints. This number decreases to 18 out of 37 in the robust optimum. Clearly, a significant reduction in the number of product rejects is achieved by using the robust optimal process settings compared to the deterministic process settings. A side view of successful products obtained in the deterministic optimum and robust optimum is given in Figure 8.9, demonstrating the difference in final product height. Comparing the experimental results in both optima, it can be concluded that the process remains critical with respect to flange width but has been made more safe with respect to minimum material thickness and wrinkling by robust optimization.

Figure 8.9 *Side view of successful products obtained in the deterministic optimum (left, $h = 69$ mm) and robust optimum (right, $h = 65$ mm)*

8.5.2 Validation of the numerical results

The numerical robustness predictions are experimentally validated by comparing the results in the deterministic and robust optimum, see Figures 8.5 and 8.6 and Table 8.3. For the flange width and wrinkling response, the numerical prediction of constraint violation in the deterministic optimum is in good agreement with the experimental results. Moreover, no violation of the wrinkling constraint is numerically predicted in the robust optimum which, agrees with the experimental results. Violation of the minimum material thickness constraint is not predicted numerically although it is encountered experimentally, both in the deterministic and robust optimum. Finally, no violation of the flange width constraint is numerically predicted in the robust optimum, although it is observed in the experiments.

Comparing the amount of response scatter in Figures 8.5 and 8.6, it can be observed that the variation of the minimum material thickness and flange width are underestimated numerically. Note that the response values for the 16 fractured products are not included in Figure 8.6. That is, the experimentally observed minimum thickness variation is larger than displayed in Figure 8.6. Also, an offset of 0.73 mm in mean flange width results is present in the robust optimum, see Figure 8.5b and Figure 8.6b. As discussed in Section 8.4, none of the 37 simulations showed violation of the minimum material thickness and flange width constraint in the robust optimum (see Figure 8.5b) but values are found close to the constraint. As a result of the numerical underestimation of response variation and the offset in mean flange width results in the robust optimum, a robust optimum is obtained which still results in a number of experimental constraint violations. Causes for this discrepancy will be discussed in Section 8.6. As another result of the underestimation of response variation and offset in mean results, the numerical prediction of the number of product rejects in both optima is also lower compared to the number of product rejects in the experiments, see

Table 8.3. However, looking at the difference in the number of product rejects between both optima, a good agreement between numerical and experimental results is obtained.

Although the overall improvement of the stretch-drawing process looks limited, since still 18 products are rejected in the robust optimum, the improvement is definitely present. Recall that 13 out of 18 products are rejected based on violation of the flange width constraint. If the discrepancy of 0.73 mm between the numerical and experimental mean flange width results were not present, the number of product rejects would decrease to 5 in the robust optimum, only caused by product fracture. Moreover, based on including 80% of material scatter through the screening step and striving for a 2σ process in robust optimization, some product rejects can be expected in the robust optimum. Keeping this in mind, it is concluded that the stretch-drawing process has been made more reliable and robust by application of the robust optimization strategy.

8.6 Discussion

For an accurate estimation of the number of product rejects, both the mean response and the response variation should be predicted accurately. For the stretch-drawing process, it is observed that the number of product rejects is underestimated numerically. Several possible causes can be distinguished. It is discussed in Section 8.2.4 that the mean response prediction of the FE model should be accurate in the whole design space of the optimization problem, not just at a single process setting. It is demonstrated in Figure 8.2b that this is not the case for numerical prediction of the minimum material thickness. Also, for the flange width response (Figure 8.2a), it is demonstrated that a small discrepancy between numerical and experimental results can lead to a significant difference in the number of product rejects. Next to an accurate FE model prediction, accurate metamodel predictions are required in the whole design space. This holds especially for the boundary between the feasible and the infeasible domain. It can be observed from Figure 8.4 that accurate metamodel approximations are required for all considered responses to obtain a correct prediction of the optimal process settings. Finally, for an accurate prediction of the scrap rate of a process, the amount of response variation should also be predicted accurately. For the stretch-drawing process, it is observed that the experimentally obtained response variation (Figure 8.6) is underestimated numerically (Figure 8.5). This discrepancy could be caused by the presence of additional sources of variation present in the forming process, but not accounted for in the modeling of input

variation. In this work, extensive attention is paid to the modeling of material scatter. More attention should be paid to accurately measuring and modeling process variation, which is recommended as a point for future research.

8.7 Conclusions

Deterministic and robust optimization of a stretch-drawing process are performed, excluding and including the effect of material scatter and process variation respectively. For quantification of material scatter, a collective of 37 coils of a forming steel is used. The optimal deterministic and robust process settings have been determined, after which the robustness of both optima has been determined numerically. The results show that the deterministic optimum is critical with respect to input variation, leading to product rejects. By accounting for input variation in optimization, a robust optimum is obtained which should not result in product rejects.

The numerically predicted process robustness for both optima is experimentally validated by two sets of 37 experiments using the collective of material. With that, this study is one of the first robust optimization analyses of forming processes that also includes experimental validation of the numerically predicted process robustness. The experimental results confirm that the robust optimum is indeed more robust in practice compared to the deterministic optimum, showing a reduction in the number of product rejects. Moreover, it enables the quantification of response variation and an estimation of the process scrap rate. This demonstrates that explicitly including material and process scatter in the optimization strategy allows for determining the robust optimal process design.

Chapter 9

Conclusions and recommendations

The objective of this research was to develop an optimization strategy applicable to forming processes liable to uncertainty. The strategy should enable finding the optimal robust process design which meets the constraints even under the presence of uncertainty. Moreover, it should allow for quantification of the response variation and, ideally, the prediction of the scrap rate of a process. Finally, the strategy should be efficient and suitable for use with computationally expensive FE simulations. These goals are achieved by treating several research topics, of which the conclusions are described in Section 9.1. Recommendations for future research are presented in Section 9.2.

9.1 Conclusions

An overview of the key conclusions drawn from this research is given in this section. Detailed conclusions per research topic have been provided at the end of each chapter.

Robust optimization strategy

A robust optimization strategy has been developed for modeling and solving simulation-based robust optimization problems. The strategy consists of the following main stages: modeling, variable screening, robust optimization, validation and sequential improvement. For modeling, a variance-based robust optimization formulation has been defined, taking into account both process robustness and process reliability. Uncertain variables are hereby quantified and accounted for explicitly in the optimization strategy using a probabilistic

approach. For solving, use is made of the single response surface method combined with Monte Carlo analyses to obtain the statistical measures of the objective function and constraints. This metamodel-based approach has been utilized to couple the time-consuming FE simulations with the optimization algorithm.

The strategy has been applied to robust optimization problems of various industrial metal forming processes, i.e. a roll forming process in Chapter 4, a V-bending process in Chapters 5 and 6, a stretching process in Chapters 6 and 7 and a stretch-drawing process in Chapter 8. The robust optimization problems were efficiently solved, showing that the strategy is suitable for industry-sized problems and for use with computationally expensive FE simulations. For all applications, the optimization strategy enabled quantification of response variation and determination of the robust optimum, which was set out as the main objective of this work. Finally, successful experimental validation of the numerical results was performed.

Sequential robust optimization

The robust optimization strategy has been extended in Chapter 5 with a sequential optimization step. This step is included to efficiently increase the accuracy of the metamodel prediction in case the numerically predicted optimum does not match with the FE simulation response at this location. A sequential improvement algorithm has been implemented that adds new DOE points to the original DOE based on an expected improvement measure. The infill points are added either locally or globally in the combined design–noise variable space such that the prediction of the robust objective function is improved.

Sequential robust optimization has been successfully applied to an analytical test function and a V-bending process. For the industrial V-bending process, a significant improvement of the robustness and reliability was obtained by optimizing the process design while accounting for the deteriorating effects of noise variables. Moreover, experimental validation of the numerical robustness results has been performed. A good agreement with the experimental outcomes resulting from multiple production trial runs was obtained, demonstrating the predicting capabilities of the metamodel-based optimization strategy.

Application of the sequential improvement algorithm to the test function and V-bending process showed that the accuracy of the metamodel prediction in the vicinity of the optimum can be efficiently improved by sequentially adding infill points. Moreover, it was concluded that the metamodel prediction accuracy increased more rapidly by placing the infill points at qualified locations than

by increasing the initial size of the DOE. This demonstrates that adding a sequential improvement step to the robust optimization strategy further increases the accuracy and efficiency of the proposed strategy.

Numerical noise

An approach has been described in Chapter 6 to handle numerical noise and minimize its deteriorating effect on the approximation quality of metamodels. Regularization was applied in the metamodel fitting procedure to deal with noisy response data resulting from FE simulations. Quantification of noise was achieved by local smoothing of response data and a coupling was made with the sequential improvement algorithm. The coupling enables termination of the update algorithm based on the magnitude of numerical noise present in the response data. That is, the update algorithm stops if no further improvement of the metamodel prediction accuracy is expected with respect to the underlying expected smooth response.

Application to a V-bending process and stretching process showed the efficient functioning of the approach. First, the deteriorating effect of noisy response data on the metamodel prediction accuracy was demonstrated. When the presence of numerical noise was neglected, erroneous metamodels and an inaccurate prediction of the optimum was obtained. This was especially the case when using interpolating metamodels in combination with dense sampling strategies. For both applications, it was shown that regularization and local smoothing reduce the deteriorating effects of numerical noise and enable quantification of its magnitude. It can be concluded from these results that, despite the presence of numerical noise, the robust optimization strategy allows for a fast and accurate convergence towards the global optimum while maintaining the benefits of metamodel-based optimization.

Material scatter

In order to find the optimal robust design, uncertainty must be quantified and included in the optimization strategy. One of the most dominant sources of scatter in forming processes is the variation of material properties. An accurate and economic approach for quantifying and modeling material properties and its associated scattering has been described in Chapter 7. By combining mechanical testing and texture analysis, a stochastic set of material data was efficiently determined based on 41 coils of a forming steel. A principal component analysis has been applied to describe material scatter for the material as a

collective, not just treating the 41 coils individually. This analysis was combined with a screening step for dimensionality reduction and subsequent efficient implementation in FE simulations. The modeling approach has been validated by the forming of 41 hemispherical cups using a stretching process.

Application of the modeling approach to the stretching process demonstrated that the observed experimental scatter can be reproduced accurately. Both the mean and the amount of response variation were predicted correctly, concluding that an efficient and accurate approach has been developed for modeling material scatter. Moreover, it was demonstrated that the correlations in material parameters must be represented accurately. That is, correlations must be included to prevent overestimation of the output scatter in the robustness analysis caused by the sampling of physically unlikely parameter combinations. Finally, in the forming of 41 cups, the effect of material scatter on the response variation increased for an increasing product height. This shows that the sensitivity of this forming process to variation in material properties increases for the material being stretched to its limits.

Robust optimization demonstrator

A final demonstrator study has been described in Chapter 8 considering a stretch-drawing process. Deterministic and robust optimization studies have been performed, excluding and including the effect of material and process scatter respectively. Robustness analyses executed in the optima resulting from the optimization studies showed that the deterministic optimum is critical with respect to input variation whereas the robust optimum was, indeed, not.

The robustness was experimentally validated for both the deterministic and robust optimum by performing a series of stretch-drawing experiments in the optima. The experimental results confirmed that the robust optimum was indeed more robust in practice compared to the deterministic optimum, showing a reduction in the number of product rejects. This demonstrates that explicitly including material and process scatter in the optimization strategy allows for determining the robust optimal process design. Moreover, it enables the quantification of response variation and an estimation of the process scrap rate, which was set out as one of the main objectives of this work. Finally, still a number of product rejects were experimentally obtained in the robust optimum. This shows that the modeling and optimization strategy is not complete yet, leading to the recommendations for future research as given in Section 9.2.

9.2 Recommendations

Based on the knowledge gained during this research, the following recommendations are made for future research. The recommendations are not only based on the conclusions as given in Section 9.1, but also discuss promising research topics outside the scope of this thesis.

Model accuracy

The use of metamodels in the robust optimization strategy hinges on the assumption that the metamodel is a correct representation of the FE simulation and that the FE simulation correctly predicts the physical process. The metamodel prediction accuracy was a research topic in this work and is to be further improved in future research. In several cases, the prediction accuracy was shown to be limited by the choice of the metamodel. Several examples of the metamodel's prediction inaccuracy have been encountered. For both the roll forming process in Chapter 4 and the V-bending process in Chapter 6, a strong non-linear response behavior was observed in the transition from the material being bent, to the material being bent and coined. The kink in the response behavior was described inaccurately by the applied metamodels, although it is an important feature to be captured for optimization. Moreover, it has been demonstrated in Chapters 5 and 8 that an accurate metamodel prediction of the FE simulation responses is crucial to correctly estimate the stochastic measures for robust optimization. For these reasons, further improving the predicting capabilities of metamodels is required and recommended as a point for future research.

When using FE simulations, a prediction error will be present with respect to the physical process due to e.g. model assumptions or discretization of the problem. Achieving a good compromise between accurate simulation and optimization results on the one hand, and computational efficiency on the other hand, is an on-going challenge. As an example of such a trade-off, using a finer mesh will increase the calculation time but will also likely decrease the discrepancy between the response of the physical process and numerical prediction. As a point for future research, it is recommended to develop an optimization strategy that makes use of this aspect by first generating a global metamodel based on coarse, but computationally cheap, FE models. The predicting capabilities of the global metamodel with respect to the physical optimum can subsequently be improved using a few finer, but more expensive, FE simulations to end up with an accurate final prediction of the optimum. Based on the combined use of

coarse and fine FE simulations, it is expected that a further efficiency increase can be achieved in the robust optimization of forming processes.

Material and process scatter

An approach for quantifying and modeling material scatter has been proposed and demonstrated in Chapter 7. Now that the influence of material scatter on the response of forming processes can be quantified, also the inverse approach can be followed to determine which groups of material properties are responsible for the majority of response variation. Given the specification limits of a forming process, one can in principle determine the allowed scatter of material properties. The robustness of a forming process can now be increased by reducing the scatter in critical material properties, which is recommended as a point for future research.

For the noise variables included in the robust optimization strategy, a normal distribution is assumed. For material scatter of the considered collective of coils, it is demonstrated in Chapter 7 that this is a good initial assumption. In practice, companies exploiting metal forming processes will experience material scatter that is non-normally distributed and possibly truncated. This is because coils are produced using multiple production lines with slight differences between the lines and the critical material properties can often only be ensured by applying material selection. This results in material collectives for which the material scatter is more complex. As a point for future research it is recommended to investigate the influence of using different distribution functions for modeling material scatter, and to extend the robust optimization strategy to enable describing more diverse material collectives.

For modeling input variation in the stretch-drawing process described in Chapter 8, extensive attention is paid to material scatter. As a point for future research, more attention should be paid to accurately modeling process variation. Whereas the blank holder force variation was measured for the robust optimization demonstrator, the friction scatter was assumed. Recent developments in friction modeling [54] open the possibility of modeling the variation in friction and lubrication conditions in a more realistic manner. Other important sources of process scatter to be included are e.g. temperature variation (and its interaction effect with friction), punch velocity variation or blank positioning.

In this research, material and process scatter have been evaluated from product to product. As a final point for future research it is recommended to investigate the modeling of material scatter within a product and process scatter during

forming. As an example, the material thickness can show variation within a sheet as a result of the production process of sheet metal by rolling. Especially for large sheets, for which this effect is more apparent, it is recommended to include geometrically correlated thickness variation using e.g. random fields [38]. Also process settings, like the blank holder force or punch velocity, can show variation during the process and can affect the final product quality.

Nomenclature

The symbols used in this thesis are classified in a Roman and Greek category. Some symbols appear more than once, their specific meaning follows from their context or from subscripts.

Roman

a	output of a layer in neural networks	
b	bias	
c	wrinkling criterion	
d	input of a layer in neural networks	
e	error	
f	objective function	
g	inequality constraint	
h	equality constraint	
h	height	[mm]
k	number of design and noise variables	
k_{g}	probability of constraint satisfaction factor	
lb	lower bound	
m	number of parameters	
n	number of observations or simulations	
n	strain hardening exponent	
n_{l}	number of points to the left	
n_{r}	number of points to the right	
p	parameter	
p	number of regression coefficients	
p_{X}	probability density function	
$p_{\mathrm{X,Y}}$	joint probability density function	
q	fraction of a full factorial design	
r	radius	[mm]
r	R-value	

s	prediction uncertainty	
t	thickness	[mm]
ub	upper bound	
w	weighing factor	
w	width	[mm]
x	design variable	
y	function or model	
z	noise variable	
z_{p}	parameter uncertainty	
z_{x}	design variable uncertainty	
$\mathbf{C}_{\mathrm{X}}$	covariance matrix	
D	forming gap	[mm]
E	Young's modulus	[GPa]
F	force	[kN]
G	activation function	
H	vertical alignment	[mm]
K	strength coefficient	[MPa]
L	length	[mm]
$\mathbf{P}$	transformation matrix	
P_0	reliability level	
P_{X}	cumulative distribution function	
$P_{\mathrm{X,Y}}$	joint cumulative distribution function	
R	correlation function	
R	radius	[mm]
R^2	coefficient of determination	
R_{m}	ultimate tensile stress	[MPa]
$\mathbf{V}$	matrix containing eigen vectors	
W	width	[mm]
$\mathbf{X}$	design matrix	
$\mathbf{X}, \mathbf{Y}$	random variables	
Y	stochastic process	
$\mathbf{Y}$	transformed data set	
Z	stochastic noise process	

Greek

α	angle	[°]
α	weighing factor	
β	regression coefficient	
ε	error	
ε	strain	
ε_1	major strain	
ε_2	minor strain	
ε_e	elastic strain	
ε_p	plastic strain	
θ	angle	[°]
λ	eigenvalue	
λ	regularization parameter	
μ	mean value	
ρ	correlation coefficient	
σ	standard deviation	
σ	stress	[MPa]
σ_0	initial static stress	[MPa]
σ^2	variance	
ϕ	probability density function of a standard normal distribution	
Δ	threshold value	
$\Delta\sigma_\mathrm{m}$	stress increment parameter	[MPa]
$\mathbf{\Lambda}$	diagonal matrix	
Φ	cumulative distribution function of a standard normal distribution	
Ω	remobilization parameter	

Abbreviations

AHSS	advanced high strength steel
ANOVA	analysis of variance
BB	Box-Behnken
BHF	blank holder force
BLUP	best linear unbiased predictor
CA	crossed array
CCD	central composite design
CDF	cumulative distribution function
CS	center springback
DACE	design and analysis of computer experiments
DD	diagonal direction
DIC	digital image correlation
DOE	design of experiments
DP	dual phase
DR	drawing ratio
DRSM	dual response surface method
EGO	efficient global optimization
EI	expected improvement
ES	end springback
FE	finite element
FEM	finite element method
FFD	full factorial design
FLC	forming limit curve
FS	front springback
GCV	generalized cross validation
HL	hidden layer
IF	interstitial free
IS	importance sampling
LCB	lower confidence bound
LDR	limiting drawing ratio
LHD	Latin hypercube design
LOOCV	leave one out cross validation
LSL	lower specification limit
LSS	least-squares smoothing
max	maximize
MCA	Monte Carlo Analysis
MEI	maximum expected improvement
MF	merit function

MI	most likely improvement
min	minimize
MLE	maximum likelihood estimation
MMF	minimizing merit function
MSE	mean square error
NN	neural networks
OL	output layer
OLHS	optimal Latin hypercube sampling
OUU	optimization under uncertainty
PC	principal component
PCA	principal component analysis
PDF	probability density function
PM	polynomial model
PSO	particle swarm optimization
RBDO	reliability-based design optimization
RD	rolling direction
RDO	robust design optimization
RMSE	root mean square error
RO	robust optimization
RSM	response surface methodology
SAO	sequential approximate optimization
SNR	signal-to-noise ratio
SPC	statistical process control
SRO	sequential robust optimization
SSE	error sum of squares
SSR	regression sum of squares
SSRD	Six Sigma robust design
SST	total sum of squares
st	subject to
SVR	support vector regression
TD	transverse direction
UD	uniform design
USL	upper specification limit

Miscellaneous

$\|.\|$	absolute value
$\|\|.\|\|$	norm
$\mathrm{Cov}(.)$	covariance
$\mathrm{E}(.)$	expected value
$\mathcal{N}(\mu, \sigma^2)$	normal distribution with mean μ and standard deviation σ
$\Pr[.]$	probability
$\mathrm{Var}(.)$	variance
$\hat{x}$	estimator of x
x'	optimal value of x
x_0	untried setting of x
x_{-i}	cross validated setting of x
x^*	current best solution of x
x^+	upper setting of x
x^-	lower setting of x
$\overline{x}$	mean of x
$\mathbf{x}^{\mathrm{T}}$	transpose of $\mathbf{x}$
$\mathbf{x}^{-1}$	inverse of $\mathbf{x}$

Appendix A

Probabilistic description of uncertainty

Following the theory as outlined in [50], suppose $\mathbf{X}$ is a random variable and n observations of $\mathbf{X}$ are given. The particular realization of a random variable or the samples of $\mathbf{X}$ are given by $\mathbf{x}$ or x_1, x_2, ..., x_n. The statistical description of a random variable $\mathbf{X}$ can be completely described by a *cumulative distribution function* (CDF) or a *probability density function* (PDF), denoted by $P_\mathrm{X}(\mathbf{x})$ and $p_\mathrm{X}(\mathbf{x})$ respectively. To calculate the *probability* $\Pr[\,]$ of $\mathbf{X}$ having a value between x_1 and x_2, the area under the PDF between these two limits needs to be calculated. This can be expressed by:

$$\Pr[x_1 < \mathbf{X} \leq x_2] = \int_{x_1}^{x_2} p_\mathrm{X}(\mathbf{x})\,\mathrm{d}\mathbf{x} = P_\mathrm{X}(x_2) - P_\mathrm{X}(x_1) \tag{A.1}$$

The PDF is the first derivative of the CDF, that is:

$$p_\mathrm{X}(\mathbf{x}) = \frac{\mathrm{d}P_\mathrm{X}(\mathbf{x})}{\mathrm{d}\mathbf{x}} \tag{A.2}$$

The random variables considered in this work are assumed to follow a normal or *Gaussian distribution*, described by a mean value μ_X and a standard deviation σ_X. Impressions of the PDF and CDF for a normal distribution with mean $\mu_\mathrm{X} = 0$ and standard deviation $\sigma_\mathrm{X} = 1$, are given in Figure A.1. General expressions for evaluating the expected value $E(\mathbf{X})$, variance $\mathrm{Var}(\mathbf{X})$ and skewness of the random variable are given by Equations (A.3), (A.4) and (A.5) respectively. When these values are known, one can determine other parameters like the mean μ_X and standard deviation σ_X [50].

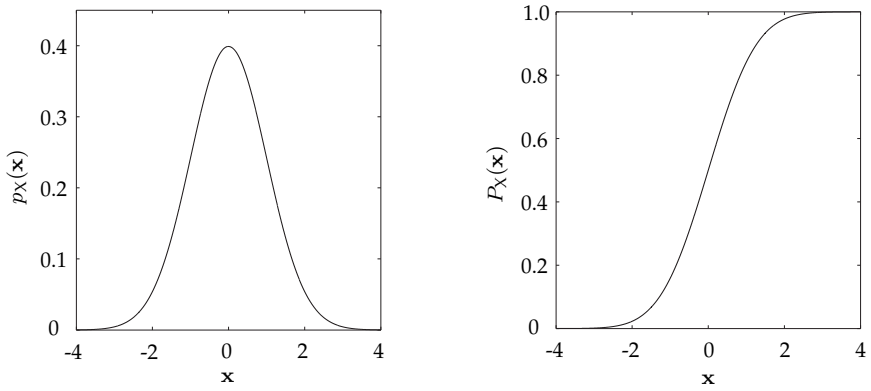

(a) (b)

Figure A.1 *(a) Probability Density Function (PDF) and (b) Cumulative Distribution Function (CDF) of a Gaussian distribution*

$$E(\mathbf{X}) = \mu_X = \int_{-\infty}^{\infty} \mathbf{x} p_X(\mathbf{x})\, \mathrm{d}\mathbf{x} \tag{A.3}$$

$$\mathrm{Var}(\mathbf{X}) = \sigma_X^2 = \int_{-\infty}^{\infty} (\mathbf{x} - \mu_X)^2 p_X(\mathbf{x})\, \mathrm{d}\mathbf{x} \tag{A.4}$$

$$\mathrm{Skewness} = \int_{-\infty}^{\infty} (\mathbf{x} - \mu_X)^3 p_X(\mathbf{x})\, \mathrm{d}\mathbf{x} \tag{A.5}$$

In most metal forming processes, it is necessary to consider more than one random variable. These variables can be modeled separately; however, it is more prudent to model the uncertainties jointly. For example, one can think of a correlation between certain material parameters, see [22, 83]. The modeling of joint uncertainties for two random variables is discussed below. However, this can easily be extended to more than two random variables.

Suppose $\mathbf{X}$ and $\mathbf{Y}$ are two random variables with their *joint PDF* denoted as

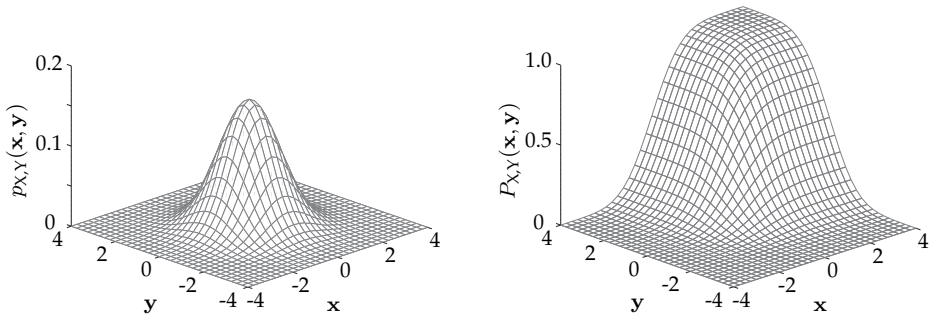

(a) (b)

Figure A.2 *(a) Joint probability density function and (b) joint cumulative distribution function of two random variables*

$p_{X,Y}(\mathbf{x},\mathbf{y})$. The *joint CDF* is given by:

$$P_{X,Y}(\mathbf{x},\mathbf{y}) = \Pr[\mathbf{X} \leq \mathbf{x}, \mathbf{Y} \leq \mathbf{y}] = \int_{-\infty}^{\mathbf{y}} \int_{-\infty}^{\mathbf{x}} p_{X,Y}(\mathbf{u},\mathbf{v})\,\mathrm{d}\mathbf{u}\,\mathrm{d}\mathbf{v} \tag{A.6}$$

For two random variables, impressions of the joint PDF and joint CDF are given in Figure A.2.

If the random variables are statistically dependent on the values of another random variable, the separate conditional probability density functions are given by:

$$p_{X|Y}(\mathbf{x}|\mathbf{y}) = \frac{p_{X,Y}(\mathbf{x},\mathbf{y})}{p_Y(\mathbf{y})} \tag{A.7}$$

or

$$p_{Y|X}(\mathbf{y}|\mathbf{x}) = \frac{p_{X,Y}(\mathbf{x},\mathbf{y})}{p_X(\mathbf{x})} \tag{A.8}$$

If $\mathbf{X}$ and $\mathbf{Y}$ are statistically independent, it holds that:

$$p_{X,Y}(\mathbf{x},\mathbf{y}) = p_X(\mathbf{x})p_Y(\mathbf{y}) \tag{A.9}$$

A measure for the dependence or independence between two random variables is given by the *covariance*:

$$\mathrm{Cov}(\mathbf{X},\mathbf{Y}) = E[(\mathbf{X}-\mu_X)(\mathbf{Y}-\mu_Y)] = E(\mathbf{XY}) - E(\mathbf{X})E(\mathbf{Y}) \tag{A.10}$$

The covariance $\mathrm{Cov}(\mathbf{X},\mathbf{Y})$ indicates the degree of linear relationship between two variables. Note that the variance is a special case of the covariance when both variables are identical. For statistically independent variables, it is shown in e.g. [50] using Equation (A.3) and Equation (A.9) that $E(\mathbf{XY}) = E(\mathbf{X})E(\mathbf{Y})$ resulting in $\mathrm{Cov}(\mathbf{X},\mathbf{Y}) = 0$. Otherwise it can be positive or negative depending on the slope of the linear relation. Nondimensionalizing the covariance results in the *correlation coefficient*:

$$\rho_{X,Y} = \frac{\mathrm{Cov}(\mathbf{X},\mathbf{Y})}{\sigma_X \sigma_Y} \tag{A.11}$$

Values for the correlation coefficient range between -1 and 1. As a rule of thumb proposed by Haldar and Mahadevan [50], two variables can be considered to be statistically independent if the magnitude of the correlation coefficient is less than ± 0.3 and can be considered correlated if the magnitude of the coefficient is greater than ± 0.9.

Appendix B

Variable screening

A summary of the screening techniques used in this work is provided in this appendix following the theory outlined in [100]. The use of fractional factorial designs for variable screening is based on the idea that if an optimization problem contains multiple variables, the optimization problem is likely to be primarily driven by some of the main or linear effects and low-order interactions rather than higher order effects and interactions. This idea is referred to as *the Sparsity-of-Effects Principle* and will be further outlined below.

B.1 Fractional factorial design

For variable reduction, enough 'understanding' of the problem under consideration is obtained by evaluating the main effects only [19]. This information can be obtained by running a fraction of a full factorial design as presented in Figure 3.2a, saving on the number of FE simulations to be performed for screening purposes.

As an example, consider the situation in which $k = 3$ variables, referred to as x_1, x_2 and x_3, are of interest. Figure B.1 shows two one-half fractions of a $2^k = 2^3$ full factorial design. Both resolution III fractional factorial designs require performing $2^{k-q}_{\text{III}} = 2^{3-1}_{\text{III}} = 4$ FE simulations. The DOE plan corresponding to the design of Figure B.1a is provided in Table B.1 where -1 denotes the lowest level of a variable whereas 1 denotes the highest level, i.e. lb and ub respectively.

The reduction of the total number of simulations using a fraction of a full factorial design comes at a cost of not being able to uniquely determine the main effects.

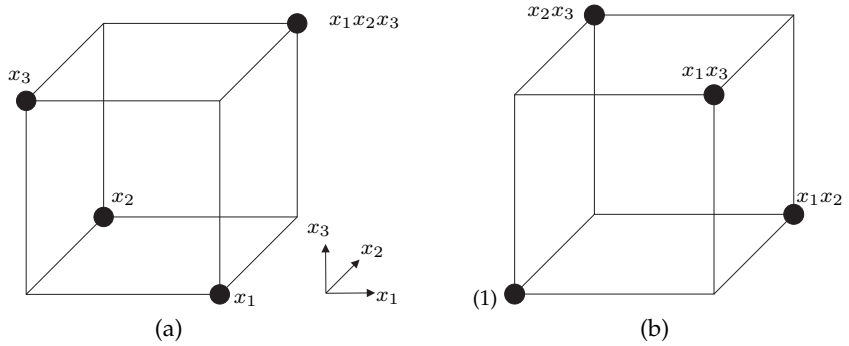

Figure B.1 2^{3-1}_{III} *fractional factorial designs*

As an example, the main effect of x_1 can be calculated from Table B.1 using Equation (3.2) resulting in:

$$\text{effect}(x_1) = \frac{y_1 - y_2 - y_3 + y_4}{2} \tag{B.1}$$

The interaction effect x_2x_3 can be calculated in a similar way resulting in:

$$\text{effect}(x_2x_3) = \frac{y_1 - y_2 - y_3 + y_4}{2} \tag{B.2}$$

Comparing Equations (B.1) and (B.2) shows that the effect of x_1 equals the effect x_2x_3. Consequently, it is impossible to differentiate between the effect of x_1 and x_2x_3. In fact, if one estimates the effect x_1, actually the effect $x_1 + x_2x_3$ is estimated. The main effect of x_1 is *aliased* or *confounded* with the two-factor interaction x_2x_3. The same holds for the main effect of x_2 which is aliased with the two-factor interaction x_1x_3, and the main effect of x_3 which is aliased with

Table B.1 2^{3-1}_{III} *fractional factorial design as visualized in Figure B.1a*

Simulation no.	x_1	x_2	x_3	y
1	1	-1	-1	y_1
2	-1	1	-1	y_2
3	-1	-1	1	y_3
4	1	1	1	y_4

Table B.2 2^{k-q}_{III} *fractional factorial designs*

Specification	k	q	n
2^{3-1}_{III}	3	1	4
2^{4-1}_{III}	4	1	8
2^{5-2}_{III}	5	2	8
2^{6-3}_{III}	6	3	8
2^{7-4}_{III}	7	4	8
2^{8-4}_{III}	8	4	16
2^{9-5}_{III}	9	5	16
2^{10-6}_{III}	10	6	16

the two-factor interaction x_1x_2. For determining which of the effects are actually significant, the *Sparsity-of-Effects Principle* states that the higher order terms can be neglected. For the purpose of screening, the estimation of the main effects using fractional factorial designs provides enough information for variable reduction. For independently estimating interaction effects, a higher order resolution (e.g. IV or V) should be employed.

For the design as given in Figure B.1a, 4 simulations are required to estimate the main effects of the three variables x_1, x_2 and x_3. That is, a one-half fraction $(1/2)^q = (1/2)^1$ fraction of the full factorial design is used. For an increasing number of variables, the fraction q of a resolution III design increases to enable estimating the main effects, see Table B.2. Figure B.1b shows an alternate fraction of the one-half fraction as given in Figure B.1a. Although both fractions can be used for variable screening, the fraction should be chosen by the engineer for which the interaction effects are expected to be small compared to the main effects.

Appendix C

Metamodeling techniques

The aim of a metamodel $\hat{\mathbf{y}}$ is to accurately approximate a true model $\mathbf{y}$. In the context of this work, the true model is the simulation response (objective or constraints). The metamodel and true model are a function of design variables $\mathbf{x}$ and (in case present) noise variables $\mathbf{z}$. For notational simplicity the dependence on $\mathbf{x}$ and $\mathbf{z}$ is omitted here. Consider a non-linear regression model, including a random error term ε, defined by:

$$\mathbf{y} = \hat{\mathbf{y}} + \varepsilon \tag{C.1}$$

What follows is a description of different types of metamodeling techniques used in this work to construct $\hat{\mathbf{y}}$.

C.1 Response surface methodology

The *Response Surface Methodology* (RSM) is a well-known method for creating an approximate model of a set of response measurements [100]. Although this method is generally used for constructing a response surface from physical experiments, many authors have applied it to numerical experiments as well. One of the reasons is that it is able to filter out numerical noise [43, 46, 107].

Using RSM, a polynomial model is fitted through the response measurements or observations $\mathbf{y}$ allowing for a random error term ε. Equation (C.1) can now be

written in matrix form as:

$$\mathbf{y} = \mathbf{X}\boldsymbol{\beta} + \boldsymbol{\varepsilon} \tag{C.2}$$

where $\mathbf{X}$ is a matrix containing the levels of independent variables, $\boldsymbol{\beta}$ is a vector of regression coefficients, and $\boldsymbol{\varepsilon}$ is a vector of random error terms. Note that the design matrix $\mathbf{X}$ can incorporate non-linear terms with respect to the variables. The order of these terms is referred to as the order of the polynomial model. The metamodel is given by $\hat{\mathbf{y}} = \mathbf{X}\boldsymbol{\beta}$. The unknown regression coefficients $\boldsymbol{\beta}$ are determined by minimizing the error sum of squares at the training points, also referred to as quadratic loss function or L_2-norm:

$$\boldsymbol{\varepsilon}^{\mathrm{T}}\boldsymbol{\varepsilon} = (\mathbf{y} - \mathbf{X}\boldsymbol{\beta})^{\mathrm{T}}(\mathbf{y} - \mathbf{X}\boldsymbol{\beta}) \tag{C.3}$$

Differentiating Equation (C.3) with respect to $\boldsymbol{\beta}$ and setting the results to zero yields the best estimation of $\boldsymbol{\beta}$:

$$\hat{\boldsymbol{\beta}} = (\mathbf{X}^{\mathrm{T}}\mathbf{X})^{-1}\mathbf{X}^{\mathrm{T}}\mathbf{y} \tag{C.4}$$

where $\hat{\boldsymbol{\beta}}$ denotes the estimator of $\boldsymbol{\beta}$. The response prediction $\hat{y}_0$ at an untried point $\mathbf{x}_0$ is now given by the explicit function:

$$\hat{y}_0 = \mathbf{x}_0^{\mathrm{T}}\hat{\boldsymbol{\beta}} \tag{C.5}$$

The variance at this location is given by [100]:

$$\mathrm{Var}(\hat{y}_0) = \sigma^2\mathbf{x}_0^{\mathrm{T}}(\mathbf{X}^{\mathrm{T}}\mathbf{X})^{-1}\mathbf{x}_0 \tag{C.6}$$

The unbiased estimation of the error variance σ^2 is given by:

$$\begin{aligned}\hat{\sigma}^2 &= \frac{\boldsymbol{\varepsilon}^{\mathrm{T}}\boldsymbol{\varepsilon}}{n-p} \\ &= \frac{\sum_{i=1}^{n} \varepsilon_i^2}{n-p} \\ &= \frac{\sum_{i=1}^{n} (\hat{y}_i - y_i)^2}{n-p}\end{aligned} \tag{C.7}$$

where n is the number of response measurements and p is the number of regression coefficients. For a linear metamodel, it holds that $p = m + 1$ where m equals the number of design variables. The prediction uncertainty of the metamodel is given by the square root of the variance as calculated in Equation (C.6).

C.1.1 Regression in response surface methodology

Instead of estimating the unknown regression coefficients based on the error sum of squares through Equation (C.3), in the case of ridge regression (see Chapter 6.3.1) these are obtained by minimizing the regularized loss function:

$$\boldsymbol{\varepsilon}^{\mathrm{T}}\boldsymbol{\varepsilon} + \lambda \boldsymbol{\beta}^{\mathrm{T}}\boldsymbol{\beta} \tag{C.8}$$

where the regularization parameter λ governs the relative importance of the regularization term, penalizing large weights, compared with the error sum of squares term. The ridge regression formulation results in the solution:

$$\hat{\boldsymbol{\beta}} = (\mathbf{X}^{\mathrm{T}}\mathbf{X} - \lambda \mathbf{I})^{-1}\mathbf{X}^{\mathrm{T}}\mathbf{y} \tag{C.9}$$

where the optimal λ can be identified by generalized cross-validation as discussed in Chapter 6.3.1. A modification of Equation (C.7) in the case of ridge regression is provided in MacKay [89].

C.2 Kriging

Computer simulations are deterministic in nature, meaning that repeated runs for the same input parameters will yield exactly the same result. Therefore, the remaining error, denoted by ε in Equation (C.1), should formally be zero as reasoned in [122]. In other words, the metamodel should interpolate through the response values at the training points.

The approach proposed in Jones et al. [65] and Sacks et al. [118] is referred to as *Design and Analysis of Computer Experiments* (DACE) where generally Kriging is used as an interpolation technique. Kriging involves a defined base function or regression part, similar to fitting an RSM metamodel. The random error term ε in Equation (C.1) is replaced by basis functions or a stochastic part $Z(\mathbf{x})$ to compute the exact predictions at the available training points:

$$\mathbf{y} = \mathbf{X}\boldsymbol{\beta} + Z(\mathbf{x}) \tag{C.10}$$

where $Z(\mathbf{x})$ is assumed to be a Gaussian stochastic process with mean zero, process variance σ_z^2, and spatial covariance function given by:

$$\text{cov}(Z(x_i), Z(x_j)) = \sigma_z^2 R(x_i, x_j) \tag{C.11}$$

where $R(x_i, x_j)$ describes the correlation between the known measurement points x_i and x_j. The correlation function R determines the shape of the metamodel between measurement points and is, in the case of a Gaussian exponential correlation function, given by:

$$R(\theta, x_i, x_j) = \exp^{-\theta(x_i - x_j)^2} \tag{C.12}$$

Now, in case m design variables are present, the correlation function depends on the m one-dimensional correlation functions as follows:

$$R(\boldsymbol{\theta}, \mathbf{x}_i, \mathbf{x}_j) = \prod_{l=1}^{m} \exp^{-\theta_l(x_{il} - x_{jl})^2} \tag{C.13}$$

The entries of the vectors $\boldsymbol{\theta} = \{\theta_1, \theta_2, \ldots, \theta_m\}^{\mathrm{T}}$ and the distance between the

known measurement points $\mathbf{x}_i$ and $\mathbf{x}_j$ determine the structure of $R(\boldsymbol{\theta}, \mathbf{x}_i, \mathbf{x}_j)$. Analogous to RSM, a Kriging metamodel is fitted in order to minimize the mean square error between the Kriging metamodel $\hat{y}(\mathbf{x})$ and the true but unknown response function $y(\mathbf{x})$ [118]:

$$\begin{aligned} &\min\ E(\hat{y}(\mathbf{x}) - y(\mathbf{x}))^2 \\ &\text{s.t. } E(\hat{y}(\mathbf{x}) - y(\mathbf{x})) = 0 \end{aligned} \tag{C.14}$$

In other words, the mean square error is minimized subject to the unbiasedness constraint that ensures there is no systematic error between the metamodel and the true function. The Best Linear Unbiased Predictor (BLUP) $\hat{y}_0$ at an untried point $\mathbf{x}_0$ is now given by [88, 122]:

$$\hat{y}_0 = \mathbf{x}_0^{\mathrm{T}}\boldsymbol{\beta} + \mathbf{r}_0^{\mathrm{T}}\mathbf{R}^{-1}(\mathbf{y} - \mathbf{X}\boldsymbol{\beta}) \tag{C.15}$$

where $\mathbf{X}$ is the design matrix containing the training points. The vector $\mathbf{r}_0$ contains the correlation between the point (x_0, y_0) and the known measurement (x_i, y_i). $\mathbf{R}$ is a matrix containing the correlation between the training points given by Equation (C.12).

The Mean Square Error (MSE) can be calculated at location x_0 by:

$$\mathrm{MSE}(y_0) = \sigma_z^2\left(1 - \begin{bmatrix}\mathbf{x}_0^{\mathrm{T}}\mathbf{r}_0^{\mathrm{T}}\end{bmatrix}\begin{bmatrix}\mathbf{0} & \mathbf{X}^T \\ \mathbf{X} & \mathbf{R}^{-1}\end{bmatrix}\begin{bmatrix}\mathbf{x}_0 \\ \mathbf{r}_0\end{bmatrix}\right) \tag{C.16}$$

The unknown Kriging parameters $\boldsymbol{\beta}$, σ_z^2, and $\boldsymbol{\theta}$ can be estimated by Maximum Likelihood Estimation (MLE) [118]. Note that maximization of the likelihood function is equivalent to a minimization of the error sum of squares when the error can be assumed to be Gaussian noise. This optimization procedure is solved using the DACE MATLAB toolbox provided by Lophaven et al. [88].

C.2.1 Regression in Kriging

If data is contaminated with noise, it makes more sense to approximate the given data instead of interpolating the data. The generalization capability of Kriging models can be improved by adding a regularization constant λ to the leading diagonal of the correlation matrix $\mathbf{R}$ as $\mathbf{R} + \lambda\mathbf{I}$ [37]. This enables a

Kriging model to regress the data and approximate noisy functions. Without the regression constant, each point is given an exact correlation with itself, forcing the metamodel to pass through the training points. The regression constant enables control on the interpolation feature of the Kriging model. The regression constant λ is now optimized along with the other unknown parameters in the MLE providing the regression Kriging predictor:

$$\hat{y}_0 = \mathbf{x}_0^{\mathrm{T}}\boldsymbol{\beta} + \mathbf{r}_0^{\mathrm{T}}(\mathbf{R} + \lambda\mathbf{I})^{-1}(\mathbf{y} - \mathbf{X}\boldsymbol{\beta}) \tag{C.17}$$

A modification of Equation (C.16) in the case of regression Kriging is provided in Forrester et al. [36].

C.3 Neural networks

The typical building blocks of neural networks are layers, basis functions, neurons and connections. Differences in the learning rules and the network topology result in different NN architectures or NN concepts. In this work, *two layer feedforward backpropagation* NN are utilized. A two layer NN architecture is presented in Figure C.1. This architecture is referred to as *feed forward* since information only proceeds forward through the network and there are no feedback loops in between the layers. Starting with the first layer of S neurons, the output $\mathbf{a}$ of the so-called *Hidden Layer* (HL) is given by:

$$\mathbf{a} = \mathbf{G}^{(1)}(\mathbf{d}_{(\mathrm{HL})}), \quad \mathbf{d}_{(\mathrm{HL})} = \mathbf{W}_{(\mathrm{HL})}\mathbf{x} + \mathbf{b}_{(\mathrm{HL})} \tag{C.18}$$

The layer includes a weight matrix $\mathbf{W}_{(\mathrm{HL})} \in \mathbb{R}^{S\times m}$, an input vector $\mathbf{x}$, a bias vector $\mathbf{b}_{(\mathrm{HL})} = \{b_{(\mathrm{HL})1}, b_{(\mathrm{HL})2}, \ldots, b_{(\mathrm{HL})S}\}^{\mathrm{T}}$, basis functions or activation functions $\mathbf{G}$ and an output vector $\mathbf{a} = \{a_1, a_2, \ldots, a_S\}^{\mathrm{T}}$. The basis functions used in the hidden layer are the *tangent sigmoid* functions $G^{(1)}(d)$ which can take any arbitrary input value $d \in \mathbb{R}$ and suppresses the output into the range $(-1, 1)$ by:

$$G^{(1)}(d) = \frac{2}{1 + \exp(-2d)} - 1 \tag{C.19}$$

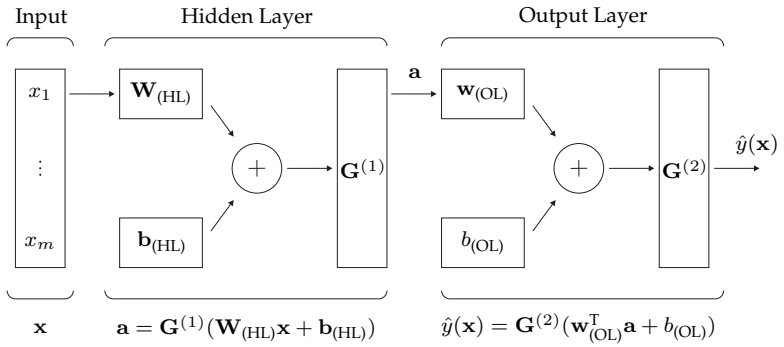

Figure C.1 *Two layer NN architecture*

The output of the linear basis function $G^{(2)}(d)$ equals its input:

$$G^{(2)}(d) = d \tag{C.20}$$

The output of the hidden layer $\mathbf{a}$ is the input for the next layer. This layer is referred to as the *Output Layer* (OL) since its output is also the output of the network. The basis functions used in the hidden layer are the tangent sigmoid function, whereas linear functions are used in output layer. These functions are preferred because of their differentiability which enables determining partial derivatives used in parameter estimation [5].

The predictor of a two layer architecture with a single network output is now given by:

$$\hat{\mathbf{y}} = \mathbf{G}^{(2)}(\mathbf{d}_{(\text{OL})}) = \mathbf{d}_{(\text{OL})}, \quad \mathbf{d}_{(\text{OL})} = \mathbf{w}_{(\text{OL})}^{\text{T}}\mathbf{a} + b_{(\text{OL})} \tag{C.21}$$

In essence, Equation (C.21) is the linear combination of the weighted tangent sigmoid basis functions. The unknown parameters in Equation (C.21) are the bias term of the output layer $b_{(\text{OL})}$, the vector with output layer weights $\mathbf{w}_{(\text{OL})} = \{w_{(\text{OL})1}, w_{(\text{OL})2}, \ldots, w_{(\text{OL})S}\}^{\text{T}}$ and the hidden layer bias vector $\mathbf{b}_{(\text{HL})}$ and weight matrix $\mathbf{W}_{(\text{HL})}$. The unknown weight and bias parameters can be estimated by minimizing the error sum of squares at the training points. This unconstrained non-linear optimization problem is solved using a *Levenberg-Marguardt* optimization algorithm. The procedure is also referred to as Bayesian regulation back propagation [89].

The variance estimation theory for non-linear regression as in Equation (C.6) also applies to NN [28]:

$$\mathrm{Var}(\hat{y}_0) = \sigma^2 \mathbf{g}_0^{\mathrm{T}} (\mathbf{J}^{\mathrm{T}} \mathbf{J})^{-1} \mathbf{g}_0 \tag{C.22}$$

where $\mathbf{J}$ is a matrix whose ijth entry is given by $\partial \hat{y}(\mathbf{x}_i)/\partial z_j$ and $\mathbf{g}_0$ is a vector whose ith entry is $\partial \hat{y}(\mathbf{x}_0)/\partial z_j$, evaluated at an untried point $\mathbf{x_0}$ and at the optimal parameter vector $\hat{\mathbf{z}}$ where $\mathbf{z}$ represents the collection of all unknown parameters. Note that for estimating the weights in NN, $\mathbf{J}$ is already calculated as part of the optimization procedure. The unbiased estimation of the error variance σ^2 is given by Equation (C.7). The procedure as described in this section is solved using the NN MATLAB toolbox [92].

C.3.1 Regression in neural networks

With many weight and bias parameters involved in NN, there is a considerable danger of over-fitting. The generalization capability can be improved by minimizing the regularized loss function as in Equation (C.8). Note that regularization both assists in avoiding over-fitting due to a high number of hidden units S (and thus many weights and biases to be determined) and the presence of numerical noise in the calculated response data. The loss function is minimized using the *Levenberg-Marguardt* algorithm as implemented in the NN MATLAB toolbox [92]. A modification of the error variance in the case of ridge regression is provided in [28].

Appendix D

Analysis of variance

A summary of the ANalysis Of VAriance (ANOVA) techniques used in this work is provided in this appendix, following the theory as outlined in [19, 100]. ANOVA is a collection of statistical techniques which can be used, among other things, to analyze the significance of a metamodel describing the response behavior. Underlying assumptions are that the random error term ε for a linear regression model (see Equation (C.1)) is normally and independently distributed with mean $\mu_\varepsilon = 0$ and variance σ_ε^2, abbreviated $\varepsilon \sim \mathcal{N}(0, \sigma_\varepsilon^2)$. Moreover, the error variance is homogeneous, i.e. the variance of the error does not vary for different variables. As a result of these assumptions, the response measurements y_i are normally and independently distributed with mean $\hat{y}_i$ and variance σ^2. This appendix focuses on techniques that can be used to validate the metamodel accuracy with respect to a set of response measurements. Additionally, ANOVA can be used to validate the aforementioned underlying assumptions, for which the interested reader is referred to [19].

D.1 Partitioning of variance

The name ANOVA refers to the decomposition of the total variability in the response variable y into components attributable to different sources of variation, i.e. the error sum of squares (SSE), the regression sum of squares (SSR) and the total sum of squares (SST):

$$\text{SSE} = \sum_{i=1}^{n} (y_i - \hat{y}_i)^2 \tag{D.1}$$

$$\text{SSR} = \sum_{i=1}^{n} (\hat{y}_i - \overline{y})^2 \tag{D.2}$$

$$\text{SST} = \sum_{i=1}^{n} (y_i - \overline{y})^2 \tag{D.3}$$

This is visualized in Figure D.1 for a linear RSM model where y_i are the response measurements, $\overline{y}$ is the mean of the n response measurements and $\hat{y}_i$ is the metamodel prediction of measurement i. The total sum of squares is partitioned into components related to error sum of squares (SSE) and the regression sum of squares (SSR):

$$\text{SST} = \text{SSE} + \text{SSR} \tag{D.4}$$

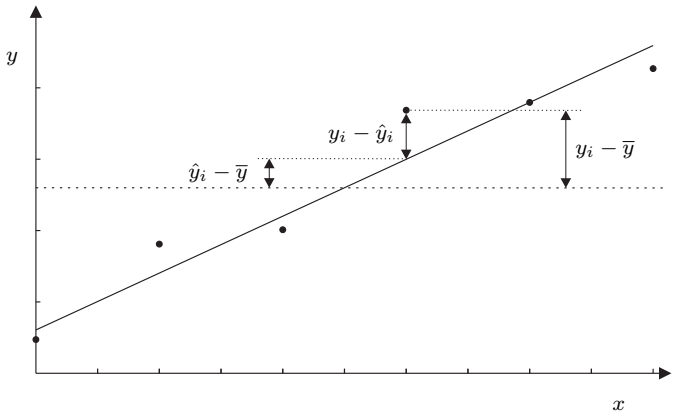

Figure D.1 *Partitioning of variation in ANOVA for a linear regression model*

D.2 Coefficient of determination

The most commonly used ANOVA statistic for providing information about the goodness-of-fit of a model is the coefficient of determination R^2:

$$R^2 = \frac{SSR}{SST} = 1 - \frac{SSE}{SST} \tag{D.5}$$

The R^2-value ranges between 0 and 1. In general, a larger R^2-value indicates a better approximation of the response measurements by the metamodel. A R^2-value of 1 indicates that the metamodel perfectly fits the response measurements.

Bibliography

[1] H. Abdi and L. J. Williams. Principal component analysis. *Wiley Interdisciplinary Reviews: Computational Statistics*, 2:433–459, 2010.

[2] M. Abspoel, M. Scholting, and E. H. Atzema. Characterisation and modelling of the stochastic behaviour of deep drawing steels. In *Proceedings of the Forming Technology Forum, Zurich, Switzerland*, 2011.

[3] H. Agarwal. *Reliability based design optimization: formulations and methodologies*. PhD thesis, University of Notre Dame, Notre Dame, USA, 2004.

[4] M. Ahammed and R. E. Melchers. Gradient and parameter sensitivity estimation for systems evaluated using Monte Carlo analysis. *Reliability Engineering and System Safety*, 91:594–601, 2006.

[5] D. Akcay Perdahcioglu. *Optimizing the dynamic behavior of structures*. PhD thesis, University of Twente, Enschede, The Netherlands, 2010.

[6] Y. G. An, H. Vegter, L. Carless, and M. Lambriks. A novel yield locus description by combining the Taylor and the relaxed Taylor theory for sheet steels. *International Journal of Plasticity*, 27(11):1758–1780, 2011.

[7] T. W. Anderson and D. A. Darling. Asymptotic theory of certain 'goodness-of-fit' criteria based on stochastic processes. *Annals of Mathematical Statistics*, 23:193–212, 1952.

[8] D. Aspenberg, R. Larsson, and L. Nilsson. An evaluation of the statistics of steel material model parameters. *Journal of Materials Processing Technology*, 212:1288–1297, 2012.

[9] E. H. Atzema, M. Abspoel, P. Kömmelt, and M. Lambriks. Towards robust simulations in sheet metal forming. *International Journal of Material Forming*, 2(1):351–354, 2009.

[10] E. H. Atzema, H. Brouwer, and P. Kömmelt. Long and short term strategy to deal with material property variation in sheet-metal forming. In *Proceedings of the International Deep Drawing Research Group (IDDRG) conference, Porto, Portugal*, 2006.

[11] S. K. Au. Reliability based design sensitivity by efficient simulation. *Computers and Structures*, 83:1048–1061, 2005.

[12] C. Auer, M. Erdbrügge, and R. Göbel. Comparison of multivariate methods for

robust parameter design in sheet metal spinning. *Applied Stochastic Models in Business and Industry*, 20:201–218, 2004.

[13] J. F. M. Barthelemy and R. T. Haftka. Approximation concepts for optimum structural design - a review. *Structural and Multidisciplinary Optimization*, 5:129–144, 1993.

[14] P. Beiter and P. Groche. On the development of novel light weight profiles for automotive industries by roll forming of tailor rolled blanks. *Key Engineering Materials*, 473:45–52, 2011.

[15] A. Ben-Tal and A. Nemirovski. Robust optimization - methodology and applications. *Mathematical Programming, Series B*, 92:453–480, 2002.

[16] Y. Bergström. Dislocation model for the stress strain behavior of polycrystalline FE with special emphasis on the variation of the densities of mobile and immobile dislocations. *Materials Science and Engineering*, 5:193–200, 1969.

[17] H. G. Beyer and B. Sendhoff. Robust optimization - A comprehensive survey. *Computer Methods in Applied Mechanics and Engineering*, 196:3190–3218, 2007.

[18] C. M. Bishop. *Pattern recognition and machine learning*. Springer Science + Business Media LCC, New York, USA, 2006.

[19] M. H. A. Bonte. *Optimisation strategies for metal forming processes*. PhD thesis, University of Twente, Enschede, The Netherlands, 2007.

[20] P. Breitkopf, H. Naceur, A. Rassineux, and P. Villon. Moving least squares response surface approximation: Formulation and metal forming applications. *Computers and Structures*, 83:1411–1428, 2005.

[21] Q. V. Bui and J. P. Ponthot. Numerical simulation of cold roll-forming processes. *Journal of Materials Processing Technology*, 202(1-3):275–282, 2008.

[22] B. D. Carleer. Applicability of stochastical methods in the control of the scatter influence of constitutive parameters. In *Proceedings of the Forming Technology Forum, Zurich, Switzerland*, 2006.

[23] D. B. Carleer. Scattering parameters is not a problem anymore for robust forming processes. In *Proceedings of the International Deep Drawing Research Group (IDDRG) conference, Sindelfingen, Germany*, 2004.

[24] W. S. Cleveland and S. J. Devlin. Locally-weighted regression: an approach to regression analysis by local fitting. *Journal of the American Statistical Association*, 83(403):596–610, 1988.

[25] P. Craven and G. Whaba. Smoothing noisy data with spline functions. *Numerical Mathematics*, 31:377–403, 1979.

[26] T. de Souza and B. Rolfe. Multivariate modelling of variability in sheet metal forming. *Journal of Materials Processing Technology*, 203:1–12, 2008.

[27] T. de Souza and B. Rolfe. Characterising material and process variation effects on springback robustness for a semi-cylindrical sheet metal forming process. *International Journal of Mechanical Sciences*, 52:1756–1766, 2010.

[28] R. D. D. de Veaux, J. Schumi, J. Schweinsberg, and L. H. Ungar. Prediction intervals

for neural networks via nonlinear regression. *Technometrics*, 40(4):273–282, 1998.

[29] DiekA. In-house implicit finite element code of the University of Twente, Enschede, The Netherlands, 2013.

[30] I. Doltsinis and Z. Kang. Robust design of structures using optimization methods. *Computer Methods in Applied Mechanics and Engineering*, 193:2221–2237, 2004.

[31] X. Du and W. Chen. Methodology for managing the effect of uncertainty in simulation-based design. *American Institute of Aeronautics and Astronautics*, 38:1471–1477, 2000.

[32] X. Du and W. Chen. Efficient uncertainty analysis methods for multidisciplinary robust design. *American Institute of Aeronautics and Astronautics*, 40(3):545–552, 2002.

[33] I. Elishakoff, R. T. Haftka, and J. Fang. Structural design under bounded uncertainty - optimization with anti-optimization. *Computers and Structures*, 53:1401–1405, 1994.

[34] M. T. M. Emmerich, K. C. Giannakoglou, and B. Naujoks. Single- and multiobjective evolutionary optimization assisted by Gaussian random field metamodels. *IEEE Transactions on Evolutionary Computation*, 10:421–439, 2006.

[35] EXAscan. Creaform Handyscan 3D portable laser scanner. Available from: `http://www.creaform3d.com/en/default.aspx`, 2012.

[36] A. Forrester, A. J. Keane, and N. W. Bresslo. Design and analysis of noisy computer experiments. *American Institute of Aeronautics and Astronautics*, 44:2331–2339, 2006.

[37] A. Forrester, A. Sobester, and A. Keane. *Engineering design via surrogate modelling: a practical guide.* John Wiley & Sons Inc., New York, USA, 2008.

[38] Ø. Fyllingen, O. S. Hopperstad, and M. Langseth. *Robustness studies of structures subjected to large deformations*. PhD thesis, Norwegian University of Science and Technology, Trondheim, Norway, 2008.

[39] G. Gantar and K. Kuzman. Optimization of stamping processes aiming at maximal process stability. *Journal of Materials Processing Technology*, 167:237–243, 2005.

[40] C. Garcia. Artificial intelligence applied to automatic supervision, diagnosis and control in sheet metal stamping processes. *Journal of Materials Processing Technology*, 164–165:1351–1357, 2005.

[41] J. Gerlach. Sensitivity and robustness analysis for quantification of the influence of material scattering. In *Proceedings of the Forming Technology Forum, Zurich, Switzerland*, 2011.

[42] R. G. Ghanem and P. D. Spanos. *Stochastic finite elements: a spectral approach, revised edition*. Dover Publications Inc., New York, USA, New York, 2003.

[43] A. A. Giunta, J. M. Dudley, R. Narducci, B. Grossman, R. T. Haftka, W. H. Mason, and L. T. Watson. Noisy aerodynamic response and smooth approximations in HSCT design. In *Proceedings of the 5th AIAA/USAF/NASA/ISSMO Symposium on Multidisciplinary Analysis and Optimization, Panama City, Florida, USA*, volume 94-4376-CP, pages 1117–1128, 1994.

[44] V. Gödel and M. Merklein. Variation of deep drawing steel grades' properties in dependency of the stress state and its impact on FEA. *International Journal of Material*

Forming, 4:183–192, 2011.

[45] V. Gödel, M. Wahl, and M. Merklein. Modelling of material properties variation in FE-simulation. In *Proceedings of the Forming Technology Forum 2011, Zurich, Switzerland*, 2011.

[46] T. Goel, R. T. Haftka, M. Papila, and W. Shyy. Generalized pointwise bias error bounds for response surface approximations. *International Journal for Numerical Methods in Engineering*, 65:2035–2059, 2006.

[47] G. H. Golub, M. Heath, and G. Wahba. Generalized cross-validation as a method choosing a good ridge parameter. *Technometrics*, 21:215–223, 1979.

[48] P. Groche, P. Beiter, and M. Henkelmann. Prediction and inline compensation of springback in roll forming of high and ultra-high strength steels. *Production Engineering*, 2(4):401–407, 2008.

[49] F. P. Grooteman. Advanced stochastic method for probabilistic analysis. Technical report, National Aerospace Laboratory, Amsterdam, The Netherlands, 1999.

[50] A. Haldar and S. Mahadevan. *Probability, reliability and statistical methods in engineering design*. John Wiley & Sons Inc., New York, USA, 2000.

[51] G. T. Halmos. *Roll forming handbook*. Taylor & Francis Group (CRC Press), Boca Raton, USA, 2006.

[52] Z. W. Han, C. Liu, W. P. Lu, L. Q. Ren, and J. Tong. Spline finite strip analysis of forming parameters in roll forming a channel section. *Journal of Materials Processing Technology*, 159(3):383–388, 2005.

[53] F. Heislitz, H. Livatyali, M. A. Ahmetoglu, G. L. Kinzel, and T. Altan. Simulation of roll forming process with the 3D FEM code PAM-STAMP. *Journal of Materials Processing Technology*, 59(1–2 special issue):59–67, 1996.

[54] J. Hol. *Multi-scale friction modeling for sheet metal forming*. PhD thesis, University of Twente, Enschede, The Netherlands, 2013.

[55] P. Hora, J. Heingärtner, N. Manopulo, L. Tong, D. Hortig, A. Neumann, and K. Roll. On the way from an ideal virtual process to the modelling of the real stochastic behavior. In *Proceedings of the Forming Technology Forum, Zurich, Switzerland*, 2011.

[56] B. Hou, W. Wang, S. Li, Z. Lin, and C. Z. Xia. Stochastic analysis and robust optimization for a deck lid inner panel stamping. *Materials and Design*, 31:1191–1199, 2010.

[57] D. Huang. *Experimental planning and sequential Kriging optimization using variable fidelity data*. PhD thesis, Ohio State University, Columbus, USA, 2005.

[58] D. Huang, T. T. Allen, W. I. Notz, and N. Zeng. Global optimization of stochastic black-box systems via sequential Kriging meta-models. *Journal of Global Optimization*, 34:441–466, 2006.

[59] Y. M. Huang and D. K. Leu. Effects of process variables on V-die bending process of steel sheet. *International Journal of Mechanical Sciences*, 40:631–650, 1998.

[60] A. F. Huele. *Statistical robust design*. PhD thesis, Universiteit van Amsterdam, Amsterdam, The Netherlands, 1998.

[61] T. Jansson, A. Andersson, and L. Nilsson. Optimization of draw-in for an automotive sheet metal part: an evaluation using surrogate models and response surfaces. *Journal of Materials Processing Technology*, 159:426–434, 2005.

[62] T. Jansson, L. Nilsson, and R. Moshfegh. Reliability analysis of a sheet metal forming process using Monte Carlo analysis and metamodels. *Journal of Materials Processing Technology*, 202:255–268, 2008.

[63] H. A. Jensen, M. A. Valdebenito, G. I. Schuëller, and D. S. Kusanovic. Reliability based optimization of stochastic systems using line search. *Computer Methods in Applied Mechanics and Engineering*, 198:3915–3924, 2009.

[64] R. Jin, X. Du, and W. Chen. The use of metamodeling techniques for optimization under uncertainty. *Structural and Multidisciplinary Optimization*, 25:99–116, 2003.

[65] D. R. Jones, M. Schonlau, and W. J. Welch. Efficient global optimization of expensive black-box functions. *Journal of Global Optimization*, 13:455–492, 1998.

[66] F. Jurecka, M. Ganser, and K. Bletzinger. Update scheme for sequential spatial correlation approximations in robust design optimisation. *Computers and Structures*, 85:606–614, 2007.

[67] Z. Kang. *Robust design optimization of structures under uncertainties*. PhD thesis, University of Stuttgart, Stuttgart, Germany, 2005.

[68] J. Kim, W. J. Song, and B. S. Kang. Probabilistic modeling of stress-based FLD in tube hydroforming process. *Journal of Mechanical Science and Technology*, 23:2891–2902, 2010.

[69] S. D. Kini. *An approach to integrating numerical and response surface models for robust design of production systems*. PhD thesis, Ohio State University, Columbus, USA, 2004.

[70] M. Kleiber, J. Knabel, and J. Rojek. Response surface method for probabilistic assessment of metal forming failures. *International Journal for Numerical Methods in Engineering*, 60:51–67, 2004.

[71] M. Kleiber, J. Rojek, and R. Stocki. Reliability assessment for sheet metal forming operations. *Computer Methods in Applied Mechanics and Engineering*, 191:4511–4532, 2002.

[72] P. N. Koch, R.-J. Yang, and L. Gu. Design for Six Sigma through robust optimization. *Structural and Multidisciplinary Optimization*, 26:235–248, 2004.

[73] A. Krabiell and W. Dahl. Zum Einfluss von Temperatur und Dehngeschwindigkeit auf die Streckgrenze von Baustahlen unterschiedlicher Festigkeit. *Arch. Eisenhüttenwesen*, 52:429–436, 1982.

[74] K. Lange. *Handbook of metal forming*. McGraw - Hill Inc., New York, USA, 1985.

[75] K. H. Lee and G. J. Park. Robust optimization considering tolerances of design variables. *Computers and Structures*, 79:77–86, 2001.

[76] K. H. Lee and G. J. Park. A global robust optimization using Kriging based approximation model. *Journal of the Japan Society of Mechanical Engineers*, 49:779–788, 2006.

[77] J. S. Lehman. *Sequential design of computer experiments for robust parameter design*. PhD thesis, Ohio State University, Columbus, USA, 2002.

[78] J. S. Lehman, T. J. Santner, and W. I. Notz. Designing computer experiments to determine robust control variables. *Statistica Sinica*, 14:571–590, 2004.

[79] D. K. Leu and C. M. Hsieh. The influence of coining force on springback reduction in V-die bending process. *Journal of Materials Processing Technology*, 196:230–235, 2008.

[80] B. Li, T. J. Nye, and D. R. Metzger. Multi-objective optimization of forming parameters for tube hydroforming process based on the Taguchi method. *International Journal of Advanced Manufacturing Technology*, 28:23–30, 2005.

[81] S. H. Li, G. Zeng, Y. F. Ma, Y. J. Guo, and X. M. Lai. Residual stresses in roll-formed square hollow sections. *Thin Walled Structures*, 47(5):505–513, 2009.

[82] Y. Q. Li, Z. S. Cui, X. Y. Ruan, and D. J. Zhang. CAE-based Six Sigma robust optimization for deep-drawing sheet metal process. *International Journal of Advanced Manufacturing Technology*, 30:631–637, 2006.

[83] M. Liewald, R. Schleich, and C. Blaich. New approaches to increase of process robustness in sheet metal forming. In *Proceedings of the Conference on Technology of Plasticity, Gyeongju, Korea*, 2008.

[84] M. Lindgren. Cold roll forming of a U-channel made of high strength steel. *Journal of Materials Processing Technology*, 186(1-3):77–81, 2007.

[85] M. Lindgren. *Experimental and computational investigation of the roll forming process*. PhD thesis, Luleå University of Technology, Luleå, Sweden, 2009.

[86] J. H. Liou and D. Y. Jang. Forging parameter optimization considering stress distributions in products through FEM analysis and robust design methodology. *International Journal of Machine Tools and Manufacture*, 37:775–782, 1997.

[87] M. Lombardi and R. T. Haftka. Anti-optimization technique for structural design under load uncertainties. *Computer Methods in Applied Mechanics and Engineering*, 157:19–31, 1998.

[88] S. N. Lophaven, H. B. Nielsen, and J. Sondergaard. DACE: a Matlab Kriging toolbox. Version 2.0 IMM-TR-2002-12, Technical University of Denmark, Copenhagen, Denmark, 2002.

[89] D. J. C. MacKay. Bayesian interpolation. *Neural computation*, 4(3):415–447, 1992.

[90] K. V. Mardia. Measures of multivariate skewness and kurtosis with applications. *Biometrika*, 57(3):519–530, 1970.

[91] L. Maretta and R. Di Lorenzo. Influence of material properties variability on springback and thinning in sheet stamping processes: a stochastic analysis. *International Journal of Advanced Manufacturing Technology*, 51:117–134, 2010.

[92] Matlab. *Matlab manual version 7.13.0*. The MathWorks Inc, Natick, Massachusetts, USA, 2013.

[93] B. Möller and M. Beer. Engineering computation under uncertainty - capabilities of non-traditional models. *Computers and Structures*, 86:1024–1041, 2008.

[94] D. C. Montgomery. *Introduction to statistical quality control*. John Wiley & Sons Inc., New York, USA, 2005.

[95] D. C. Montgomery. *Design and analysis of experiments*. John Wiley & Sons Inc., New York, USA, 2009.

[96] L. P. Moreira and G. Ferron. Influence of the plasticity model in sheet metal forming simulations. *Journal of Materials Processing Technology*, 155–156:1596–1603, 2004.

[97] User Manual MSC.Marc. *User manual MSC.Marc volume B: element library*. MSC.Software Corporation, USA, 2010.

[98] M. De Munck, D. Moens, W. Desmet, and D. Vandepitte. A response surface based optimisation algorithm for the calculation of fuzzy envelope FRFs of models with uncertain properties. *Computers and Structures*, 86:1080–1092, 2008.

[99] M. Muzammil, P. Singh, and F. Talib. Optimization of gear blank casting process by using Taguchi's robust design technique. *Quality Engineering*, 15:351–359, 2003.

[100] R. H. Myers and D. C. Montgomery. *Response surface methodology*. John Wiley & Sons Inc., New York, USA, 2002.

[101] H. Naceur, Y. Guo, and S. Benelechi. Response surface methodology for design of sheet forming parameters to control springback effects. *Computers and Structures*, 84:1651–1663, 2006.

[102] H. C. Noh and T. Park. Monte Carlo simulation-compatible stochastic field for application to expansion-based stochastic finite element method. *Computers and Structures*, 84:2363–2372, 2006.

[103] J. T. Oden, T. Belytschko, J. Fish, T. J. R. Hughes, C. Johnson, D. Keyes, A. Laub, L. Petzold, D. Srolovitz, and S. Yip. Simulation based engineering science. Technical report, National Science Foundation, Arlington, USA, 2006.

[104] M. A. Osman, M. Shazly, A. El-Mokaddem, and A. S. Wifi. Springback prediction in V-die bending: modelling and experimentation. *Journal of Achievements in Materials and Manufacturing Engineering*, 38(2):179–186, 2010.

[105] R. Padmanabhan. *Reliability-based optimization for multidisciplinary system design*. PhD thesis, University of Notre Dame, Notre Dame, USA, 2003.

[106] R. Padmanabhan, M. C. Oliveira, J. L. Alves, and L. F. Menezes. Influence of process parameters on the deep drawing of stainless steel. *Finite Elements in Analysis and Design*, 43:1062–1067, 2007.

[107] M. Papila and R. T. Haftka. Response surface approximations: noise, error repair and modeling errors. *American Institute of Aeronautics and Astronautics*, 38:2336–2343, 2000.

[108] J. Paralikas, K. Salonitis, and G. Chryssolouris. Optimization of roll forming process parameters - a semi-empirical approach. *International Journal of Advanced Manufacturing Technology*, 47(9):1041–1052, 2010.

[109] G. J. Park, T. H. Lee, K. H. Lee, and K. H. Hwang. Robust design: an overview. *American Institute of Aeronautics and Astronautics*, 44:181–191, 2006.

[110] M. S. Phadke. *Quality engineering using robust design*. Prentice Hall, Englewood

Cliffs, New Jersey, USA, 1989.

[111] J. Post. *On the constitutive behaviour of Sandvik Nanoflex*. PhD thesis, University of Twente, Enschede, The Netherlands, 2004.

[112] W. H. Press, S. A. Teukolsky, W. T. Vetterling, and B. P. Flannery. *Numerical recipes*. Cambridge University Press, Cambridge, United Kingdom, 2007.

[113] R. K. Ray, J. J. Jonas, and R. E. Hook. Cold rolling and annealing textures in low carbon and extra low carbon steels. *International Materials Reviews*, 39(4):129–172, 1994.

[114] R. G. Regis and C. A. Shoemaker. Constrained global optimization of expensive black box functions using radial basis functions. *Journal of Global Optimization*, 31:153–171, 2005.

[115] J. Repalle and R. V. Grandhi. Design of forging process variables under uncertainties. *Journal of Materials Engineering and Performance*, 14:123–131, 2005.

[116] W. J. Roux, N. Stander, and R. T. Haftka. Response surface approximations for structural optimization. *International Journal for Numerical Methods in Engineering*, 42:517–534, 1998.

[117] J. O. Royset and E. Polak. Reliability-based optimal design using sample average approximations. *Probabilistic Engineering Mechanics*, 19:331–343, 2004.

[118] J. Sacks, Welch W. J., T. J. Mitchell, and H. P. Wynn. Design and analysis of computer experiments. *Statistical Science*, 4:409–423, 1989.

[119] T. Saenz de Argandon, J. Larranaga, A. Legarda, and L. Galdos. Roll forming set-up influence in the forming forces and profile quality. *Key Engineering Materials*, 504–506:1249–1254, 2012.

[120] A. Sahai, U. Schramm, T. Buranathiti, W. Chen, J. Cao, and C. Z. Xia. Sequential optimization and reliability assessment method for metal forming processes. In *Proceedings of the AIP conference, Columbus, USA*, 2004.

[121] M. Salmani Tehrani, H. Moslemi Naeini, P. Hartley, and H. Khademizadeh. Localized edge buckling in cold roll-forming of circular tube section. *Journal of Materials Processing Technology*, 177(1-3):617–620, 2006.

[122] T. Santner, B. Williams, and W. Notz. *The design and analysis of computer experiments*. Springer - Verlag, New York, USA, 2003.

[123] A. Savitzky and M. J. E. Golay. Smoothing and differentiation of data by simplified least squares procedures. *Journal of Analytical Chemistry*, 36:1627–1639, 1964.

[124] M. Schonlau. *Computer experiments and global optimization*. PhD thesis, University of Waterloo, Ontario, Canada, 1997.

[125] G. I. Schuëller and H. A. Jensen. Computational methods in optimization considering uncertainties - an overview. *Computer Methods in Applied Mechanics and Engineering*, 198:2–13, 2008.

[126] A. Selman, A. H. van den Boogaard, and J. Huétink. Wrinkling prediction procedure in thin sheet metal forming processes with adaptive mesh refinement. Part II : Wrinkling with contact. Technical report, Netherlands Institute for Metals Research

(NIMR), Delft, The Netherlands, 2001.

[127] B. Senthilkumar, S. Ponnambalam, and N. Jawahar. Process factor optimization for controlling pull-down defects in iron castings. *Journal of Materials Processing Technology*, 209:554–560, 2009.

[128] H. D. Sherali and V. Ganesan. An inverse reliability-based approach for designing under uncertainty with application to robust piston design. *Journal of Global Optimization*, 37(1):47–62, 2006.

[129] R. Shivpuri and W. Zhang. Robust design of spatially distributed friction for reduced wrinkling and thinning failure in sheet drawing. *Materials and Design*, 30:2043–2055, 2009.

[130] J. Shlens. A tutorial on principal component analysis. Technical report, New York University, Center for Neural Science, New York, USA, 2009.

[131] A. Y. D. Siem and D. den Hertog. Kriging models that are robust with respect to simulation errors. Center discussion paper 2007 - 68 1 - 29, University of Tilburg, Tilburg, The Netherlands, 2007.

[132] M. Sigvant. Influence on simulation results from material and process scatter. In *Proceedings of the International Deep Drawing Research Group (IDDRG) conference, Porto, Portugal*, 2006.

[133] T. W. Simpson, V. Toropov, V. Balabanov, and F. A. C. Viana. Design and analysis of computer experiments in multidisciplinary design optimization: a review of how far we have come - or not. In *Proceedings of the 12th AIAA/USAF/NASA/ISSMO Symposium on Multidisciplinary Analysis and Optimization, Victoria, Canada*, volume 2008–5802, 2008.

[134] T. de Souza. *Analysis of springback variation in sheet metal forming*. PhD thesis, Deaking University, Geelong, Australia, 2009.

[135] M. Strano. Optimization under uncertainty of sheet-metal-forming processes by the finite element method. *Proceedings of the Institution of Mechanical Engineers, Part B: Journal of Engineering Manufacture*, 220:1305–1315, 2006.

[136] G. Sun, G. Li, Z. Gong, X. Cui, X. Yang, and Y. Q. Li. Multiobjective robust optimization method for drawbead design in sheet metal forming. *Materials and Design*, 31:1917–1929, 2010.

[137] G. Taguchi. *Systems of experimental design*. Unipub / Kraus International Publication, New York, USA, 1987.

[138] Y. Tang and J. Chen. Robust design of sheet metal forming process based on adaptive importance sampling. *Structural and Multidisciplinary Optimization*, 39(5):531–544, January 2009.

[139] Ö. Tekaslan, U. Şeker, and A. Özdemir. Determining springback amount of steel sheet metal has 0.5 mm thickness in bending dies. *Materials and Design*, 27:251–258, 2006.

[140] Ö. Tekaslan, N. Gerger, and U. Şeker. Determination of spring-back of stainless steel sheet metal in V-bending dies. *Materials and Design*, 29:1043–1050, 2008.

[141] A. E. Tekkaya and P. A. F. Martins. Accuracy, reliability and validity of finite element analysis in metal forming: a users perspective. *Engineering Computations*, 26:1026–1056, 2009.

[142] A. N. Tikhonov and V. Y. Arsenin. *Solutions of ill-posed problems*. John Wiley & Sons Inc., New York, USA, 1977.

[143] V. Toropov, F. van Keulen, V. Markine, and H. de Boer. Multipoint approximations for structural optimization problems with noisy response functions. In *Proceedings of the 7th AIAA/USAF/NASA/ISSMO Symposium on Multidisciplinary Analysis and Optimization, Bellevue, USA*, volume A96-38701, pages 10–31, 1996.

[144] K. L. Tsui. A critical look at Taguchi's modelling approach for robust design. *Journal of Applied Statistics*, 23:81–96, 1996.

[145] F. van Keulen and V. V. Toropov. New developments in structural optimization using adaptive mesh refinement and multi-point approximations. *Engineering Optimization*, 29:217–234, 1997.

[146] P. van Liempt. Workhardening and substructural geometry of metals. *Journal of Materials Processing Technology*, 45:459–464, 1994.

[147] H. Vegter, Y. G. An, H. Pijlman, and J. Huétink. Advanced mechanical testing on aluminum alloys and low carbon steel for sheet forming. In *Proceedings of the International Conference on Numerical Simulation of 3D Sheet Metal Forming Processes (NUMISHEET), Besancon, France*, 1999.

[148] H. Vegter and A. H. van den Boogaard. A plane stress yield function for anisotropic sheet material by interpolation of biaxial stress states. *International Journal of Plasticity*, 22(3):557–580, 2006.

[149] Volkswagen Aktiengesellschaft. Volkswagen Polo body (licence for use of image DB2009AU00660 is granted by Volkswagen Aktiengesellschaft), September 2013.

[150] B. J. Williams, T. J. Santner, and W. I. Notz. Sequential design of computer experiments to minimize integrated response functions. *Statistica Sinica*, 10:1133–1152, 2000.

[151] K. Yang and B. El-Haik. *Design for Six Sigma; A roadmap for product development*. McGraw - Hill Inc., New York, USA, 2003.

[152] G. Zeng, S. H. Li, Z. Q. Yu, and X. M. Lai. Optimization design of roll profiles for cold roll forming based on response surface method. *Materials and Design*, 30(6):1930–1938, 2009.

[153] F. Zhang. *Identifying nonlinear variation patterns in multivariate manufacturing processes*. PhD thesis, Texas A&M University, College Station, USA, 2004.

[154] W. Zhang and R. Shivpuri. Probabilistic design of aluminium sheet drawing for reduced risk of wrinkling and fracture. *Reliability Engineering and System Safety*, 94:152–161, 2009.

Research deliverables

The key deliverables of this research project are presented below, i.e. journal publications, conference proceedings, reports, miscellaneous activities and awarded grants.

Journal publications

1. J.H. Wiebenga, A.H. van den Boogaard, and G. Klaseboer. Sequential robust optimization of a V-bending process using numerical simulations. *Structural and Multidisciplinary Optimization*, 46(1), 137-153, **2012**.

2. J.H. Wiebenga, M. Weiss, B. Rolfe and A.H. van den Boogaard. Product defect compensation by robust optimization of a cold roll forming process. *Journal of Materials Processing Technology*, 213(6), 978-986, **2013**.

3. J.H. Wiebenga, and A.H. van den Boogaard. On the effect of numerical noise in approximate optimization of forming processes using numerical simulations. *International Journal of Material Forming*, DOI 10.1007/s12289-013-1130-2, **2013**.

4. J.H. Wiebenga, E.H. Atzema, Y.G. An, H. Vegter and A.H. van den Boogaard. Effect of material scatter on the plastic behavior and stretchability in sheet metal forming. *Journal of Materials Processing Technology*, 214(2), 238-252, **2014**.

5. J.H. Wiebenga, E.H. Atzema, and A.H. van den Boogaard. Stretching the limits of forming processes by robust optimization: A demonstrator. Submitted. **2014**.

Conference proceedings

1. J.H. Wiebenga, G. Klaseboer and A.H. van den Boogaard. Robust optimization of metal forming processes using a metamodel-based strategy. In: *Proceedings of the European Scientific Association For Material Forming Conference (ESAFORM 2011)*, Belfast, Northern Ireland, **2011**.

2. J.H. Wiebenga, G. Klaseboer and A.H. van den Boogaard. Efficient robust optimization of metal forming processes using a sequential metamodel based strategy (session keynote presentation). In: *Proceedings of the International Conference on Numerical Simulation of 3D Sheet Metal Forming Processes (NUMISHEET 2011)*, Seoul, South Korea, **2011**.

3. J.H. Wiebenga, M. Weiss, B. Rolfe and A.H. van den Boogaard. A numerical approach to robust in-line control of roll forming processes. In: *Proceedings of the International Conference on Metal Forming*, Krakow, Poland, **2012**.

4. J.H. Wiebenga, E.H. Atzema, R. Boterman, M. Abspoel, A.H. van den Boogaard. Accounting for material scatter in sheet metal forming simulations. In: *Proceedings of the International Deep Drawing Research Group Conference (IDDRG 2013)*, Zurich, Switzerland, **2013**.

5. J.H. Wiebenga, E.H. Atzema and A.H. van den Boogaard. Stretching the limits of forming processes by robust optimization: A demonstrator. In: *Proceedings of the International Conference on Numerical Simulation of 3D Sheet Metal Forming Processes (NUMISHEET 2014)*, Melbourne, Australia, **2014**.

Reports

1. J.H. Wiebenga. Optimization under uncertainty of metal forming processes - an overview. *Literature report*, University of Twente, Enschede, The Netherlands, **2010**.

Miscellaneous

1. During this research project, the company Innprove Solutions was founded by J. Hol and J.H. Wiebenga. Innprove Solutions is an engineering company providing consultancy services and software solutions in the field of virtual design, tribological modeling and optimization (`www.innprove.com`). Innprove Solutions is a spin-off company of the University of Twente and the Materials innovation institute (M2i).

2. On March 22nd 2012, the symposium Robust Design in Forming Technology 2012 took place, organized by E.H. Atzema of Tata Steel and J.H. Wiebenga. The goal of this one-day mini-symposium was to discuss the latest developments and industrial applications of robust design and optimization in forming technology. Participants: 60. Location: Tata Steel congress centre in IJmuiden, in the Netherlands.

3. Within this research project and the preceding project [19], the software package OPTFORM has been developed. OPTFORM is a stand-alone optimization software for the robust design and optimization of forming processes using FE simulations. The robust optimization strategy and tools presented in this thesis form the foundation of the OPTFORM software.

Grants

1. This research was awarded by the Dutch Technology Foundation STW with a Valorisation Grant 1 (€25.000) to fund the transfer of excellent technical scientific research to the users (`www.stw.nl`). The author gratefully acknowledges STW for the funding of a commercial and technical feasibility study, to be performed by Innprove Solutions.

Dankwoord

Ergens boven de Indische Oceaan, januari 2014.

Het was de zomer van 2009 toen ik de vraag voorgeschoteld kreeg: 'Heb je interesse om een promotieonderzoek uit te voeren?' Mijn interesse was gewekt, maar ik had geen idee wat een promotieonderzoek inhield. Nu, vier en een half jaar later, ben ik onderweg naar Melbourne, Australië, voor de laatste conferentie in het kader van mijn promotieonderzoek. De vliegtijd bedraagt 22 uur, tijd genoeg dus om eens achterover te leunen en het laatste deel van mijn proefschrift op papier te zetten.

Het onderzoek zoals beschreven in dit proefschrift is uitgevoerd aan de Universiteit Twente onder de leerstoel Nonlinear Solid Mechanics binnen de vakgroep Technische Mechanica. Het project is onderdeel geweest van het programma van het onderzoeksinstituut M2i onder het projectnummer M22.1.08.303. Ik wil iedereen bedanken die op enige wijze heeft bijgedragen aan dit onderzoek en de totstandkoming van dit proefschrift. Een aantal mensen wil ik in het bijzonder op deze plek noemen en dank zeggen.

Als eerste wil ik mijn begeleider en promotor Ton van den Boogaard bedanken. Ton, door jouw ervaring in het vakgebied heb ik met mijn onderzoek een vliegende start kunnen maken. Op inhoudelijk vlak kon ik mij geen beter begeleider wensen. Papers, samenvattingen, rapporten, ze werden steevast voorzien van kritisch en opbouwend commentaar. Zelfs met de toenemende drukte in jouw agenda bleef je de puntjes op de welbekende 'i' zetten. Dank daarvoor! Daarnaast wil ik Han Huétink, Bert Geijselaers en Timo Meinders bedanken. Han, dank voor je begeleiding en humor in de opstartfase van het project. Geijs en Timo, bedankt voor jullie opmerkingen tijdens de groepsbijeenkomsten en daarbuiten. Juist doordat jullie iets meer afstand hadden tot de dagelijkse voortgang van mijn onderzoek, waren de opmerkingen vaak 'out-of-the-box' en brachten ze mij daarmee regelmatig tot nieuwe inzichten en ideeën. Timo, bij jou kom ik zo nog even terug…

Part of the work described in this thesis was conducted during a stay at the Deakin University in Geelong, Australia. I would like to thank Bernard Rolfe and Matthias Weiss for making this (still ongoing) cooperation possible and for providing the supervision. I would like to thank Jascha Marnette, Buddhika Abeyrathna and Akbar Abvabi for their work and assistance in the numerical and experimental studies. More importantly, I would like to thank you guys for a great time Down Under. Enjoying the sunshine and taking a surf at the world's greatest surf coast, with a tempting kangaroo steak ready to grill on a seaside barbeque, was a great way to spend the weekend (and the Friday afternoon). No worries, cheers mates.

Een groot deel (lees: het overgrote deel) van de resultaten beschreven in dit proefschrift hadden niet tot stand kunnen komen zonder de samenwerking met de industriële partners. Ik wil Eisso Atzema en Pascal Kömmelt (Tata Steel), Gerrit Klaseboer en Remco van Ravenswaaij (Philips), Corijn Snippe (Bosch) en Martin Petzoldt (Inpro) bedanken voor de actieve ondersteuning tijdens het onderzoek. Eisso en Gerrit, in het bijzonder wil ik jullie bedanken voor jullie intensieve inzet en de fijne samenwerking welke ons mooie resultaten heeft opgeleverd. Op deze plaats wil ik ook de stagiaires en afstudeerders bedanken waarmee ik samengewerkt heb om dit resultaat neer te zetten: Jaap Horenberg, Rudi Littelink, Rolf van der Velde, Maiko Buurman, Ivar Postma en Alice Baron. Het vele experimentele werk had niet zonder jullie hulp, overuurtjes en doorzettingsvermogen plaats kunnen vinden. Ook wil ik Tata Steel, en in het bijzonder Romke Boterman, bedanken voor de uitvoering van de vele experimenten welke in het laatste deel van dit proefschrift beschreven zijn. Ten slotte, dank aan Henk Vegter en Yuguo An voor de vele korte maar zeer waardevolle brainstorm- dan wel troubleshootingsessies.

Ik wil M2i en de Universiteit Twente bedanken voor de ruimte die ik heb gekregen om mijn werktijd flexibel in te delen, het ondersteunen van mijn verblijf in Australië, de mogelijkheid om een bedrijf te starten tijdens mijn promotieonderzoek, en de rest. De vrijheid die ik hierin kreeg heeft al met al zeer stimulerend voor mij gewerkt. Ik wil mijn collega's van Technische Mechanica en Ontwerp, Productie en Management bedanken voor de prettige werksfeer, voor de vele uurtjes koffiedrinken en de daarbij behorende gezelligheid. Jos Havinga, bedankt voor het deelnemen aan mijn leescommissie en je kritische blik op mijn proefschrift. Debbie en Tanja, zonder jullie hulp zou ik de helft mijn tijd aan organisatorische zaken kwijt zijn geweest. Bedankt voor alle hulp hierin en natuurlijk de dagelijkse verse koffie. Nico van Vliet en Axel Lok, bedankt voor het veelvuldig oplossen van problemen met software licenties, een weigerende laptop, tekort aan geheugencapaciteit (van mijn laptop) en andere

ICT gerelateerde zaken. Een speciaal woord van dank ben ik verschuldigd aan mijn kamergenoten Johan Hol en Daan Waanders voor het aanhoren van mijn (zinnige en onzinnige) opmerkingen, mijn frustratie over de muziekkeuze van de dag en voor het opeten van de kantoor-snoepjes. Het was een gezellige en mooie tijd en wij gaan nog even door. Johan, kerelt, zo langzamerhand horen ook wij bijna in het rijtje van Jip en Janneke, Peppi en Kokki, en Bert en Ernie thuis. Wij hebben veel tijd met elkaar doorgebracht om Innprove Solutions van de grond te krijgen, maar het is gelukt en dat is mede te danken aan jouw positiviteit, doorzettingsvermogen en vrolijkheid. Samen met Timo hebben wij heel wat mooie tripjes gemaakt, met Seoul als hoogtepunt. Mannen, bedankt voor de gezelligheid, humor, afleiding buiten het werk om en de vriendschap.

Dan it wichtichste diel fan myn proefskrift: ik wol myn famylje, skoanfamylje en freonen betankje foar jimme ynteresse en stipe yn de ôfrûne tiid. Heit en mem, tank foar jimme lústerjend ear, de motivearjende wurden yn 'e rin fan myn stúdzje en promoasje, en de leafde dy't ik van jimme krij. Jacob, tank datst myn paranimf bist en foar de ôflieding en bierkes neist it wurk. Guon dingen binne promoasjeûndersyk-eigen en sadwaande hie ik by dy altyd mar in pear wurden nedich om begrepen te wurden. Griete, leaf suske fan my, Remkes en Adriana, tank foar jimme waarmte en ynteresse. Leave Hilberta, it binne fjouwer enervearjende jierren west. Tegearre nei Swolle, in hûs keapje en ferbouwe, in heal jier yn Australië wenje, en doe't wy werom kamen binne we trout. Op 28 maaie 2013 hawwe wy it moaiste en leafste mantsje fan'e wrâld krigen, ús soan Brend Aizo. Neist dit alles wie ik dwaande mei myn promoasje, it gong faaks ta skea fan de tiid dy't wy tegeare hiene. Tank foar dyn begryp, dyn stipe en dyn leafde. Jimme meitsje my lokkich, ik hâld fan jimme.

Jan Harmen